



# SEARCHING FOR CHARGED LEPTON FLAVOUR VIOLATION IN TOP QUARK INTERACTIONS WITH THE ATLAS DETECTOR

By

WILLIAM GEORGE

A thesis submitted to  
the University of Birmingham  
for the degree of  
DOCTOR OF PHILOSOPHY

Particle Physics Research Group  
School of Physics and Astronomy  
College of Engineering and Physical Sciences  
University of Birmingham  
October 2023

---

## ABSTRACT

A search for charged lepton flavour violating (CLFV)  $t\mu\tau u_k$  interactions is presented, where  $u_k = \{u, c\}$ , using the ATLAS Run 2 dataset at  $\sqrt{s} = 13.0$  TeV. Observation of such a process, which is strictly prohibited in the Standard Model (SM) of particle physics, would be a clear indicator of new physics. The search targets  $t\mu\tau u_k$  interactions in both single top quark production and  $t\bar{t}$  decay, considering events with two muons, a hadronically-decaying tau lepton and at least one jet, of which exactly one must be  $b$ -tagged. In absence of a significant excess above the SM background, an exclusion limit is placed on the CLFV branching ratio  $\mathcal{B}(t \rightarrow \mu\tau q) < 8.7 \times 10^{-7}$  at 95% confidence level (CL). Constraints are placed on SM effective field theory Wilson coefficients ranging from  $c_{\ell equ}^{3(2313)}/\Lambda^2 < 0.10 \text{ TeV}^{-2}$  for  $\mu\tau ut$  to  $c_{\ell equ}^{1(2323)}/\Lambda^2 < 1.8 \text{ TeV}^{-2}$  for  $\mu\tau ct$  (95% CL). The  $gu_k \rightarrow t\mu\tau$  process could be mediated by a scalar leptoquark. Assuming a fixed hierarchy of couplings to lepton-quark pairs, exclusion limits are placed on leptoquark coupling strengths  $1.12 < \lambda < 3.29$  for masses between 0.5 and 2.0 TeV. The sensitivity of the search is statistically limited and would benefit greatly from the inclusion of future ATLAS datasets. The new ATLAS ITk detector will be crucial to recording high quality data after Run 3; quality assurance measurements are presented which validate the technologies employed by the ITk strip sensors.

Dedicated to my parents, and to Mimi.

## AUTHOR'S CONTRIBUTIONS

Successful operation of the LHC and the ATLAS detector rely on the work of hundreds of experts and shifters monitoring the data-taking process around the clock, seven days of the week. Analysis of the data involves the work of hundreds more members across the ATLAS collaboration to ensure the data are of high quality and to produce and validate simulations of collision events. The work described in this thesis would not have been possible without the efforts of all of those involved in the LHC and ATLAS.

Chapter 2 presents theoretical material to give context to and motivate the following chapters and is not the work of the author. The same is true of Chapter 3, which gives an overview of the LHC and the ATLAS detector, drawing from Ref. [1]. However, the author has contributed to detector operation through ATLAS control room shifts, monitoring the status and data-taking quality of the Inner Detector during the Run 3 period of LHC operation.

Chapter 4 describes the author's qualification task for ATLAS authorship. In addition to assembling the described setup and performing measurements of ITk test devices, the author was involved in the annealing of these devices and in the testing of miniature sensors, which is not discussed here.

Chapter 5 gives an introduction to the simulation and reconstruction of physics events with the ATLAS detector; this is not the work of the author. Chapters 6 and 7 describe an analysis performed by this author. The MC samples described in Section 6.3 are ATLAS samples and have not been produced by the author. The exception to this is the set of signal samples described in Section 6.3.2 which have been generated by the author using

---

a setup produced by a collaborator. Preliminary results from this analysis have already been released in [2] which are also the work of the author. The re-optimised analysis with improved sensitivity, discussed in Chapters 6 and 7, is undergoing the final steps of ATLAS approval having been unblinded and a draft publication prepared. The projection of expected exclusion limits to larger datasets in Chapter 8 is also the work of the author.

## ACKNOWLEDGEMENTS

I would like to thank all of the people who have helped and advised me throughout my PhD and made the work in this thesis possible. First of all, my supervisors, Miriam Watson and Laura Gonella, for all of your support and guidance in the past four years and beyond. I have learned so much from you both and cannot thank you enough for providing me with direction and motivation throughout my research. Thank you particularly to Miriam for all of the helpful feedback on drafts of my thesis, even in the hours before submission.

I also owe thanks to everyone in the Birmingham particle physics group, in particular in the ATLAS and BILPA groups, for feedback throughout my PhD and for providing such a friendly and supportive environment. It has been a pleasure to work alongside so many talented scientists. Many thanks go to Laura, Phil Allport and Ioannis Kopsalis for all of the help and expertise you provided on ITk measurements, both in and out of the lab, and for the opportunities to present work in international ITk strip community meetings. I am also very grateful to all of the members of the charged lepton flavour violation analysis for their advice, expertise and collaboration: Miriam Watson, Chris Hawkes and Alexis Stampekis at the University of Birmingham, Markus Cristinziani and Gabriel Gomes, at the University of Siegen and Carlo Gottardo at CERN. Special thanks must go to Jacob, for the constant support and suggestions you have provided via Skype be it day or night, and to Miriam, for your advice and insight throughout.

Thanks also go to my friends and fellow students, particularly Gareth, Harry and Júlia, for all of the fun and moral support along the way. In addition, thanks to all of those I met at CERN for some unforgettable adventures exploring Switzerland and some hard to

---

remember canettes. Thank you to all of my friends in Birmingham who have made the eight years such a fantastic and memorable experience. I am very sad to be leaving Birmingham after so many amazing years and will be a regular visitor.

To my amazing partner Mimi, for encouraging me every day and for putting up with me when I was stressed and tired. I don't know how I would have done it without you.

Finally, I would like to thank my incredible family, for your unwavering support in everything I do and have done over the last 26 years, for which I will always be grateful. I would not be where I am today without you.

# Contents

	Page
<b>List of Figures</b>	<b>xii</b>
<b>List of Tables</b>	<b>xvi</b>
<b>Definition of acronyms</b>	<b>xviii</b>
<b>1 Introduction</b>	<b>1</b>
<b>2 Theory</b>	<b>4</b>
2.1 The Standard Model of particle physics . . . . .	5
2.1.1 Development of the Standard Model . . . . .	5
2.1.2 Theoretical framework . . . . .	9
2.1.3 Electroweak symmetry breaking . . . . .	13
2.1.4 The generation of fermion masses . . . . .	15
2.1.5 Flavour in the SM . . . . .	16
2.2 Beyond the Standard Model . . . . .	17
2.2.1 Neutrino mass and oscillation . . . . .	17
2.2.2 Charged lepton flavour violation . . . . .	19
2.2.3 Effective field theory . . . . .	22
<b>3 The ATLAS experiment</b>	<b>24</b>
3.1 The Large Hadron Collider . . . . .	24

---

3.2	The ATLAS detector . . . . .	27
3.2.1	Inner detector . . . . .	29
3.2.2	Calorimeters . . . . .	31
3.2.3	Muon spectrometer . . . . .	33
3.2.4	Trigger and data acquisition system . . . . .	34
<b>4</b>	<b>The ATLAS inner tracker upgrade</b>	<b>36</b>
4.1	Silicon radiation detectors in high energy physics . . . . .	38
4.1.1	Electronic properties of silicon . . . . .	38
4.1.2	Silicon radiation sensors . . . . .	42
4.1.3	Effect of radiation on silicon detectors . . . . .	43
4.2	The ATLAS inner tracker upgrade . . . . .	44
4.3	ITk strip sensor QA programme . . . . .	46
4.3.1	QA test devices . . . . .	46
4.3.2	Test chip measurement setup . . . . .	48
4.3.3	Test chip and MD8 measurements . . . . .	52
4.3.4	Conclusions . . . . .	65
<b>5</b>	<b>Physics at the LHC</b>	<b>67</b>
5.1	Hadron collider physics . . . . .	68
5.2	Physics simulation . . . . .	70
5.2.1	Event generation . . . . .	70
5.2.2	Pileup and underlying event modelling . . . . .	71
5.2.3	Detector simulation . . . . .	72
5.3	Physics object reconstruction and calibration . . . . .	73
5.3.1	Electrons . . . . .	73
5.3.2	Muons . . . . .	75
5.3.3	Jets . . . . .	76

5.3.4	Flavour tagging . . . . .	77
5.3.5	Missing transverse energy . . . . .	78
5.3.6	Hadronically-decaying tau leptons . . . . .	78
5.3.7	Non-prompt lepton rejection . . . . .	80
5.3.8	Overlap removal . . . . .	81
5.4	Top quark physics . . . . .	81
<b>6</b>	<b>Searching for CLFV in top quark interactions</b>	<b>83</b>
6.1	Overview of CLFV searches . . . . .	83
6.2	Analysis strategy . . . . .	85
6.2.1	Effective field theory framework . . . . .	87
6.2.2	Leptoquark model . . . . .	89
6.3	Data and simulated samples . . . . .	91
6.3.1	Data . . . . .	92
6.3.2	EFT signal samples . . . . .	93
6.3.3	Leptoquark signal samples . . . . .	95
6.3.4	$t\bar{t}$ and $t\bar{t}\gamma$ . . . . .	96
6.3.5	Single top samples . . . . .	97
6.3.6	$t\bar{t}V$ . . . . .	98
6.3.7	Weak boson processes . . . . .	98
6.3.8	Other SM . . . . .	99
6.4	Object and event selection . . . . .	99
6.4.1	Event pre-selection and triggering . . . . .	100
6.4.2	Analysis regions . . . . .	102
6.4.3	Fitted SR observable . . . . .	105
6.4.4	Background composition . . . . .	109
6.4.5	Non-prompt muon composition . . . . .	111

6.4.6	Fake $\tau_{\text{had-vis}}$ composition . . . . .	114
6.5	Fake $\tau_{\text{had-vis}}$ estimation . . . . .	118
6.6	Non-prompt muon estimation . . . . .	123
6.7	Systematic uncertainties . . . . .	124
6.7.1	Experimental uncertainties . . . . .	124
6.7.2	Theoretical uncertainties . . . . .	126
6.7.3	Cross-section uncertainties . . . . .	131
6.7.4	Fake estimation uncertainties . . . . .	132
<b>7</b>	<b>CLFV search results</b>	<b>134</b>
7.1	Statistical analysis framework . . . . .	134
7.1.1	Parameter estimation . . . . .	135
7.1.2	Nuisance parameter treatment . . . . .	137
7.1.3	Extracting limits on the CLFV process . . . . .	138
7.1.4	Expected results: full Asimov fit . . . . .	140
7.1.5	Expected results: Mixed data and Asimov fit . . . . .	144
7.2	Results . . . . .	156
7.2.1	Preliminary results . . . . .	156
7.2.2	Full results . . . . .	160
7.3	EFT interpretation . . . . .	169
7.3.1	EFT interpretation procedure . . . . .	169
7.3.2	EFT results . . . . .	170
7.4	Leptoquark interpretation . . . . .	175
7.4.1	LQ interpretation procedure . . . . .	175
7.4.2	Exclusion limits on the LQ model . . . . .	178
7.4.3	LQ results . . . . .	178
<b>8</b>	<b>Conclusions</b>	<b>183</b>

<b>References</b>	<b>188</b>
<b>Appendices</b>	<b>203</b>
<b>A Event selection</b>	<b>203</b>
A.1 Analysis framework for preliminary results . . . . .	203
A.2 Signal contamination removal . . . . .	204
<b>B Herwig alternative signal sample reweighting</b>	<b>207</b>
B.1 Reweighting procedure . . . . .	209
B.2 Signal parton shower uncertainty . . . . .	211
<b>C Fake <math>\tau_{\text{had-vis}}</math> background estimation</b>	<b>213</b>
C.1 Fake $\tau_{\text{had-vis}}$ SF parametrisation . . . . .	213
<b>D Statistical analysis</b>	<b>216</b>
D.1 Validity of asymptotic approximation in limit-setting . . . . .	216
<b>E EFT interpretation</b>	<b>219</b>
E.1 Additional information on EFT samples . . . . .	219
<b>F Leptoquark interpretation</b>	<b>221</b>

# List of Figures

2.1	Particle content of the Standard Model. . . . .	8
2.2	Feynman diagrams for $e^-e^- \rightarrow e^-e^-$ scattering. . . . .	12
2.3	Feynman diagram demonstrating CLFV via a neutrino oscillation. . . . .	19
2.4	Corrections to Higgs boson self-energy. . . . .	21
3.1	Planned LHC/HL-LHC run schedule as of January 2022. . . . .	25
3.2	The CERN accelerator complex in January 2022. . . . .	26
3.3	Diagram of the ATLAS detector. . . . .	28
3.4	Diagram of the ATLAS inner detector. . . . .	29
3.5	Diagram of the ATLAS calorimeters. . . . .	32
3.6	Diagram of the ATLAS muon spectrometer. . . . .	34
4.1	Diagram of the ATLAS ITk. . . . .	37
4.2	The development of a depletion region across a p-n junction. . . . .	40
4.3	Layout of the ATLAS Inner Tracker upgrade. . . . .	45
4.4	Diagram showing structures on ATLAS test chip. . . . .	47
4.5	ITk QA test chip setup: silicon QA piece mounted on a PCB. . . . .	49
4.6	ITk QA test chip setup: measurement instruments. . . . .	50
4.7	Image of test chip showing coupling capacitor and field oxide capacitor structures. . . . .	51
4.8	Plot of MD8 IV curves for six MD8 devices. . . . .	55
4.9	Plot of MD8 bulk capacitance for two MD8 devices. . . . .	58
4.10	Plot of IV scans of bias resistors. . . . .	59

4.11	Plot of effective resistance of PTP structures. . . . .	65
5.1	Mean number of interactions per bunch crossing during Run 2. . . . .	72
5.2	Feynman diagrams showing top quark production processes at the LHC. . .	82
6.1	Example Feynman diagrams for the EFT signal processes . . . . .	86
6.2	Diagram demonstrating hierarchy of leptoquark Yukawa couplings. . . . .	91
6.3	Example Feynman diagrams for the LQ signal processes. . . . .	95
6.4	Distribution of the $H_T$ variable in $VR\mu$ . . . . .	107
6.5	Distribution of the $H_T$ variable for signal and background processes. . . . .	108
6.6	Lepton composition of background processes entering each analysis region. .	110
6.7	Origin of muons according to MC truth information. . . . .	113
6.8	Parton initiating jets truth matched to fake $\tau_{\text{had-vis}}$ . . . . .	115
6.9	Number of interaction vertices in each event for $\tau_{\text{had-vis}}$ candidates. . . . .	116
6.10	Distribution of JVT score for the jet seeding $\tau_{\text{had-vis}}$ reconstruction. . . . .	117
6.11	Distribution of jet width in $CR\tau$ . . . . .	119
6.12	Number of $\tau_{\text{had-vis}}$ with 1-prong and 3-prong in $CR\tau$ . . . . .	120
6.13	Distribution of data in $CR\tau$ after subtraction of the true $\tau_{\text{had-vis}}$ background in MC, along with MC fake $\tau_{\text{had-vis}}$ distribution. . . . .	121
6.14	Fake $\tau_{\text{had-vis}}$ SFs and fake $\tau_{\text{had-vis}}$ estimation in SR. . . . .	121
7.1	Pre-fit and post-fit plots for the fit to an Asimov dataset. . . . .	141
7.2	Normalisation factors computed in the fit to an Asimov dataset. . . . .	141
7.3	Correlation matrix for the fit to an Asimov dataset. . . . .	143
7.4	Pre-fit and post-fit plots for the fit to a mixed data and Asimov dataset. . .	145
7.5	Normalisation factors computed in the fit to a mixed data and Asimov dataset.	145
7.6	Post-fit nuisance parameter values for the fit to a mixed data and Asimov dataset. . . . .	147

7.7	Plots showing $\pm 1\sigma$ variations of pulled nuisance parameters. . . . .	148
7.8	Pre-fit and post-fit plots of $VR\mu$ for the fit to a mixed data and Asimov dataset. . . . .	150
7.9	Correlation matrix for the fit to a mixed data and Asimov dataset. . . . .	151
7.10	Ranking of NP for the fit to a mixed data and Asimov dataset. . . . .	152
7.11	Ranking of NP for the fit to a mixed data and Asimov dataset with signal injection. . . . .	155
7.12	Preliminary pre-fit and post-fit plots for the fit to the unblinded dataset. . . . .	157
7.13	Preliminary fitted value of $\mu_{CLFV}$ . . . . .	157
7.14	Pre-fit and post-fit plots for the fit to the unblinded dataset. . . . .	161
7.15	Fitted value of $\mu_{CLFV}$ . . . . .	162
7.16	Pre-fit and post-fit plots for the fit to the unblinded dataset. . . . .	163
7.17	Post-fit nuisance parameter values for the fit to the unblinded dataset. . . . .	166
7.18	Ranking of NP for the fit performed using data across all analysis regions. . . . .	167
7.19	Exclusion limits on SMEFT Wilson coefficients. . . . .	173
7.20	Exclusion limits on $\mathcal{B}(t \rightarrow \mu\tau q)$ and SMEFT Wilson coefficients. . . . .	174
7.21	Expected pre-fit event yields in the SR including LQ signal contributions. . . . .	177
7.22	Exclusion limits on the cross-section of the $gu_k \rightarrow S_1\ell \rightarrow t\ell\ell'$ process. . . . .	179
7.23	Exclusion limits on the $S_1$ leptoquark coupling strength $\lambda$ and mass $m_{S_1}$ . . . . .	182
A.1	Signal and background distributions in early analysis region $CR\mu$ . . . . .	205
A.2	Distribution of the $H_T$ variable in $VR\mu$ . . . . .	206
B.1	Invariant mass plots for hadronic taus decays $\tau^\pm \rightarrow \nu_\tau \pi^\pm \pi^0$ & $\tau^\pm \rightarrow \nu_\tau \pi^\pm$ . . . . .	210
B.2	Effect of $\pm 1\sigma$ variations of the signal parton shower nuisance parameters. . . . .	212
C.1	Alternative parametrisation of fake $\tau_{\text{had-vis}}$ scale factors. . . . .	215

D.1	Plots of p-values for signal-plus-background and background-only hypotheses using toy datasets and comparison of limits obtained using toys to limits using the asymptotic approximation. . . . .	218
E.1	$H_T$ distributions for each of the EFT signal contributions. . . . .	220
F.1	Exclusion limits at on the cross-section of the $gu_k \rightarrow S_1 \ell \rightarrow t \ell \ell'$ process. . .	225
F.2	Exclusion limits at on the cross-section of the $gu_k \rightarrow S_1 \ell \rightarrow t \ell \ell'$ process. . .	226

# List of Tables

2.1	Fermion content of the Standard Model. . . . .	11
4.1	Fluences and TID of test devices. . . . .	53
4.2	MD8 leakage currents for six MD8 devices. . . . .	54
4.3	Measurements of bias resistance. . . . .	60
4.4	Coupling capacitor capacitance and current measurements. . . . .	61
4.5	Measurements of inter-strip resistance. . . . .	62
4.6	Measurements of inter-strip capacitance. . . . .	63
5.1	<b>Tight</b> and <b>Loose</b> electron definitions. . . . .	74
5.2	<b>Tight</b> and <b>Loose</b> muon definitions. . . . .	76
5.3	<b>Tight</b> and <b>Loose</b> $\tau_{\text{had-vis}}$ definitions. . . . .	80
6.1	SMEFT operators capable of introducing CLFV $t\mu\tau u_k$ interactions. . . . .	88
6.2	Indirect constraints on CLFV $t\mu\tau u_k$ EFT operators. . . . .	88
6.3	MC generators used to simulate signal and background processes. . . . .	92
6.4	Theoretical cross-sections for CLFV $t\mu\tau u_k$ interactions. . . . .	94
6.5	Values of leptoquark coupling and mass parameters considered. . . . .	96
6.6	Trigger selection for all data taking years used in the CLFV analysis. . . . .	100
6.7	Description of common selection cuts applied to regions used in the analysis. . . . .	101
6.8	Definitions of analysis regions. . . . .	103
6.9	MC yields for each analysis region. . . . .	111
6.10	Values of fake $\tau_{\text{had-vis}}$ SFs binned in jet width and track multiplicity. . . . .	122

7.1	Expected limits on $\mathcal{B}(t \rightarrow \mu\tau q)$ . . . . .	144
7.2	Preliminary exclusion limits on $\mathcal{B}(t \rightarrow \mu\tau q)$ . . . . .	158
7.3	Preliminary exclusion limits on SMEFT Wilson coefficients. . . . .	159
7.4	Post-fit event yields for the signal region (SR) and $CRt\bar{t}\mu$ . ‘Total’ refers to the sum of the signal and background yields, with the systematic uncertainty taking into account correlations as determined by the fit. . . . .	164
7.5	Post-fit event yields in the SR. . . . .	165
7.6	Expected limits on $\mathcal{B}(t \rightarrow \mu\tau q)$ . . . . .	168
7.7	Quark flavour in the CLFV vertex for $t\bar{t}$ decay signal. . . . .	170
7.8	Exclusion limits on SMEFT Wilson coefficients. . . . .	171
7.9	Exclusion limits on the $S_1$ leptoquark coupling strength $\lambda$ for different masses $m_{S_1}$ . . . . .	181
8.1	Expected exclusion limits on CLFV $t\mu\tau u_k$ interactions with the inclusion of Run 3 and HL-LHC datasets. . . . .	186
8.2	Theoretical cross-sections in $pp$ collisions at $\sqrt{s} = 13.0$ and $13.6$ TeV. . . . .	187
B.1	Tau lepton branching fractions for inclusive EFT signal samples. . . . .	208
D.1	Expected exclusion limits on $\mu_{\text{CLFV}}$ extracted from the mixed data and Asimov fit using both MC toys and the asymptotic approximation. . . . .	217
F.1	Theoretical cross-sections for the process $gc \rightarrow S_1\ell \rightarrow t\ell\ell'$ . . . . .	223
F.2	Theoretical cross-sections for the process $gc \rightarrow S_1\ell \rightarrow t\ell\ell'$ . . . . .	224

# Definition of acronyms

<b>2HDM</b>	two Higgs doublet model
<b>ALICE</b>	A Large Ion Collider Experiment
<b>ATLAS</b>	A Toroidal LHC ApparatuS
<b>BEH</b>	Brout-Englert-Higgs
<b>BF</b>	branching fraction
<b>BSM</b>	beyond the SM
<b>CCE</b>	charge collection efficiency
<b>CERN</b>	the European Organization for Nuclear Research
<b>CKM</b>	Cabibbo–Kobayashi–Maskawa
<b>CL</b>	confidence level
<b>CLFV</b>	charged lepton flavour violation
<b>CM</b>	centre-of-mass
<b>CMS</b>	Compact Muon Solenoid
<b>CPV</b>	charge-parity violation
<b>CR</b>	control region
<b>CV</b>	capacitance-voltage
<b>DAQ</b>	data acquisition system
<b>dim-6</b>	dimension-6
<b>DIS</b>	deep inelastic scattering
<b>DUT</b>	device-under-test
<b>ECAL</b>	electromagnetic calorimeter

<b>EFT</b>	effective field theory
<b>EW</b>	electroweak
<b>EWSB</b>	electroweak symmetry-breaking
<b>FCal</b>	forward calorimeter
<b>FSR</b>	final state radiation
<b>GSW</b>	Glashow-Salam-Weinberg
<b>GUT</b>	grand unified theory
<b>HCAL</b>	hadronic calorimeter
<b>HL-LHC</b>	high luminosity Large Hadron Collider (LHC)
<b>HLT</b>	high-level trigger
<b>HV</b>	high voltage
<b>IBL</b>	Insertable B-Layer
<b>ID</b>	inner detector
<b>IP</b>	interaction point
<b>ISR</b>	initial state radiation
<b>ITk</b>	Inner Tracker
<b>IV</b>	current-voltage
<b>JER</b>	jet energy resolution
<b>JES</b>	jet energy scale
<b>JVT</b>	jet vertex tagger
<b>L1</b>	level-1
<b>LAr</b>	liquid argon
<b>LHC</b>	Large Hadron Collider
<b>LHCb</b>	Large Hadron Collider beauty
<b>LFV</b>	lepton flavour violation
<b>LO</b>	leading order
<b>LQ</b>	leptoquark
<b>PDF</b>	parton density function
<b>PMNS</b>	Pontecorvo–Maki–Nakagawa–Sakata
<b>QA</b>	quality assurance

<b>QCD</b>	Quantum Chromodynamics
<b>QED</b>	Quantum Electrodynamics
<b>QFT</b>	quantum field theory
<b>MC</b>	Monte Carlo
<b>ME</b>	matrix element
<b>MIP</b>	minimum-ionising particle
<b>MPI</b>	multiple parton interactions
<b>MS</b>	muon spectrometer
<b>NIEL</b>	non-ionising energy loss
<b>NLO</b>	next-to-leading order
<b>NNLO</b>	next-to-next-to-leading order
<b>NP</b>	nuisance parameter
<b>PFlow</b>	particle flow
<b>PLV</b>	prompt lepton veto
<b>POI</b>	parameter of interest
<b>PTP</b>	punch-through protection
<b>SCT</b>	semiconductor tracker
<b>SF</b>	scale factor
<b>SM</b>	Standard Model
<b>SMEFT</b>	Standard Model effective field theory
<b>SR</b>	signal region
<b>SUSY</b>	supersymmetry
<b>TES</b>	tau energy scale
<b>TID</b>	total ionising dose
<b>TRT</b>	transition radiation tracker
<b>vev</b>	vacuum expectation value
<b>VR</b>	validation region

# Chapter 1

## Introduction

With the discovery of the Higgs boson by the ATLAS and CMS collaborations at the LHC [3, 4], the Standard Model (SM) provides a complete description of three of the four fundamental forces of nature. Nevertheless, there remain a number of unanswered questions about the nature of the universe for which the SM provides no answer. The next challenge facing particle physicists will be to search for hints of a deeper underlying theory which can address these open questions. One possible indication of beyond the SM (BSM) physics would be an observation of charged lepton flavour violation (CLFV). Charged lepton flavour is strictly conserved in the SM and, while neutrino oscillations indicate lepton flavour violation (LFV) in neutral leptons, this does not introduce CLFV at scales to which experiments are sensitive.

One of the areas of analysis of the ATLAS experiment is the study of the top quark, the heaviest of the known fundamental particles. Top quark pairs are produced copiously at the LHC and their decay signature is well understood so they provide a sensitive probe for new physics processes. According to the SM, charged leptons must be produced in association with either their antiparticle, for example through  $Z \rightarrow \mu^+ \mu^-$ , or with a neutrino of the same flavour, such as via  $W \rightarrow \mu^- \bar{\nu}_\mu$ , a condition known as lepton flavour conservation. This

condition is not imposed, however, by many BSM theories which could allow CLFV to be observed at the LHC. This thesis will present an analysis searching for  $t\mu\tau u_k$  interactions forbidden by the SM. The analysis makes use of the ATLAS Run 2 dataset corresponding to  $140.1\pm 1.2 \text{ fb}^{-1}$  of  $pp$  collisions<sup>1</sup> at  $\sqrt{s} = 13.0 \text{ TeV}$  [5].

The LHC experiments are currently taking data from the machine's third period of operation (Run 3) which is expected to increase the total integrated luminosity collected by the ATLAS detector to  $300 \text{ fb}^{-1}$ . At the end of Run 3, upgrades will begin on the LHC machine to increase the instantaneous luminosity. The ATLAS detector will also undergo an upgrade in this period to maintain physics performance as the LHC enters the high luminosity phase. The upgrade to the tracking detector will increase the granularity of the detector, to maintain tracking performance as the number of particles traversing the detector in a given time increases. As well as this, the detector must be capable of withstanding the harsh radiation environment it will be exposed to during this period of operation. A new all-silicon tracking detector will be installed into the ATLAS detector for the high luminosity LHC (HL-LHC) era. The new Inner Tracker (ITk) will consist of a pixel detector surrounded by a strip detector at larger radius and is currently approaching the production stage. A rigorous programme of quality assurance (QA) is underway to ensure the sensors which have been designed will meet the required specifications during production.

This thesis presents the work undertaken by the author over the course of four years of research. Chapter 2 introduces the development and theoretical framework of the SM of particle physics, before discussing its shortcomings and possible extensions to address these, giving particular attention to models which introduce CLFV. Chapter 3 presents an overview of the LHC accelerator complex and the design of the ATLAS detector. Chapter 4 describes the working principle of silicon radiation sensors, as used in charged particle tracking detectors,

---

<sup>1</sup>The amount of data delivered to the LHC experiments is measured by the integrated luminosity in units of  $\text{fb}^{-1}$  where  $1 \text{ fb}^{-1} = 10^{43} \text{ cm}^{-2}$ .

before discussing the future upgrade of the ATLAS tracking detector. Chapters 5 to 7 present the methodology and results of the first direct search for CLFV in  $t\mu\tau u_k$  interactions, using data from the ATLAS detector. Finally, Chapter 8 draws conclusions on the results of the preceding chapters and discusses possible future studies.

# Chapter 2

## Theory

The SM of particle physics provides a coherent description of the fundamental particles making up the universe and the interactions between them. The model is built upon quantum field theory (QFT) and successfully describes the behaviour of three of the fundamental forces mediating the interactions between matter particles. The strong, weak and electromagnetic interactions can all be shown to originate in the exchange of force particles, known as bosons. While a theory successful in incorporating gravity and providing a unified description of all four fundamental forces has so far eluded theorists, the gravitational interaction is significantly weaker than the other three forces and can therefore be neglected up to all but the highest energy scales.

---

## 2.1 The Standard Model of particle physics

### 2.1.1 Development of the Standard Model

The particle content of the SM can be separated into two classes: fermions, which make up the matter content of the universe, and bosons, which mediate the forces. Fermions, so-called because they obey Fermi-Dirac statistics [6, 7], are particles with half-integer spin angular momentum (spin), while bosons obey Bose-Einstein statistics [8–10], and possess integer spin. A crucial distinction between these two classes arises from the Pauli exclusion principle which states that any two identical fermions may not occupy the same quantum mechanical state [11]. As a consequence, fermions are assigned to energy levels when placed inside a potential, first occupying the lowest energy states. Electronic states within the atom are defined by the three quantum numbers which specify the electron probability density within the atom, along with the spin projection onto a given reference axis which may either be up or down. This behaviour gives rise to the structure of atomic energy levels as described by the Bohr model of the atom [12].

All of the matter encountered on a daily basis is made up of just three particles, which together make up all of the chemical elements of the periodic table. Elements consist of unique combinations of protons and electrons, with variable numbers of neutrons. The electron was the first fermion to be discovered, in 1897 by J. J. Thomson [13]. Unlike the electron, the proton and neutron were found to be composite particles made up of the fundamental up and down quarks. Together with the neutrino, which is produced alongside the electron in nuclear  $\beta$ -decay, these four fundamental particles constitute the first generation of fermions. These are supplemented by two additional generations, identical in all properties except mass.

The first suggestions of a second family, or generation, of fundamental particles emerged in 1947. The muon had been discovered ten years earlier [14] but was initially mistaken for

---

the pion, predicted by Yukawa as the mediator of interactions between nucleons [15], due to its similar mass. Studies in Bristol provided the first evidence that the muon and pion were distinct particles [16], now recognised as the discovery of the pion. The same year saw the observation of cloud chamber events in which two particles of opposite charge appeared with no incoming track [17]. These were later identified as originating from neutral kaon decays, marking the first sighting of second generation quarks.

The observation and cataloguing of a plethora of hadrons in the following years led Murray Gell-Mann to propose a classification system known as the “eightfold way” [18], much like that of chemical elements in the periodic table. The descriptions of protons, neutrons and the other hadrons known at the time in terms of constituent particles, known as quarks, proved a useful mathematical framework for explaining the eightfold way. George Zweig similarly proposed that mesons and baryons are composite particles made up of fundamental constituents [19], noting that the constituents may only be a useful mathematical construction rather than physical particles. Experimental evidence for quarks finally arrived when electron scattering experiments at the Stanford Linear Accelerator Center (SLAC) demonstrated inelastic scattering rates consistent with point-like constituents within hydrogen and deuterium nuclei, as described in [20], in a manner very similar to the discovery of atomic structure by Rutherford scattering [21]. It is now understood that the confinement property of the strong interaction prevents the existence of bare quarks outside of bound hadrons for any measurable period of time. The observation of hadrons, such as the  $\Omega^-$  baryon predicted by Gell-Mann, consisting of three quarks of the same flavour, seemingly in contradiction with the Pauli exclusion principle, led to the suggestion that quarks possessed an extra unobservable charge [22, 23], now called colour charge.

Further experiments at SLAC led to the discovery of the tau lepton in 1975 [24] through the sighting of  $e^+e^- \rightarrow e^\pm\mu^\mp + X$  events, where  $X$  represents  $\geq 2$  undetected particles, consistent with originating from the decay of a pair of particles with mass 1.6-

---

2.0 GeV/ $c^2$ . The top quark, discovered at the Tevatron collider in 1995 [25, 26], is the most massive fundamental particle observed. The first direct observation of tau neutrino interactions in 2000 by the purpose-built DONUT experiment at Fermilab [27] completed the picture of the matter content of the SM. To date there is no evidence for further generations of fermions. The reason for the existence of three copies of the matter particles is not understood.

The modern concept of the photon as the quantised form of light originates with Einstein in 1905 [28]. A description of photon-fermion interactions in the formalism of relativistic QFT, known as Quantum Electrodynamics (QED), led to the 1965 Nobel Prize being awarded to Feynman, Schwinger and Tomonaga for their role in the development of the theory [29]. Building upon the ideas of QED, similar theories were sought after for the weak and strong interactions. In 1968 a unified description of the weak and electromagnetic interactions, given by the Glashow-Salam-Weinberg (GSW) theory [30, 31], was proposed. In addition to predicting charged  $W^\pm$  bosons that could mediate  $\beta$ -decay, the model required a neutral  $Z$  boson. In remarkable consistency with the theory, both of these particles were discovered fifteen years later by the UA1 and UA2 collaborations with the SPS  $p\bar{p}$  collider at CERN [32–35].

The pion, understood to mediate the interactions between nucleons, is held together by the strong force, as is the case for all other hadrons. The strong force is in turn mediated by the exchange of electrically neutral gluons. A description of the interactions of quarks with eight gluon fields coupling to colour charge forms the theory of Quantum Chromodynamics (QCD) [36], formalised in 1973. Indirect observations of gluons were reported in 1979 by the MARK-J experiment at the PETRA  $e^+e^-$  collider [37] based on the observation of events with three “jets” (collimated clusters of hadrons). Quarks and antiquarks are expected to be produced in pairs so the production of an odd number of jets is taken to result from the radiation of a high energy gluon.

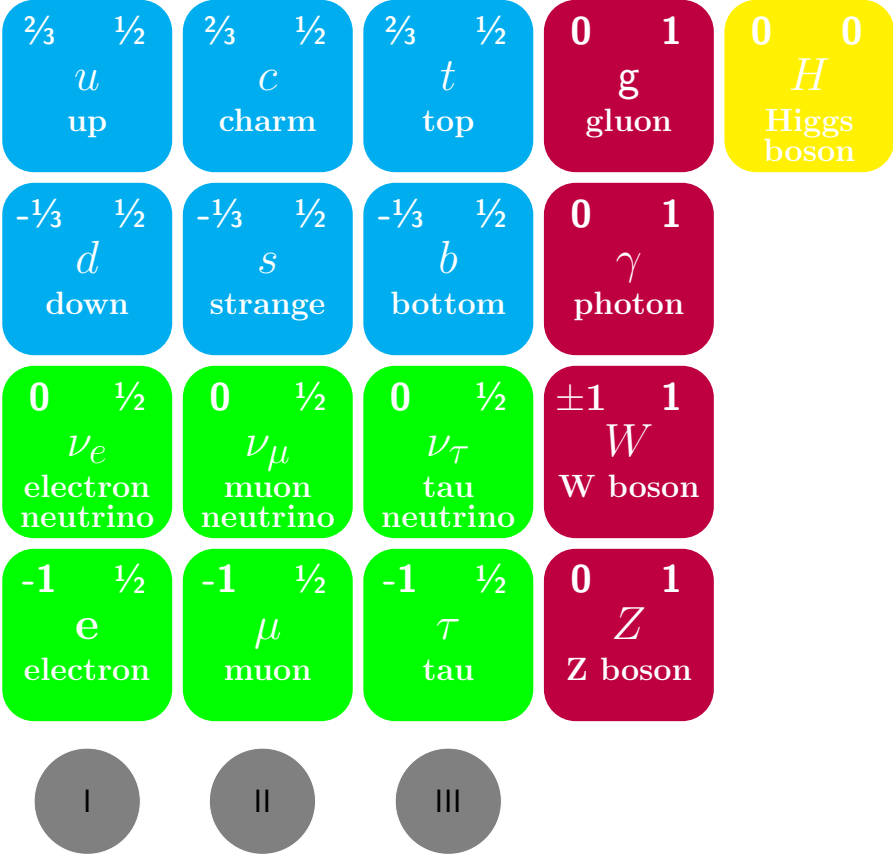


Figure 2.1: Particle content of the SM. Quarks (leptons) are shown in blue (green), gauge bosons are shown in red and the Higgs boson is shown in yellow. The fermion generations are denoted in grey circles at the bottom of the figure. Electric charge and spin of the particle are indicated in the top left and right corners, respectively.

The particle content of the SM is shown in Fig. 2.1. In addition to the vector bosons discussed above, the model features a single scalar, the Higgs boson, which is a consequence of the mechanism through which the SM particles acquire mass.

### 2.1.2 Theoretical framework

For the description of the SM it is useful to introduce the concept of the Lagrangian. Classically, the Lagrangian,  $L$ , of a system represents the difference of the kinetic and potential energies,  $L = T - V$ . Lagrangian mechanics provides a framework for deriving the equations of motion of the system via a set of differential equations known as the Euler-Lagrange equations. For a field theory it is more convenient to consider the Lagrangian density,  $\mathcal{L}$ , where  $L = \int \mathcal{L} d^3\underline{x}$ , which is expressed in terms of the fields and their space and time derivatives. In QFT, this formalism can be used to write a Lagrangian<sup>1</sup>, from which analogues of the classical Euler-Lagrange equations provide the equations of motion [38].

The SM Lagrangian is constructed with the requirement that it is invariant under gauge transformations. This corresponds to the requirement that the physics of the model itself is not changed by unobservable symmetries of the underlying theory. Gauge symmetry can be understood by looking at classical electromagnetism. The magnetic and electric fields,  $\underline{B}$  and  $\underline{E}$ , respectively, can be described in terms of vector and scalar potentials,  $\underline{A}$  and  $\phi$ , respectively, by

$$\begin{aligned}\underline{B} &= \underline{\nabla} \times \underline{A}, \\ \underline{E} &= -\underline{\nabla}\phi - \partial_t \underline{A}.\end{aligned}\tag{2.1}$$

The fields  $\underline{A}$  and  $\phi$  are not themselves observable and it can be shown that transformations

---

<sup>1</sup>The Lagrangian density  $\mathcal{L}$  is commonly referred to as the Lagrangian in the context of QFT.

of these underlying fields

$$\begin{aligned}\underline{A} &\rightarrow \underline{A} + \nabla\chi, \\ \phi &\rightarrow \phi - \partial_t\chi,\end{aligned}\tag{2.2}$$

where  $\chi$  is a scalar, can be made without changing the observable  $\underline{B}$  and  $\underline{E}$  fields. Such a transformation is referred to as a gauge transformation and  $\underline{B}$  and  $\underline{E}$  are said to be gauge invariant quantities. For a constant  $\chi$  this is a global gauge transformation, while for  $\chi = \chi(\underline{x}, t)$  the transformation is a local gauge transformation.

It can be shown that imposing a local phase invariance ( $\psi(x) \rightarrow e^{i\chi(x)}\psi(x)$ ) on the Lagrangian for a freely-propagating spin- $\frac{1}{2}$  particle,

$$\mathcal{L} = \bar{\psi}(i\gamma^\mu\partial_\mu - m)\psi,\tag{2.3}$$

leads to the requirement of an additional term in  $\mathcal{L}$  corresponding to the interactions with a massless vector field, consistent with the photon [38]. In the context of the unified electroweak (EW) theory, the application of the gauge principle gives rise to three fields  $W_\mu^{(i)}$  where  $i \in \{1, 2, 3\}$ , corresponding to the  $SU(2)_L$  symmetry of weak isospin, and a field  $B_\mu$ , corresponding to the  $U(1)_Y$  symmetry of weak hypercharge. The breaking of EW symmetry, resulting in the familiar weak and electromagnetic fields, is discussed later. Similarly, the eight gluon fields of the strong interactions are necessary consequences of imposing invariance of  $\mathcal{L}$  under  $SU(3)$  symmetry, corresponding to the exchange of three colour charges in QCD. The SM, constructed using the principle of gauge invariance, is seen to provide a very good description of experimental data, with symmetry group  $SU(3)_c \times SU(2)_L \times U(1)_Y$ .

The interactions in which each of the fermions take part depend on their charge under the respective force. All of the fermions are charged under the weak interaction, carrying weak isospin, while only quarks are charged under the strong interaction, carrying colour charge. All, with the exception of the neutrinos, are electrically charged and take part in the electromagnetic interaction. The charges of the SM fermions under the electromagnetic

Table 2.1: Fermion content of the SM showing particle charges under the SM EW gauge groups.  $T$  represents weak isospin with third component  $T_3$ ,  $Y$  is weak hypercharge and  $Q$  is electric charge.

	$T$	$T_3$	$Y$	$Q$
$\nu_L$	$\frac{1}{2}$	$\frac{1}{2}$	-1	0
$\ell_L$	$\frac{1}{2}$	$-\frac{1}{2}$	-1	-1
$\ell_R$	0	0	-2	-1

	$T$	$T_3$	$Y$	$Q$
$u_L$	$\frac{1}{2}$	$\frac{1}{2}$	$\frac{1}{3}$	$\frac{2}{3}$
$d_L$	$\frac{1}{2}$	$-\frac{1}{2}$	$\frac{1}{3}$	$-\frac{1}{3}$
$u_R$	0	0	$\frac{4}{3}$	$\frac{2}{3}$
$d_R$	0	0	$-\frac{2}{3}$	$-\frac{1}{3}$

and weak interactions can be seen in Table 2.1. The fermions are split into left- ( $f_L$ ) and right-chiral ( $f_R$ ) fields since the weak interaction is parity-violating and couples only to  $f_L$ .

The left-chiral neutrino field,  $\nu_L$ , is only charged under weak isospin and as such only participates in the weak interaction. It is unclear whether a right-chiral neutrino field,  $\nu_R$ , exists in nature. If it does exist,  $\nu_R$  is uncharged under all of the SM fields and so would only interact with other particles gravitationally. As such it is not included in the SM, hence its omission from Table 2.1, and such a field is referred to as a “sterile” neutrino.

The interactions of fermions with the gauge bosons can be represented by Feynman diagrams, with a simple example being  $e^-e^- \rightarrow e^-e^-$  scattering mediated by a virtual photon, shown in Fig. 2.2. The bosons themselves can also be charged and interact with one-another or even self-interact; such is the case for the gluon which itself carries colour charge. The self-interacting behaviour of the gluon results in the short-range interaction of the force it mediates.

Each vertex has an associated coupling strength which determines the probability for a given interaction to occur. In the case of the photon-electron interaction, shown in

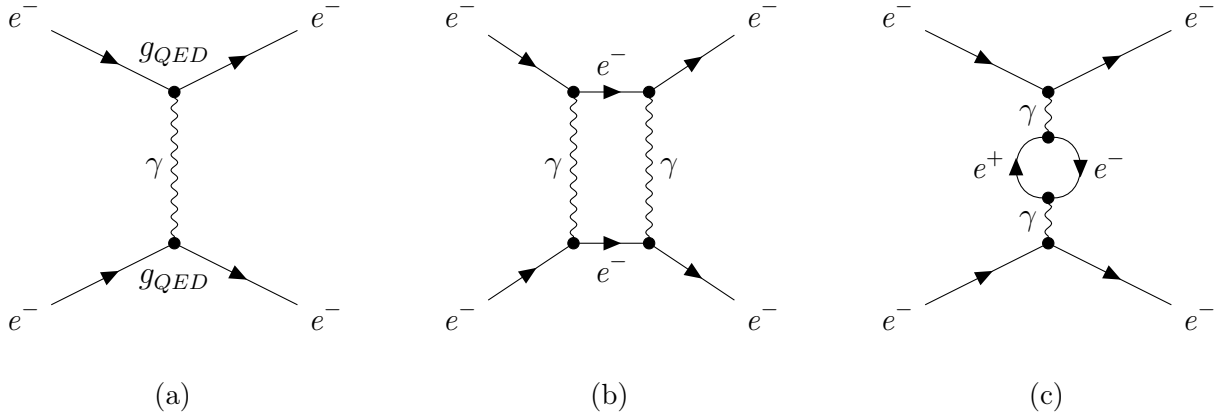


Figure 2.2: Leading order (a) and next-to-leading order (b-c) Feynman diagrams for  $e^-e^- \rightarrow e^-e^-$  scattering demonstrating the photon-electron vertex. In (b) and (c) the coupling labels have been dropped.

Fig. 2.2a, this is  $g_{QED} = e$ . Feynman rules provide prescriptions for how the so-called complex matrix element,  $\mathcal{M}$ , for a process arises from interaction vertices, represented in the form of Feynman diagrams. The probability of interaction, or the cross-section of a process, is then proportional to  $|\mathcal{M}^*\mathcal{M}|$  with a proportionality factor which takes into account phase-space considerations. This formulation is Lorentz-invariant and allows for measurable quantities, such as interaction and decay rates, to be calculated.

Each of the QED vertices in Fig. 2.2 contribute a factor  $g_{QED}$  to the matrix element,  $\mathcal{M}$ . Fig. 2.2a is a leading order (LO) diagram for the  $e^-e^- \rightarrow e^-e^-$  scattering process since it contains the smallest number of coupling factors. Higher order diagrams, featuring additional particle exchange between the electrons or corrections to the photon, also contribute to  $e^-e^- \rightarrow e^-e^-$  scattering, as shown in Fig. 2.2. The matrix element calculation therefore takes the form of a series in increasing powers of the coupling constant which is only convergent if the coupling constant is less than unity.

In general, the loops introduced by higher order diagrams, whose internal momenta are not constrained and must be integrated over, introduce divergences into the calculations.

These can be treated by a process called renormalisation which involves redefining the bare physical quantities of the Lagrangian to absorb the divergences. The diagram in Fig. 2.2c, along with all higher order corrections to the photon propagator, can be replaced by an effective propagator with a coupling  $g_{QED}(\mu)$  where  $\mu$  represents the energy scale of the photon propagator [39]. This leads to a scale dependence for the coupling, which is no longer constant. Since the coupling constant can be measured experimentally and is seen to be finite, the value at a given scale  $\mu_0$  can be related to the strength at a different scale.

While the QED coupling is seen to increase at larger energy scales,  $\alpha_{QCD}$  exhibits the opposite behaviour, growing rapidly as the energy scale decreases. Since perturbative calculations can only be made in regimes where the coupling constant is small enough that the power series converges, calculations in QCD can only be made at higher energy scales.

### 2.1.3 Electroweak symmetry breaking

Mass terms for the fundamental particles are forbidden in the SM by the gauge symmetry of the Lagrangian. Considering the simple case of the freely-propagating electromagnetic field,  $A^\mu$ , the Lagrangian is

$$\mathcal{L}_{EM} = -\frac{1}{4}F_{\mu\nu}F^{\mu\nu}, \quad (2.4)$$

where  $F^{\mu\nu} = \partial^\mu A^\nu - \partial^\nu A^\mu$ . It can be seen that gauge transformations such as Eq. (2.2)<sup>2</sup> leave  $\mathcal{L}_{EM}$  unchanged. A mass term of the form  $-\frac{1}{2}m_A A^\mu A_\mu$ , however, would not be invariant under the same transformation. A field mediated by massless gauge bosons should give rise to long-range interactions, as is the case for the electromagnetic interaction, mediated by the massless photon. This is clearly not the case for the weak interaction, implying these forces must be mediated by massive force particles, as confirmed by the discovery of the  $W^\pm$  and  $Z$  bosons.

---

<sup>2</sup> $A^\mu \rightarrow A^\mu + \partial^\mu \chi$  in four-vector notation, where  $\mu \in \{t, x, y, z\}$ .

The mechanism needed to explain this mass generation while respecting gauge invariance was proposed in 1964 [40–42] and is commonly known as the Higgs or Brout-Englert-Higgs (BEH) mechanism. It requires the addition of a new scalar field,  $\phi$ , which is required to be colourless but charged under the weak interaction, forming a weak isospin doublet

$$\phi = \begin{pmatrix} \phi^+ \\ \phi^0 \end{pmatrix} = \frac{1}{\sqrt{2}} \begin{pmatrix} \phi_1 + i\phi_2 \\ \phi_3 + i\phi_4 \end{pmatrix} \quad (2.5)$$

and is required to be complex to satisfy gauge invariance. Two scalar fields,  $\phi^+$  and  $\phi^0$ , are needed to give masses to the  $W^\pm$  and  $Z$  bosons. The mechanism describes how the scalar field, the Higgs field, acquires a non-zero expectation value; that is, the lowest-energy configuration of the field corresponds to a non-vanishing field presence. The finite vacuum expectation value (vev) of the Higgs field is in contrast to the other fields of the SM which all have zero vacuum expectation. The presence of this field in the vacuum state then has the effect of endowing mass on the particles which interact with it.

The requirement that the vev is non-zero can be satisfied by a potential of the form,

$$V(\phi) = \mu^2(\phi^*\phi) + \lambda(\phi^*\phi)^2, \quad (2.6)$$

where  $\lambda$  and  $\mu$  are constants taking real and complex values, respectively. If  $\mu^2 < 0$ , this potential has a minimum for  $|\phi|^2 = -\mu^2/\lambda$ , which takes the form of a ring. The symmetry of the potential is spontaneously broken since the field must select a minimum value. Since the broken symmetry corresponds to the  $SU(2)_L \times U(1)_Y$  group, this process is known as electroweak symmetry-breaking (EWSB).

By choosing the vacuum state to be  $\phi^+ = 0$ ,  $\phi^0 = \nu$ , where  $\nu = -\mu^2/\lambda$  is the vev, mass terms arise for the four gauge boson fields of the EW interaction,  $W_\mu^{(i)}$  and  $B_\mu$ , in terms of their respective couplings,  $g_W$  and  $g'$ . Performing a diagonalisation of the resulting mass matrix to identify the physical gauge boson fields, it can be shown that the EW bosons gain

the following masses:

$$m_W = \frac{1}{2}g_W \nu \quad m_Z = \frac{1}{2}\sqrt{g_W^2 + g'^2} \nu \quad m_\gamma = 0 \quad (2.7)$$

where the physical bosons are mixtures of the massless bosons corresponding to the broken  $SU(2)_L$  and  $U(1)_Y$  symmetries [39]:

$$\begin{pmatrix} W_\mu^+ \\ W_\mu^- \end{pmatrix} = \frac{1}{\sqrt{2}} \begin{pmatrix} 1 & -i \\ 1 & i \end{pmatrix} \begin{pmatrix} W_\mu^{(1)} \\ W_\mu^{(2)} \end{pmatrix} \quad (2.8)$$

$$\begin{pmatrix} A_\mu \\ Z_\mu \end{pmatrix} = \begin{pmatrix} \cos(\theta_W) & \sin(\theta_W) \\ -\sin(\theta_W) & \cos(\theta_W) \end{pmatrix} \begin{pmatrix} B_\mu \\ W_\mu^{(3)} \end{pmatrix} \quad (2.9)$$

The angle  $\theta_W$  is known as the weak mixing angle. The mechanism also predicts the existence of a massive scalar with a mass  $m_H = \sqrt{2\lambda\nu^2}$ , the Higgs boson. Since the SM does not predict the values of  $\mu^2$  or  $\lambda$ , the masses of the weak gauge bosons and the Higgs boson itself must be measured by experiment.

### 2.1.4 The generation of fermion masses

Fermion masses are not generated in the same manner as those of the gauge bosons, but arise through their interactions with the non-vanishing scalar field after EWSB. As was the case for bosons, a mass term for fermions does not respect  $SU(2)_L \times U(1)_Y$  symmetry. However, terms describing the interactions of the Higgs field,  $\phi$ , and its conjugate  $\tilde{\phi}$ , with a left-handed fermion  $SU(2)_L$  doublet and the corresponding right-handed singlet do meet this requirement and can be written

$$\mathcal{L}_{\text{Yukawa}} = -y_{ij}^d \bar{d}_L^i \phi d_R^j - y_{ij}^u \bar{u}_L^i \tilde{\phi} u_R^j - y_{ij}^e \bar{e}_L^i \phi e_R^j \quad (+h.c.)^3, \quad (2.10)$$

where the indices  $\{i, j\} \in \{1, 2, 3\}$  represent the three generations of fermions. After EWSB, using the same choice of gauge as in Section 2.1.3, terms with  $\phi$  gives rise to masses for the

<sup>3</sup>+*h.c.* indicates that the Hermitian conjugate term must also be considered.

lower parts of the fermion doublets ( $e_i$  and  $d_i$ ) while terms with  $\tilde{\phi}$  impart mass to upper parts ( $u_i$ ) [39]. Since the SM contains no right-handed neutrino term, the neutrino remains massless. The fermion masses are given by

$$m_{ij}^f = \frac{\nu}{\sqrt{2}} y_{ij}^f, \quad (2.11)$$

where the index  $f$  represents the separate matrices for the up-type quarks, down-type quarks and charged lepton fields, respectively, The values of  $y_{ij}^f$ , the Yukawa matrices, are not predicted by the SM so the fermion masses have to be measured experimentally, as was the case for the bosons.

### 2.1.5 Flavour in the SM

With the exception of the Yukawa terms coupling the fermions to the Higgs field, the SM Lagrangian exhibits flavour universality. The coupling strength of the fermions to the Higgs field is expressed in terms of the complex Yukawa matrices which must be diagonalised to obtain the physical fermion masses. The matrices  $y_{ij}^f$  can be diagonalised by transformations of the fermion fields [43] such that

$$\hat{y}_{ij}^f = A_L^{f\dagger} y_{ij}^f A_R^f, \quad (2.12)$$

is diagonal, with

$$\begin{aligned} \psi_L^j &\rightarrow A_L^f \psi_L^j, \\ \psi_R^j &\rightarrow A_R^f \psi_R^j. \end{aligned} \quad (2.13)$$

The majority of  $\mathcal{L}_{\text{SM}}$  is invariant under such transformations with the exception of the charged-current weak interaction which couples up and down components of  $SU(2)_L$  doublets. The rotations of the fermion fields induce a flavour-violating term which allows mixing between different generations in the interactions of the  $W^\pm$  boson [44]:

$$\mathcal{L}_{cc} = \frac{1}{\sqrt{2}} g_W \left( \bar{u}_L^i \gamma^\mu \underbrace{(A_L^{u\dagger} A_L^d)}_{\equiv V_{\text{CKM}}} d_L^j + \bar{\nu}_L^i \gamma^\mu \underbrace{(A_L^{\nu\dagger} A_L^e)}_{\rightarrow 1} e_L^j \right) (+h.c) \quad (2.14)$$

In the quark sector this gives rise to the Cabibbo–Kobayashi–Maskawa (CKM) matrix,  $V_{\text{CKM}} \equiv A_L^{u\dagger} A_L^d$ , which encodes the mixing between different quark generations. In the lepton sector, however, the absence of a right-handed neutrino field allows a choice of  $A_L^\nu = A_L^e$  which does not introduce mixing between generations. The consequence of this is that lepton flavour is expected to be conserved in the SM, while flavour-changing interactions involving quarks are permitted in charged-current interactions.

## 2.2 Beyond the Standard Model

The discovery of the Higgs boson at the LHC [3, 4], and the subsequent evidence that its properties are consistent with those predicted by the SM, marks a profound shift in the field of particle physics. The SM now stands validated and is yet to be proven wrong; however, there remain outstanding problems which it cannot explain. It offers no candidates for the origin of dark matter and, in its original form, no mechanism for the observed flavour oscillations of neutrinos [45–47]. Additionally, the SM contains a significant number of free parameters which must be extracted from experimental data, such as the masses of the fundamental particles. All of this hints that the SM is an effective model of a more complete theory and motivates searches for new physics which could explain the questions it leaves open. As such, the focus of the field is now on further precision tests of SM, including in the Higgs sector, and on direct searches for BSM physics.

### 2.2.1 Neutrino mass and oscillation

In the SM, which does not contain a  $\nu_R$  field, neutrinos are massless and lepton flavour is conserved in all interactions. However, the observation of neutrino oscillations demonstrates the existence of neutrino masses. Furthermore, it demonstrates that for the neutrinos, as is

the case for the quark fields, there is a misalignment between the mass eigenstates, which determine the propagation behaviour, and the “flavour” eigenstates, which take part in the weak interaction.

It is common to label the mass states by  $\nu_i$  where  $i \in \{1, 2, 3\}$  and the flavour states by  $\nu_\alpha$  where  $\alpha \in \{e, \mu, \tau\}$ . The rotations between these two bases can be described by a  $3 \times 3$  unitary matrix known as the Pontecorvo–Maki–Nakagawa–Sakata (PMNS) matrix:

$$\begin{bmatrix} \nu_e \\ \nu_\mu \\ \nu_\tau \end{bmatrix} = \underbrace{\begin{bmatrix} U_{e1} & U_{e2} & U_{e3} \\ U_{\mu1} & U_{\mu2} & U_{\mu3} \\ U_{\tau1} & U_{\tau2} & U_{\tau3} \end{bmatrix}}_{U_{\text{PMNS}}} \begin{bmatrix} \nu_1 \\ \nu_2 \\ \nu_3 \end{bmatrix} \quad (2.15)$$

Since the neutrinos only interact weakly, their production and subsequent detection are always via the weak interaction. For production via the charged current weak interaction, the resulting neutrino will be in a mass state  $\nu_i$  with probability  $U_{\alpha i}$ , where  $\alpha$  is the flavour of the associated charged lepton. However, the mass state in which the neutrino is produced cannot be resolved experimentally. Instead the neutrino is detected in a given flavour state with a probability again given by  $U_{\text{PMNS}}$ . The propagating neutrino is therefore a superposition of the three mass eigenstates which interfere, resulting in oscillation probabilities which depend on the squared mass differences  $\Delta m_{ij}^2 = m_i^2 - m_j^2$ , the propagation length and the neutrino energy. In the simplified case of oscillations between two flavours, the probability is [39]

$$P(\nu_\alpha \rightarrow \nu_\beta) \propto \sin^2 \left( \Delta m_{ij}^2 \frac{L}{4E} \right), \quad (2.16)$$

where  $L$  is the distance of propagation and  $E$  is the energy of the neutrino. It is this interference which gives rise to the observed oscillations. It can be seen that in the absence of a mass difference between the  $\nu_i$  there would be no oscillations.

The SM can be extended to incorporate neutrino oscillations by the inclusion of the sterile neutrino fields and subsequent generation of mass following EWSB. If neutrino masses



CLFV, some at rates which could already be within the experimental sensitivity of the LHC experiments [48]; some of these models are discussed below.

### Extended Higgs sectors

The BEH mechanism requires the existence of at least one complex scalar doublet. The idea of extended Higgs sectors containing additional scalar fields are popular BSM theories, proposed to explain some of the shortcomings of the SM. In particular, extensions involving an additional EW doublet, known as two Higgs doublet models (2HDMs), have been proposed as possible sources of additional charge-parity violation (CPV) needed to explain the observed matter-antimatter asymmetry of the universe [49]. Type-III 2HDMs introduce CLFV because both doublets couple to the lepton fields such that off-diagonal couplings cannot be avoided [50]. The Higgs boson discovered at the LHC shows good consistency with the hypothesis of a single scalar doublet but extended Higgs sectors have not yet been ruled out.

### Grand unified theories

Above the scale of EWSB, the electromagnetic and weak interactions are combined into a unified interaction as described by the GSW theory. This raises the possibility that at an even greater energy, there is a single interaction which unifies this description with the strong interaction. The prospect of a grand unified theory (GUT) is further motivated by the observation that the running of the SM coupling constants, as governed by the renormalisation group equations, should become equal in strength at  $\Lambda_{GUT} \sim 10^{15}$  GeV [38].

In 1974 a model capable of describing such a unification with gauge group  $SU(5)$  was proposed by Georgi and Glashow [51]. The model predicts 24 gauge bosons, of which half couple the lepton and quark fields and are known as leptoquarks (LQs). Such particles



Figure 2.4: Corrections to Higgs boson self-energy.

necessarily introduce quark-to-lepton interactions which violate both lepton number as well as baryon number. Such transitions, however, render the proton unstable, which poses a problem for minimal GUT models. A number of other models propose the existence of LQs [52] and current constraints, summarised in Ref. [53], are highly model-dependent.

An additional problem with such models is the difference between the EW scale and the energy scale of the  $SU(5)$  theory. The masses of the LQs are produced in the  $SU(5) \rightarrow SU(3)_c \times SU(2)_L \times U(1)_Y$  symmetry breaking process, analogously to the generation of the weak boson masses by EWSB, and are therefore expected to be of the order  $\Lambda_{GUT}$ . As a scalar particle the SM Higgs boson receives corrections to its mass from quantum loop diagrams such as Fig. 2.4, the size of which depend quadratically on the momentum exchanged within these loops [39]. If there is no cut-off to the momentum scale of these corrections then the Higgs boson mass should be driven towards  $\Lambda_{GUT}$ . Aside from a “fine-tuning” of the higher-scale physics, a mechanism is required to protect the Higgs boson mass from such corrections.

## Supersymmetry

The large discrepancy between  $m_H$  and  $\Lambda_{GUT}$  is known as the EW hierarchy problem since there is no known mechanism to explain why the mass is not inflated by these corrections to very large values. In the absence of a GUT being realised in nature the same argument

applies to the Planck mass,  $M_P$ . Above the Planck mass it is expected that the strength of gravitational interactions matches that of the other fundamental forces, meaning the effects of quantum gravity can no longer be ignored.

One such theory, which is proposed to be capable of addressing this problem, is supersymmetry (SUSY) which posits the existence of a corresponding supersymmetric partner to each SM particle. In the case of an exact supersymmetry, in which particle and supersymmetric partner masses are equal, the loop contributions from SM particles are perfectly cancelled by those of the corresponding SUSY partners [39]. SUSY models typically introduce CLFV through the introduction of couplings between the leptons and their supersymmetric partners [44]. Additionally, models of SUSY require a second Higgs doublet. As well as addressing the hierarchy problem, SUSY provides possible dark matter candidates whose absence from the SM is another shortcoming of the theory.

The absence of evidence for SUSY following Runs 1 and 2 of the LHC strongly constrains the model space and rules out an exact supersymmetry. Nevertheless, the theory is not completely excluded and the latest constraints are summarised in Ref. [53].

### 2.2.3 Effective field theory

When considering processes for which the energy scale,  $\Lambda$ , of the process is much greater than the experimental sensitivity, an effective field theory (EFT) framework can be employed. A familiar example of an EFT is the Fermi theory of  $\beta$ -decay [54]; at energies much less than  $m_W$  the process  $d \rightarrow ue^- \bar{\nu}_e$  can be treated as a point-like four fermion interaction. In the context of the SM, the strength of this method is that it allows for calculations of the rates and kinematics of BSM processes without knowledge of the high-energy theory.

A useful framework for probing new physics extensions to the SM is the Standard

Model effective field theory (SMEFT) which extends  $\mathcal{L}_{\text{SM}}$  with all possible contractions of the SM fields which respect the gauge symmetry of the SM [55]:

$$\mathcal{L}_{\text{SMEFT}} = \mathcal{L}_{\text{SM}} + \sum_{i,n} \frac{c_i^{(n)}}{\Lambda^{n-4}} \mathcal{O}_i^{(n)}. \quad (2.17)$$

Here  $\mathcal{O}$  represent the terms introducing new interactions between SM fields,  $c$  are complex numbers known as Wilson coefficients which control the coupling strength of the new interaction, and  $\Lambda$  is the energy scale of the new physics process. The index  $n$  denotes the dimension<sup>4</sup> of the new interaction while  $i$  denotes a given new operator. The implication of the construction is that  $\Lambda$  may correspond to some new particle which introduces the BSM coupling. The new operators introduced are ordered by dimension since operators of higher dimension are suppressed by higher powers of  $\Lambda$ . The SMEFT framework will be used to interpret the results of the search for  $t\mu\tau u_k$  CLFV interactions discussed in Chapters 6 and 7.

---

<sup>4</sup>Dimension here refers to the mass dimension, equivalent to  $\frac{1}{\text{length}}$  in natural units of  $c = \hbar = 1$ .

# Chapter 3

## The ATLAS experiment

### 3.1 The Large Hadron Collider

The LHC is the largest particle collider constructed and collides beams of protons at centre-of-mass energies of up to  $\sqrt{s} = 13.6$  TeV with a maximum design energy of 14 TeV [56]. It is installed in a tunnel under the French-Swiss border near Geneva at the European Organization for Nuclear Research (CERN). The machine uses two rings to accelerate proton beams which are forced to collide at four interaction points around the ring. The proton collision programme provides studies of a wide variety of physics processes at the highest energies probed. The LHC is currently in its third running period (Run 3) at  $\sqrt{s} = 13.6$  TeV, which began in 2022. Previous running periods at 7-8 TeV (Run 1), from 2009-2013, and 13 TeV (Run 2), from 2015-2018, have also been completed and data from all of these runs continue to be analysed. Fig. 3.1 provides a summary of past and future LHC and HL-LHC running periods along with their energies and the integrated luminosity, which provides a metric for the number of collisions and is discussed below.

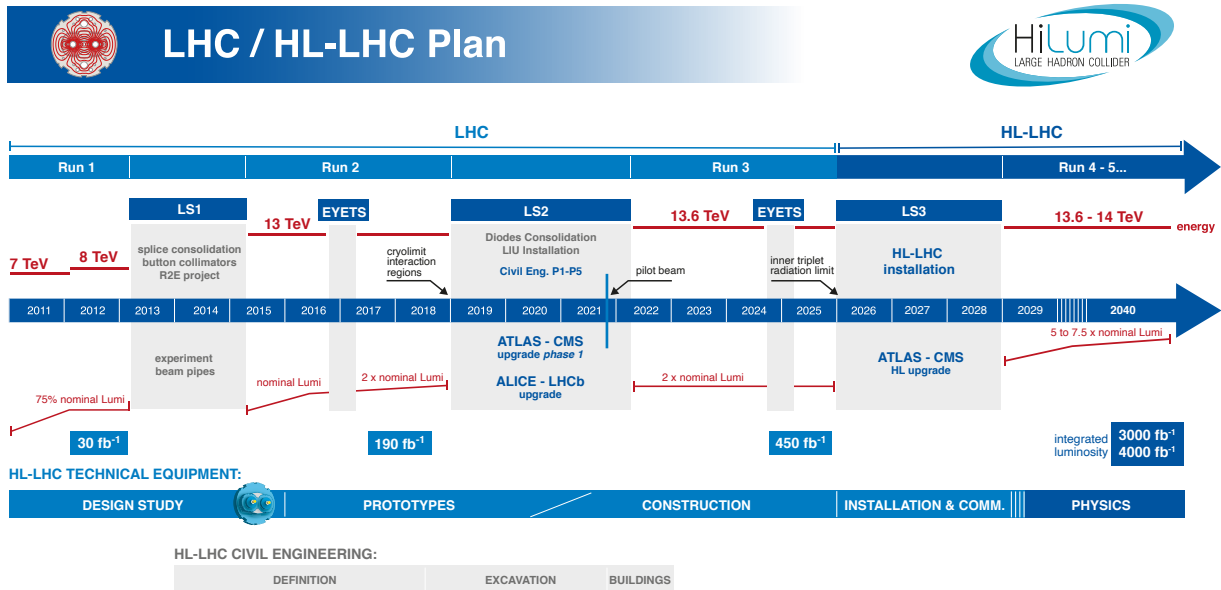


Figure 3.1: Planned LHC/HL-LHC run schedule as of January 2022 [57].

Before entering the LHC ring, protons are accelerated up to 450 GeV in a series of increasingly powerful accelerators, shown in Fig. 3.2. Once this energy is reached, the protons are injected into the LHC where they are further accelerated to the peak energy using radio frequency cavities which subject the protons to a rapidly oscillating electromagnetic field. Protons are injected in discrete clusters known as bunches to ensure the effect of the oscillating field is always to accelerate the protons. Superconducting dipole electromagnets are used to guide the beams around the LHC ring while quadrupoles are used to focus the beams. Bunches of protons circulating in opposite directions are then steered into collisions at four interaction points around the ring at which large detectors are installed. The largest two detectors, named A Toroidal LHC ApparatuS (ATLAS) [1] and Compact Muon Solenoid (CMS) [58], are general purpose detectors. The Large Hadron Collider beauty (LHCb) experiment [59] focuses on the interactions of  $b$ -quarks to measure the rates of CPV effects. The LHC is also capable of accelerating and colliding beams of heavy ions which are studied primarily by

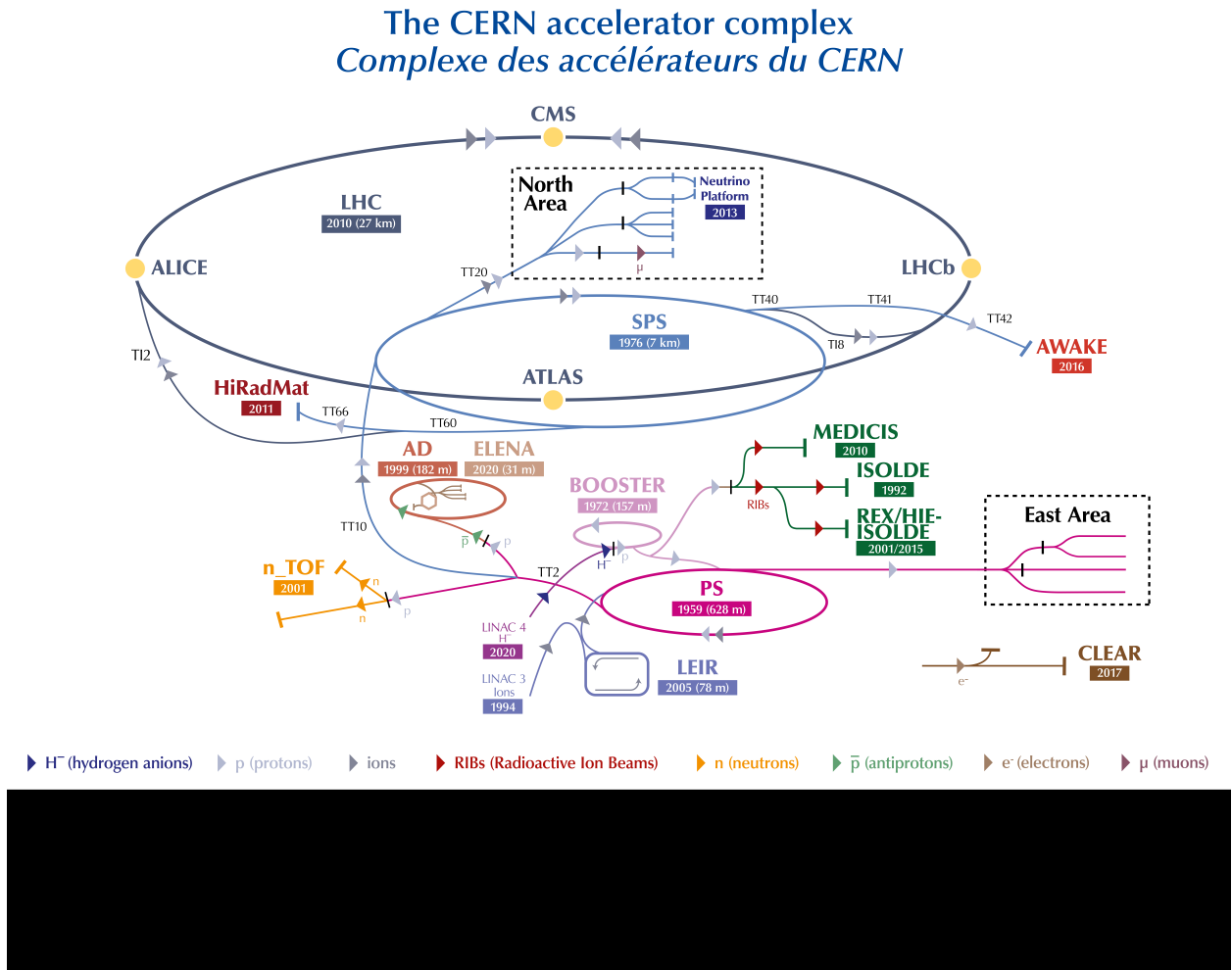


Figure 3.2: The CERN accelerator complex in January 2022 [61].

A Large Ion Collider Experiment (ALICE) [60]. Collisions between the quarks and gluons within the proton, known collectively as partons, lead to the production of all of the particles described by the SM of particle physics and possibly hypothetical BSM particles.

At an interaction point the number of collisions occurring per second per cross sectional area is given by the instantaneous luminosity,  $\mathcal{L}$ , which is a parameter of the LHC machine. The time integral of the instantaneous luminosity, the integrated luminosity  $L$ , can be used to calculate the expected number of times a given physics process with cross-section  $\sigma_{process}$

occurs:

$$N_{\text{exp}} = L\sigma_{\text{process}}. \quad (3.1)$$

Proton beams in the LHC are split into  $n_b$  bunches containing  $N_b$  protons per bunch which circulate with a frequency  $f_{\text{rev}}$ . Under the assumption that the profile of the beam is Gaussian the instantaneous luminosity can be expressed as [56]

$$\mathcal{L} = \frac{N_b^2 n_b f_{\text{rev}} \gamma}{4\pi \eta_n \beta^*} F \quad (3.2)$$

where  $\eta_n$  and  $\beta^*$  are parameters of the beam known as the normalised transverse beam emittance and beta function, respectively;  $\gamma$  is the relativistic gamma factor accounting for relativistic length contraction;  $F$  is a geometric factor arising from the beams colliding at an angle to one-another, which reduces the luminosity. A maximum of 2556 bunches per ring was reached during Run 2 [62]. A bunch spacing of 25 ns determines the collision frequency at the detectors. The LHC aims to deliver instantaneous luminosities of  $10^{34} \text{ cm}^2\text{s}^{-1}$  to the ATLAS and CMS experiments. The actual performance exceeded this for the majority of Run 2, reaching  $2.1 \times 10^{34} \text{ cm}^2\text{s}^{-1}$  in 2018 [62].

## 3.2 The ATLAS detector

The ATLAS experiment is intended to allow the study of any physics processes occurring at the energy scale of the LHC. A diagram of the ATLAS detector is shown in Fig. 3.3. It consists of a tracking detector which measures the momentum of charged particles and tags their production point along the beam-line; calorimeters which provide a destructive measurement of the energy of both charged and neutral particles; and a dedicated muon tracking system as the outermost layer.

The detector consists of several concentric cylindrical sub-detectors which provide almost hermetic coverage around the interaction point. Components of the sub-detectors are

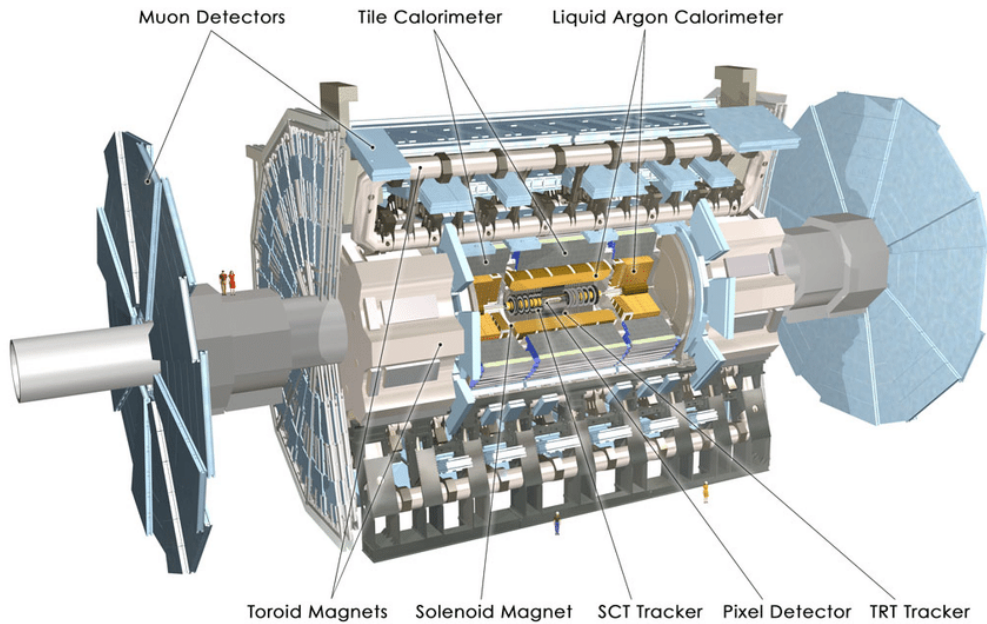


Figure 3.3: Diagram of the ATLAS detector [63].

split between the barrel and end-cap regions which refer to the curved face and flat ends of the cylindrical geometry, respectively. It is useful to define the standard coordinate system used to describe the ATLAS detector relative to the nominal interaction point (IP) at the centre of the detector. The direction from the IP to the middle of the LHC is defined as the x-axis, while the y-axis is defined as the vertical from the IP. Finally, the beam pipe which runs through the centre of the detector defines the z-axis. The x-y plane is known as the transverse plane as it is perpendicular to the beam direction. The angle around the beam pipe in the transverse plane is the azimuthal angle,  $\phi$ , while angles in the y-z plane are described by the “pseudorapidity”,  $\eta = -2 \ln(\tan[\theta/2])$ , where  $\theta$  is the polar angle, defined relative to the beam line.

Below is an overview of the key detector systems within ATLAS used to reconstruct the passage of particles produced in LHC collisions. A complete description of the detector may be found in [1].

### 3.2.1 Inner detector

The inner detector (ID) is the closest detector to the interaction point and is fully immersed in a solenoidal magnetic field of 2 T which acts to deflect charged particles. The trajectories of deflected particles are reconstructed using position measurements (“hits”) in three sub-detectors, which allows a measurement of the momentum of the particle in the transverse plane, the  $p_T$ . The ID is designed to provide good momentum resolution for tracks with  $p_T > 0.5$  GeV. The direction in which the track is bent allows the charge of the particle to be identified. A diagram of the ID can be seen in Fig. 3.4.

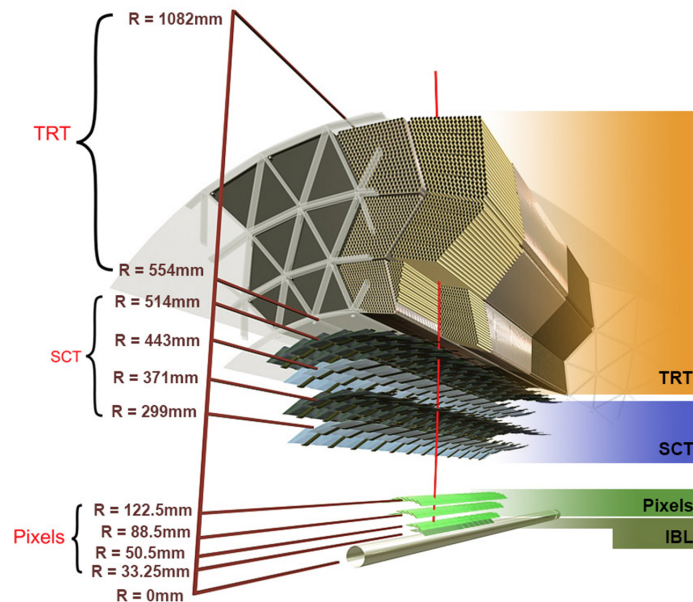


Figure 3.4: Diagram of the ATLAS inner detector [64].

The innermost part is the silicon pixel detector; this provides high granularity hits to separate the large numbers of tracks which result from LHC collisions by identifying the primary collision vertex. Due to the high operating luminosity, events contain many proton-proton collisions per bunch crossing, an effect known as pile-up. The ATLAS detector measured a mean number of 33.7 interactions per bunch crossing between 2015 and 2018. In

addition to measuring the position of the primary vertex to suppress the effects of pile-up it is necessary to reconstruct the position of secondary vertices in order to identify in-flight decays of short-lived particles, such as  $B$ -mesons. Such measurements are particularly important for identifying events with top quark decays.

The pixel detector consists of four layers in the barrel region, including the Insertable B-Layer (IBL) which was introduced between Runs 1 and 2 [65], and three end-cap layers. The fine granularity achievable with pixel sensors makes these ideal for operation close to the interaction point but their high cost precludes use at larger radii. Surrounding the pixel detector, where the track density is lower, is the semiconductor tracker (SCT) made up of silicon strip sensors which extend the precision tracking capabilities of the detector to radial distances of 610 mm out from the interaction point. The SCT consists of four barrel layers and nine end-cap layers, each of which uses pairs of sensors arranged back-to-back to provide two-dimensional position information. The coverage of the pixel and SCT detectors extends to  $|\eta| < 2.5$  with charged particles expected to leave up to four (eight) hits in the pixel (SCT). The technology used in silicon radiation sensors is discussed in detail in Chapter 4.

The third component of the ID is the transition radiation tracker (TRT); this complements precision measurements from the pixel and SCT with in excess of 30 additional hits to radial distances of just over a meter. The additional coverage provided by the TRT significantly improves the momentum resolution, which depends on the radius over which it is measured, for  $|\eta| < 2.0$ . The active technology within the TRT is drift tubes filled with a mixture of xenon, carbon dioxide and oxygen gases. Charged particles traversing the tubes ionise the gas within, liberating electrons which drift in an electric field and are read out from a wire in the centre of the tube.

The TRT consists of alternating layers of drift tubes and transition radiation material. Transition radiation is produced when a charged particle passes between two dielectric media.

This radiation is detected in the drift tubes and distinguished from the signal of particles produced at the primary vertex by the signal amplitude. The detection of transition radiation is used to distinguish between electrons and pions.

### 3.2.2 Calorimeters

Calorimeters providing a destructive measurement of the energy of incident particles are situated outside the solenoid magnet. An electromagnetic calorimeter (ECAL) measures the energy of charged particles and photons to provide precision measurements of the energies of electrons and photons in the coverage of the ID. Particles which are not fully absorbed in the ECAL pass into the hadronic calorimeter (HCAL); this is capable of measuring the energy of neutral and charged particles which couple to the strong interaction. This is necessary for the reconstruction of showers of hadrons, known as jets, as well as missing transverse energy, both of which are discussed further in Chapter 5. Particles passing through the HCAL are typically charged or neutral hadrons, as well as muons. Both calorimeters are of a sampling design which uses alternating layers of absorbing material and detector material, as opposed to a homogeneous design where the same material performs both roles. The absorber is a dense material in which incident particles are likely to interact and produce secondary particles which lead to the development of a shower.

For a high-energy electron passing through matter the dominant energy loss mechanism is through bremsstrahlung, while high-energy photons are most likely to undergo pair production ( $\gamma \rightarrow e^+e^-$ ). As a result, an electron or photon incident on a block of material produces a cascade of secondary electrons and photons of lower energy, known as an electromagnetic shower. Below a certain critical energy the energy loss of electrons due to ionisation exceeds that of bremsstrahlung losses and the shower size stops increasing. The ECAL consists of lead absorber and liquid argon (LAr) active layers and covers the region

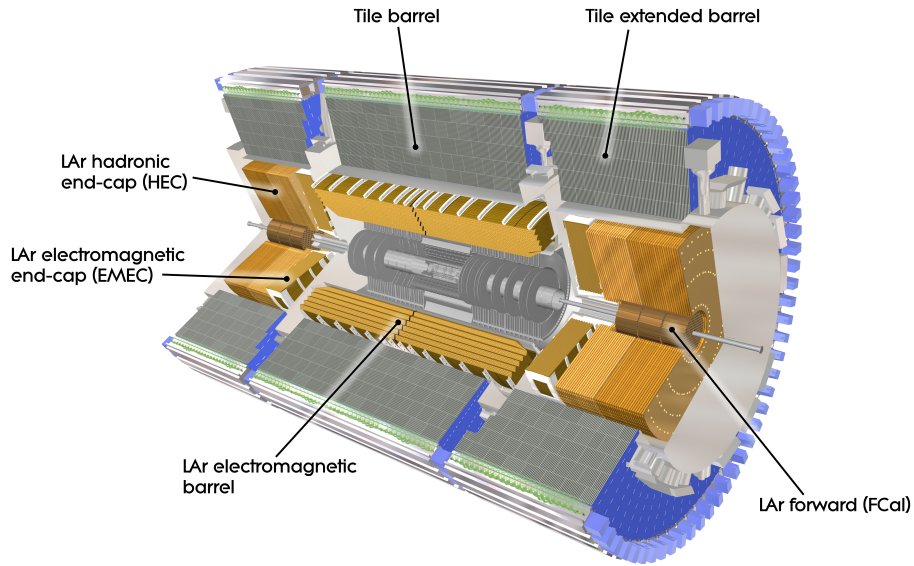


Figure 3.5: Diagram of the ATLAS calorimeters [66].

$0 < |\eta| < 3.2$ . Charged particles in the shower cause ionisation within the LAr and the resulting electrons and ions drift in an electric field, inducing a signal on an electrode.

Hadronic calorimetry is provided by a steel-scintillator detector in the barrel region ( $0 < |\eta| < 1.7$ ) and copper-LAr detectors in the end-cap region ( $1.5 < |\eta| < 3.2$ ). The plastic scintillator tiles have a base component of polystyrene which releases ultraviolet photons following excitation by the passage of a charged particle. Other organic compounds in the tiles absorb the scintillation light and re-emit radiation of a longer wavelength; this is collected in wavelength-shifting fibres and read out into photo-multiplier tubes.

Hadronic showers result from the interaction of high-energy hadrons with nuclei via the strong interaction. The secondary particles produced in such interactions are mainly pions but also include neutrons and heavy nuclear fragments, the latter of which result in energy losses which are invisible to the detector. The amount of material required to contain a hadronic shower far exceeds that which would contain an electromagnetic shower. If the HCAL fails to contain the full shower, the energy reconstruction is severely degraded. In

iron, the characteristic electromagnetic interaction length, known as the radiation length, is  $13.8 \text{ g cm}^{-2}$ <sup>1</sup> while the characteristic length for nuclear interactions is  $132.1 \text{ g cm}^{-2}$  [67]. For these reasons, the resolution of HCAL is significantly worse than that of the ECAL, which makes the reconstruction of particles decaying to hadrons more difficult.

The  $\eta$  coverage of the calorimeters is complemented by the forward calorimeter (FCal) which provides electromagnetic and hadronic calorimetry to  $|\eta| < 4.9$ . The FCal also uses LAr for sampling while the absorber medium is either copper or tungsten. The energy resolution of the calorimeters improves with increasing energy. This complements the performance of the tracker, whose momentum resolution degrades with increasing particle momentum. The layout of the ATLAS calorimeters can be seen in Fig. 3.5.

### 3.2.3 Muon spectrometer

Muons entering the ATLAS detector behave as minimum-ionising particles (MIPs) and are able to penetrate both calorimeters, depositing little energy. The muon spectrometer (MS) uses large toroid magnets providing a magnetic field of approximately 0.5 T (1.0 T) in the barrel (end-cap) to deflect the particles whose trajectories are measured in tracking chambers. The MS is designed to provide precision momentum measurements for muons with  $p_T \gtrsim 3 \text{ GeV}$ .

Two detector types provide precision muon tracking; monitored drift tubes instrument the region covering  $|\eta| < 2.7$  while additional cathode strip chambers cover  $2.0 < |\eta| < 2.7$ . The tracking chambers are complemented by triggering chambers in the region  $|\eta| < 2.7$ ; these provide timing information to allow association of the muon to the correct bunch crossing, along with position information orthogonal to that provided by the tracking chambers.

---

<sup>1</sup>The unit of  $\text{g cm}^{-2}$  indicates that the radiation length has been multiplied by the density of the material.

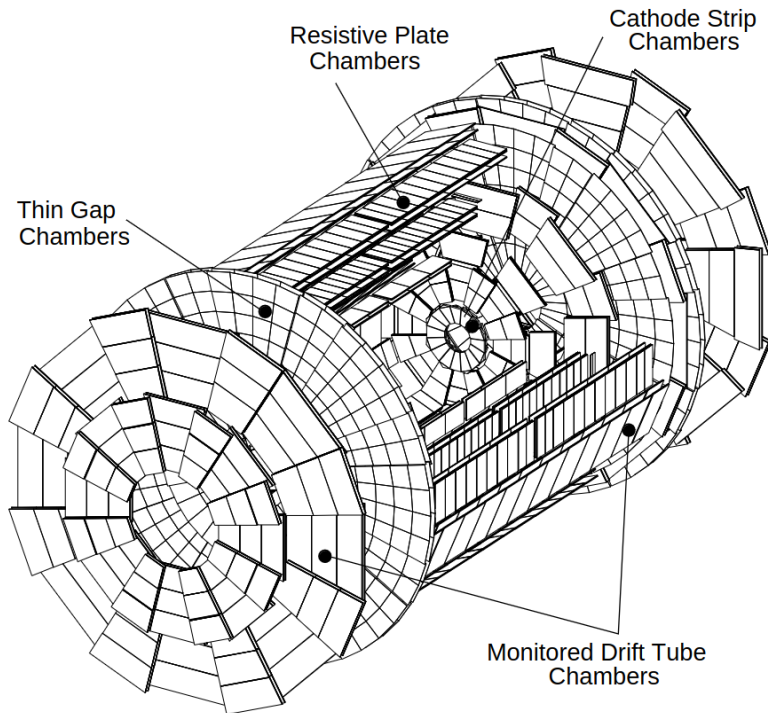


Figure 3.6: Diagram of the ATLAS muon spectrometer [68].

Resistive plate chambers cover  $|\eta| < 1.05$  while thin gap chambers cover  $1.05 < |\eta| < 2.7$ , although the triggering coverage is limited to  $|\eta| < 2.4$ . Each of these subdetectors are shown in Fig. 3.6.

### 3.2.4 Trigger and data acquisition system

LHC collisions occur at the bunch crossing rate of 40 MHz with the majority of collisions resulting only in soft QCD interactions. To select events containing interesting physics information and to reduce the data-taking rate to levels which can be read-out and stored, a trigger system is required. The trigger system also ensures that signals in each of the detector systems are associated with the correct bunch crossings. This is a key consideration since the muon time-of-flight typically exceeds the time between bunch crossings, as does the lifetime of calorimeter signals.

The ATLAS detector uses a two-level trigger system to select potentially interesting physics events [69]. The level-1 (L1) trigger is hardware-based and is installed on the detector to reduce the rate to a maximum of 100 kHz. Using information from the calorimeters and MS, a L1 decision is made within  $2.5 \mu\text{s}$  of the event, during which time the event information is stored in buffers on the detector systems. Events passing the L1 trigger are sent to the data acquisition system (DAQ) system and high-level trigger (HLT), a software-based trigger which further reduces the event rate to 1.2 kHz.

The HLT uses additional detector information, including that from the ID, to examine regions-of-interest identified by the L1. Event data from all detector systems are collected and assembled into a single data structure. As well as event selection to reduce the rate, the HLT classifies selected events into “streams” which label events for physics analysis, data quality monitoring or detector calibration. Events selected by the HLT are moved to the CERN data centre for permanent storage. Once stored in the data centre, offline reconstruction can be run on the events for use in physics analyses. This will be discussed further in Chapter 5.

A trigger chain refers to the combination of L1 seeds and HLT algorithms which identified an event as being of interest. Together the collection of chains employed by the detector make up the trigger menu which determines the types of events saved by ATLAS. For any given physics analysis one or more trigger chains are chosen from the menu to provide an initial event selection.

# Chapter 4

## The ATLAS inner tracker upgrade

Following the conclusion of the third run of the LHC, the machine will be upgraded to increase the instantaneous luminosity provided to the detectors. This will allow significantly larger samples of data to be collected by the experiments, providing greater sensitivity to rare physics processes. As shown by Fig. 3.1, the expected instantaneous luminosity during Runs 4 and 5 is expected to reach  $5.0 - 7.5 \times 10^{34} \text{ cm}^2\text{s}^{-1}$ , leading to a total integrated luminosity of 3000-4000  $\text{fb}^{-1}$  [70]. The HL-LHC introduces a number of experimental challenges for tracking and vertexing performance, as well as detector lifetime. The ATLAS detector will therefore receive a number of upgrades to prepare for data-taking at the HL-LHC.

The ATLAS experiment employs silicon detector technology for the inner detector (ID) to measure the trajectory of charged particles, to allow inference of their momentum and the point along the beam line at which they were produced. This chapter discusses the use of silicon radiation sensors in high energy physics and the effect of radiation on the operating characteristics of the devices. Following this, the planned upgrade to the ID to increase the tracking precision and improve the radiation hardness is presented. The upgrade corresponds to a complete replacement of the current pixel detector, SCT and TRT with a new detector,

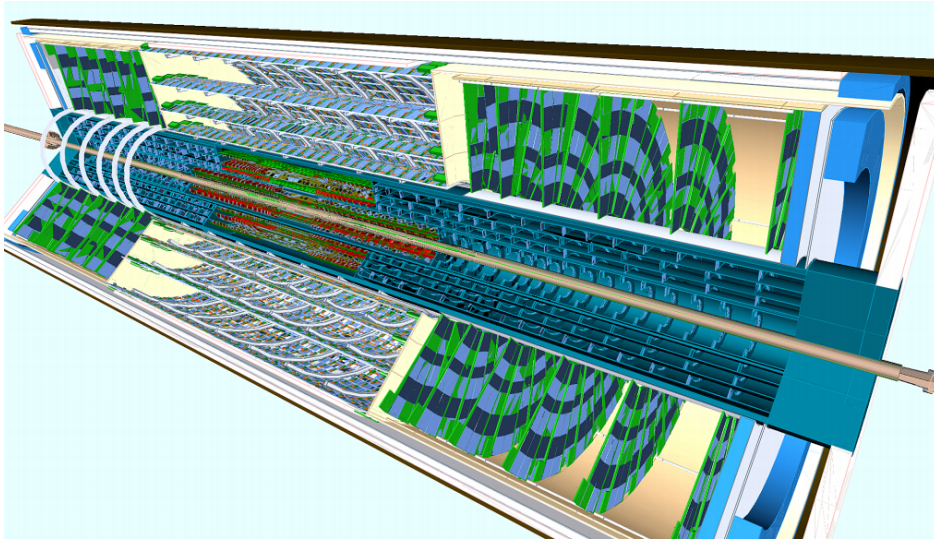


Figure 4.1: Diagram of the ATLAS ITk as implemented in the GEANT4 simulation programme [71]. The beampipe is shown in brown at the centre of the diagram; surrounding this are the pixel and strip detectors which both extend the full length of the diagram.

the Inner Tracker (ITk), composed entirely of silicon radiation sensors. The ITk is composed of a pixel detector to provide the highest precision close to the beamline and a strip detector to extend the tracking capability to larger radii. A diagram of the new detector can be seen in Fig. 4.1.

A quality assurance (QA) programme is in place to provide confidence that sensors destined for the experiment will perform as expected in the harsh environment of the HL-LHC. The author's contribution to this programme has been the development and installation of a parametric testing setup used to extract key electrical characteristics of the sensors from test devices. A number of measurements of QA devices made by the author during the pre-production phase of the sensor project are discussed. The setup has been validated by comparison of the results between other institutes. These measurements will be crucial to monitoring the fabrication quality of sensors during the production phase which has since begun.

## 4.1 Silicon radiation detectors in high energy physics

### 4.1.1 Electronic properties of silicon

Elements with four valence electrons (tetravalent) achieve a stable electronic configuration by forming four covalent bonds to fill their outer electronic shell. Silicon crystals form a diamond cubic lattice structure in which each atom forms a covalent bond with four neighbours. At room temperature silicon has a small band gap of 1.12 eV [72] between its valence and conduction bands; at temperatures above absolute zero thermal fluctuations can excite an electron to the conduction band, breaking the covalent bond. In the conduction band an electron can move under the influence of an external electric field applied to the crystal, allowing a current to flow. The excitation of an electron leaves behind a vacancy in the valence band, known as a hole. A hole effectively carries a positive charge corresponding to that of the newly ionised atom. A vacancy may be filled with an electron belonging to a neighbouring atom, resulting in the hole moving through the lattice, which allows it to conduct an electric current. The production of electrons and holes in this manner is known as thermal generation. As the temperature increases, more energy is available for thermal generation and the concentration of charge carriers within the lattice increases. The inverse process is also possible; a free electron may also recombine with a hole, reducing the concentration of charge carriers within the crystal.

In intrinsic silicon at room temperature, the concentration of free charge carriers is sufficiently low that it is not particularly conductive. However, if impurity atoms are introduced into the silicon lattice, in a process known as doping, then its conductivity can be greatly increased. Introducing pentavalent atoms at lattice sites results in an additional free electron per dopant atom, since only four of the valence electrons of the dopant can form covalent bonds with the surrounding silicon atoms. The crystal itself remains electrically

neutral since the negative charge of the free electron is balanced by the fixed net positive charge of the ionised dopant atom. Conversely, a trivalent atom added to the lattice will result in the formation of three covalent bonds with surrounding silicon atoms and an additional hole. Silicon doped with pentavalent (“donor”) atoms is known as n-type while that with trivalent impurities (“acceptors”) is known as p-type. In intrinsic silicon, thermal generation results in equal concentrations of electrons and holes, while the process of doping results in a large excess of one type, which is referred to as the majority carrier. In doped silicon the concentration of the majority charge carriers depends on the doping concentration and not the temperature. The concentration of minority charge carriers, which result from thermal generation, is still strongly temperature-dependent.

By depositing doped silicon of one type onto a substrate of the opposite doping type, a p-n junction is formed. The large concentration of holes in the p-type region results in a steep concentration gradient which causes holes to diffuse towards the n-type silicon. Conversely, there is a net movement of electrons from the n-type region towards the p-type region. When these charge carriers meet, recombination occurs giving rise to a region containing a fixed space charge of ionised dopant ions. The electrostatic potential that develops as the space charge region grows, known as the built-in potential,  $V_0$ , produces an electric field which acts to oppose further diffusion across the interface. Holes are repelled from the positive space charge in the n-type region and electrons from the negative space charge in the p-type region which reduces the diffusion current. Charge carriers entering the space charge region drift under the influence of the electric field; these may be thermally generated carriers, or any minority carriers which enter from the edges of the undepleted regions. When the drift of charge carriers due to the electric field balances the diffusion current, equilibrium is reached. The p-n junction is then characterised by a region which is devoid of mobile charge carriers and contains a fixed space charge, known as the depletion region. A diagram showing the electric field and potential across the p-n junction after the development of the space charge

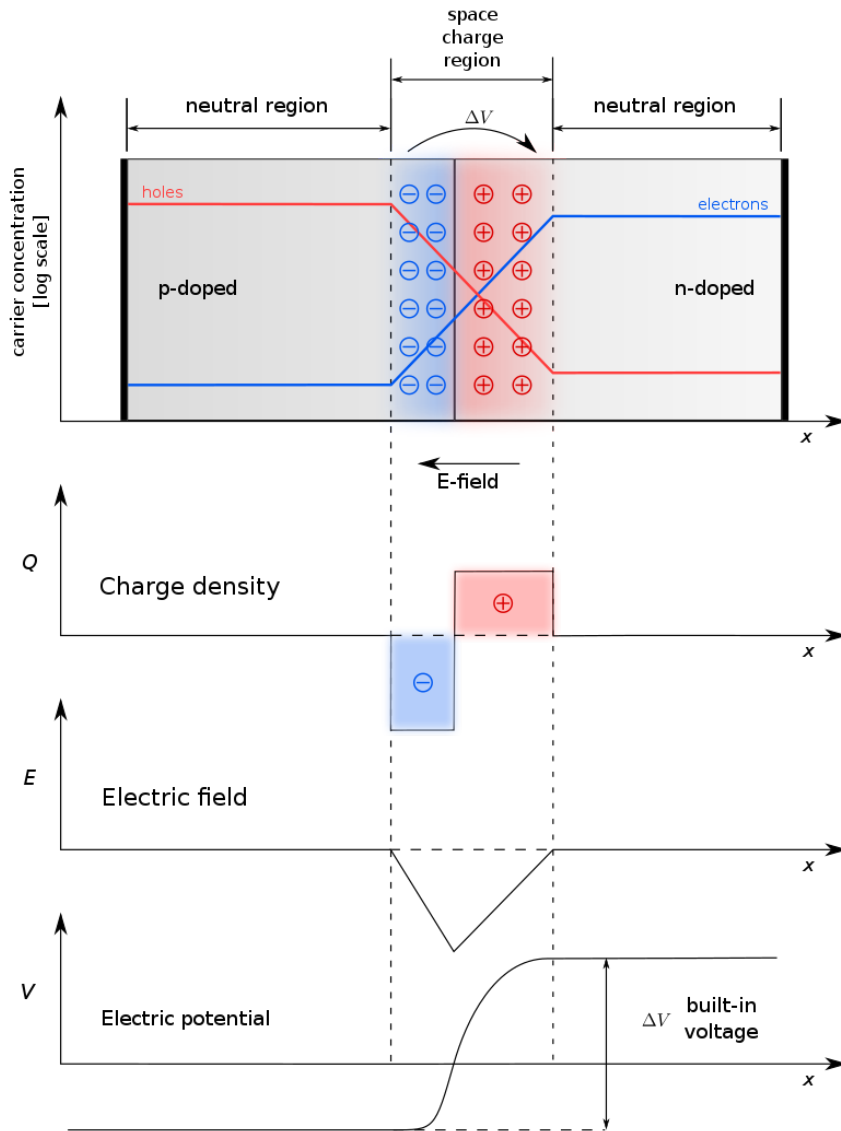


Figure 4.2: The development of a depletion region across a p-n junction formed in silicon in the absence of an external electric field. The space charge is formed of dopant ions, negative in the p-type region and positive in the n-type region. Image from [73].

region, also known as the depletion region, is shown in Fig. 4.2.

Since the overall charge in the depletion region is required to be zero, the doping concentration of each region can be related to the width of the depletion region on each side of the junction by

$$N_D d_n = N_A d_p, \quad (4.1)$$

where  $N_D$  and  $N_A$  are the donor and acceptor concentrations, respectively, and  $d_n$  and  $d_p$  are the widths of the depletion region extending from the junction into the n- and p-type sides, respectively. From Eq. (4.1) it can be seen that if one region is doped more strongly than the other, the depletion region will be asymmetric around the interface.

In the presence of an applied electric field the potential across the junction is changed and the device is no longer in equilibrium. Application of a forward bias voltage, equivalent to the injection of electrons to the n-type material, decreases the size of the built-in potential which results in an increased diffusion current. As a result of this, the width of the depletion region will decrease. Conversely, applying a reverse bias voltage increases the height of the potential barrier and enlarges the depletion region. The width of the depletion region under the influence of a reverse bias voltage,  $V_{\text{bias}}$ , is given by

$$d = \sqrt{\frac{2\epsilon_{\text{Si}}(N_A + N_D)}{qN_A N_D}(V_0 + V_{\text{bias}})}, \quad (4.2)$$

where  $q$  is the elementary charge and  $\epsilon_{\text{Si}}$  is the permittivity of silicon [72].

The drift current is independent of the applied bias but is strongly temperature dependent. Under reverse bias, minority carriers generated in or entering the depletion region drift under the electric field, giving rise to a small leakage current. The dependence of this reverse leakage current,  $I$ , on temperature,  $T$ , is seen to be

$$I \propto T^2 \exp\left(-\frac{E_{\text{eff}}}{2kT}\right), \quad (4.3)$$

where  $k$  is the Boltzmann constant and effective gap energy  $E_{\text{eff}} = 1.21$  eV [74]. While the generation rate due to thermal excitation of electrons from the valence band to the conduction band is low, defects in the doped silicon lattice create additional energy levels in the band gap which aid in the thermal generation process. This appearance of defects is important in the context of radiation damage to the lattice.

### 4.1.2 Silicon radiation sensors

A charged particle traversing a reverse-biased silicon p-n junction will ionise atoms within the lattice and resulting charges in the depletion region will drift under the influence of the electric field. If an electrode is placed on the surface of the device, the movement of charge within the sensor will induce a current on the electrode, making it possible to determine when a charged particle has passed through the device. This is the operating principle of silicon radiation sensors.

In its simplest form a silicon sensor consists of a single channel which is used to infer the passage of a charged particle: a pad detector formed from a highly doped implant deposited onto a less doped substrate. However, such a detector provides no position information in the plane parallel to the detector surface. The highly doped implant is therefore segmented into strips to provide 2D position information or segmented in both directions to form a pixel detector which provides 3D position information. Strip sensors consist of a low doped bulk with highly doped strips of the other type implanted at the surface. These sensors are operated under high reverse-bias voltages to fully deplete the bulk, thereby maximising the induced signal in the read-out electronics.

An oxide layer, mostly  $SiO_2$ , forms naturally on top of the silicon device which provides electrical isolation to the implants. A metal read-out strip is then placed on the surface

of the oxide layer and the electrical connection between implant and this read-out strip is induced capacitively. The metal strip is wire-bonded to the read-out electronics. In order to apply a bias voltage to the strip implants, they are connected to a surrounding bias rail. To maintain electrical isolation between the neighbours, implants are connected to the bias rail via high resistance polycrystalline silicon resistors. This is important as charge sharing between neighbouring strips resulting from poor electrical isolation degrades the position resolution of a tracking detector.

Above a certain applied reverse-bias voltage, the reverse current is seen to rise rapidly. This results from the acceleration of the minority carriers in the depletion region to an energy at which they are able to produce further ionisation. This causes a rapid multiplication in the current and is known as avalanche breakdown. The voltage at which this occurs is called the breakdown voltage and acts as an upper limit on the reverse bias voltage at which the sensor can operate. It is important that this breakdown voltage is significantly greater than the full depletion voltage of the sensor otherwise the sensor will have to operate partially depleted, which leads to decreased signal.

### 4.1.3 Effect of radiation on silicon detectors

A key design requirement for tracking detectors operating at hadron colliders is radiation hardness - the ability to withstand high doses of both ionising and non-ionising radiation. Radiation damage to silicon sensors is typically grouped into two categories: damage to the bulk caused by the displacement of atoms from lattice sites, and damage to the surface caused by the build-up of trapped charge in the oxide and at the interface between the bulk and the oxide. Surface damage is the result of energy deposited through ionisation; it depends on particle energy but is independent of the type of particle. Bulk damage results from non-ionising energy losses (NIEL). It depends not only on particle energy but also on the

type of particle, since the fraction of energy lost to non-ionising processes differs between particles. For this reason, it is useful to scale the expected NIEL for a particle of a given energy to that of a 1 MeV neutron and quote the radiation dose in terms of an equivalent 1 MeV neutron fluence ( $n_{\text{eq}}/\text{cm}^2$ ). Since the oxide does not have a regular lattice structure like the silicon bulk, displacement damage does not lead to changes in its properties. Conversely, ionisation does not cause damage to the bulk of the sensor.

## Annealing

Annealing is the process by which the effects of radiation damage are seen to evolve with time. Defects created by displacement damage may be mobile in the lattice and can go on to form more complex defects or may be removed, for example if a displaced silicon atom recombines with a lattice vacancy. The optimal time to take advantage of the beneficial annealing process has been found to be 80 min at 60°C, which is approximately equivalent to 7 days at 25°C [75]. This is therefore used as the standard annealing procedure for sensors being tested.

## 4.2 The ATLAS inner tracker upgrade

Successful data-taking in the HL-LHC era requires a tracking detector capable of resolving tracks in high pile-up and high radiation conditions. One of the key motivations for the construction of the ITk is the requirement for increased radiation hardness. The SCT was originally designed to operate for up to 700 fb<sup>-1</sup> of data-taking [76]; however, during the HL-LHC phase, the ATLAS detector is expected to receive 3000 fb<sup>-1</sup> of  $pp$  collisions [71], necessitating a significant improvement in the radiation hardness of the detector. In addition to this, the detector is required to have finer granularity to maintain its current tracking

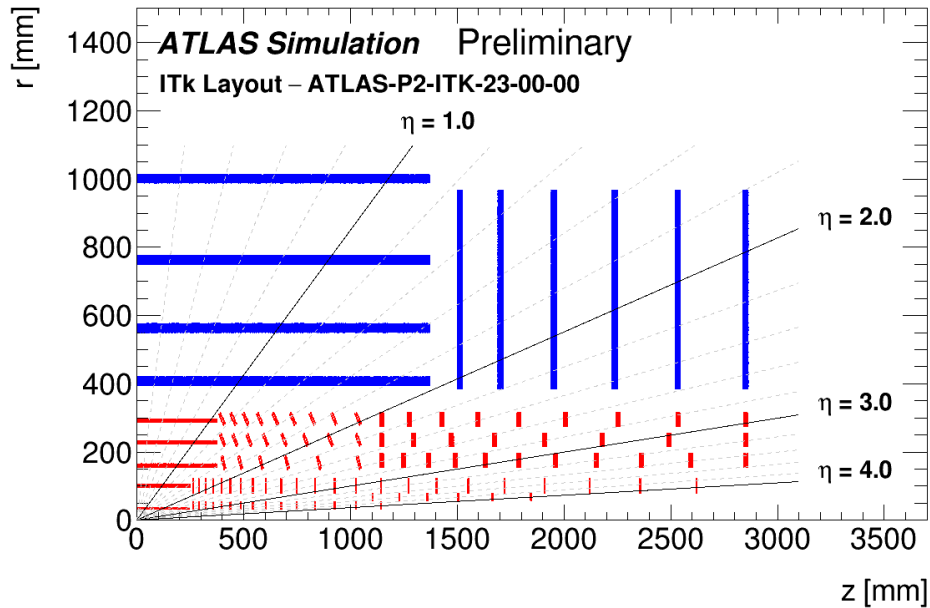


Figure 4.3: Layout of the ATLAS Inner Tracker upgrade (ITk) [77]. Layers of the pixel and strip detector are shown in red and blue, respectively.

performance under conditions of increased pile-up. The maximum number of interactions seen per bunch crossing in Run 2 was less than 90, while at the HL-LHC pile-up is expected to peak at 200 interactions per bunch crossing [71]. The performance of the detector will therefore rely heavily on its vertexing ability to correctly associate tracks to their primary vertex. The all-silicon design will also replace the TRT, which would be unable to cope with the increased hit occupancy it would encounter during the HL-LHC era. The layout of the ITk is shown in Fig. 4.3 with the pixel detector components in red and strip detector components in blue.

## 4.3 ITk strip sensor QA programme

### 4.3.1 QA test devices

The purpose of the strip sensor QA programme is to verify that the required specifications of the sensors will be achieved throughout the production phase. The program uses test devices produced on the edge of the main sensor wafers which allow for efficient measurement of the electrical properties of the sensors. Testing is carried out before and after irradiating the devices to ensure the detector system will be capable of delivering good tracking performance after irradiation to the high fluence expected during the HL-LHC phase. The methodology for the testing process is documented in Ref. [78]. The author’s contribution to this project has been the assembly and validation of the testing setup described in Section 4.3.2, the annealing and preparation of test devices, and performing the measurements discussed in Section 4.3.3. These measurements were the focus of the first year of the author’s PhD; the author continued performing measurements of QA devices throughout the second year of study and not all measurements are discussed here. For all of the QA tests performed, a number of conditions of the test, such as the temperature and relative humidity, as well as the relevant extracted parameters are stored centrally in a database. A document setting out the QA database inputs for the strip sensor QA programme has been prepared, to which the author of this report was one of the main contributors.

The test structures include miniature versions of the main ITk strip sensors (referred to as “minis”), simple diode structures and “test chips”. The testing programme for mini sensors involves charge collection efficiency (CCE) and current-voltage (IV) measurements to characterise the sensor leakage current. The author has performed mini sensor measurements, both as part of the QA programme and during studies into the Birmingham irradiation setup, but these are not discussed further. The diodes discussed in this report have  $8\text{ mm} \times 8\text{ mm}$

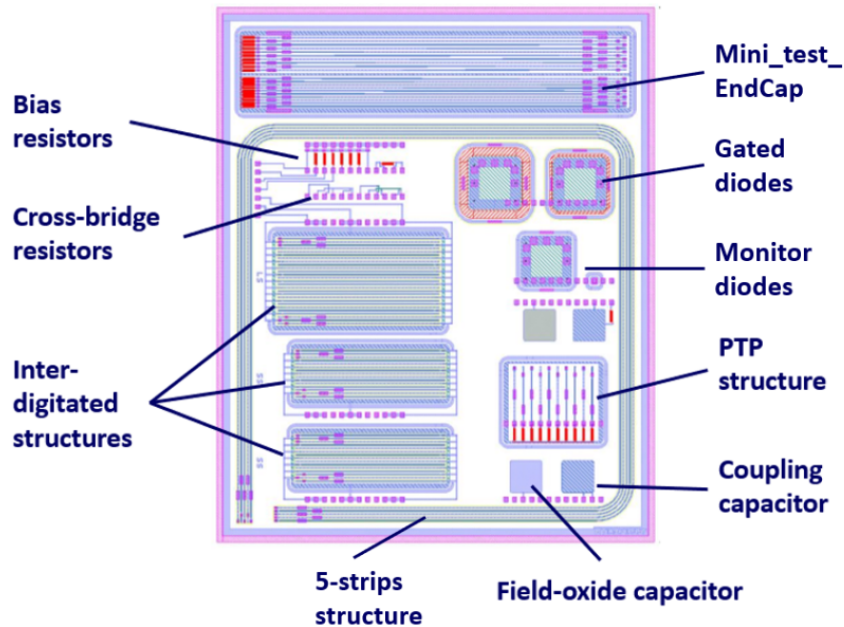


Figure 4.4: Diagram showing structures on the test chip taken from [78]. Labels added.

dimensions and are referred to as “MD8”s. These provide an additional measurement of the leakage current and can be used to extract the full depletion voltage of the sensor through capacitance-voltage (CV) measurements. The MD8 consists of a highly-doped n-type implant deposited onto the p-type bulk and resembles an unsegmented pad detector. The implant is surrounded by a guard ring which can be grounded to prevent the implant being sensitive to surface currents from the edge of the silicon. The test chip is a 10 mm×12 mm device featuring numerous test structures which allow for the extraction of key parameters of the sensors and provides probes of both bulk and surface damage effects. The back side of the test chip and MD8 piece, the backplane, has a metal contact to allow a bias potential to be applied to the bulk.

A labelled diagram of the test chip is shown in Fig. 4.4, from which a number of important structures which will be regularly tested can be seen. Bias resistors, identical to those employed on the full-size sensors, are used for measurements of the bias resistance,  $R_{\text{bias}}$ . The coupling capacitor allows the properties of the coupling oxide to be studied and is used

to extract the coupling capacitance,  $C_{\text{coupl}}$ . The interdigitated structures allow measurements of inter-strip properties, in particular of inter-strip resistance and capacitance,  $R_{\text{int}}$  and  $C_{\text{int}}$ , respectively. The punch-through protection (PTP) structure is used to characterise the performance of punch-through protection, used to safeguard the electronics of the detector in the case of unusually large charge deposition. Measurements of these properties will be discussed in Section 4.3.3.

### 4.3.2 Test chip measurement setup

The silicon piece with the test chip and MD8 is mounted on a PCB and secured inside a testing box, as shown in Fig. 4.5. To provide electrical connections to different structures the test chip has many metal pads available, each of which can be wire-bonded to a PCB or contacted with needles on a probe station. The measurement setup uses a “splitting box” to connect measurement instruments to two switching matrices which in turn connect to various channels of the test chip. This allows efficient automated testing of the many test chip structures as well as the MD8. The switching matrices allow the connections between each measurement instrument and test chip pad to be switched on and off by a control PC. The setup has been developed by collaborators and adapted by the author for use with equipment in the Birmingham lab.

The measurement setup, including electrical instruments, for the test chip can be seen in Fig. 4.6. The measurement instruments used to perform electrical measurements are a Keithley 2410 sourcemeter for biasing and current measurements, a Keithley 6487 precision ammeter for low current measurements, and a Keysight E4980AL precision LCR meter for capacitance measurements. The testing box itself is placed inside a climate chamber which maintains stable temperature and is flushed with nitrogen to maintain low relative humidity, ideally below 5%. Higher humidity can influence the results of the measurements, in particular

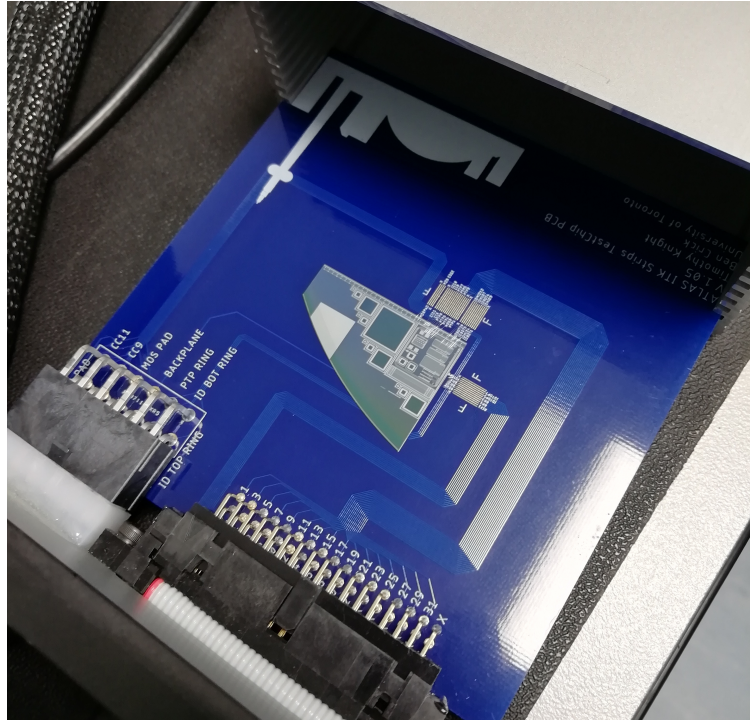


Figure 4.5: ITk QA test chip setup: silicon QA piece mounted on a PCB which is secured inside the testing box.

increasing the surface leakage current which can result in early breakdown. Testing of the unirradiated structures is performed at  $21.0^{\circ}\text{C}$  while post-irradiation tests are carried out at  $-20.0^{\circ}\text{C}$ .

The setup is controlled with Python scripts which perform the testing of each structure and record the measurements. The scripts were produced by collaborators to communicate with test equipment and run IV and CV measurements. These scripts have then been adapted and extended by the author to work with the equipment used in Birmingham. Measurement parameters, such as the waiting time between applying a voltage and making a measurement, and the instrument measurement speed, have been optimised to achieve stable, reproducible measurements.

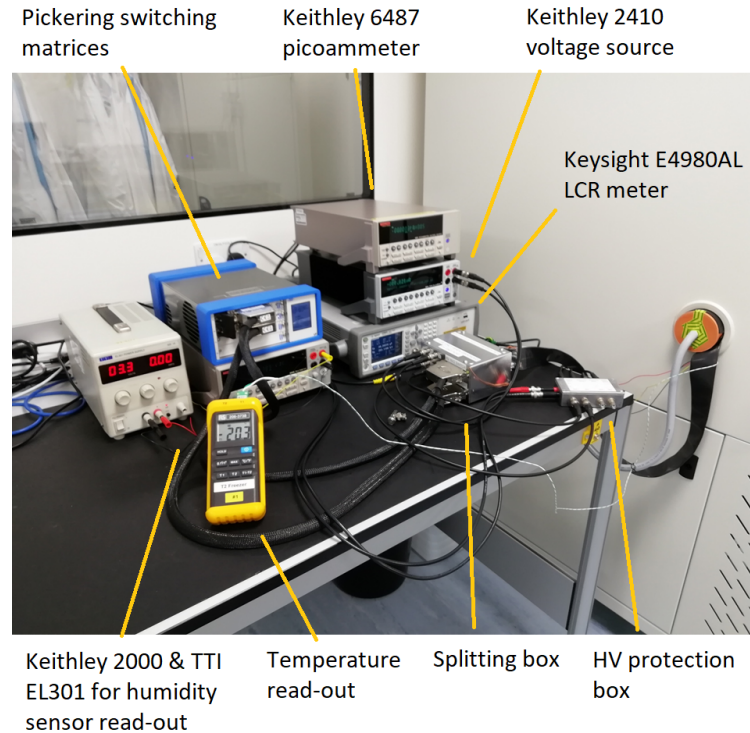


Figure 4.6: ITk QA test chip setup: measurement instruments and splitting matrices, along with splitting box and high voltage (HV) protection box shown next to the climate chamber.

### Corrections to capacitance measurements

The capacitances probed in the QA measurements are very small so the switching matrices and splitting box introduce non-negligible stray capacitances. Stray capacitance is additional capacitance resulting from cabling and other conductive components between the measurement instrument and the device-under-test (DUT).

Two different capacitance correction schemes have been investigated to account for this stray capacitance. Both methods treat stray capacitance as being in parallel with the capacitance of the DUT, in which case the measured capacitance is the sum of the two. The first method uses a PCB with no test chip mounted to measure the capacitance of a given channel and subtract this from measurements made when a test chip is present on the

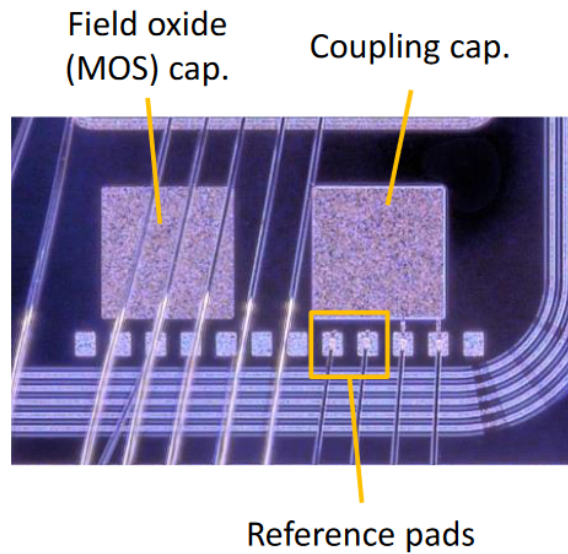


Figure 4.7: Image of test chip showing coupling capacitor and field oxide capacitor structures with spare wire-bonding (“reference”) pads labelled.

PCB. A second approach was to use spare wire-bonding pads on the test chip which are not connected to any test structure (“reference pads”) to perform a correction; two reference pads can be seen in Fig. 4.7. A reference measurement is performed using these neighbouring spare pads which can be subtracted from the capacitance found when using the pads connected to the structure-of-interest. In addition, measurements with a blank PCB are used to find any capacitance differences between measurement and reference channels.

The second approach was introduced to account for the possible influence of neighbouring test chip structures on the overall stray capacitance. In practise, however, such effects are seen to be small and these two approaches give consistent results. The accuracy of the Keysight LCR meter is given as 0.05% so measurement uncertainties are expected to be very low. Nevertheless, for measurements of inter-strip capacitance on the scale of 1-6 pF, the first approach was used to avoid introducing uncertainties from multiple measurements. Where the measured capacitance is larger, in the cases of MD8 and coupling capacitor measurements, the second approach is used. In both cases the measurement results discussed below are in

line with those from other measurements of these devices [79]. The magnitude of the stray capacitance differs between connection channels but is seen to be as large as 65 pF.

### 4.3.3 Test chip and MD8 measurements

Measurements have been performed on a number of test chip and MD8 devices. Tests are carried out before irradiation, to check the electrical properties of the devices meet required processing standards, and after irradiation, to understand the expected performance of the sensors towards the end of the HL-LHC era.

An unirradiated device was used to commission the system and understand the capacitance corrections. Two test chip and MD8 pieces, referred to as “site verification” pieces, have been measured and the results compared with other sites in the QA programme to validate the consistency of the individual setups and procedures. One site verification piece is unirradiated while the other has been gamma-irradiated using a cobalt-60 source at UJP Praha in Prague. The IV characteristics of three additional MD8 devices have also been evaluated. The fluence/dose of the measured devices, along with those to which the sensors are expected to receive at the HL-LHC are shown in Table 4.1. After irradiation sensors are annealed for 80 minutes at 60°C which has been determined to correspond to the optimal bulk annealing of the sensors [75], as has been discussed in Section 4.1.3. The site verification devices form the basis of the discussion in this section.

Table 4.1: Fluences and total ionising doses of test devices along with the expected maximum fluence received by the strip sensor system at the HL-LHC according to [71].

	Fluence / $n_{\text{eq}}/\text{cm}^2$	Total ionising dose / kGy
<b>Test chip &amp; MD8 devices</b>		
Site commissioning (unirrad.)	-	-
Site verification (unirrad.)	-	-
Site verification ( $\gamma$ irradi.)	-	660
<b>Additional MD8 devices</b>		
Unirradiated	-	-
Proton irradiated	$4.7 \times 10^{14}$	-
Proton irradiated	$1.5 \times 10^{15}$	-
<b>Expected maximum</b>		
Endcap region	$8.2 \times 10^{14}$	336
Barrel region	$5.4 \times 10^{14}$	238

### Bulk properties

The MD8 provides important measurements of the leakage current and full depletion voltage, key bulk properties of silicon devices. Leakage current is extracted as a function of voltage by measuring the current between the implant and the backplane of the silicon, with no bias applied to the guard ring. The IV curves measured for six MD8 devices are shown in Fig. 4.8 along with the maximum allowed values before and after irradiation. It can be seen that there is a clear hierarchy to the sizes of the measured currents depending on whether or not the device has been irradiated and on the type of radiation.

Table 4.2: MD8 leakage currents between pad and backplane at a reverse bias voltage of 500 V for six MD8 devices. Currents for the unirradiated devices have been corrected to  $-20^{\circ}\text{C}$  using Eq. (4.3). The associated uncertainty is the quoted accuracy of the measurement instrument.

Device	Leakage current at 500 V / A
Site commissioning (unirrad.)	$2.94 \pm 0.10 \times 10^{-10}$
Additional unirrad. MD8	$1.83 \pm 0.10 \times 10^{-10}$
Site verif. (unirrad.)	Early breakdown
Site verif. (gammas)	$2.8 \pm 1.0 \times 10^{-8}$
Protons ( $4.7 \times 10^{14} n_{\text{eq}}/\text{cm}^2$ )	$8.98 \pm 0.02 \times 10^{-6}$
Protons ( $1.5 \times 10^{15} n_{\text{eq}}/\text{cm}^2$ )	$25.13 \pm 0.04 \times 10^{-6}$

The currents of the proton irradiated devices are several orders of magnitude higher than those of the unirradiated devices. The defects created in the lattice by displacement damage introduce new energy levels within the bandgap of silicon. New energy levels in the middle of the bandgap increase the rate of thermal generation which results in an increased leakage current.

Gamma irradiation causes surface damage to the sensor through ionisation in the oxide layer. Most of the electron-hole pairs formed will recombine but in some cases the more mobile electron avoids recombination and, with the sensor under reverse-bias, is able to drift towards the read-out electrode, leaving behind the hole. The hole is much less mobile and will drift slowly towards the bulk-oxide interface where there are many hole traps, increasing the total oxide charge. Such a charge build-up leads to reduced isolation between strips and increased leakage currents at the surface of the device. In addition, gamma irradiation by cobalt-60 contributes to bulk damage by the production of Compton electrons with an

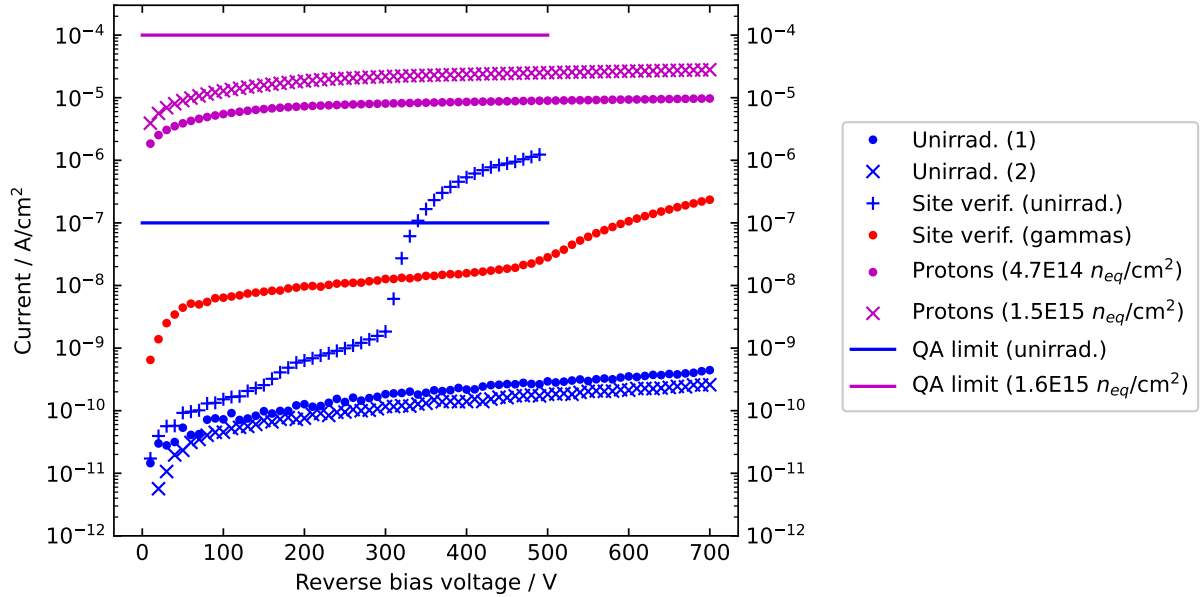


Figure 4.8: Plot of MD8 current between pad and backplane as a function of bias voltage for six MD8 devices. IV curves are shown in blue for unirradiated devices, red for gamma-irradiated devices, and magenta for proton-irradiated devices. Currents for the unirradiated devices have been corrected to  $-20\text{C}$  using Eq. (4.3). Also shown are the maximum current limits permitted by the ITk QA requirements up to 500 V.

energy of up to around 1 MeV. However, it can be seen that the current in the gamma irradiated sample is several orders of magnitude lower than in the proton irradiated devices. The Compton electrons responsible for bulk damage will produce point defects in the lattice but do not produce more complex defect clusters which are thought to be responsible for increasing leakage current [80]. The increased current after gamma irradiation is therefore attributed to the surface current as a result of ionisation damage.

The leakage current is a principal contributor to the detector noise. Therefore, ITk strip sensors are required to have a leakage current below  $0.1 \mu\text{A}/\text{cm}^2$  normalised to  $-20.0^\circ\text{C}$  up to 500 V before irradiation, and below  $0.1 \text{mA}/\text{cm}^2$  normalised to  $-20.0^\circ\text{C}$  up to 500 V after irradiation to a fluence of  $1.6 \times 10^{15} n_{\text{eq}}/\text{cm}^2$ . These requirements are represented by

the blue and magenta horizontal lines in Fig. 4.8. It can be seen that with the exception of the site verification piece in which an early breakdown is observed, these specifications are met for all devices. The leakage current for the gamma-irradiated device meets even the pre-irradiation requirements.

For the unirradiated site verification piece (shown with blue ‘+’ markers on Fig. 4.8) an early breakdown was seen at around 300 V in the IV scan. Early breakdown can result from high humidity in the test box which increases the surface leakage current. However, the humidity was below 5% and the breakdown was seen to be repeatable at the same voltage. It is possible that the breakdown resulted from a processing defect or as a result of damage to the device, as other devices from this batch did not show the same behaviour. Additional care was taken with the handling of samples to ensure mechanical damage was avoided. The other unirradiated samples showed no breakdown and had much lower leakage currents. In both cases the currents in these devices are well below the pre-irradiation requirement of  $0.1 \mu\text{A}/\text{cm}^2$ .

The gamma-irradiated diode also exhibits a breakdown, however, this occurs at a much higher voltage of 510 V and is much softer than the breakdown of the unirradiated sample. This breakdown is likely to be a consequence of radiation damage to the sensor, due to the increase of the electric field near the surface of the sensor. The reduction in the voltage at which breakdown occurs is affected by both bulk and surface damage.

To extract the voltage at which the bulk of a sensor is fully depleted,  $V_{\text{FD}}$ , the capacitance between the implant and the backplane of the MD8 is measured as a function of voltage. Since the doping of the strip implant is much greater than the doping of the bulk, the depletion region width as given in Eq. (4.1) reduces to

$$d \approx \sqrt{\frac{2\epsilon_{Si}}{qN_A}(V_0 + V_{bias})}. \quad (4.4)$$

The depletion region is devoid of majority charge carriers so the sensor can be treated as a

parallel plate capacitor with the depletion region acting as the dielectric. Using this treatment the bulk capacitance is given by

$$C = \frac{\epsilon_{Si} A}{d} = \sqrt{\frac{\epsilon_{Si} q N_A}{2(V_0 + V_{bias})}} A, \quad (4.5)$$

where  $A$  is the area of the sensor.

Based on Eq. (4.5) it can be seen that the capacitance is expected to decrease as a function of reverse bias voltage until the bulk is fully depleted at which point it should remain constant; the quantity  $1/C^2$  is expected to be linear as a function of  $V_{bias}$  before  $V_{FD}$  and flat afterwards. From a plot of  $1/C^2$  against bias voltage,  $V_{FD}$  can be extracted by the extrapolation of straight lines fitted to the two regions to find the point of intersection, as shown for the site verification MD8s in Fig. 4.9. Gamma irradiation is not expected to influence  $V_{FD}$  so it is likely that the difference between the gamma irradiated sample and the unirradiated sample was present before irradiation. In both cases a smooth CV curve is obtained and the QA specification that the  $V_{FD}$  is less than 350 V before irradiation is met.

### Bias resistance

The bias resistor structures are identical to those on the main sensors which provide a high resistance electrical connection between the bias rail and the strip implants. A simple IV measurement is used to extract  $R_{bias}$ , which is expected to satisfy  $R_{bias} = 1.5 \pm 0.5 \text{ M}\Omega$  at  $20^\circ\text{C}$ . For each test chip, three bias resistors can be tested via wire-bonds and the resulting values of  $R_{bias}$  are shown in Table 4.3. The IV curves for each of the bias resistors on the gamma irradiated sample and one of the unirradiated samples are shown in Fig. 4.10. Tests of bias resistors on both of the unirradiated test chips have met this requirement with average values of  $1.55 \pm 0.02 \text{ M}\Omega$  and  $1.53 \pm 0.02 \text{ M}\Omega$ , where the uncertainty is propagated from the fit to the IV curve. The uncertainties on the individual measurements found using the covariance matrix of the linear fit to the IV curves are shown in Table 4.3.

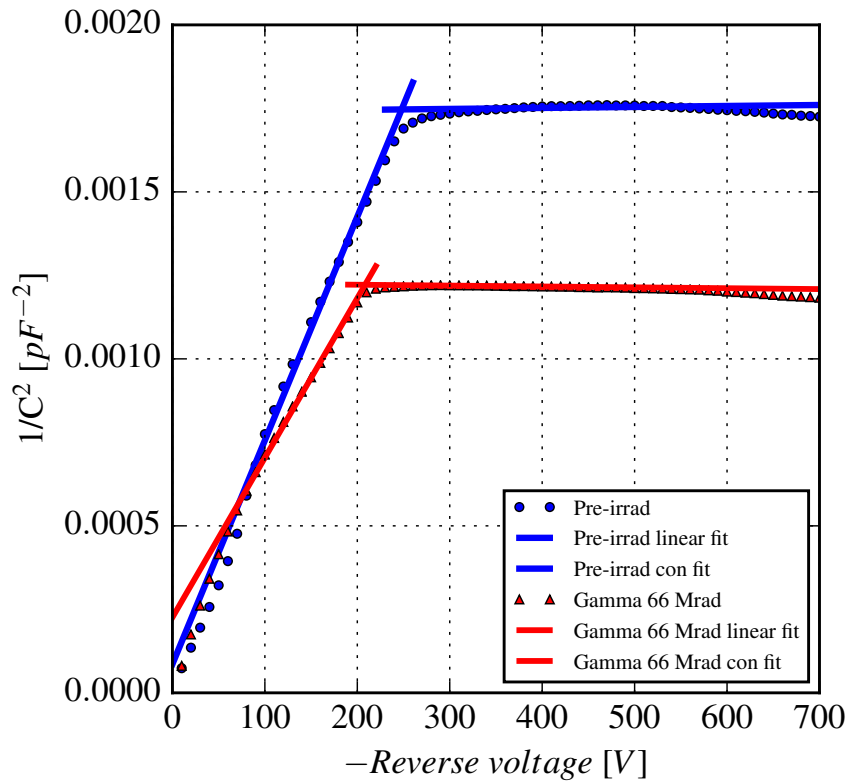


Figure 4.9: Plot of MD8 bulk capacitance as a function of reverse bias voltage for two MD8 devices showing the extraction of the full depletion voltage. Plot produced by Dr Ioannis Kopsalis. Measurement data are shown as markers while solid lines represent linear fits to the rising slope (“linear”) and constant plateau (“con”).

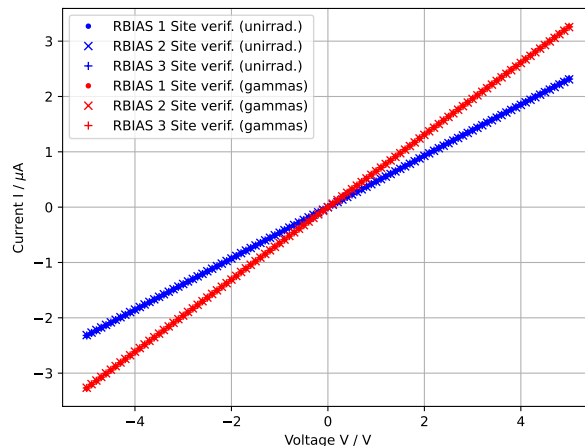


Figure 4.10: Plot of IV scans of bias resistors on the site verification test chips (one unirradiated, one gamma irradiated). IV curves are shown in blue for unirradiated devices and red for gamma-irradiated devices. For each device, three IV curves are shown corresponding to each resistor which can be tested with wire-bonds.

After gamma irradiation all three resistors tested showed increased resistances with an average of  $2.16 \pm 0.02 \text{ M}\Omega$ . The increased resistance originates from the temperature dependence of  $R_{\text{bias}}$  [81] so these are also consistent with the QA requirements. Corrected to  $20^\circ\text{C}$  using the temperature-dependence from [81] the resistance is  $1.81 \pm 0.02 \text{ M}\Omega$ , which is consistent with the higher  $R_{\text{bias}}$  after gamma-irradiation seen in this reference. The cause of the increased  $R_{\text{bias}}$  is not yet understood. Nevertheless,  $R_{\text{bias}}$  is seen to remain within the QA specification even for a total ionising dose (TID) of 660 kGy, a significantly higher dose than the maximum expected for strip sensors at the HL-LHC.

### Coupling oxide properties

The coupling capacitor structure consists of a highly-doped square implant onto which an oxide layer is grown before a square metal contact is placed on the top. A capacitance measurement between the implant and the metal allows  $C_{\text{coupl}}$  to be extracted. The capacitive

Table 4.3: Measurements of bias resistance on the site verification and commissioning test chips (one unirradiated, one gamma irradiated). The uncertainty comes from the covariance matrix of the linear fit to the IV curve.

	$R_{\text{bias}} / \text{M}\Omega$		
Site commissioning (unirrad.)	$1.553 \pm 0.031$	$1.551 \pm 0.031$	$1.553 \pm 0.031$
Site verif. (unirrad.)	$1.529 \pm 0.032$	$1.534 \pm 0.032$	$1.532 \pm 0.031$
Site verif ( $\gamma$ irradi.)	$2.152 \pm 0.042$	$2.163 \pm 0.043$	$2.157 \pm 0.044$

coupling between the implant and metal enables signal read-out so the coupling capacitance is required to be greater than 20 pF/cm, where the capacitance is normalised to a strip length of 3.4 cm. Measured  $C_{\text{coupl}}$  values can be seen in Table 4.4; it can be seen that all devices exceed the QA requirements. These values have been measured manually, rather than with Python scripts, so the uncertainty has been taken as twice the least significant digit which is seen to be stable ( $\pm 0.2$  pF) for both the measured capacitance and the reference pad measurement (see Section 4.3.2).

The coupling capacitor structure also provides a measurement of the current through the dielectric which should be below 10 nA for potential differences up to 100 V. This is to ensure that there will be no breakdown through the dielectric if a large charge in the sensor generates a large potential difference across the coupling capacitor. Such a breakdown would allow a large current to flow into the read-out electronics which may be damaged. The current requirement was found to be met in all of the structures measured. The current in each device when 100 V is applied across the dielectric is shown in Table 4.4, along with the uncertainty given by the quoted accuracy of the measurement instrument.

Table 4.4: Coupling capacitor capacitance and current measurements for site verification test chips.

	Current at 100 V / nA	$C_{\text{coupl}}$ / (pF/cm)
Site commissioning (unirrad.)	$3.9 \pm 0.7$	$22.0 \pm 0.3$
Site verif. (unirrad.)	$2.5 \pm 0.7$	$21.8 \pm 0.3$
Site verif ( $\gamma$ irradi.)	$1.7 \pm 0.7$	$24.7 \pm 0.3$

### Inter-strip properties

The interdigitated structure consists of a number of strip implants surrounded by a bias ring and a guard ring. The strips are not connected to the bias ring; instead, alternating strips are connected at opposite ends of the structure to wire-bonding pads, providing a total implant length equal to the strip length in the main sensors. Main sensors in different parts of the detector have strips of different lengths and at different angles. Each test chip features three interdigitated structures which allows for extraction of inter-strip properties from structures with varying total implant length and angles.

To measure  $R_{\text{int}}$  the bulk of the chip is fully depleted and the bias ring held at ground. A voltage sweep from -5 to 5 V is applied to one set of strips while the current is measured at the other set.  $R_{\text{int}}$  is extracted from the inverse of the slope of the IV curve. Inter-strip resistance is required to be a factor of ten greater than the bias resistance to ensure good isolation between neighbouring implants. At a temperature of -20°C this corresponds to a requirement of  $R_{\text{int}} > 18 \text{ M}\Omega$ . Charge sharing between neighbouring strips degrades the sensor's position resolution. The measured values of  $R_{\text{int}}$  are shown in Table 4.5. It can be seen that the uncertainties on the unirradiated results are significant. This is a result of the very small currents probed being at the limit of the measurement instrument. The quoted uncertainties result from the covariance matrix of the linear fit to the IV curves. Nevertheless,

Table 4.5: Measurements of inter-strip resistance for each interdigitated structure on the site verification and commissioning test chips.

	$R_{\text{int}} / \Omega$		
Site commissioning (unirrad.)	$(6 \pm 2) \times 10^{11}$	$(7.2 \pm 0.8) \times 10^{12}$	$(3.7 \pm 0.8) \times 10^{12}$
Site verif. (unirrad.)	$(5 \pm 4) \times 10^{11}$	$(7.4 \pm 0.7) \times 10^{12}$	$(5 \pm 8) \times 10^{11}$
Site verif ( $\gamma$ irradi.)	$(8.22 \pm 0.01) \times 10^6$	$(12.47 \pm 0.03) \times 10^7$	$(8.81 \pm 0.02) \times 10^6$

the measured currents remain well below 100 pA in these devices, setting a lower limit of 50 G $\Omega$  on  $R_{\text{int}}$ , well in excess of the QA requirements. The parametric testing setup was designed to probe irradiated devices; measurements of  $R_{\text{int}}$  after gamma irradiation show much more reasonable uncertainties.

The unirradiated samples showed high  $R_{\text{int}}$ , well in excess of the QA specification. However,  $R_{\text{int}}$  was seen to be significantly lower after gamma irradiation and did not pass the QA requirements. This is due to ionisation in the oxide layer leading to a build-up of positive charge at the oxide-bulk interface. This positive interface charge attracts a layer of electrons between the strips which reduces their isolation. The TID received by the gamma irradiated samples is almost a factor of two higher than that expected at the HL-LHC. It has been observed that devices irradiated to even higher TIDs with protons are seen to have larger  $R_{\text{int}}$  which do pass the specifications [82]. That the gamma irradiated devices did not meet the specification therefore does not pose a major problem to the QA procedure. The TID received by sensors at the HL-LHC originates from a variety of particles, not just from photons.

The same setup as above is used to extract  $C_{\text{int}}$  with the voltage sweep applied to one set of strips and the LCR meter probing the second set.  $C_{\text{int}}$  is defined as the capacitance contribution from both neighbouring strips per unit strip length. Inter-strip capacitance

Table 4.6: Measurements of inter-strip capacitance for each interdigitated structure on the site verification and commissioning test chips. The accuracy of the Keysight LCR meter is given as 0.05% so measurement uncertainties are expected to be very low; the spread in measured values is much larger than this and is quantified by the average and associated standard deviation in the final column.

	$C_{\text{int}} / (\text{pF}/\text{cm})$			
	Upper	Middle	Lower	Average
Site commissioning (unirrad.)	1.25	1.08	0.88	$1.07 \pm 0.15$
Site verif. (unirrad.)	0.808	0.744	0.870	$0.807 \pm 0.051$
Site verif ( $\gamma$ irradi.)	0.79	0.98	0.92	$0.895 \pm 0.081$

contributes to the noise of the read-out electronics so is required to be less than 1 pF/cm after irradiation, which ensures it is significantly less than  $C_{\text{coupl}}$ . This quantity can increase as a result of surface radiation damage due to charge build-up in the oxide deforming the electric field between the strips. The measured values of  $C_{\text{int}}$  are shown in Table 4.6. Both of the site verification devices showed  $C_{\text{int}}$  in line with the QA specification, while the site commissioning device showed  $C_{\text{int}}$  above the specification. This is consistent with the results from measurements of other test chips which show some devices failing the QA requirements, both before and after irradiation [79, 82]. Higher than expected  $C_{\text{int}}$  values are attributed to the contribution of stray capacitance from between the strip ends and the guard ring. Since the  $C_{\text{int}}$  values are not significantly in excess of the requirements this is not expected to significantly degrade sensor performance.

## Punch-through protection

During the operation of the LHC, it is possible that a beam can be scattered into the detector, introducing a large charged particle flux through the tracking detector. The resulting charge produced in the depleted sensors could generate a large potential across the coupling capacitor, allowing a large current to flow into the read-out electronics. To prevent this, the ends of the implants are designed such that a high voltage on the implant results in a punch-through mechanism between the implant and the bias rail.

The punch-through protection (PTP) structure consists of the ends of ten implants connected to a bias rail by a bias resistor, all of which is surrounded by a guard ring. The parametric testing setup can be used to extract  $V_{\text{PTP}}$  for five channel ends on each test chip. Testing this structure involves applying a voltage to individual implants and measuring the current between the implant and the bias rail, while the backplane of the sensor is held at a high negative potential to bias the bulk. From the gradient of the IV curve the effective resistance can be plotted as a function of voltage, as shown in Fig. 4.11.

Fig. 4.11 shows plots of effective resistance against voltage for the two site verification devices and demonstrates how the value of  $V_{\text{PTP}}$  is extracted. The voltage at which the effective resistance is half that of the nominal bias resistance,  $R_{\text{bias}} = 1.5 \text{ M}\Omega$ , is defined to be the punch-through protection voltage,  $V_{\text{PTP}}$ . For the two unirradiated devices  $V_{\text{PTP}}$  was found to be  $13.81 \pm 0.02 \text{ V}$  and  $11.93 \pm 0.01 \text{ V}$  (not shown), while for the gamma irradiated sample, a punch-through voltage of  $10.66 \pm 0.07 \text{ V}$  was seen. The propagated uncertainty on the values of  $V_{\text{PTP}}$  using the accuracy of the instruments is seen to be low so the uncertainty quoted on the average is the standard deviation of the five  $V_{\text{PTP}}$  values for each device. It can be seen that  $R_{\text{eff}}$  of the gamma irradiated device is higher than that of the unirradiated device before the onset of the punch-through effect, which is due to the temperature-dependence of  $R_{\text{bias}}$  discussed earlier. To correct for this  $V_{\text{PTP}}$  can be calculated as the voltage at which the

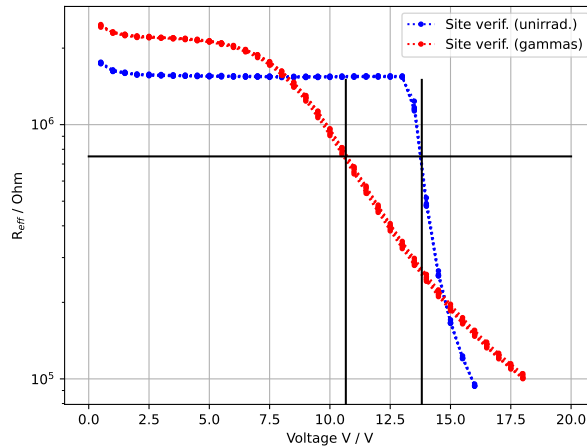


Figure 4.11: Plot of effective resistance from IV scans of PTP structures on the site verification test chips. Curves corresponding to the five PTP structures which can be probed are shown for each device. Curves are shown in blue for unirradiated devices and red for gamma-irradiated devices. The horizontal black line corresponds to a resistance of  $0.75 \text{ M}\Omega$ , corresponding to half the nominal  $R_{\text{bias}}$ .

effective resistance is half that of the initial effective resistance. If this is done,  $V_{\text{PTP}}$  is found to be  $10.06 \pm 0.09 \text{ V}$ .

To ensure the protection of the read-out electronics,  $V_{\text{PTP}}$  should be significantly lower than the voltage limit of the coupling capacitor. It can be seen that this requirement is satisfied in all of the devices. Both before and after irradiation,  $V_{\text{PTP}}$  falls well below  $100 \text{ V}$ , the voltage to which the coupling capacitor has been tested for dielectric breakdown.

#### 4.3.4 Conclusions

With the current inner detector reaching the end of its life and significant increases in luminosity anticipated at the HL-LHC, the performance of the ITk detector is crucial for ATLAS vertexing and reconstruction capabilities. The measurements discussed in this chapter

provide important validation of the technology developed for use in the detector. Test devices produced on the periphery of the main sensor wafers have shown good agreement with the required specifications of the QA programme. Some deviations from the specification are observed in the measurement of inter-strip properties but these are not indicative of serious flaws in the main sensor design or fabrication process. On the basis of the measurements here Birmingham was approved as a test chip and MD8 testing facility and continues to undertake QA measurements of these devices during the production phase of the project.

# Chapter 5

## Physics at the LHC

At the LHC, large numbers of hadronic collisions can occur during bunch crossings, each of which produces many final state particles resulting from interactions between constituent partons. This poses significant challenges for the simulation and analysis of physics events. Simulation of LHC collisions is highly complex, with the range of relevant energy scales spanning both perturbative and non-perturbative regimes of QCD, and the production of high final-state particle multiplicities. The high-multiplicity environment requires the development of algorithms capable of triggering and reconstructing the process-of-interest against a background of pile-up noise, while avoiding the double-counting of detector signals. This chapter will give an overview of the structure of LHC events and discuss how these affect their simulation and reconstruction. Particular attention is given to the reconstruction of leptons and hadrons within the ATLAS detector.

## 5.1 Hadron collider physics

The rate at which a physics process occurs is proportional to its cross-section, which depends on the Lorentz-invariant matrix element (ME) integrated over the available phase-space. For interactions with two particles in the final and initial-states, such as  $e^+e^- \rightarrow \mu^+\mu^-$ , the cross-section in the centre-of-mass (CM) frame is given by [39]

$$\sigma = \frac{1}{64\pi^2 s} \frac{p_f}{p_i} \int |\mathcal{M}|^2 d\Omega, \quad ^1 \quad (5.1)$$

where  $\sqrt{s}$  is the CM energy, i.e. the energy carried by the  $\gamma$  or  $Z$  boson propagator, and  $p_f$  ( $p_i$ ) is the magnitude of the three-momentum of the final (initial) state particles in the CM frame. The integral covers the solid angle  $d\Omega = d(\cos\theta)d\phi$  where  $\theta$  is the scattering angle and  $\phi$  corresponds to rotations around the incident particle axis. Differential cross-sections can also be calculated to predict the kinematic distributions of processes, such as the angular distribution of muons in  $e^+e^- \rightarrow \mu^+\mu^-$  production.

At hadron colliders, the processes of interest are the interactions between the quarks and gluons within the colliding protons. This complicates the calculation of cross-sections because the initial-state momentum of the partons is unknown. Calculation of the rates of processes at the LHC therefore relies on factorising the partonic interaction, which is calculable in perturbative QCD, from the dynamics of partons within the proton, which results from non-perturbative physics describing interactions between the valence quarks, virtual gluons and sea quarks<sup>2</sup>. Protons at the LHC are made to collide at a small crossing angle, so it is assumed that the momentum of the initial-state is zero in the transverse plane:  $p_T = \sqrt{p_x^2 + p_y^2} = 0$ . The cross-section of a process  $ab \rightarrow X$  occurring at the LHC is then expressed as [83]

$$\sigma_{ab \rightarrow X} = \int dx_a dx_b f(x_a, Q^2) f(x_b, Q^2) \hat{\sigma}_{ab \rightarrow X}(x_a, x_b, Q^2), \quad (5.2)$$

<sup>1</sup>This assumes an ultra-relativistic regime in which particles can be treated as massless.

<sup>2</sup>Sea quarks refers to both quarks and anti-quarks.

where  $x_{a,b}$  are the momentum fractions of partons  $a, b$  within the proton and  $\hat{\sigma}_{ab \rightarrow X}$  represents the cross-section for the partonic cross-section, given by Eq. (5.1) for a two-body final-state. The function  $f(x, Q^2)$  is the parton density function (PDF) of the proton which, to first approximation, represents the probability to find a parton with a momentum fraction  $x$  when probed at momentum scale  $Q$  and is treated as being a process-independent property of the hadron. This treatment relies on being able to factorise the partonic interaction from the proton structure, assuming the two are independent. Since PDFs are not perturbatively calculable, these must be constructed using global fits to data from multiple experiments with assumptions about their analytical form. This includes deep inelastic scattering (DIS) datasets from the HERA  $ep$  collider at DESY [84], which are the most sensitive inputs across a large region of phase-space, as well as data from the LHC and the Tevatron  $p\bar{p}$  collider at Fermilab [85], which provide key constraining power for the gluon PDF at high  $x$ ; a review of the data used to construct PDFs can be found in Ref. [86].

$Q$  is referred to as the factorisation scale and commonly written as  $\mu_F$ . In addition to dependence on  $\mu_F$ , the process of renormalisation discussed in Section 2.1.2 introduces dependence of the cross-section on the choice of renormalisation scale,  $\mu_R$ . In calculations of cross-sections at colliders these two scales are typically set to a common value representative of the interaction being studied. The choice of scales introduces theoretical uncertainties into the calculations of cross-sections and other observables at the LHC, as will be discussed further in Section 6.7.

The discussion above describes the hard-scatter process, which refers to the high energy partonic interaction of interest. On top of this, additional hadronic activity is produced as a result of multiple parton interactions (MPI), referring to secondary scattering processes between the colliding protons. Pile-up interactions also contribute to LHC events; most of the additional collisions involve inelastic  $pp$  scattering which produce a shower of low energy hadrons.

---

## 5.2 Physics simulation

### 5.2.1 Event generation

Analysis of LHC collision data requires a model to which the data can be compared. A number of event generators have been developed for the purpose of simulating collision events. First, the ME for the hard-scatter process is calculated to a given order in perturbation theory, usually next-to-leading order (NLO) in QCD for current LHC analyses. The ME calculation is then convoluted with PDFs and integrated over the available phase space using Monte Carlo (MC) integration methods. Partons produced at high energy will produce additional radiation through  $g \rightarrow q\bar{q}$  and  $q \rightarrow gq$  splitting processes leading to the production of very high particle multiplicities. Both incoming and outgoing partons are subject to these splitting processes leading to a shower of coloured particles known as a parton shower. Initial state radiation (ISR), where hard radiation is emitted from incoming partons before the hard-scatter process, typically leads to the production of additional jets, while final state radiation (FSR) usually contributes additional structure to jets from outgoing partons. Photons or other bosons can also be radiated from the initial and final states. Below an energy scale on the order of 1 GeV, the strong interaction is confining and partons undergo the non-perturbative process of hadron formation. The task of evolving the low multiplicity and high energy final state resulting from the fixed-order ME calculation into a large number of confined hadrons is performed by parton shower generators, again making use of MC integration methods.

A number of ME generators are employed by ATLAS to simulate physics processes of interest. These include SHERPA [87], a general purpose event generator which can also perform showering and hadronisation, as well as MADGRAPH5\_AMC@NLO [88] and POWHEG BOX [89–92], which generate the hard partonic process which can be showered by

another program. BSM processes can also be generated at LO by providing generators such as `MG_AMC@NLO`<sup>3</sup> and `SHERPA` with the relevant Feynman rules from which they can compute MEs.

A large number of parameters control the modelling of the parton shower. To ensure the best simulation of LHC events, these parameters are optimised based on experimental data. Three generators commonly used to model parton shower and hadronisation of events within the ATLAS collaboration are `PYTHIA` [93], `HERWIG` [94, 95] and `SHERPA`. An optimised set of parameters for the `PYTHIA 8` generator has been produced for use in ATLAS event simulation, referred to as the A14 tune [96], which is used in conjunction with the NNPDF 2.3 LO PDF set [97]. For events modelled with `SHERPA` and `HERWIG` the respective default tunes are used [94, 95, 98]. Where `PYTHIA` or `HERWIG` are used, the `EVTGEN` program [99] is used to improve the modelling of the decays of bottom and charm hadrons.

### 5.2.2 Pileup and underlying event modelling

Jets are formed by partons produced in the hard-scatter interaction but also from MPI and pile-up interactions. These processes must also be considered in simulation for a correct model of the particle multiplicity in LHC events. Pile-up is accounted for in MC simulations by overlaying samples of inelastic  $pp$  scattering events onto the process of interest. Inelastic scattering events have been generated with `PYTHIA 8.186` [100] using the NNPDF 2.3 LO PDF. A dedicated set of tuned parameters, the A3 tune, has been used for this purpose [101]. ATLAS MC production for Run 2 is split into three data-taking periods corresponding to the years 2015+2016, 2017 and 2018 to reflect the different detector and machine conditions. MC samples for each period are then corrected to match the pile-up distribution observed in data during the corresponding period, which can be seen in Fig. 5.1.

---

<sup>3</sup>`MADGRAPH5_AMC@NLO` has been shortened to `MG_AMC@NLO`.

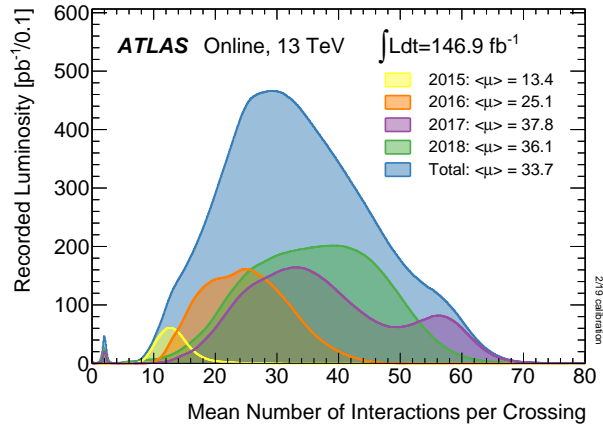


Figure 5.1: The mean number of interactions per bunch crossing for each year during Run 2 of the LHC as recorded by the ATLAS detector [102, 103]. The integrated luminosity is higher than used in the analysis as it corresponds to all data recorded during stable beams before the application of data quality requirements.

### 5.2.3 Detector simulation

To produce an accurate model of LHC events the outputs of parton shower generators, known as generator-level events, must be passed through a simulation of the ATLAS detector. The GEANT4 toolkit [104] is used to simulate the interaction of particles with material as well as the digitisation of detector signals. This simulation therefore accounts for the geometrical acceptance and limited resolution of the detector and provides a model that can be compared to ATLAS data. Some MC samples used to evaluate systematic uncertainties related to the modelling of physics processes have relied on a fast-simulation of the calorimeter system [105].

## 5.3 Physics object reconstruction and calibration

To perform an analysis with the events selected by the trigger menu discussed in Section 3.2, the detector signals must be reconstructed into “physics objects” such as muons and jets. The algorithms used to reconstruct and calibrate each of the physics objects discussed in this thesis are described below.

### 5.3.1 Electrons

The reconstruction of electrons uses clustered energy deposits (“clu”) in the ECAL matched to tracks in the ID [106]. Electron candidates are required to have  $p_T > 10$  GeV and  $|\eta_{\text{clu}}| < 2.47$ . Candidates are rejected if they satisfy  $1.37 < |\eta_{\text{clu}}| < 1.52$  which corresponds to the transition region from the barrel to the endcap of the ECAL. This region features cables and other instrumentation for the ID and ECAL which degrade the energy resolution for candidates reconstructed in this region [1].

The energy calibration of electron candidates is discussed in Ref. [107]. A multivariate discriminant is constructed using both cluster and track information to distinguish between real electrons and hadronic showers in the ECAL. Different threshold values for the discriminant correspond to different identification quality definitions. Electron candidates are also required to be isolated from additional activity within a given radial distance,  $\Delta R$ . Isolation can be defined in terms of calorimetric variables, such as the scalar total of calorimeter cluster energy in the transverse plane ( $E_T$ ) excluding that of the candidate cluster, or track variables, such as the total track  $p_T$  excluding that of the candidate track. These isolation requirements are imposed to suppress the selection of electrons which originate from the decay of hadrons, known as non-prompt electrons.

The two classes of electrons defined for the purpose of the analysis can be seen in Table 5.1. **Tight** electrons impose strict identification and isolation criteria while **Loose** electrons are defined for use in the overlap removal procedure discussed in Section 5.3.8 to prevent them being misidentified as other objects. Both classes of electrons place requirements on the transverse and longitudinal impact parameters,  $d_0$  and  $z_0$ , respectively, to ensure these objects originate from the hard-scatter process. The requirement on the transverse impact parameter takes into account the uncertainty on  $d_0$ ,  $\sigma_{d_0}$ .

Table 5.1: **Tight** and **Loose** electron definitions. The identification criteria are described in Refs. [106, 108]; the isolation criteria are discussed in Section 5.3.7.

	<b>Electron selection</b>	
	<b>Tight</b>	<b>Loose</b>
$p_T$	$> 10 \text{ GeV}$	$> 10 \text{ GeV}$
$ \eta_{\text{clu}} $	$< 2.47$	$< 2.47$
Identification criteria	<b>TightLH</b>	<b>LooseAndBLayerLH</b>
Isolation criteria	<b>PLVTight</b>	-
$ d_0 /\sigma_{d_0}$	$< 5$	$< 5$
$ z_0 \sin(\theta) $	$< 0.5 \text{ mm}$	$< 0.5 \text{ mm}$

Following reconstruction and the application of identification and isolation requirements, it is necessary to correct the simulation efficiencies to those measured in data. This is done by the application of scale factors derived in  $Z/\gamma^* \rightarrow ee$  and  $J/\psi \rightarrow ee$  events [106, 108]. Such events are expected to contain two prompt electrons; by the application of stringent identification or isolation requirements to one, the other provides an unbiased candidate which can be used to measure the efficiency of the selection requirement. This is referred to as a tag-and-probe method.

### 5.3.2 Muons

Muons within ATLAS can be identified by tracks in the ID and MS along with energy deposits in the calorimeters characteristic of a MIP and can be reconstructed based on combinations of these signatures [109]. Muon candidates in this analysis are reconstructed from tracks in the ID matched to partial or full tracks in the MS. Additionally, candidates in the region  $|\eta| < 0.1$  reconstructed from tracks in the ID matched to isolated calorimeter clusters are considered. A calibration of the muon momentum scale is applied using the procedure described in Ref. [110]. Muon candidates are required to have  $p_T > 10$  GeV and  $|\eta| < 2.5$ . Muon identification requirements are imposed on the number of hits in the ID and MS and the compatibility of these having originated from a single muon. Isolation requirements are also imposed on muon candidates to suppress the selection of non-prompt muons, as was the case for electrons; these are discussed in Section 5.3.7.

Two categories of muons are defined, as shown in Table 5.2. A **Tight** selection is designed to select prompt muons originating from the hard-scatter interactions by imposing stringent isolation requirements. A **Loose** selection is defined to preferentially select non-prompt muons originating from heavy flavour hadronic decays by relaxing the isolation criteria and inverting the transverse impact parameter requirement. Both definitions require muons to pass the **Medium** identification criteria.

Efficiency corrections are derived with tag-and-probe methods in  $Z/\gamma^* \rightarrow \mu\mu$  and  $J/\psi \rightarrow \mu\mu$  events [109, 111]. Corrections are made for reconstruction, identification, isolation and track-to-vertex association (TTVA) criteria.

Table 5.2: **Tight** and **Loose** muon definitions. The identification criteria are described in Ref. [109]; the isolation criteria are discussed in Section 5.3.7.

	<b>Muon selection</b>	
	<b>Tight</b>	<b>Loose</b>
$p_T$	$> 10 \text{ GeV}$	$> 10 \text{ GeV}$
$ \eta $	$< 2.5$	$< 2.5$
Identification criteria	<b>Medium</b>	<b>Medium</b>
Isolation criteria	<b>PLVTight</b>	<b>PLVLoose</b>
$ d_0 /\sigma_{d_0}$	$< 3$	$> 3$
$ z_0 \sin(\theta) $	$< 0.5 \text{ mm}$	$< 0.5 \text{ mm}$

### 5.3.3 Jets

To reconstruct jet candidates the anti- $k_T$  clustering algorithm [112] is applied to clusters of calorimeter cells with radius parameter  $R = 0.4$  [113, 114]. Candidates are then calibrated using the particle flow (PFlow) algorithm [115] which attempts to identify individual particles by combining information from the calorimeters with track information from the ID. This technique allows low energy particles which diverge from the jet cone under the influence of the magnetic field in the ID to be included in the clustering process. Additionally, it allows contributions associated to tracks matched to pile-up vertices to be excluded.

A calibration of the jet energy scale (JES) is performed to correct the measured jet energies to those expected at generator-level [116]. This aims to remove pile-up contributions and accounts for the unmeasured energy component of the hadronic shower, as well as energy lost in inactive material or falling outside of the reconstruction cone. Corrections are applied to both MC and data using a calibration derived in simulated dijet events. A further calibration is applied to jets in data to correct for differences between data and

simulation using analysis of dijet, multijet,  $Z$ +jet and  $\gamma$ +jet events. Measurements are also made of the jet energy resolution (JER) to ensure this is consistent between data and simulation [116]. Where simulation is seen to provide better resolution than observed in the data, a smearing procedure is applied to the MC. Where the resolution is worse in simulation than in data, no smearing is applied; instead, an additional systematic uncertainty is applied to the simulation to account for the difference. This uncertainty covers the full difference between the resolutions for the given region of jet  $p_T$  and  $\eta$ .

A likelihood discriminant called the jet vertex tagger (JVT) [117] is employed to further suppress jets from pile-up interactions, based on the fractions of jet  $p_T$  associated to the primary vertex and other identified vertices, applying the `JVTtight` cut for jets with  $p_T < 60$  GeV and  $|\eta| < 2.4$ . Scale factors are applied to correct efficiency differences in data and simulation after the application of the JVT cut. Reconstructed jet candidates must satisfy  $p_T > 25$  GeV and  $|\eta| < 2.5$ .

### 5.3.4 Flavour tagging

The top quark decays almost exclusively by  $t \rightarrow Wb$  in the SM so identification of jets initiated by bottom quarks,  $b$ -tagging, is an important tool for selecting events with top quarks. The DL1r algorithm [118] is used to tag jets containing  $b$ -hadrons. It relies on the vertexing capabilities of the pixel detector to reconstruct the displaced vertices at which hadronic decays occur. Several algorithms based on identifying the impact parameter of tracks and topology of secondary decay vertices, as well as reconstruction of the  $b \rightarrow c \rightarrow s$  decay chain, are combined in a neural network which outputs the probabilities that the jet is  $b$ -,  $c$ - or light-flavoured<sup>4</sup>. A cut on the output discriminant corresponding to a 77% efficiency for tagging real  $b$ -jets in top quark decays is employed. This cut corresponds to a rejection

---

<sup>4</sup>Light-flavour jets refers to any jet initiated by  $u$ -,  $d$ -,  $s$ -quarks or gluons

factor<sup>5</sup> of 5 (170) for  $c$ -jets (light-flavour jets) [118]. Efficiency corrections are applied to simulation for jets that originate from the hadronisation of  $b$ -quarks [119],  $c$ -quarks [120], and light-flavour partons [121].

### 5.3.5 Missing transverse energy

The initial transverse momentum of the partons is typically negligible compared to the centre-of-mass energy of the collision; this is the underlying assumption for the collinear factorisation discussed in Section 5.1. Therefore if all products of the hard-scatter process are detected, their momenta in the transverse plane are expected to sum to zero. Any non-vanishing net transverse momentum is used to define a vector, the inverse of which is the missing transverse momentum vector. The magnitude of this quantity is known as the missing transverse energy,  $E_T^{\text{miss}}$  [122]. Since neutrinos interact with regular matter via the weak interaction alone and leave no signal in the detector they are a common source of  $E_T^{\text{miss}}$ . In this analysis, no selection is made based on  $E_T^{\text{miss}}$ .

### 5.3.6 Hadronically-decaying tau leptons

Unlike electrons and muons, which are both stable on the timescale taken to traverse the ATLAS detector, tau leptons decay inside the beam pipe and must be reconstructed from their decay products. Hadronically-decaying tau leptons,  $\tau_{had}$ , produce a number of charged and neutral hadrons, as well as at least one neutrino which is not detected. The visible decay products of  $\tau_{had}$  are reconstructed as  $\tau_{had-vis}$  candidates [123–125] from jets clustered with the anti- $k_T$  algorithm with radius  $R = 0.4$  using a local hadronic jet calibration [126] to correct the response of the calorimeter. Candidates must have  $p_T > 10$  GeV and  $|\eta| < 2.5$ , with those

---

<sup>5</sup>The rejection factor is defined as the reciprocal of the mis-tagging efficiency.

in the region  $1.37 < |\eta| < 1.52$  rejected, as is the case for electrons. A dedicated tau energy scale (TES) calibration is applied to the candidates, first removing energy deposits likely to originate from pile-up, then correcting the energy to that expected at generator-level making use of the PFlow algorithm [127]. The TES is calibrated using a tag-and-probe method based on  $Z/\gamma^* \rightarrow \tau_\mu \tau_{had}$  events, where  $\tau_\mu$  denotes a  $\tau$  which decays to a muon and neutrinos. A separate calibration is applied to  $\tau_{had-vis}$  candidates with one and three associated tracks, referred to as 1-prong (1p) or 3-prong (3p). Candidates with other numbers of tracks are not reconstructed.

This reconstruction procedure can reconstruct jets and electrons in addition to true  $\tau_{had-vis}$ ; these are referred to as fake  $\tau_{had-vis}$  candidates. The identification of  $\tau_{had-vis}$  is performed by a neural network (RNN) which discriminates between true  $\tau_{had-vis}$  and misidentified candidates likely to originate from a jet [128]. The network uses track and calorimeter information associated to the candidate along with high-level variables, such as the invariant mass of the track system. A boosted decision tree discriminant, the eBDT, suppresses the misidentification of electrons as 1-prong  $\tau_{had-vis}$  candidates using information from the TRT and calorimeters [123].

The analysis defines two categories of  $\tau_{had-vis}$  candidates, described in Table 5.3. **Tight**  $\tau_{had-vis}$  are required to satisfy **RNNMedium** identification, corresponding to an efficiency of 75% (60%) for true 1-prong (3-prong)  $\tau_{had-vis}$ . **Loose**  $\tau_{had-vis}$  are only required to pass **RNNLoose**, which corresponds to an efficiency of 85% (75%) for true 1-prong (3-prong)  $\tau_{had-vis}$ . **Tight** candidates populate the analysis selection while **Loose** candidates are used in the overlap removal procedure. In both cases, the **eBDTMedium** criteria is used to suppress electrons being misidentified as  $\tau_{had-vis}$ .

Scale factors are used to correct for efficiency differences between simulation and data resulting from  $\tau_{had-vis}$  reconstruction, identification and electron-rejection criteria [123,

Table 5.3: **Tight** and **Loose**  $\tau_{\text{had-vis}}$  definitions. The identification criteria are described in Ref. [128]; the electron rejection criteria are discussed in Ref. [123].

	$\tau_{\text{had-vis}}$ selection	
	Tight	Loose
$p_T$	$> 20$ GeV	$> 20$ GeV
$ \eta $	$< 2.5$	$< 2.5$
Identification criteria	RNNMedium	RNNLoose
Electron-rejection criteria	eBDTMedium	eBDTMedium

[125, 128]. The scale factors to correct for the application of  $\tau_{\text{had-vis}}$  reconstruction and identification are derived in  $Z/\gamma^* \rightarrow \tau_\mu \tau_{had}$  events using a tag-and-probe method, with separate calibrations for 1-prong and 3-prong candidates. Efficiency corrections for the eBDT are derived in a  $Z/\gamma^* \rightarrow ee$  tag-and-probe analysis.

### 5.3.7 Non-prompt lepton rejection

Non-prompt leptons are traditionally suppressed by imposing isolation requirements on lepton candidates. Isolation criteria aim to suppress candidates reconstructed inside clusters of energy likely to originate from jet activity. Since these often originate from decay of heavy flavour hadrons inside  $b$ - and  $c$ -jets, exploiting flavour-tagging techniques can improve the discrimination between prompt and non-prompt leptons. A boosted decision tree known as the prompt lepton veto (PLV) combines lepton isolation information with the outputs of jet reconstruction and  $b$ -tagging algorithms run on tracks associated to the leptons [129]. Despite the name of the algorithm, which is historic, it is intended to veto non-prompt leptons. This discriminant was first used in Ref. [130]. The PLV is used to impose isolation requirements on electron and muon candidates, as shown in Tables 5.1 and 5.2.

### 5.3.8 Overlap removal

It is possible that multiple physics objects are reconstructed from the same detector signals, such as the decay products of a  $\tau$  lepton being reconstructed as both jet and  $\tau_{\text{had-vis}}$  candidates. A sequential overlap removal procedure is applied to avoid detector signals being double-counted following the standard ATLAS recommendation [131]. The procedure involves the removal of physics objects found within a given radius of each other and is described in Ref. [132]. For all leptons the `Loose` definitions are used in the overlap removal procedure.

## 5.4 Top quark physics

The top quark is the most massive particle in the SM and is unique among quarks in that it decays before it is able to hadronise. It is typically reconstructed from its decay products rather than as a single jet. The largest source of top quarks at the LHC is the production of a top quark-antiquark pair,  $t\bar{t}$ , predominantly through the process of gluon-gluon fusion, as shown in Fig. 5.2a. Quark-antiquark annihilation and quark-gluon fusion processes can also produce  $t\bar{t}$  pairs. Single top quarks can be produced in association with other particles, such as a  $W$  boson (Fig. 5.2b), or along with a light quarks through either a  $t$ - or  $s$ -channel process (Fig. 5.2c and Fig. 5.2d, respectively).

In the SM, top quarks decay via the weak interaction to a  $W$  boson and a down-type quark, almost always a bottom quark since the third generation of quarks mix very little with other generations in weak decays ( $|V_{tb}| \approx 1$ ). The decay products of the top are therefore determined by the decay of the  $W$  boson, which decays to a  $qq'$  pair in approximately two thirds of cases, or to a lepton-neutrino pair in one third of cases. In Fig. 5.2a the  $t\bar{t}$  pair is said to decay semi-leptonically, with one  $W$  boson decaying to a  $qq'$  pair and the other decaying to a lepton-neutrino pair. The signature of a top quark decay in the ATLAS detector

is a  $b$ -tagged jet along with two additional jets or a lepton accompanied by  $E_T^{\text{miss}}$ .

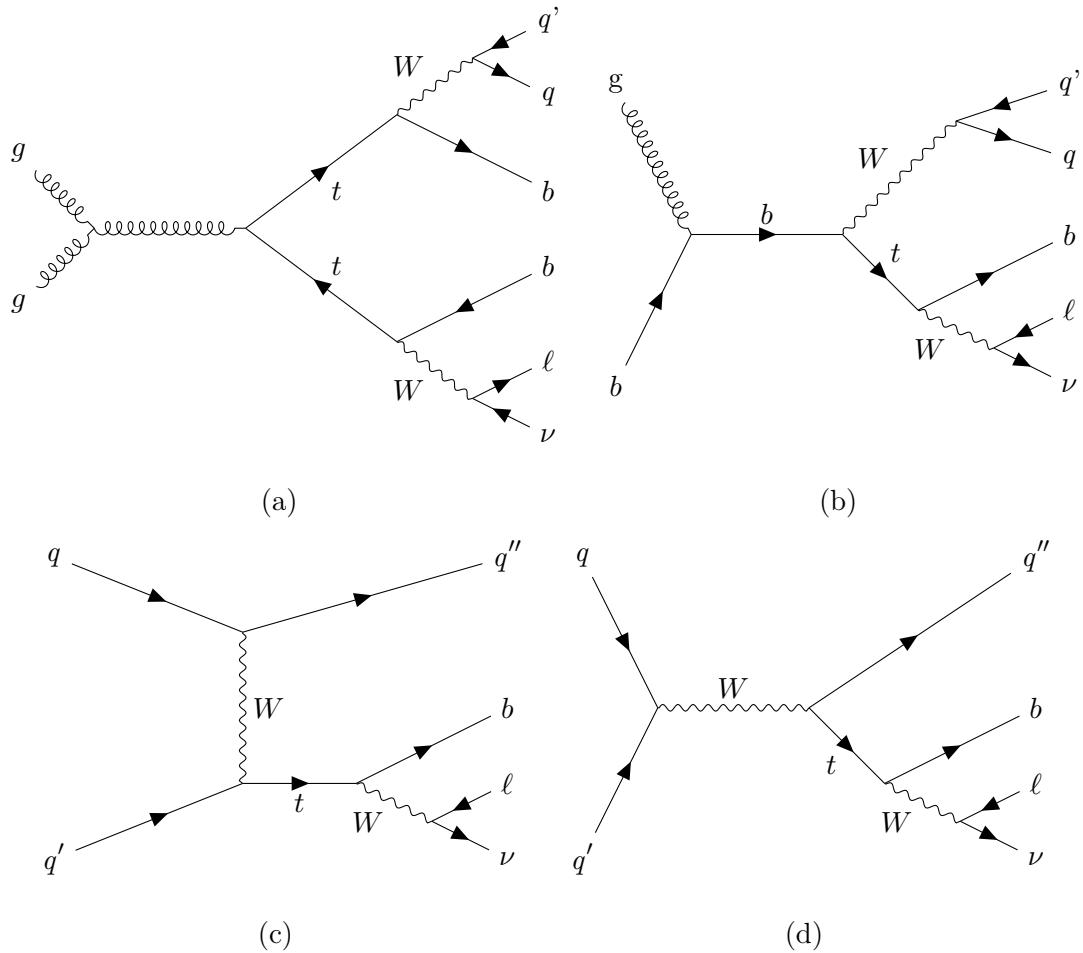


Figure 5.2: LO Feynman diagrams showing top quark production processes at the LHC: the production of a  $t\bar{t}$  pair which decays semi-leptonically (a); the production of a single top quark in association with a  $W$  boson (b), in the  $t$ -channel (c) and in the  $s$ -channel (d).

In the presence of new physics capable of inducing CLFV top quark interactions, new production and decay mechanisms become available. This is the focus of the search discussed in Chapters 6 and 7. Meanwhile, both the single top quark production and top quark pair production processes pose as backgrounds to the CLFV search.

# Chapter 6

## Searching for CLFV in top quark interactions

The SM leaves open many questions about the nature of the universe. As of yet, there is no clear direction to be explored, which motivates model-independent searches for new physics. The lepton flavour-conserving nature of the SM is an accidental symmetry arising due to the absence of  $\nu_R$ , as discussed in Chapter 2. In general, BSM theories introducing new interactions between leptons will introduce new sources of LFV. This chapter describes a model-independent search for a CLFV top quark interaction, treated as a  $t\mu\tau u_k$  contact interaction, where  $u_k = \{u, c\}$ . The analysis uses the full ATLAS Run 2 dataset corresponding to  $140.1 \pm 1.2 \text{ fb}^{-1}$  of  $pp$  collisions at  $\sqrt{s} = 13.0 \text{ TeV}$  [5].

### 6.1 Overview of CLFV searches

Processes introducing CLFV interactions have been searched for across a large range of energy scales [44]. The most precise probes of CLFV processes come from muon decay experiments.

In particular, the following exclusion limits on the branching ratios for neutrinoless decays of muons into electrons have been reported:  $\mathcal{B}(\mu^+ \rightarrow e^+ \gamma) < 4.2 \times 10^{-13}$  reported in 2016 by the MEG collaboration [133] and  $\mathcal{B}(\mu^+ \rightarrow e^+ e^+ e^-) < 1.0 \times 10^{-12}$  in 1988 by the SINDRUM collaboration [134], both at 90% confidence level (CL).

Searches for CLFV involving third generation fermions, Higgs and  $Z$  bosons have been performed at collider experiments. Searches by ATLAS have focused on the decays of the Higgs and  $Z$  bosons to pairs of different-flavour charged leptons, setting limits of  $\mathcal{B}(H \rightarrow e\tau) < 0.47\%$ ,  $\mathcal{B}(H \rightarrow \mu\tau) < 0.28\%$  [135] and  $\mathcal{B}(Z \rightarrow e\tau) < 8.1 \times 10^{-6}$ ,  $\mathcal{B}(Z \rightarrow \mu\tau) < 9.5 \times 10^{-6}$  [136] (all at 95% CL). A similar search for the CLFV decay of the Higgs boson has been carried out by the CMS experiment, setting limits of  $\mathcal{B}(H \rightarrow e\tau) < 0.61\%$  and  $\mathcal{B}(H \rightarrow \mu\tau) < 0.25\%$  (both to 95% confidence level) [137]. The Belle and LHCb collaborations have searched for CLFV decays of the tau lepton, setting exclusion limits of  $\mathcal{B}(\tau \rightarrow 3\mu) < 2.1 \times 10^{-8}$  [138] and  $\mathcal{B}(\tau \rightarrow 3\mu) < 4.6 \times 10^{-8}$  [139], respectively (both at 90% CL).

The first direct search for CLFV interactions involving a top quark was performed by ATLAS, setting upper limits of  $\mathcal{B} \rightarrow \ell^\pm \ell'^{\mp} q < 1.86 \times 10^{-5}$  at 95% CL, where  $q = \{u, c\}$  and  $\ell, \ell' = \{e, \mu, \tau\}$  with 80 fb<sup>-1</sup> of  $pp$  collision data [140]. The analysis searched for events with three light leptons ( $e$  or  $\mu$ ) resulting from the production of a top quark pair with one top decaying via the BSM CLFV process and the other decaying leptonically via the SM. More recently CMS searched for the CLFV process using both top quark pair decay and single top production in association with different flavour leptons,  $gq \rightarrow \ell^\pm \ell'^{\mp} t$ , in channels with hadronic and leptonic SM top decays, setting limits of  $\mathcal{B}(t \rightarrow e\mu q) < 0.07 - 2.59 \times 10^{-6}$  [141] and  $\mathcal{B}(t \rightarrow e\mu q) < 0.009 - 0.258 \times 10^{-6}$  [142], respectively, at 95% CL. The CMS results also set exclusion limits on EFT Wilson coefficients corresponding to four-fermion  $te\mu\mu_k$  interactions.

The analysis described in this chapter is the first direct search for a  $t\mu\tau u_k$  CLFV interaction. Prior to this search only indirect constraints have been placed on the Wilson coefficients mediating  $t\mu\tau u_k$  interactions based on the reinterpretation [143] of an ATLAS  $t \rightarrow u_k Z$  flavour-changing neutral current search [144] considering a possible  $t \rightarrow \mu\tau u_k$  signal. The current search targets both top quark production and decay in final states with two muons and one hadronically-decaying tau lepton using the full ATLAS Run 2  $pp$  collision dataset of  $140 \text{ fb}^{-1}$ . The limit on the signal process is also interpreted in the EFT framework, as well as in the context of a scalar leptoquark model. The first results from this search can be found in Ref. [2]. The EFT operators capable of introducing these CLFV interactions are flavour-dependent, so the analysis targets different operators to those in Refs. [140–142].

## 6.2 Analysis strategy

Two CLFV processes are considered in the search: the production of a  $t\bar{t}$  pair, one of which undergoes the decay  $t \rightarrow \mu\tau u_k$ ; and the production of a single top quark in association with a muon-tau lepton pair,  $gu_k \rightarrow t\mu\tau$ . Representative Feynman diagrams for these processes are shown in Fig. 6.1. The EFT framework used for the principal analysis is discussed in Section 6.2.1.

The analysis uses MC samples to build a model for the signal and background processes to which data samples can be compared to infer the presence of any signal contribution. Selected events are split into subsets used to study the signal process, known as the signal region (SR), and to constrain the important background processes, known as control regions (CRs). Section 6.4 describes the event selection and definition of these analysis regions. The CRs are enriched in events from a particular background process and are used to correct the modelling of non-prompt and fake lepton backgrounds, discussed in Sections 6.5 and 6.6.

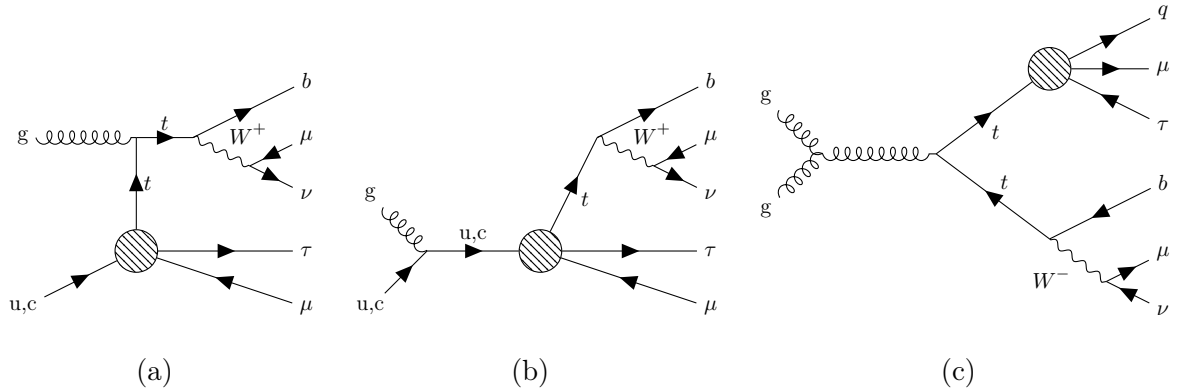


Figure 6.1: Example Feynman diagrams for the EFT signal processes. Diagrams (a) and (b) show the  $t$ - and  $s$ -channel diagrams contributing to the  $gu_k \rightarrow t\mu\tau$  process while (c) shows top quark pair production in which one top undergoes the decay  $t \rightarrow \mu\tau u_k$ . The hashed circle represents the CLFV vertex.

These arise from events with a non-prompt muon candidate, originating from a hadronic decay inside a jet, or from events with a fake  $\tau_{\text{had-vis}}$  candidate, usually a misidentified quark- or gluon-initiated jet. The presence or absence of the signal process is extracted through a profile likelihood fit to the SR and one of the CRs. The systematic uncertainties presented in Section 6.7 are included in the fit as nuisance parameters (NPs). In all of these sections where not specified, “signal” refers to an inclusive EFT signal sample including contributions from all considered EFT operators inducing CLFV interactions, the normalisation of which is specified below.

A leptoquark (LQ) interpretation is also considered in which the production of a single top quark in association with two different flavour opposite charge leptons,  $gu_k \rightarrow t\mu\tau$ , is introduced by an intermediate scalar LQ. The model used is discussed in Section 6.2.2 and the interpretation is performed using the same analysis framework.

During the development of the analysis, all regions with signal contributions greater than 10% of the background remain “blinded”; in practice this only concerns the SR. Only

once the analysis methodology has been finalised, and selections and corrections defined, are the data in these regions considered. This convention is used to reduce the likelihood of the analysis being biased by studying the data in signal-sensitive regions while corrections to fake lepton backgrounds and the treatment of systematic uncertainties are being devised.

### 6.2.1 Effective field theory framework

The analysis uses the SMEFT framework, introduced in Section 2.2.3, to conduct a model-independent search for new physics considering all operators capable of introducing a  $t\mu\tau u_k$  vertex. There is one operator at dimension-5, known as the Weinberg operator [55]. This is responsible for generating Majorana mass terms for the neutrinos by coupling the left-chiral neutrino field to the Higgs field and is therefore not of interest for CLFV. Using the Warsaw basis [55], there are six independent operators at dimension-6 (dim-6) which are capable of introducing CLFV interactions between two up-type quarks and two leptons, as shown in Ref. [143]. These are shown in Table 6.1. The indices  $i, j, k, l \in \{1, 2, 3\}$  denote the flavour of the fermion fields; these operators are flavour-dependent since new physics may not necessarily couple equally to different generations of fermions. As discussed in Section 2.2.3, all of these operators are gauge invariant under the  $SU(3)_c \times SU(2)_L \times U(1)_Y$  symmetry of the SM. Further CLFV-inducing operators exist at dimension-8 but these are suppressed by an additional factor of  $\Lambda^2$  in the Lagrangian, given in Eq. (2.17). Therefore in this analysis, only the contribution from dimension-6 operators is considered.

Table 6.1: SMEFT operators capable of introducing two quark-two lepton CLFV interactions involving a top quark in the Warsaw basis [55]. The indices  $i, j, k, l$  represent the flavour of the fermion fields.  $\sigma^I$  are the Pauli matrices with  $I \in \{1, 2, 3\}$ ,  $\epsilon = i\sigma^2$  and  $\sigma_{\mu\nu} = \frac{i}{2}[\gamma_\mu, \gamma_\nu]$  where  $\gamma_\mu$  are the Dirac gamma matrices.  $l$  and  $q$  represent the left-handed weak isospin doublets for the lepton and quark fields, while  $u$  and  $e$  represent the right-handed weak isospin singlets.

Operator	Wilson coefficient	Lorentz structure
$\mathcal{O}_{lq}^{-(ijkl)} = (\bar{l}_i \gamma^\mu l_j)(\bar{q}_k \gamma_\mu q_l) - (\bar{l}_i \gamma^\mu \sigma^I l_j)(\bar{q}_k \gamma_\mu \sigma_I q_l)$	$c_{lq}^{-(ijkl)}$	Vector
$\mathcal{O}_{eq}^{(ijkl)} = (\bar{e}_i \gamma^\mu e_j)(\bar{q}_k \gamma_\mu q_l)$	$c_{eq}^{(ijkl)}$	Vector
$\mathcal{O}_{lu}^{(ijkl)} = (\bar{l}_i \gamma^\mu l_j)(\bar{u}_k \gamma_\mu u_l)$	$c_{lu}^{(ijkl)}$	Vector
$\mathcal{O}_{eu}^{(ijkl)} = (\bar{e}_i \gamma^\mu e_j)(\bar{u}_k \gamma_\mu u_l)$	$c_{eu}^{(ijkl)}$	Vector
$\mathcal{O}_{lequ}^{1(ijkl)} = (\bar{l}_i e_j) \epsilon (\bar{q}_k u_l)$	$c_{lequ}^{1(ijkl)}$	Scalar
$\mathcal{O}_{lequ}^{3(ijkl)} = (\bar{l}_i \sigma^{\mu\nu} e_j) \epsilon (\bar{q}_k \sigma_{\mu\nu} u_l)$	$c_{lequ}^{3(ijkl)}$	Tensor

Table 6.2: Indirect constraints on CLFV  $t\mu\tau u_k$  EFT operators from [143] based on the reinterpretation of an ATLAS  $t \rightarrow u_k Z$  flavour-changing neutral current search [144] considering a possible  $t \rightarrow \mu\tau u_k$  signal. The limits on Wilson coefficients assume  $\Lambda = 1$  TeV.

$u_k$	$c_{lq}^{-(ijk3)}$	$c_{eq}^{(ijk3)}$	$c_{lu}^{(ijk3)}$	$c_{eu}^{(ijk3)}$	$c_{lequ}^{1(ijk3)}$	$c_{lequ}^{1(ij3k)}$	$c_{lequ}^{3(ijk3)}$	$c_{lequ}^{3(ij3k)}$
u	12.0	12.0	12.0	12.0	26.0	26.0	3.4	3.4
c	14.0	14.0	14.0	14.0	29.0	29.0	3.7	3.7

A Wilson coefficient is assigned to each of the operators shown in Table 6.1. Unlike the vector operators,  $\mathcal{O}_{lequ}^{1(ijkl)}$  and  $\mathcal{O}_{lequ}^{3(ijkl)}$  are not Hermitian so their Hermitian conjugate must also be considered, with corresponding Wilson coefficients  $c_{lequ}^{1(jilk)}$  and  $c_{lequ}^{3(jilk)}$ . The contributions of each of these operators to the decay width of the top quark, as calculated in [143], is given by

$$\begin{aligned} \Gamma(t \rightarrow \ell^\pm \ell'^\mp q) = & \frac{m_t}{6144\pi^3} \left(\frac{m_t}{\Lambda}\right)^4 \left[ 4|c_{lq}^{-(jik3)}|^2 + 4|c_{eq}^{(jik3)}|^2 + 4|c_{lu}^{(jik3)}|^2 + 4|c_{eu}^{(jik3)}|^2 \right. \\ & \left. + |c_{lequ1}^{1(jik3)}|^2 + |c_{lequ1}^{1(ij3k)}|^2 + 48|c_{lequ3}^{3(jik3)}|^2 + 48|c_{lequ3}^{3(ij3k)}|^2 \right]. \end{aligned} \quad (6.1)$$

The current constraints on these Wilson coefficients from [143] are shown in Table 6.2 and are based on the reinterpretation of an ATLAS  $t \rightarrow u_k Z$  flavour-changing neutral current search [144].

For this search the scale of new physics,  $\Lambda$ , is set to a value of 1 TeV and the interpretation is performed in terms of the dimensionless Wilson coefficients. In the development of the analysis, the signal normalisation is chosen to correspond to each of the Wilson coefficients for the operators in Table 6.1 having values of 0.3. This value corresponds roughly to the limits obtained in Ref. [140]. The final discriminant used in the profile likelihood fit is not capable of differentiating between the different EFT operator contributions so each operator is considered independently with the Wilson coefficient for the other operators set to zero<sup>1</sup>.

## 6.2.2 Leptoquark model

As discussed in Section 2.2.2, LQs introduced as additional gauge bosons of a unified symmetry provide a natural source of CLFV. The study of scalar LQs has also gained interest in recent years as BSM explanations for possible deviations from the SM in flavour physics [48, 145].

In this analysis, the production of a single top quark via the production of a single LQ

---

<sup>1</sup>Plots showing the fitted discriminant for each EFT contribution can be seen in Appendix E

is considered. The LQ model considered is that of a scalar  $S_1$  LQ, described in Refs. [146, 147], which is capable of introducing CLFV  $t\mu\tau u_k$  interactions leading to the final state targeted by the analysis. The model is completely described by the value of the Yukawa coupling strength to each quark  $i$  and lepton  $j$  pair,  $\lambda_{ij}$ , and the LQ mass,  $m_{S_1}$ . For the  $t\mu\tau u_k$  interaction initiated by an up or charm quark there are six relevant couplings:  $\lambda_{t\tau}$ ,  $\lambda_{c\tau}$ ,  $\lambda_{u\tau}$ ,  $\lambda_{t\mu}$ ,  $\lambda_{c\mu}$  and  $\lambda_{u\mu}$ . To consider all of these couplings simultaneously, a flavour hierarchy is assumed which relates the coupling values.

LQ couplings to first generation fermions are constrained by atomic parity violation experiments, while third generation couplings are generally seen to be the least tightly constrained [147]. It is therefore common in the literature to assume that LQ models allowing multi-generational interactions couple more strongly to higher generations. The scale of such a hierarchy, however, varies between proposed LQ models [148–150]. For this analysis, the  $t\tau$  coupling is assumed to be the largest and each step down in quark or lepton generation is assumed to introduce a factor of ten suppression, as shown by Fig. 6.2. The coupling to the SM fermions may therefore be described by a single parameter  $\lambda$ :

$$\lambda_{ij} \in \begin{pmatrix} \lambda_{t\tau} & \lambda_{c\tau} & \lambda_{u\tau} \\ \lambda_{t\mu} & \lambda_{c\mu} & \lambda_{u\mu} \\ \lambda_{te} & \lambda_{ce} & \lambda_{ue} \end{pmatrix} \equiv \lambda \begin{pmatrix} 10 & 1 & 0.1 \\ 1 & 0.1 & 0.01 \\ 0.1 & 0.01 & 0.001 \end{pmatrix}. \quad (6.2)$$

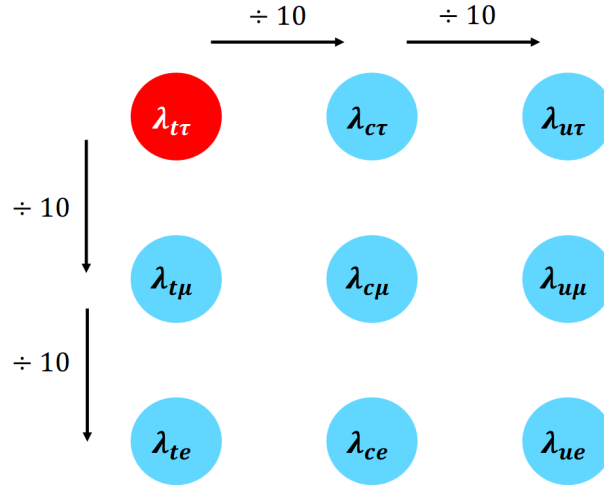


Figure 6.2: Diagram demonstrating the assumed hierarchy of  $S_1$  leptoquark Yukawa couplings to lepton-quark pairs. Image produced by Dr Jacob Kempster.

### 6.3 Data and simulated samples

This section describes the ATLAS collision data used in the analysis, along with the simulated MC samples to which these were compared. A summary of the signal and dominant background MC samples used in the analysis is given in Table 6.3. Some smaller background processes are not listed in Table 6.3 but are discussed in Section 6.3.8. Unless otherwise stated, all background processes were generated at NLO in QCD. The EFT and LQ signal samples were generated at LO since MADGRAPH5\_AMC@NLO (shortened to MG\_AMC@NLO) does not generate BSM processes at NLO.

MC samples used in the analysis were scaled to reflect the expected number of events, taking into account the cross-section of the process and the luminosity of the dataset available (Eq. (3.1)). Beyond LO, generators assign non-uniform weighting to MC events, to account for higher-order terms and interference effects, and may include negative weights, to perform matching from the ME to the parton shower. MC samples were therefore normalised such that the total sum of weights reflects the expected number of events. In addition to this, a

Table 6.3: Overview of MC generators used to simulate signal and significant background processes. The default SHERPA scale setting is described in Ref. [151].

Process	Generator	Parton shower	ME PDF	Scale choice
<b>Signal</b>				
EFT signal	MG_AMC@NLO 2.9.5	PYTHIA 8	NNPDF 3.1 NLO	See Section 6.3.2
LQ signal	MG_AMC@NLO 2.9.5	PYTHIA 8	NNPDF 3.0 NLO	$m_{S_1}$
<b>Main background</b>				
$t\bar{t}$	POWHEG Box v2	PYTHIA 8	NNPDF 3.0 NLO	$\sqrt{m_t^2 + p_T^2}$
$tW$	POWHEG Box v2 [152]	PYTHIA 8	NNPDF 3.0 NLO	$m_t$
$t/\bar{t}$ (s-channel)	POWHEG Box v2 [153]	PYTHIA 8	NNPDF 3.0 NLO	$m_t$
$t/\bar{t}$ (t-channel)	POWHEG Box v2 [153, 154]	PYTHIA 8	NNPDF 3.0 NLO	$4\sqrt{m_b^2 + p_{T,b}^2}$
$tZq$ trilepton	MG_AMC@NLO 2.3.3	PYTHIA 8	NNPDF 3.0 NLO	$4\sqrt{m_b^2 + p_{T,b}^2}$
$tWZ$ ( $Z \rightarrow \ell\ell$ )	MG_AMC@NLO 2.3.3	PYTHIA 8	NNPDF 3.0 NLO	$m_t$
$t\bar{t}\ell\ell$	MG_AMC@NLO 2.8.1	PYTHIA 8	NNPDF 3.0 NLO	$0.5 \cdot \sum_i \sqrt{m_i^2 + p_{T,i}^2}$
$t\bar{t}H$	POWHEG Box v2	PYTHIA 8	NNPDF 3.0 NLO	$\sqrt[3]{m_T(t) m_T(\bar{t}) m_T(H)}$
$t\bar{t}W$	SHERPA 2.2.10	SHERPA 2.2.10	NNPDF 3.0 NNLO	$0.5 \cdot \sum_i \sqrt{m_i^2 + p_{T,i}^2}^2$
$WZ$	SHERPA 2.2.2	SHERPA 2.2.2	NNPDF 3.0 NNLO	SHERPA <i>default</i>
$ZZ$	SHERPA 2.2.2	SHERPA 2.2.2	NNPDF 3.0 NNLO	SHERPA <i>default</i>
$Z(\rightarrow \ell\ell)+\text{jets}$	SHERPA 2.2.1	SHERPA 2.2.1	NNPDF 3.0 NNLO	SHERPA <i>default</i>
$W(\rightarrow l\nu)+\text{jets}$	SHERPA 2.2.1	SHERPA 2.2.1	NNPDF 3.0 NNLO	SHERPA <i>default</i>
$VVV$	SHERPA 2.2.2	SHERPA 2.2.2	NNPDF 3.0 NNLO	$\sqrt{\hat{s}}$

number of scale factors which correct the efficiency to reconstruct different physics objects were applied, as discussed in Section 5.3. The total weighting applied to a MC event was given by the product of these scale factors with the MC event weight and luminosity weight.

### 6.3.1 Data

The ATLAS data samples used in the analysis correspond to the full Run 2 dataset of  $140.1 \pm 1.2 \text{ fb}^{-1}$  [5] collected by the detector between 2015 and 2018 at a centre-of-mass energy of  $\sqrt{s} = 13 \text{ TeV}$ .

### 6.3.2 EFT signal samples

Two processes contribute to the EFT signal process considered in this analysis: the production of a single top quark in association with a muon and a tau lepton,  $gu_k \rightarrow t\mu\tau$ , and top quark pair production in which one top undergoes the decay  $t \rightarrow \mu\tau u_k$ . The single top quark produced via the  $gu_k \rightarrow t\mu\tau$  process and the second top quark in the case of  $t\bar{t}$  production is required to decay leptonically via the SM. Representative Feynman diagrams for these processes have been shown in Fig. 6.1. For the generation of signal MC all charged lepton flavour combinations were considered ( $t\mu\tau u_k, t\mu\mu u_k, t\tau u_k$ ), since the same MC is shared by other analyses, and both hadronic and leptonic tau decays were allowed. This search considers only events with a  $t\mu\tau u_k$  vertex.

For the  $t\bar{t}$  decay samples, separate samples were produced per EFT operator in Table 6.1, including both  $t \rightarrow \mu\tau u$  and  $t \rightarrow \mu\tau c$  decays, in addition to an “inclusive” sample in which all operator contributions were included. For the single top production process, independent samples were produced for the processes  $gu \rightarrow t\mu\tau$  and  $gc \rightarrow t\mu\tau$  for each EFT operator in Table 6.1 since the PDFs differ for up and charm quarks. Inclusive samples, including the effect of all operators at the same time, were also produced for each of the processes  $gu \rightarrow t\mu\tau$  and  $gc \rightarrow t\mu\tau$ .

A UFO model [155] built with FEYNRULES 2.0 [156] based on the DIM6TOP model [157] specifies the Feynman rules for the operators given in Table 6.1 to allow MG\_AMC@NLO to compute the matrix element for the CLFV processes. Dynamic renormalisation and factorisation scales were used; these were chosen to be the centre-of-mass energy of the incoming partons for decay diagrams and half the sum of the transverse masses of all final state particles and partons for production diagrams.

Table 6.4: Theoretical cross-sections for single top quark production and  $t\bar{t}$  decays through CLFV interactions for vector, scalar and tensor EFT operators. The cross-section for each of the vector operators is the same. These values were calculated for a top quark mass of 172.5 GeV, a top quark decay width of 1.51 GeV, a new physics scale of  $\Lambda = 1$  TeV and Wilson coefficient values of 1.0. The scale variation and PDF uncertainties are given.

$i, j = e, \mu, \tau$	cross-section $\sigma_{\text{-scale}}^{+\text{scale}} \pm \text{PDF} / \text{fb}$		
	$\mathcal{O}_{lq/eq/lu/eu}^{-(ijk3)}$	$\mathcal{O}_{lequ}^{1(ijk3)}$	$\mathcal{O}_{lequ}^{3(ijk3)}$
<b>Production <math>\ell\ell'ut</math></b>	$118_{-19}^{+24} \pm 1$	$101_{-16}^{+21} \pm 1$	$2150_{-320}^{+410} \pm 20$
<b>Production <math>\ell\ell'ct</math></b>	$7.9_{-1.0}^{+1.2} \pm 1.6$	$6.1_{-0.8}^{+1.0} \pm 1.5$	$153_{-18}^{+21} \pm 29$
<b>Decay <math>\ell\ell'qt</math></b>	$6.9_{-1.3}^{+1.8} \pm 0.1$	$3.46_{-0.66}^{+0.90} \pm 0.03$	$166_{-32}^{+43} \pm 2$

The cross-sections for the signal processes are shown in Table 6.4. The values for the  $t \rightarrow \mu\tau u_k$  process were calculated according to Eq. (6.1) from which the cross-section is calculated as<sup>3</sup> [143]

$$\sigma_{\text{CLFV}}^{\text{decay}} = 2 \sigma_{t\bar{t}} \mathcal{B}(t \rightarrow W(\ell\nu_\ell)b) \frac{\Gamma(t \rightarrow \ell^\pm \ell'^\mp q)}{\Gamma_t}. \quad (6.3)$$

where  $\Gamma_t = 1.51$  GeV is the top decay width at LO and  $\mathcal{B}(t \rightarrow W(\ell\nu_\ell)b) = 0.326$  [158]. The cross-section of the  $t\bar{t}$  sample is calculated at next-to-next-to-leading order (NNLO) in QCD, as discussed below in Section 6.3.4. The cross-sections for the CLFV single top production process were taken directly from the MC generator since no analytical expression is present in the literature. In both cases the cross-section is proportional to the square of the Wilson coefficient values, since there is no SM interference term.

<sup>3</sup>The top quark width  $\Gamma_t$  in Eq. (6.3) should include the additional width coming from the new interaction but for Wilson coefficient values to which the analysis is sensitive, the contribution of the additional width is negligible.

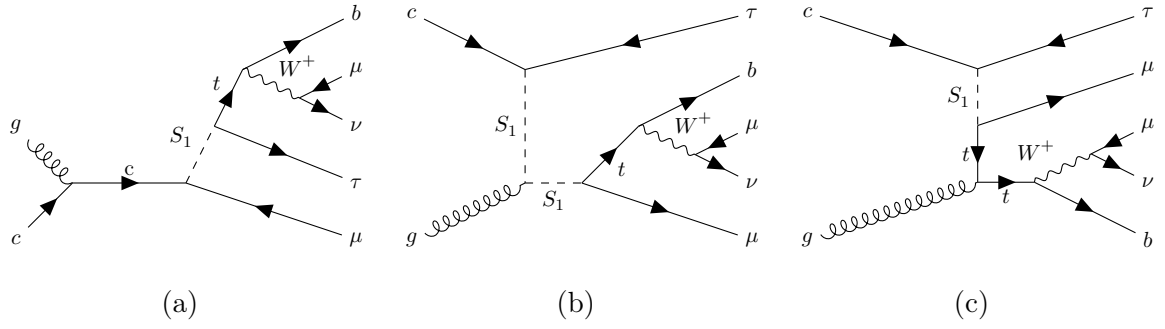


Figure 6.3: Example Feynman diagrams for the LQ signal processes. Diagrams (a) and (b) show resonant LQ production while (c) shows off-shell LQ exchange.

### 6.3.3 Leptoquark signal samples

For the LQ interpretation, the production of a single scalar LQ,  $S_1$ , in association with a muon and a tau lepton is considered. The generated process is  $gc \rightarrow S_1 \ell \rightarrow t \ell \ell'$  where  $\ell \ell' = \mu \tau$ . Both resonant and non-resonant LQ production were considered, for which representative Feynman diagrams for the process are shown in Fig. 6.3. The samples were generated using the UFO model described in Refs. [146, 147].

The cross-section and kinematics of the LQ process in general depend on the mass,  $m_{S_1}$ , and coupling to the SM,  $\lambda$ , of the LQ. Table 6.5 shows the values of  $m_{S_1}$  and  $\lambda$  for which samples have been produced. These values were chosen to give a range of cross-sections to which the analysis is expected to be sensitive. The cross-section for the  $gc \rightarrow S_1 \ell \rightarrow t \ell \ell'$  process ranges from 0.087 fb for  $m_{S_1} = 1000$  GeV and  $\lambda = 0.5$ , to 114 fb for  $m_{S_1} = 500$  GeV and  $\lambda = 2.0$ . A full breakdown of the generator cross-sections can be seen in Appendix F.

Based on the hierarchy of flavour couplings discussed in Section 6.2.2, the process  $gu \rightarrow S_1 \ell \rightarrow t \ell \ell'$  is suppressed relative to  $gc \rightarrow S_1 \ell \rightarrow t \ell \ell'$ . The cross-section of the process is seen to scale with the square of the production vertex coupling, so a suppression factor of 100 is expected if PDF differences are ignored. The analysis therefore focuses on the

$gc \rightarrow S_1\ell \rightarrow t\ell\ell'$  process since this gives greater sensitivity to the coupling  $\lambda$ . Samples have also been generated for the  $gu \rightarrow S_1\ell \rightarrow t\ell\ell'$  process but some of these were produced incorrectly, resulting in the flavour hierarchy of the couplings being broken. As a result these samples were not used in the analysis. Instead the charm-initiated samples were reweighted to take into account the expected effect of including up-initiated diagrams. The reweighting procedure will be discussed in Section 7.4.

Table 6.5: Values of coupling  $\lambda$  and mass  $m_{S_1}$  for which the process  $gc \rightarrow S_1\ell \rightarrow t\ell\ell'$  ( $\ell \in \{\mu, \tau\}$ ) has been generated.

$\mu\tau ct$	$\lambda$						
	0.5	1.0	1.5	2.0	2.5	3.0	3.5
500	✓	✓	✓	✓			
750	✓	✓	✓	✓			
1000	✓	✓	✓	✓			
1250		✓	✓	✓	✓		
1500			✓	✓	✓	✓	
1750			✓	✓	✓	✓	
2000				✓	✓	✓	✓
2250				✓	✓	✓	✓
2500					✓	✓	✓

### 6.3.4 $t\bar{t}$ and $t\bar{t}\gamma$

One of the leading backgrounds to the analysis comes from  $t\bar{t}$  events. This process is expected to produce at most two prompt leptons so enters the trilepton selection via a non-prompt or fake lepton. These samples were generated the POWHEG BOX v2 generator using PYTHIA 8

for parton shower and hadronisation modelling. The  $h_{\text{damp}}$  parameter, which regulates the  $p_T$  of the first real emission beyond leading order, is set to  $1.5 m_t$ . The value of this parameter was optimised using studies on observables sensitive to the emission of radiation from the  $t\bar{t}$  system with ATLAS data at centre-of-mass energies of  $\sqrt{s} = 7, 8, \text{ and } 13 \text{ TeV}$  [159].

Events with a  $t\bar{t}$  pair can also be produced with photon radiation from an incoming charged parton, the top quarks themselves, or any charged particle in the final state. A dedicated sample of  $t\bar{t}\gamma$  events is modelled at LO in QCD using MG\_AMC@NLO 2.3.3 [88] and PYTHIA 8. Some events in the  $t\bar{t}$  sample will feature photon radiation in the matrix element process. To prevent double-counting of these events, an overlap removal procedure is applied to the  $t\bar{t}$  and  $t\bar{t}\gamma$  samples so that they provide events from orthogonal regions of phase space; this procedure is described in Ref. [160].

The cross-section for  $t\bar{t}$  production was calculated at NNLO in QCD, including the resummation of soft gluon emissions to next-to-next-to-leading logarithmic accuracy. For a top quark mass of 172.5 GeV the cross-section is calculated using TOP++ 2.0 to be  $\sigma(t\bar{t})_{\text{NNLO+NNLL}} = 832 \pm 51 \text{ pb}$  [161–167].

### 6.3.5 Single top samples

The production of a single top quark in association with a  $W$  boson is also expected to result in at most two prompt leptons but enters the selection via a non-prompt or fake lepton. At NLO  $tW$  production includes  $t\bar{t}$ -like diagrams which overlap with those in the  $t\bar{t}$  sample. The  $tW$  sample uses a diagram removal scheme [168] to account for overlap between  $tW$  and  $t\bar{t}$  diagrams. In addition to removing doubly-resonant  $t\bar{t}$ -like diagrams, this method removes interference terms between  $tW$  and  $t\bar{t}$ . This is considered as a source of theoretical uncertainty, discussed in Section 6.7.

Additional samples simulating the production of top quarks in association with weak bosons,  $tZ$  and  $tWZ$ , are also used. In both cases the  $Z$  boson was required to decay leptonically. Smaller background contributions come from single top production in the  $s$ - and  $t$ -channels since these processes are only expected to produce one prompt lepton. Collectively all single top samples are referred to as  $t + X$ .

### 6.3.6 $t\bar{t}V$

The production of a  $t\bar{t}$  pair in association with a scalar or vector boson is a common source of trilepton events. The leading contributions to the  $t\bar{t}W$  process were modelled at NLO in QCD for matrix elements including a maximum of one additional jet and at LO for events with two additional jets. Reweighting is applied to this sample to account for the inclusion of EW corrections of order  $\alpha_S^2\alpha^2$  to the squared matrix element. An additional SHERPA 2.2.10 sample models terms of order  $\alpha_S\alpha^3$  at LO.

The production of  $t\bar{t}Z$  in which the  $Z$  boson decays leptonically is considered, along with  $t\bar{t}H$  production. The cross-sections were calculated including QCD and EW corrections at NLO accuracy as reported in Ref. [169].

### 6.3.7 Weak boson processes

Events with a single  $W$  or  $Z$  boson produced in association with additional jets only enter the event selection with fake or non-prompt leptons. These processes are modelled at NLO (LO) in QCD for up to two (four) additional jets. Matrix element calculations were provided by the COMIX [170] and OPENLOOPS [171–173] generators. Generated samples are matched to the SHERPA parton shower with the MEPS@NLO method [151, 174–176]. The same matching procedure was used for the other weak boson processes described below.

The production of a  $Z$  boson in association with a photon is also considered.  $Z\gamma$  production was modelled with matrix elements calculated at LO in QCD for up to three additional jets. As with the  $t\bar{t}$  and  $t\bar{t}\gamma$  samples, an overlap removal procedure is applied to the  $Z$ +jets and  $Z\gamma$  samples to prevent double counting.

The production of pairs of weak bosons are common multi-lepton processes.  $WZ$  and  $ZZ$  production can decay to multiple leptons and pose irreducible backgrounds to signal-sensitive regions.  $WW$  produces at most two charged leptons but can enter the selection as a fake process. All final states with at least one boson decaying leptonically are considered. Matrix elements are calculated at NLO (LO) in QCD for up to one (three) additional jets. These samples take into account both off-shell effects and contributions from diagrams with Higgs bosons, such as  $gg \rightarrow H \rightarrow ZZ \rightarrow \ell\ell\ell$ . The rare production of triboson events is also considered. Matrix elements are calculated to NLO accuracy for the inclusive process and to LO for up to two additional jets.

### 6.3.8 Other SM

A number of other rare SM processes which produce multi-lepton final states have also been considered. These include the production of three or four top quarks,  $t\bar{t}$  in association with a pair of  $W$  bosons and the production of a weak boson in association with a Higgs boson. They are collectively referred to as “other” in figures and tables used later in this chapter.

## 6.4 Object and event selection

Experimentally, the CLFV signal process of interest gives rise to an opposite-charge different-flavour charged lepton pair, along with the products of a SM top quark decay. This analysis

targets the case in which the SM top quark decay is  $t \rightarrow \ell\nu_\ell b$ , resulting in a trilepton final state. Compared to the dilepton case, the requirement of a third lepton significantly reduces the acceptance for SM backgrounds.

### 6.4.1 Event pre-selection and triggering

Events are selected based on passing single electron and single muon trigger chains [177–179]. The single electron (muon) triggers selected have an  $E_T$  ( $p_T$ ) threshold as well as identification and isolation requirements. Triggers with low thresholds are chosen for each data period in combination with higher threshold triggers which have looser identification/isolation requirements to improve the selection efficiency at high  $E_T/p_T$ . The triggers used are shown in Table 6.6.

Table 6.6: Trigger selection for all data taking years used in the CLFV analysis [177]. The number following “e” (“mu”) is the lepton  $E_T$  ( $p_T$ ) threshold while “lh” and “i” suffixes denote additional identification and isolation requirements, respectively.

	Electron triggers	Muon triggers
<b>2015</b>	HLT_e24_lhmedium_L1EM20VH	HLT_mu20_iloose_L1MU15
	HLT_e60_lhmedium	HLT_mu50
	HLT_e120_lhloose	
<b>2016–2018</b>	HLT_e26_lhtight_nod0_ivarloose	HLT_mu26_ivarmedium
	HLT_e60_lhmedium_nod0	HLT_mu50
	HLT_e140_lhloose_nod0	

Scale factors are applied to selected events in simulation to account for mismodelling of the probability for electrons and muons to pass the triggers. Both electron and muon

trigger efficiencies are determined using tag-and-probe methods in  $Z/\gamma^* \rightarrow ee$  [178] and  $Z/\gamma^* \rightarrow \mu\mu$  [179], respectively.

Selected events are required to have at least one reconstructed lepton identified as having fired a trigger - a process known as trigger-matching. Since the reconstructed  $p_T$  and  $E_T$  used in the analysis can differ from the corresponding online quantities used in trigger thresholds, a trigger-matched lepton must have a  $p_T$  greater than the trigger threshold by 1 GeV (5%) for electrons (muons) [180, 181]. These requirements, based on ATLAS recommendations, ensure the trigger is maximally efficient for selected lepton candidates, such that differences in efficiency between simulation and data are small and can be corrected by the trigger scale factors.

Quality requirements are applied to events to remove those recorded during periods of poor detector performance as well as those which are not likely to originate from a hard-scatter interaction. Each event must have an associated primary vertex within the expected interaction region reconstructed from at least two tracks with  $p_T$  greater than 500 MeV [182, 183]. A jet cleaning tool [184] is employed to remove events featuring jets which are likely to originate from noise in the calorimeters or from non-collision backgrounds, such as cosmic muons, using the ‘‘LOOSEBAD’’ selection.

Table 6.7: Description of common selection cuts applied to all regions used in the analysis. ‘‘Light lepton’’ refers to electrons and muons.

<b>Preliminary cuts</b>	
Number of leptons	$N_\ell = 3$
Leading light lepton $p_T$	$> 27$ GeV
Trigger matching	$\geq 1$ trigger-matched light lepton
Sum of lepton charges	$\sum_i q_i = \pm 1$

The initial selection criteria applied to the events is summarised in Table 6.7. Events must contain exactly three leptons which may be electrons, muons or  $\tau_{\text{had-vis}}$ , as defined in Tables 5.1 to 5.3. The trigger thresholds were higher in 2016–2018 than in 2015 (see Table 6.6); therefore the highest  $p_T$  (“leading”) lepton must have a  $p_T > 27$  GeV. A further requirement is placed on the sum of the lepton charges to reject events with three leptons of the same charge, since this is not a signature of the signal process.

### 6.4.2 Analysis regions

Signal events arising from a  $t\mu\tau u_k$  interaction are expected to contain a muon, a  $\tau_{\text{had-vis}}$  and an additional charged lepton originating from the SM decay of the top quark, along with jets and  $E_T^{\text{miss}}$ . Since  $\tau_{\text{had-vis}}$  are more difficult for the ATLAS detector to reconstruct than muons, the SR requires events in which the third lepton is a muon. Events with an electron, a muon and a  $\tau_{\text{had-vis}}$  are not considered to avoid introducing a third source of lepton fakes into the SR. The SR therefore requires two muons, one  $\tau_{\text{had-vis}}$  and at least one jet, of which exactly one jet must be  $b$ -tagged. The two muons are required to have the same charge (same sign, SS) because many high cross section background processes produce  $\ell^+\ell^-$  pairs. While the signal is evenly split between events with same-sign and opposite-sign (OS) muons, the total background is much larger when considering events with OS muons.

The individual cuts applied to each analysis region are shown in Table 6.8. In addition to the SR which targets the signature of the  $t\mu\tau u_k$  interaction signal, CRs are defined for two fake lepton backgrounds present in the SR; these are events with fake  $\tau_{\text{had-vis}}$  candidates or non-prompt muons. Events with fake muon candidates are expected to be negligible according to MC simulations. The CRs are designed to be signal-depleted such that they can be used to study the background modelling even whilst the SR remains blinded.

Table 6.8: Definitions of analysis regions. In the SR muons are required to have the same charge (SS) while in  $\text{CR}\tau$  they are required to have opposite charge (OS). The final row shows a simultaneous cut applied to the sum of the leading muon  $p_T$  and dilepton invariant masses; it is discussed further in the text.

	<b>SR</b>	<b>CR<math>\tau</math></b>	<b>CR<math>t\bar{t}\mu</math></b>	<b>VR<math>\mu</math></b>
Lepton flavour	$2\mu 1\tau_{\text{had-vis}}$		$2\mu 1e (\ell_3 = \mu)$	$3\mu$
Muon charges	SS	OS	-	-
Muon $p_T$ cut	$> 15 \text{ GeV}$	$> 15 \text{ GeV}$	$> 10 \text{ GeV}$	$> 12 \text{ GeV}$
Lowest $p_T$ muon selection	<b>Tight</b>	<b>Tight</b>	<b>Loose</b>	<b>Tight</b>
$N_{\text{jets}}$	$\geq 1$	$\geq 2$	$\geq 1$	$\geq 2$
$N_{b\text{-tags}}$	1	1	$\leq 2$	1
$m_{\ell\ell}^{OS}$	-	-	-	$> 15 \text{ GeV}$
$ m_{\ell\ell}^{OS} - M_Z $	-	$< 10 \text{ GeV}$	$> 10 \text{ GeV}$	$> 10 \text{ GeV}$
Signal contamination	-	-	$< 400 \text{ GeV}$	$< 400 \text{ GeV}$
$3p_T^{\text{Lead.}\mu} + \sum m_{\ell\ell}^{OS}$	-	-	$< 400 \text{ GeV}$	$< 400 \text{ GeV}$

$\text{CR}\tau$  targets events with fake  $\tau_{\text{had-vis}}$  candidates. A very similar selection to the SR is applied but events are required to have OS muons, which results in a much larger background yield. The region is seen to be enriched in events with two OS muons from  $Z$ +jets with  $Z \rightarrow \mu\mu$  or dileptonic  $t\bar{t}$  decays in which a jet is misidentified as a  $\tau_{\text{had-vis}}$  candidate. To reduce the contribution from muon pairs originating from  $J/\psi$  or  $\Upsilon$  meson resonances, the invariant mass of the OS muon pair is required to exceed 15 GeV.  $\text{CR}\tau$  also contains a requirement that the invariant mass of the dimuon pair falls within 10 GeV of the  $Z$  boson mass. This is to suppress contamination from the  $g u_k \rightarrow t\mu\tau$  signal whose dimuon invariant mass spectrum tends towards higher values than  $M_Z$ .

A second CR targets events with non-prompt muons from heavy-flavour hadronic decays.  $\text{CR}t\bar{t}\mu$  selects events with two muons and one electron and is seen to be enriched

in events from dileptonic  $t\bar{t}$  decays. Non-prompt muons tend to have a softer  $p_T$  spectrum than those originating from the hard-scatter interaction so the region requires the lowest  $p_T$  lepton to be a muon. To further enrich the selection with events with non-prompt muons, the third muon is required to satisfy the **Loose** criteria while the leading muon and electron are required to be **Tight**. **Loose** muons have weaker isolation requirements and have inverted transverse impact parameter requirements, as shown in Table 5.2. The requirement of an electron-muon pair, along with a veto on events with a dimuon invariant mass within 10 GeV of the  $Z$  boson mass, provides a pure selection of  $t\bar{t}$  events. This is desirable to reject  $Z$ +jets events with  $Z \rightarrow \mu\mu$  and a fake electron.

Additionally a validation region (VR) is defined which uses events with three reconstructed muons to validate the modelling of the non-prompt muon background. As with  $CR\tau$ ,  $VR\mu$  requires that the invariant masses of OS dimuon pairs exceeds 15 GeV to avoid background events from low mass resonances. Events in which either of the OS dimuon invariant masses fall within 10 GeV of the  $Z$  boson mass are rejected; this suppresses the large backgrounds from diboson processes which typically produce three or four prompt leptons.

The large initial normalisation chosen for the signal, corresponding to a Wilson coefficient value of 0.3 for a scale of new physics  $\Lambda = 1$  TeV, means a large pre-fit signal contamination is present in  $CRt\bar{t}\mu$  and  $VR\mu$ . Signal contamination in these regions results from events in which the tau lepton produced in the CLFV vertex decays leptonically. An additional cut is therefore applied to these regions to suppress signal contamination. The cross section of the CLFV single top production process far exceeds that of the CLFV  $t\bar{t}$  decay process and provides the main source of signal contamination. This process tends to produce leptons with much greater  $p_T$  than the background processes so cuts on invariant masses and lepton  $p_T$  are seen to be effective at reducing any contamination. Cuts on a single variable were investigated but were not sufficiently effective to reduce the signal contamination below 10% of the expected background yield; simultaneous cuts on two variables were therefore

investigated. The most effective of these was found to be a cut on the sum of leading muon  $p_T$  and dimuon invariant masses. The effect of this cut on simulation in  $VR\mu$  is shown in Fig. 6.4 while the signal and background distributions used to study this cut can be seen in Appendix A.2.

The SR and  $CR\tau$  have an additional requirement that muon  $p_T$  exceeds 15 GeV to reduce the background from non-prompt muons which tend to have lower  $p_T$ . In the muon control regions a lower  $p_T$  cut is used to retain events with non-prompt muons.

### 6.4.3 Fitted SR observable

The presence of any CLFV signal in the data is inferred with a binned profile likelihood fit. The sensitivity to the signal process is dominated by the production process which is known to produce high  $p_T$  final state objects. Binning of the SR in the  $p_T$  of the leading muon and  $H_T$ , the scalar sum of the  $p_T$  of all lepton and jet candidates, were considered. In both cases the signal distribution peaks at significantly higher values than the expected background distribution. The  $p_T$  of the second muon and  $\tau_{\text{had-vis}}$  candidate were not considered to reduce sensitivity to mismodelling of fake backgrounds.

Binning of the SR in leading muon  $p_T$  and  $H_T$  have been tested using the full profile likelihood setup, which will be discussed in Section 7.1, under the assumption that the data perfectly matches the expectation. Similar sensitivity is seen for the two variables and is seen to derive almost entirely from choice of the low bound for the final bin of the distribution. As will be discussed in Chapter 7, the modelling of the  $t\bar{t}W$  process is one of the leading sources of systematic uncertainty. Binning as a function of the  $H_T$  variable is seen to provide slightly better discrimination between signal and  $t\bar{t}W$  so is chosen as the variable in which the SR is binned.

Since the majority of the signal falls primarily into the final bin, the expected sensitivity is increased by reducing the background yield in this bin. The final binning choice was made to increase the signal sensitivity while maintaining sufficient background contribution in the final bin to reduce the impact of possible fluctuations in data. While the Poissonian uncertainty on the number of recorded data events is taken into account in the likelihood function, large fluctuations here are still expected to have a significant effect on the analysis sensitivity. The chosen SR binning is the same as that shown in Fig. 6.4. This binning in  $H_T$  is also adopted for  $CRt\bar{t}\mu$  and  $VR\mu$ , while the binning of  $CR\tau$  is discussed in Section 6.5. Fig. 6.5 shows separately the signal and background contributions in the SR using a finer binning than used in the profile likelihood fit, to highlight kinematic differences.

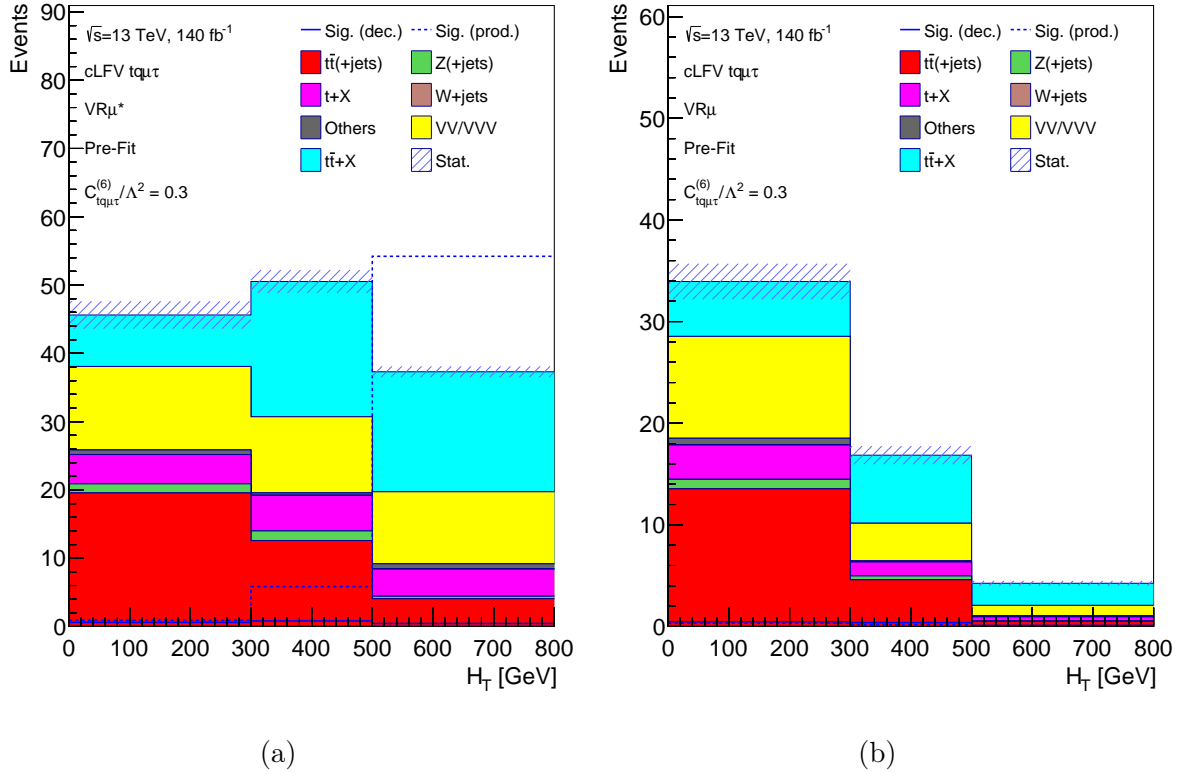


Figure 6.4: Distribution of the  $H_T$  variable, corresponding to the scalar sum of lepton and jet  $p_T$ , in  $VR\mu$  according to MC simulation before (a) and after (b) the application of the cut to remove signal contamination. The final bin does not have an upper bound. Signal events would be expected at high  $H_T$  if the CLFV signal is realised in nature. The same distribution over a larger range of  $H_T$  values can be seen in Fig. A.2.

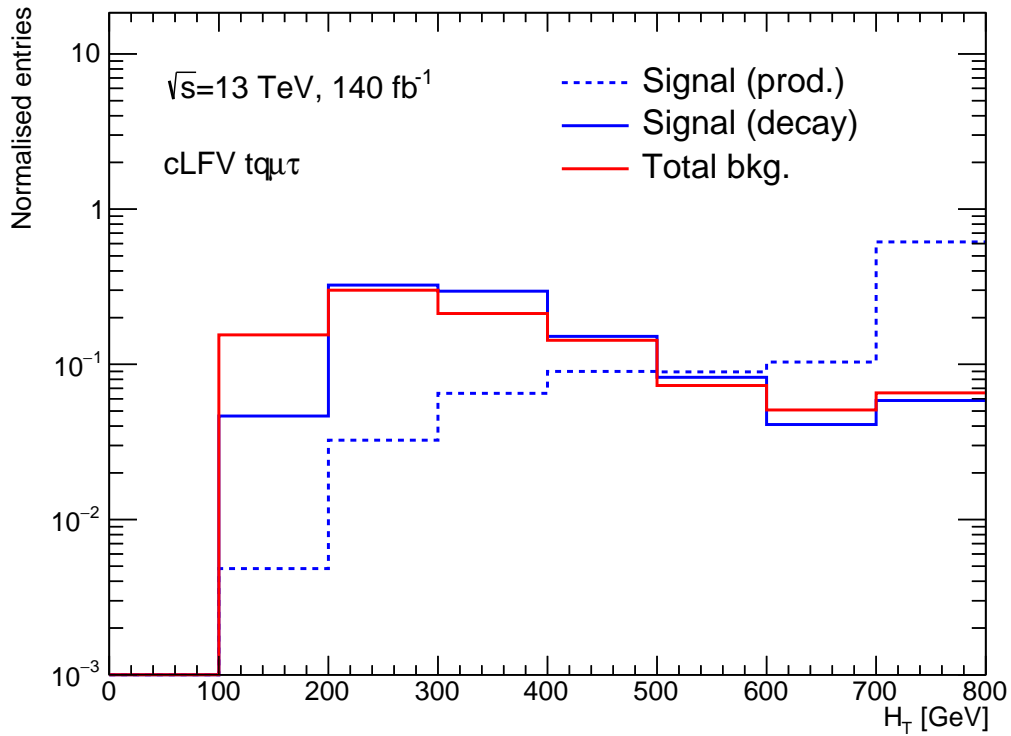


Figure 6.5: Distribution of the  $H_T$  variable, corresponding to the scalar sum of lepton and jet  $p_T$ , in the SR for signal processes and the sum of all background processes according to MC simulation. Each of the three distributions is normalised to unity to compare the different shapes. The final bin does not have an upper bound. The binning used here differs from that in the profile likelihood fit to highlight kinematic differences between signal and background.

### 6.4.4 Background composition

Fig. 6.6 shows the lepton composition of the background processes entering each region according to MC simulation. Both CRs are highly enriched in background processes featuring the type of fake lepton candidate they target: CR $\tau$  is seen to be populated by events from  $Z$ +jets or dileptonic  $t\bar{t}$  production featuring a  $\tau_{\text{had-vis}}$  candidate while CR $t\bar{t}\mu$  contains dileptonic  $t\bar{t}$  events with an additional non-prompt muon. Many physics processes can produce events which have the same or similar signature to the signal process and constitute a background to the search. The SR selects events from a wide variety of SM processes and includes events with three prompt, real leptons or as many as two fake leptons. No events are seen in the simulation in which all three leptons are fake. It can be seen that approximately half of the events in the SR contain fake or non-prompt leptons. VR $\mu$  has a very similar background composition to the SR, featuring similar proportions of events with non-prompt muons.

The rate at which fake leptons pass identification and isolation criteria is not always well-modelled by simulation. Rate corrections are therefore applied to events with non-prompt muon and fake  $\tau_{\text{had-vis}}$ , as will be discussed further in Sections 6.5 and 6.6. Some events are seen to contain both a non-prompt muon and a fake  $\tau_{\text{had-vis}}$  candidate. Such events can originate from the semi-leptonic  $t\bar{t}$  process which is expected to produce a single charged lepton along with four or more jets. These events are corrected for the presence of both a non-prompt muon and a fake  $\tau_{\text{had-vis}}$  candidate.

The yields of the signal and SM background processes contributing to each of these regions are listed in Table 6.9. It can be seen that the signal yields in both CRs and in VR $\mu$  are low. While shown separately here to demonstrate the background breakdown, in future sections small background contributions from  $t\bar{t}\gamma$  and  $Z\gamma$ , along with other processes that enter the event selection with a fake or non-prompt electron, are grouped together and

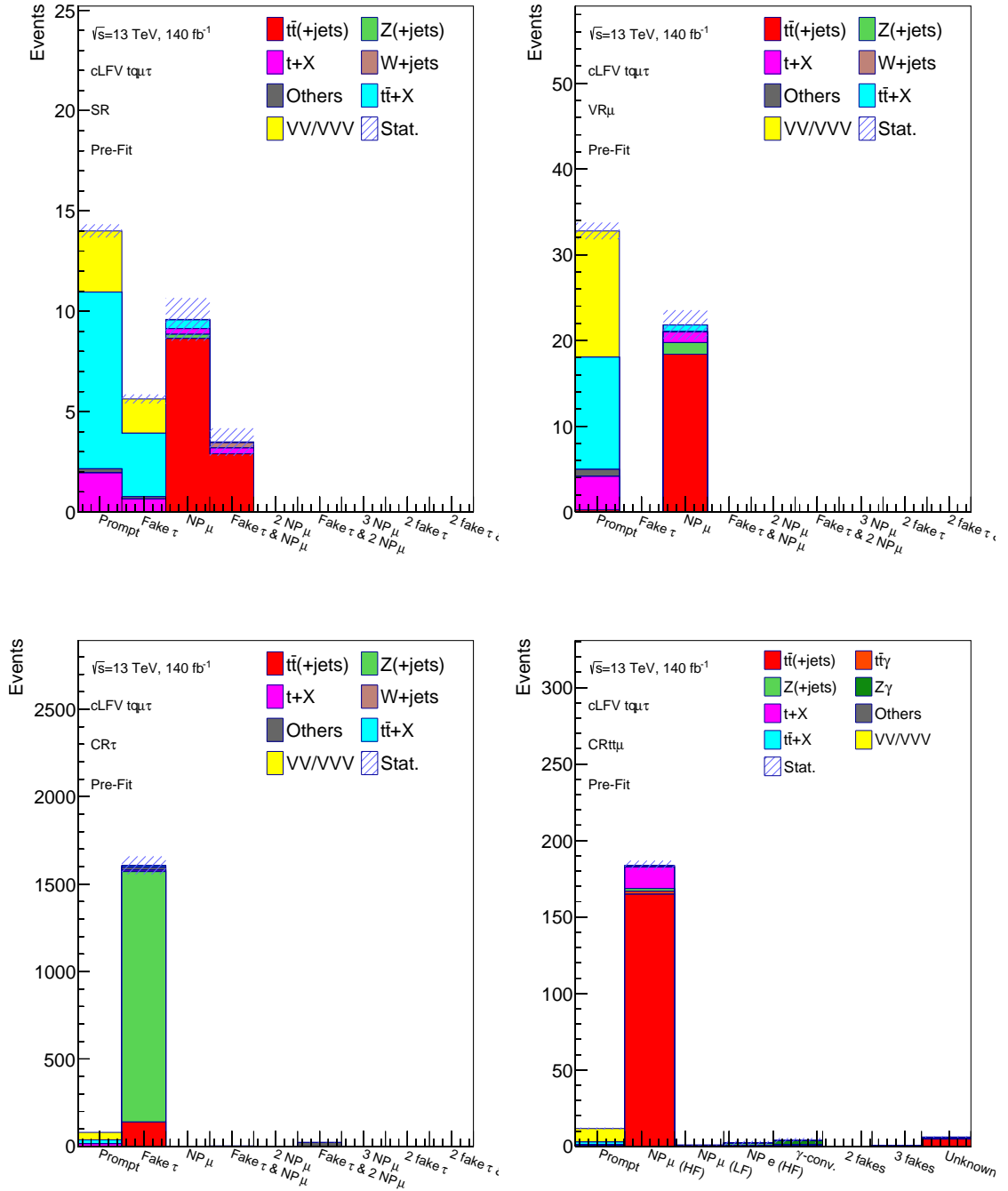


Figure 6.6: Lepton composition of SM background processes entering each analysis region according to MC simulation. Regions are labelled on the plots themselves. Note the different fake lepton classification for the CRt $\bar{t}\mu$  plot due to the presence of electron fakes in this region.

labelled “fake electron”.

Table 6.9: MC yields broken down by physics process for each analysis region. The uncertainty is the MC statistical uncertainty. Signal yields here correspond to the inclusive EFT signal using Wilson coefficient values of  $|c| = 0.3$  and  $\Lambda = 1$  TeV.

Process	SR	CR $\tau$	CR $t\bar{t}\mu$	VR $\mu$
$t\bar{t}$	11.5±1.2	142.1±4.3	171.9±2.6	18.6±1.6
$t\bar{t}W$	5.02±0.16	1.116±0.090	1.185±0.078	3.12±0.12
$t\bar{t}H$	3.513±0.063	1.318±0.034	1.252±0.034	3.442±0.058
$t\bar{t}Z$	3.25±0.11	28.36±0.34	0.865±0.080	7.31±0.17
$t + X$	3.17±0.30	22.7±0.93	14.7±1.4	5.14±0.43
$WZ$	4.03±0.28	30.58±0.54	7.26±0.46	7.52±0.27
$ZZ$	0.627±0.067	14.82±0.30	1.77±0.14	7.17±0.66
$VVV$	0.1217±0.0072	0.156±0.013	0.238±0.031	0.0516±0.0047
$Z$ +jets	0.21±0.13	1432±52	3.1±1.8	1.36±0.63
$W$ +jets	0.26±0.26	0.41±0.41	0.0±0.0	0.0±0.0
Other	0.340±0.048	39.5±1.5	1.1±0.47	0.89±0.59
$t\bar{t}\gamma$	0.0±0.0	0.0±0.0	2.79±0.33	0.0±0.0
$Z\gamma$	0.0±0.0	0.0±0.0	2.8±1.7	0.0±0.0
Total background	32.1±1.3	1713±52	209.0±3.9	54.6±2.0
EFT signal (decay)	5.87±0.11	0.77±0.04	0.77±0.12	0.955±0.043
EFT signal (prod.)	178.7±2.4	4.44±0.37	0.67±0.14	0.54±0.13

### 6.4.5 Non-prompt muon composition

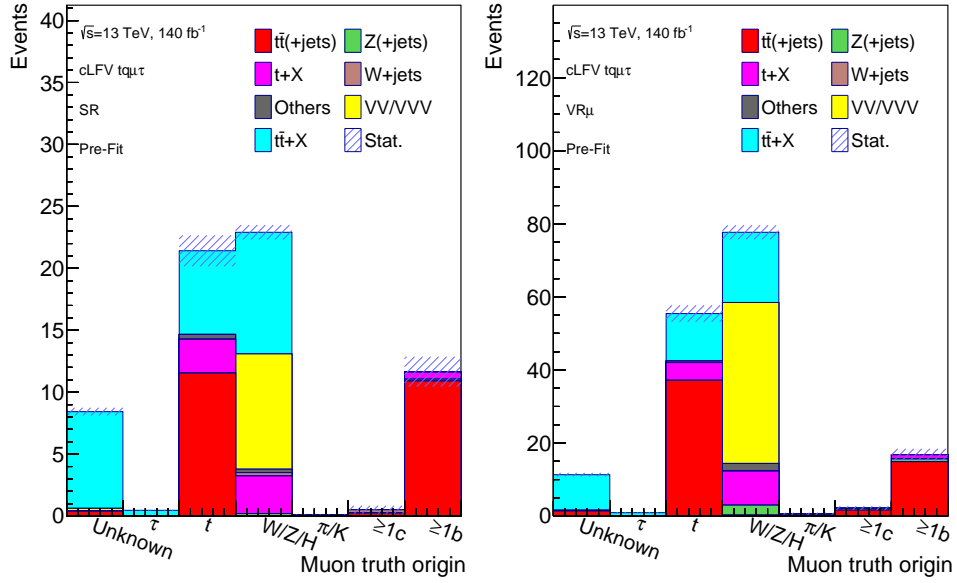
The dominant background process in the SR is  $t\bar{t}$  which is reconstructed with three leptons due to the presence of a non-prompt muon from a heavy-flavour decay inside a jet, typically a

$b$ -jet. Isolation requirements based on the PLV algorithm are used to suppress this background but a non-negligible contribution is still present. A non-prompt lepton can satisfy the PLV requirements if it possesses a large fraction of the parent hadron momentum or is produced collinear to the parent such that it appears to have originated from the primary vertex.

The rate at which non-prompt muons pass isolation criteria may not be well-modelled by simulation. The probability to pass isolation criteria will also depend on the source and kinematics of the non-prompt muons. For muons above 12 GeV the PLV is trained on a sample of  $t\bar{t}$  events and uses  $b$ -tagging variables; it is therefore better at rejecting non-prompt muons from heavy flavour decays than those from kaon or pion decays. Care has been taken therefore to ensure the composition of non-prompt muons is compatible between the SR,  $VR_\mu$  and  $CRt\bar{t}\mu$ .

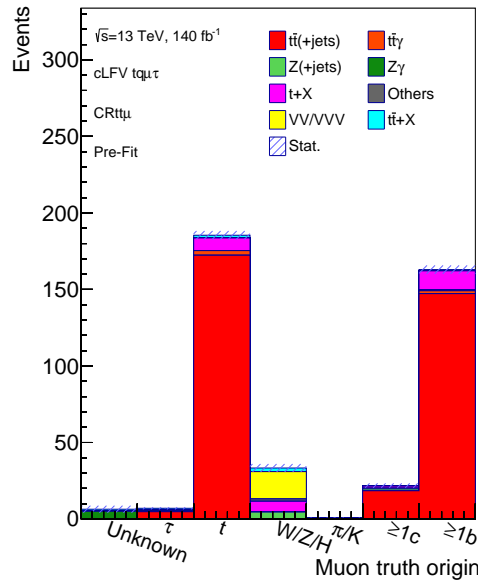
Below 12 GeV the PLV uses a different algorithm which excludes flavour-tagging information, since at low  $p_T$  non-prompt muons are also seen to arise from light-flavour hadronic decays. The 12 GeV muon  $p_T$  cut applied to  $VR_\mu$  therefore ensures the non-prompt muon composition is very similar to that of the SR. This cut suppresses  $Z$ +jets events in which pion or kaon decays produce soft muons.

Fig. 6.7 shows the origin of muons in the SR,  $CRt\bar{t}\mu$  and  $VR_\mu$  according to MC truth information. During event generation, information about the identities and kinematics of particles produced in simulation are stored in the MC truth record. This can be used to match reconstructed physics objects to particles in the truth record which provides important information about the composition of the expected background in the analysis. It can be seen that non-prompt muons result mostly from the decay of  $B$  mesons across all three regions. In events with a non-prompt muon, the non-prompt muon is typically that with the lowest  $p_T$ .



(a)

(b)



(c)

Figure 6.7: Origin of muons in the SR (a),  $VR_\mu$  (b) and  $CRt\bar{t}\mu$  (c) according to MC truth information. Prompt muons are produced in the decays of  $\tau$  leptons, top quarks, Higgs bosons or EW bosons, while non-prompt muons are produced in the decays of mesons or baryons inside jets. Hadrons with at least one  $b$ -quark are labelled “ $\geq 1b$ ”, while those with no  $b$ -quark but at least one  $c$ -quark are labelled “ $\geq 1c$ ”.

### 6.4.6 Fake $\tau_{\text{had-vis}}$ composition

Fake  $\tau_{\text{had-vis}}$  candidates are suppressed by the  $\tau_{\text{had-vis}}$  identification algorithm but still form a non-negligible background to the analysis. The probability for a jet to be misidentified as a  $\tau_{\text{had-vis}}$  can depend on the flavour of the jet as well as its kinematics. Jet substructure depends on the flavour of the partons initiating the jet. Jets faking  $\tau_{\text{had-vis}}$  are typically initiated by a light quark or a gluon since b-jets tend to have a higher number of tracks than  $\tau_{\text{had-vis}}$  jets.

When estimating the fake  $\tau_{\text{had-vis}}$  background, the jet flavour and the physics process from which the jet originates would ideally be the same between CR $\tau$  and the SR. This helps to ensure that the kinematics of the fake objects are compatible. As shown by Fig. 6.6, fake  $\tau_{\text{had-vis}}$  in the SR originate from a variety of processes and it has not been possible to define a CR enriched in fake taus from these same processes. Instead CR $\tau$  is defined such that the flavour of jets which are misidentified as  $\tau_{\text{had-vis}}$  candidates is consistent with that of the SR. Differences in the kinematic features of these events are then taken into account by the fake estimation procedure. This will be discussed further in Section 6.5.

To ensure the SR is compatible with CR $\tau$  the parton flavour of the jet misidentified as a  $\tau_{\text{had-vis}}$  is compared in simulation between regions, as shown in Fig. 6.8. It can be seen that these are very compatible, with consistent quark-gluon ratios of  $3.64 \pm 0.29$  in CR $\tau$  and  $3.58 \pm 0.72$  in the SR. The fake  $\tau_{\text{had-vis}}$  background estimation, which is discussed in Section 6.5, will also account for any small differences in quark/gluon ratios.

It is not clear why there are more fake  $\tau_{\text{had-vis}}$  candidates from  $d$ -quarks than  $u$ -quarks in simulation, as shown in Fig. 6.8. In the SR the difference between  $d$ - and  $u$ -quarks initiating fake  $\tau_{\text{had-vis}}$  is predominantly due to the  $t\bar{t}$  contribution. These events arise from semi-leptonic  $t\bar{t}$  decays in which the fake  $\tau_{\text{had-vis}}$  candidate comes from the hadronic  $W$

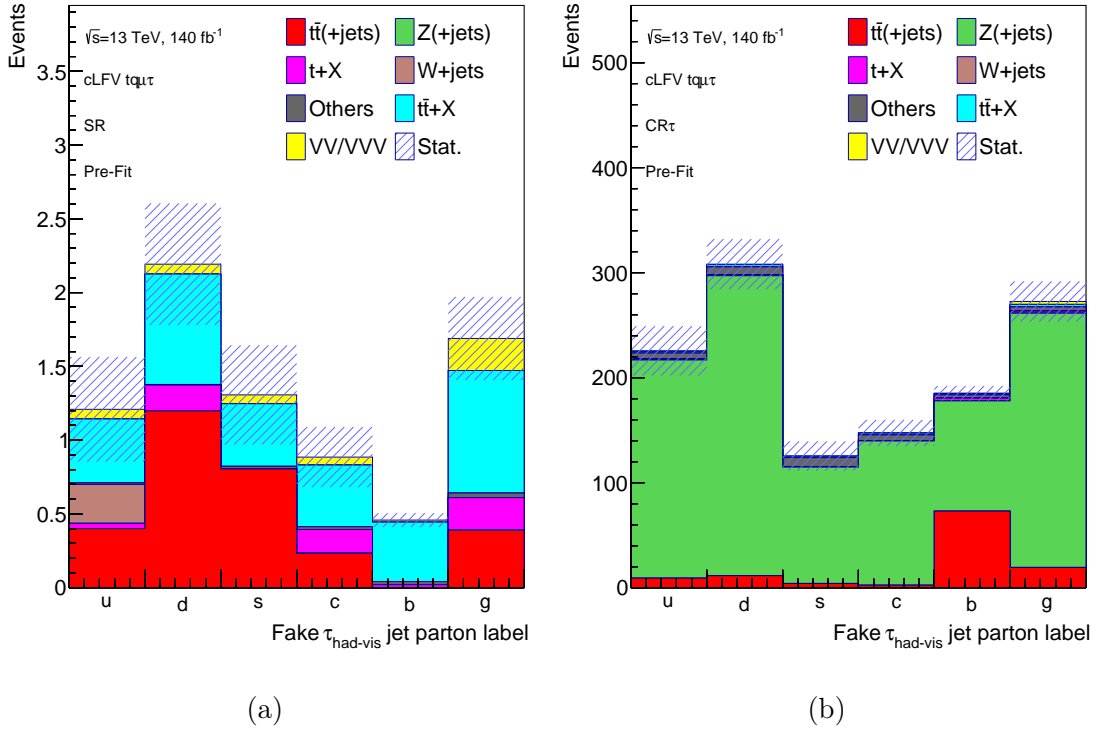


Figure 6.8: Parton initiating jets truth matched to fake  $\tau_{\text{had-vis}}$  in the SR (a) and  $\text{CR}\tau$  (b). The hatched band represents the MC statistical uncertainty.

boson decay. Since  $|V_{ud}| \gg |V_{us}| \approx |V_{cd}|$  roughly equal numbers of  $d$ - and  $u$ -quarks would be expected. Nevertheless, jets initiated by  $d$ - and  $u$ -quarks are not expected to have different jet shapes or fake rates [185].

In simulation  $\text{CR}\tau$  features a contribution from events in which the reconstructed  $\tau_{\text{had-vis}}$  is not truth-matched. This contribution comes predominantly from  $t\bar{t}$  and  $Z$ +jets events, as is the case for events with truth-matched  $\tau_{\text{had-vis}}$ . The  $\tau_{\text{had-vis}}$  candidates with no associated truth object are believed to be jets resulting from pileup interactions. From Fig. 6.9 it can be seen that in simulation the relative fraction of unknown objects faking  $\tau_{\text{had-vis}}$  tends to increase with the number of interaction vertices in the event. Fig. 6.10 shows the JVT score, introduced in Section 5.3.3, for jets seeding  $\tau_{\text{had-vis}}$  reconstruction for events

in  $\text{CR}\tau$ . Jets with a JVT score of 1 are likely to originate from a hard-scatter interaction while a score of 0 indicates the jet is more likely to have originated from a pileup interaction. It can be seen that the JVT score peaks at 0 for these  $\tau_{\text{had-vis}}$  which are not truth-matched, further supporting the hypothesis that these objects are jets from pileup interactions. These misidentified  $\tau_{\text{had-vis}}$  are included in the fake estimation.

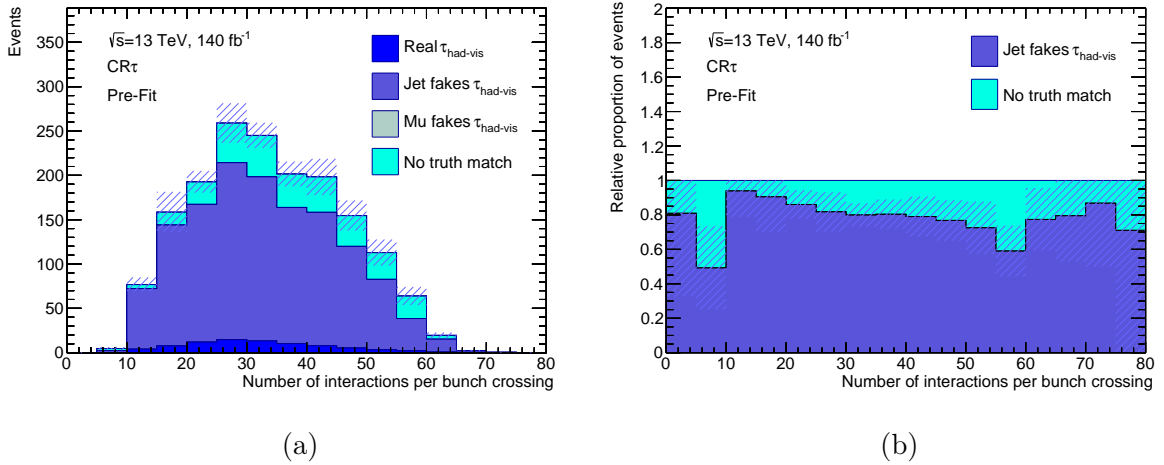


Figure 6.9: Distribution of (a) number of interaction vertices in each event and (b) relative fraction of unknown objects faking  $\tau_{\text{had-vis}}$  as a function of this variable in  $\text{CR}\tau$ . Events are classified according to whether the  $\tau_{\text{had-vis}}$  is truth-matched to a real  $\tau$  lepton, a jet, a muon, or is not truth matched. The hatched band represents the MC statistical uncertainty.

Muons can be misidentified as  $\tau_{\text{had-vis}}$  candidates if they deposit a large amount of energy in the hadronic calorimeter. A small contribution of muons faking  $\tau_{\text{had-vis}}$  is present in simulation in the SR, amounting to 7.8% of events. This fake process is not seen in  $\text{CR}\tau$  and would be expected to require different correction factors to those used for misidentified jets. The correction factors derived in  $\text{CR}\tau$  are therefore only applied to jets faking  $\tau_{\text{had-vis}}$ . Since the muon faking  $\tau_{\text{had-vis}}$  background is only a small contribution to the SR it is modelled by MC simulation.

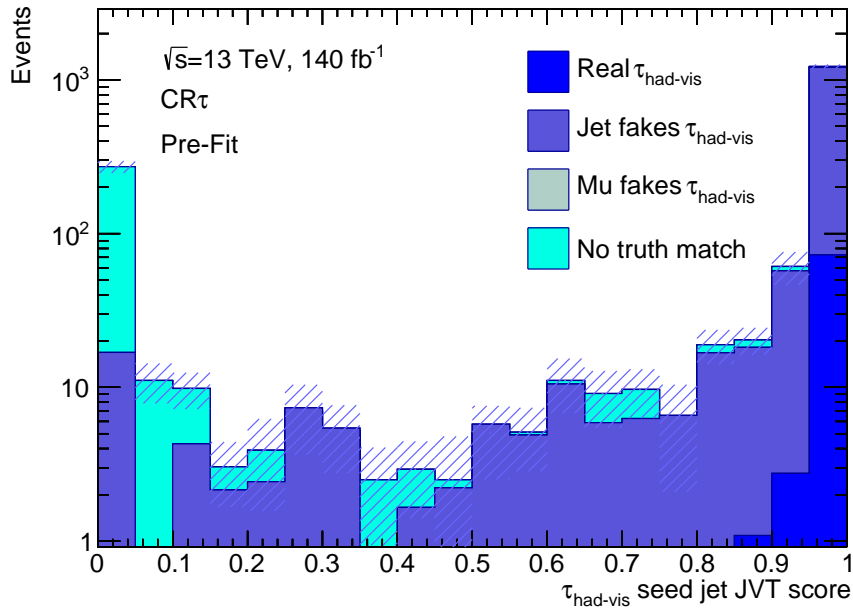


Figure 6.10: Distribution of JVT score for the jet seeding  $\tau_{\text{had-vis}}$  reconstruction in CR $\tau$ . Jets with a JVT score of 1 are likely to originate from a hard-scatter interaction while a score of 0 indicates the jet is more likely to have originated from a pileup interaction. Events are classified according to whether the  $\tau_{\text{had-vis}}$  is truth-matched to a real  $\tau$  lepton, a jet, a muon, or is not truth matched. The hatched band represents the MC statistical uncertainty.

## 6.5 Fake $\tau_{\text{had-vis}}$ estimation

A scale factor method is used to estimate the background from fake  $\tau_{\text{had-vis}}$ . This involves applying multiplicative factors to the MC simulation to correct for any mismodelling of the fake  $\tau_{\text{had-vis}}$  background.

The method requires the definition of a control region in which the scale factors (SFs) are derived. Once these regions are defined, the fake  $\tau_{\text{had-vis}}$  background in data is estimated by subtracting events with true  $\tau_{\text{had-vis}}$  in MC from the data. It is desirable that the CR is sufficiently fake-enriched that the uncertainty from the subtraction of the true  $\tau_{\text{had-vis}}$  component is low. SFs are then derived from the fakes in data measured in the CR as follows:

$$SF_i = \frac{N_{\text{data},i}^{\text{CR}} - N_{\text{MC,non-fake},i}^{\text{CR}}}{N_{\text{MC,fake},i}^{\text{CR}}} \quad (6.4)$$

The index  $i$  denotes a particular bin in a distribution, since SFs are binned in kinematic variables of the fake object. The estimated yield in data in the SR is then found by applying the SFs to events in simulation with a fake  $\tau_{\text{had-vis}}$  candidate:

$$N_{\text{data,fakes},i}^{\text{SR}} = SF_i \times N_{\text{MC,fake},i}^{\text{SR}} \quad (6.5)$$

The SFs are binned in  $\tau_{\text{had-vis}}$  track multiplicity and in the width of the jet used to seed the  $\tau_{\text{had-vis}}$  reconstruction. The jet width,  $w$ , is defined as:

$$w = \frac{\sum_j \Delta R^j p_T^j}{\sum_j p_T^j} \quad (6.6)$$

where  $j$  denotes each jet constituent and  $\Delta R^j$  is the radial distance between each constituent and the centre of the jet. Separate identification algorithms are used for 1-prong and 3-prong  $\tau_{\text{had-vis}}$  which could lead to differences in the probability for jets to be misidentified as  $\tau_{\text{had-vis}}$ . The parametrisation in jet width is intended to capture potential mismodelling of the quark/gluon fractions of jets faking  $\tau_{\text{had-vis}}$  since gluon-initiated jets are expected to have

a larger width than those initiated by quarks [185]. This binning will also account for any small differences in quark-gluon fractions between the SR and  $\text{CR}\tau$ . The jet width and track multiplicity distributions in  $\text{CR}\tau$  can be seen in Figs. 6.11 and 6.12.

A previous implementation of the method used the  $p_T$  of the  $\tau_{\text{had-vis}}$  candidate to derive SFs instead of jet width. Within the statistical uncertainties on the resulting fake estimation, these parametrisations were seen to be completely consistent. Other variables, including the angular separation between the  $\tau_{\text{had-vis}}$  candidate and muons in the event, have also been examined to check for further kinematic dependencies of the SFs. In general, the values of the derived SFs in these cases do not differ significantly from an inclusive (unbinned) SF so no further kinematic dependence is considered; plots of these SFs can be seen in Appendix C.

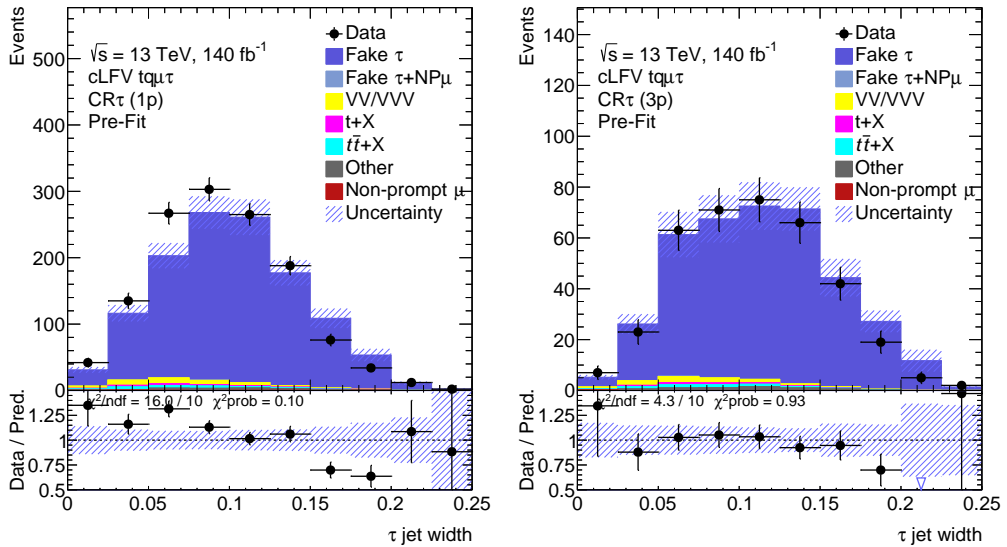


Figure 6.11: Distribution of jet width in data and MC in  $\text{CR}\tau$  before application of fake  $\tau_{\text{had-vis}}$  SFs for 1-prong and 3-prong  $\tau_{\text{had-vis}}$ . The uncertainty band includes the statistical and systematic uncertainties on the background prediction.

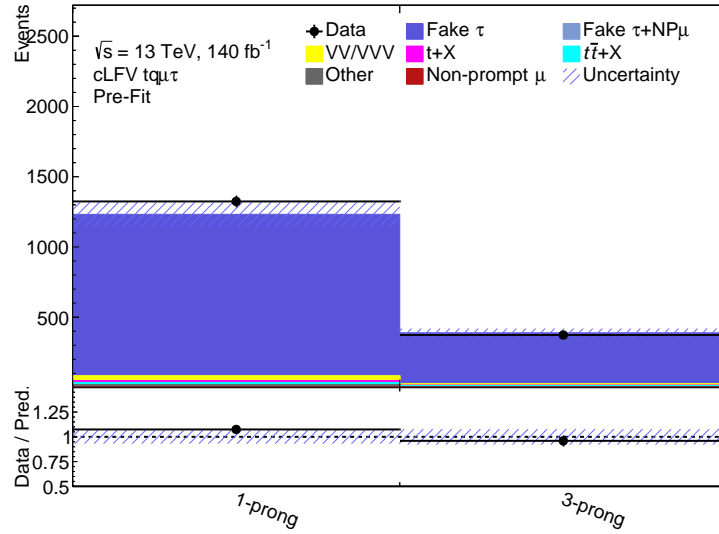


Figure 6.12: Number of  $\tau_{\text{had-vis}}$  with 1-prong and 3-prong in data and MC in  $\text{CR}\tau$  before application of fake  $\tau_{\text{had-vis}}$  SFs. The uncertainty band includes the statistical and systematic uncertainties on the background prediction.

Fig. 6.13 shows the distributions from which the SFs are derived. The distribution of data in  $\text{CR}\tau$  after subtraction of the true  $\tau_{\text{had-vis}}$  background according to MC simulation is labelled “data fakes”, while the fake  $\tau_{\text{had-vis}}$  distribution according to simulation is labelled “MC fakes”. The derived SFs can be seen in Fig. 6.14a and in Table 6.10. Finally, the distribution of fake  $\tau_{\text{had-vis}}$  in the SR before and after the application of SFs can be seen in Fig. 6.14b. Uncertainties on the SF are discussed in Section 6.7.4 but take into account the statistical uncertainties on the SFs as well as sources of modelling and instrumental uncertainties on the true and fake  $\tau_{\text{had-vis}}$  MC components in  $\text{CR}\tau$  and the SR.

During the development of the analysis a fake factor method was also implemented to estimate the fake  $\tau_{\text{had-vis}}$  background. This is similar to the SF method but does not use the MC prediction of the fake  $\tau_{\text{had-vis}}$  background at all. As for the SF method, the true  $\tau_{\text{had-vis}}$  background according to MC is subtracted from data in  $\text{CR}\tau$  to obtain a distribution of fake  $\tau_{\text{had-vis}}$  in data. By inverting the  $\tau_{\text{had-vis}}$  identification criteria to form an orthogonal region,

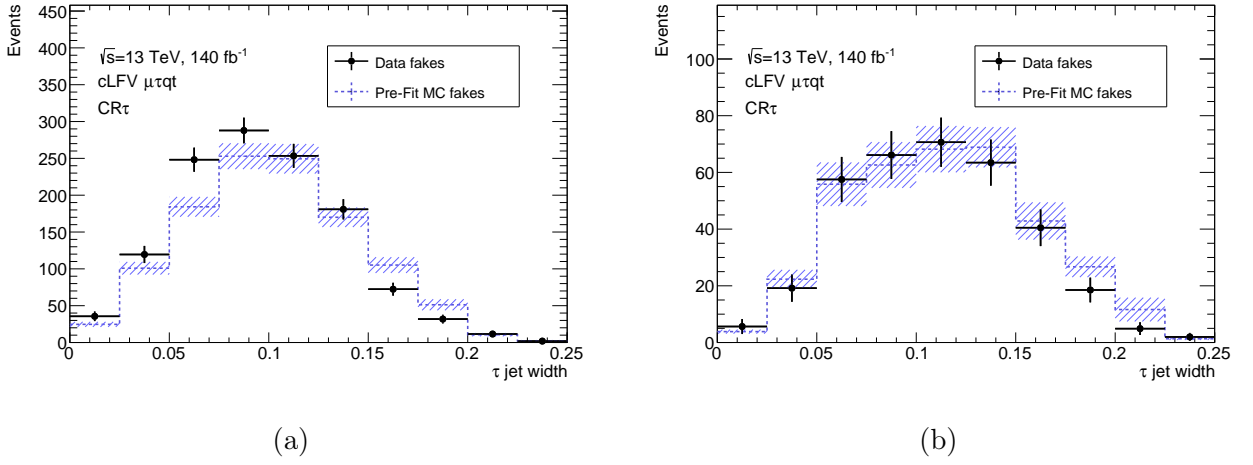


Figure 6.13: Distribution of data in  $CR\tau$  after subtraction of the true  $\tau_{\text{had-vis}}$  background in MC, along with MC fake  $\tau_{\text{had-vis}}$  distribution, for  $\tau_{\text{had-vis}}$  with (a) one and (b) three charged tracks. The hatched band indicates the MC statistical uncertainty.

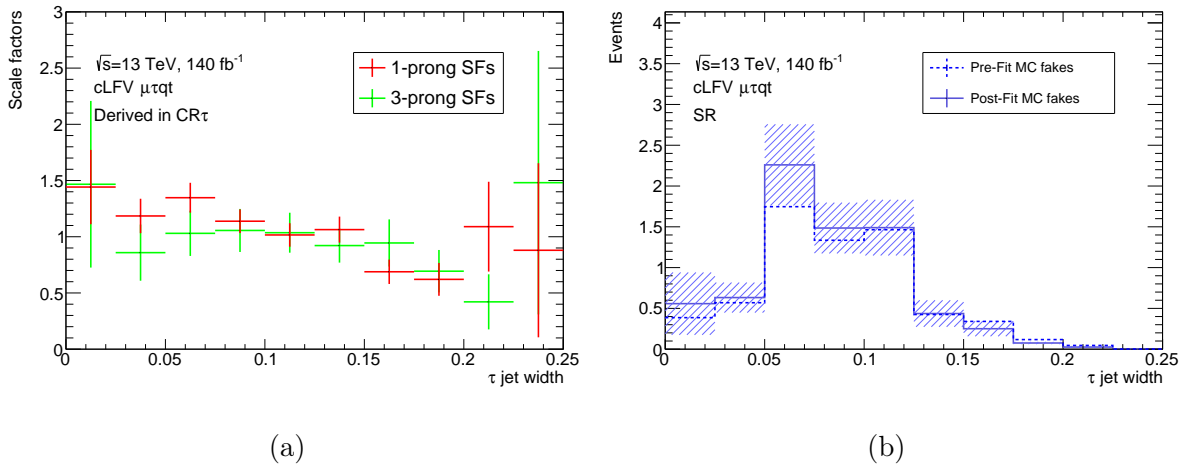


Figure 6.14: Fake  $\tau_{\text{had-vis}}$  SFs binned in jet width shown for  $\tau_{\text{had-vis}}$  with one and three charged tracks (a); fake  $\tau_{\text{had-vis}}$  estimation in the SR before and after application of SFs (b). The hatched band indicates the MC statistical uncertainty.

Table 6.10: Values of fake  $\tau_{\text{had-vis}}$  SFs binned in jet width and track multiplicity and associated statistical uncertainty.

Jet width	SF values	
	1-prong	3-prong
0.000-0.025	1.44±0.33	1.46±0.74
0.025-0.050	1.18±0.15	0.85±0.24
0.050-0.075	1.34±0.13	1.03±0.20
0.075-0.100	1.13±0.10	1.05±0.19
0.100-0.125	1.01±0.10	1.03±0.17
0.125-0.150	1.06±0.11	0.92±0.15
0.150-0.175	0.68±0.10	0.94±0.20
0.175-0.200	0.62±0.14	0.69±0.18
0.200-0.225	1.08±0.39	0.42±0.24
0.225-0.250	0.87±0.77	1.5±1.2

fake factors are defined as the ratio of the “data fakes” in  $\text{CR}\tau$  to those in the inverted region. The fake factors can then be used to estimate the fake  $\tau_{\text{had-vis}}$  contribution to the SR by inverting the  $\tau_{\text{had-vis}}$  identification in the SR. The two methods were found to give consistent estimations of the fake  $\tau_{\text{had-vis}}$  background within the respective statistical uncertainties. Due to the low event yield found when inverting the  $\tau_{\text{had-vis}}$  identification requirements in the SR, the statistical uncertainty on the fake estimation from the fake factor method is relatively large compared to that from the SF method.

## 6.6 Non-prompt muon estimation

The rate of the non-prompt muon background is corrected by including  $CRt\bar{t}\mu$  in the profile likelihood fit used to extract the signal normalisation. A template method is employed in which an unconstrained normalisation factor is included to allow the normalisation of this background to float in the fit, while the kinematics are taken from simulation. By including the fake estimation in the profile likelihood fit, the treatment of the uncertainty in the fake estimation procedure is deferred to the fit machinery, as all systematics are defined as nuisance parameters.

To implement the template fit this normalisation factor,  $k(\text{NP}\mu)$ , is applied to all events with non-prompt muons, including those that also feature a fake  $\tau_{\text{had-vis}}$ . Events with fake  $\tau_{\text{had-vis}}$  are corrected by the SFs discussed in Section 6.5 before the profile likelihood fit is performed. The results of the non-prompt muon background estimation will be discussed together with the fit setup in Section 7.1. During the development of the analysis, the fake factor method was investigated as an alternative non-prompt muon estimation technique. The background estimates with these two methods were seen to be consistent within uncertainties and the template method was found to provide a greater expected sensitivity to the signal process.

## 6.7 Systematic uncertainties

This section describes the sources of systematic uncertainty considered in the analysis. Experimental uncertainties result from imperfect knowledge of the detector and collision conditions, as well as the propagated uncertainties from the calibration of physics objects. Theoretical uncertainties relate to the modelling of SM background processes to the search, including the calculation of cross-sections and the configuration of MC generators. These uncertainties can affect both the shape and normalisation of signal and background processes and are included as nuisance parameters in the profile likelihood fit, which will be discussed in Section 7.1.

### 6.7.1 Experimental uncertainties

**Luminosity:** The uncertainty on the integrated luminosity delivered to the ATLAS detector in Run 2 is 0.83%, calculated as described in Ref. [5] using the LUCID-2 detector for primary luminosity measurements.

**Pileup:** Uncertainties on the scale factors used to correct the pile-up distribution in MC samples to match that measured in the data are considered. Scale factors are applied separately for 2015+2016, 2017 and 2018 MC samples.

**Lepton reconstruction efficiencies:** The scale factors used to correct lepton reconstruction efficiencies are derived in tag-and-probe analyses, as discussed in Section 5.3, and carry uncertainties. For electrons, individual nuisance parameters are considered for uncertainties on identification, isolation, reconstruction and trigger scale factors [106, 108]. For muons, each of the identification, isolation, track-to-vertex association and trigger efficiencies have separate

statistical and systematic uncertainties for which nuisance parameters are assigned [109, 111]. Scale factors correct for efficiency differences between simulation and data resulting from  $\tau_{\text{had-vis}}$  reconstruction, identification and electron-rejection criteria [125, 128]. The associated uncertainties are considered as a single NP for reconstruction and ten NPs for identification covering different  $p_T$  ranges for 1-prong and 3-prong  $\tau_{\text{had-vis}}$ . Three NPs are assigned for electron-rejection scale factors accounting for the  $\tau_{\text{had-vis}}$  efficiency and true electron misidentification efficiency.

**Lepton energy/momentum scales:** Corrections are applied to simulation to account for differences in lepton energy/momentum scale and resolution between data and MC. Two NPs are assigned to electron scale and resolution uncertainties [106, 107], while for muons four NPs are assigned, with separate uncertainties for ID and MS track resolution [109, 110]. Uncertainties in the calibration of the tau energy scale are accounted for by five NPs based on the tag-and-probe measurement described in Refs. [125, 127].

**Jet energy scale and resolution:** A significant number of NPs result from the JES calibration which depends on the  $p_T$  and  $\eta$  of the reconstructed jets. Unless an analysis is particularly sensitive to JES is unnecessary to consider each of these NPs individually. Therefore the *category reduction* scheme presented in Ref. [116] is employed which combines multiple NPs into 30 independent components. Similarly, the large number of NPs resulting from the JER calibration are reduced to a total of thirteen.

**Jet vertex tagger:** A combined statistical and systematic uncertainty on scale factors applied to correct efficiency differences in data and simulation after the application of the JVT is considered [117]. SFs were derived using a tag-and-probe analysis in  $Z \rightarrow \mu\mu$  events using a selection with  $|\Delta\phi(Z, \text{jet})| > 2.8$  to measure the efficiency for hard-scatter jets. The

systematic uncertainty accounts for efficiency differences observed between MC samples produced with SHERPA and POWHEG+PYTHIA 8 as well as mismodelling in the  $|\Delta\phi(Z, \text{jet})|$  distribution.

**Flavour-tagging uncertainties:** Nineteen nuisance parameters are considered to account for uncertainties in the correction of  $b$ -tagging efficiency differences between data and simulation. Efficiencies are derived in samples of  $t\bar{t}$  events for  $b$ -jets and  $c$ -jets or  $Z$ +jets events for light-flavour jets [119–121]. The NPs result from a reduction in the number of systematic uncertainties, using the same technique as for the JES uncertainties, as discussed in Ref. [186]. The result is nine NPs for tagging  $b$ -jets, four NPs each for the mistagging of  $c$ -jets and light-flavour jets, as well as two NPs for the extrapolation of SFs to high  $p_T$ .

**MC statistical uncertainty:** The finite number of simulated events in the MC samples contributes further systematic uncertainty. This results in two or three NPs for each bin used in the profile likelihood fit; one combines the MC statistical uncertainty from all SM background processes, while additional NPs account for the MC statistical uncertainty of each signal process.

## 6.7.2 Theoretical uncertainties

The modelling of signal and SM background processes introduces systematic uncertainties. These are typically evaluated by the use of alternative MC samples or by the application of alternative MC generator weights corresponding to a variation of the nominal generator setup. Modelling uncertainties are considered for the signal processes and the dominant background processes shown in Table 6.3. They are not included for triboson processes or for the small background contributions discussed in Section 6.3.8 and these are instead assigned

large normalisation uncertainties, discussed below in Section 6.7.3.

Particular attention is given to the modelling of the  $t\bar{t}$  process to account for the observation that the POWHEG generator predicts a harder top quark  $p_T$  distribution than observed in data [187], and because this is the largest background contribution to the SR. Close attention is also given to the  $t\bar{t} + X$  processes which are the dominant contribution to the most signal-enriched bin of the SR discriminant used in the profile likelihood fit. In some cases not all uncertainties are considered for all processes due to the availability of alternative MC samples or weights. Nevertheless, as will be discussed in Section 7.1, the analysis is seen to be heavily limited by statistics and the absence of these systematic uncertainties is not expected to affect the sensitivity.

**Scale variations:** Variations of the renormalisation and factorisation scales,  $\mu_R$  and  $\mu_F$ , are considered to account for missing higher order terms in the ME calculation. For the majority of processes,  $\mu_R$  and  $\mu_F$  are varied independently by factors of two around their original values to produce separate NPs; this procedure is used for the signal samples,  $t\bar{t}$ ,  $tW$ ,  $t\bar{t}H$ ,  $t\bar{t}W$  and  $t\bar{t}Z$ . For the weak boson processes, seven variations of  $\mu_R$  and  $\mu_F$  by factors of two are evaluated, considering cases where these are changed both independently and simultaneously but excluding variations of  $\mu_R$  and  $\mu_F$  in opposite directions. An envelope around the largest shifts is used to assign a single NP.

**PDF set:** Uncertainties entering the PDF set used in the generation of the sample are considered. Where possible these are evaluated using the PDF4LHC prescription [86]: a set of 30 Hessian eigenvariations are considered, each of which is assigned a NP which is profiled in the fit. For EFT signal,  $t\bar{t}Z$  and weak boson samples, however, PDF uncertainties are estimated using sets with 100 variations; the standard deviation of this set is used to define a symmetrised uncertainty. The generator weights needed to evaluate the PDF uncertainty

are missing from the  $Z \rightarrow \mu\mu$  samples and therefore this contribution is neglected. The  $Z \rightarrow \mu\mu$  process only provides a significant contribution to the fake  $\tau_{\text{had-vis}}$  control region. Since events with a fake  $\tau_{\text{had-vis}}$  only make up a small proportion of the SR this effect has not been considered further.

**$\alpha_S$ :** For the  $t\bar{t}$  process the uncertainty arising from the value of  $\alpha_S$  is estimated using PDF sets evaluated with  $\alpha_S(M_Z) = 0.117$  and  $\alpha_S(M_Z) = 0.119$ . The uncertainty is evaluated relative to the nominal value of  $\alpha_S(M_Z) = 0.118$ ; it is seen to have a negligible impact on the analysis and has therefore not been considered for other background processes.

**Matching of NLO calculation to parton shower for  $t\bar{t}$ :** Beyond LO, matching the parton-level event from the ME generator to the parton shower generator is complicated by the need to avoid double-counting higher order corrections included in the ME calculation. The nominal  $t\bar{t}$  sample uses the POWHEG matching scheme [89–91]. The uncertainty introduced by the matching procedure is evaluated by comparing a  $t\bar{t}$  sample generated by POWHEG+HERWIG 7.1.3 to one generated by AMC@NLO+HERWIG 7.1.3 which uses a different matching method, the MC@NLO scheme [188, 189].

**Additional  $t\bar{t}$  radiation modelling:** When matching the parton-level events to the parton shower at NLO with the POWHEG method, a scale,  $h_{\text{damp}}$ , must be chosen to regulate the  $p_T$  of the hardest emission, which is described by the ME calculation [159]. To evaluate the uncertainty introduced by the choice of  $h_{\text{damp}}$ , an alternative POWHEG+PYTHIA 8  $t\bar{t}$  sample with  $h_{\text{damp}} = 3.0 m_{\text{top}}$  is compared to the nominal ( $h_{\text{damp}} = 1.5 m_{\text{top}}$ )<sup>4</sup>.

---

<sup>4</sup>As would be expected, the  $p_T$  of the hardest additional emission beyond the lowest order process is seen to be slightly higher for the sample with a larger value of  $h_{\text{damp}}$ .

**Interference between  $t\bar{t}$  and  $tW$ :** As was discussed in Section 6.3.5, the  $tW$  sample neglects interference with  $t\bar{t}$  as a consequence of the method used to remove overlap with  $t\bar{t}$  diagrams [159, 168]. To understand the sensitivity to the missing interference contribution, the nominal sample is compared to a POWHEG+PYTHIA 8  $tW$  sample using a diagram subtraction scheme which retains this contribution [159]. The difference between these two samples is taken as an additional uncertainty intended to encode the size of the interference effects.

**Initial- and final-state radiation:** The uncertainty arising from the modelling of ISR is evaluated using variations of the `Var3c` parameter in the A14 PYTHIA tune, corresponding to variations of  $\alpha_S$  in the initial-state shower [190]. This uncertainty is considered for the EFT and LQ signal processes, as well as the  $t\bar{t}$ ,  $tW$ ,  $t\bar{t}H$  and  $t\bar{t}Z$  backgrounds. Modelling of FSR is evaluated using weights corresponding to variations of  $\mu_R$  for QCD emissions in the final state shower. This is considered for both EFT and LQ signal processes, as well as the  $t\bar{t}$ ,  $tW$  and  $t\bar{t}H$  backgrounds.

**Parton shower and hadronisation modelling:** To estimate the uncertainty relating to the choice of parton shower and hadronisation model, MC samples showered with PYTHIA are compared to those showered with HERWIG. These two generators use different frameworks for the evolution of the shower as well as different models for the hadronisation process. A comparison of the two samples provides an assessment of the sensitivity to this choice of modelling.

- For  $t\bar{t}$  and  $t\bar{t}H$  the nominal sample showered with PYTHIA 8 is compared to an equivalent sample showered with HERWIG 7.1 using the same ME generator settings. The alternative showering uses the HERWIG 7.1 set of tuned parameters along with the MMHT LO PDF set [191].

- Nominal EFT signal samples generated with MG\_AMC@NLO+PYTHIA 8 are compared to samples generated with MG\_AMC@NLO+HERWIG 7.1. It has been seen, however, that the branching fractions for  $\tau$  lepton decays are incorrect in the production signal samples produced with HERWIG. A reweighting procedure has therefore been performed using MC truth information to correct for this mismodelling, in order to avoid convoluting effects due to the mismodelling of tau branching fractions with genuine differences in parton shower models. The reweighting procedure is discussed further in Appendix B.
- For the  $t\bar{t}Z$  process a set of HERWIG 7.2 samples were available with the same version of MG\_AMC@NLO as the nominal  $t\bar{t}Z$  samples used in this analysis. However, these samples are known to mismodel tau polarisation. Therefore an older set of MG\_AMC@NLO+HERWIG 7.0  $t\bar{t}Z$  samples is used and compared to a set of MG\_AMC@NLO+PYTHIA 8 samples produced with the same version of MG\_AMC@NLO to ensure a like-for-like comparison.

**$t\bar{t}W$  generator uncertainty:** A combined generator uncertainty is evaluated separately for the QCD and EW  $t\bar{t}W$  samples. This is motivated by the mild tension between measured values of the  $t\bar{t}W$  cross-section and theoretical predictions, as summarised in Ref. [192], and in particular by the studies shown in Ref. [193]. The latest ATLAS measurement [194] shows a  $2.1\sigma$  deviation from the theoretical reference cross-section agreed by the LHC Top working group. The nominal QCD sample (SHERPA 2.2.10) is compared to a sample generated with MG\_AMC@NLO+PYTHIA 8 using FxFx merging. The nominal EW sample (SHERPA 2.2.10) is compared to a LO MG\_AMC@NLO+PYTHIA 8. This follows the procedure used in Ref. [194].

For modelling systematics evaluated via the use of alternative MC generator weights, the sum of weights used to normalise the sample to the correct luminosity is recalculated

to avoid double-counting cross-section uncertainties. This is to take into account shape and acceptance effects from sources of modelling uncertainty. Normalisation-only cross-section uncertainties are included separately as discussed below.

### 6.7.3 Cross-section uncertainties

Uncertainties on the cross-section of background processes are summarised below:

- The uncertainty on the cross-section of  $t\bar{t}$  production is found to be 6.1% by combining in quadrature the following effects: independent variations of  $\mu_R$  and  $\mu_F$  by factors of two; variations in the PDF and  $\alpha_S$  using the PDF4LHC prescription [86] with the MSTW2008 68% CL NNLO [195, 196], CT10 NNLO [197, 198] and NNPDF2.3 5f FFN [97] PDF sets; and the effect of a variation of  $\pm 1$  GeV in the top quark mass [199].
- The dominant contributions to processes with a single top quark are from  $tW$  and  $tZq$  production. For  $tW$  production, independent variations of  $\mu_R$  and  $\mu_F$  by factors of two are combined in quadrature with PDF uncertainties using the MSTW2008 90% CL NNLOPDF set [200] based on the calculations in Refs. [201, 202], yielding an uncertainty of 5.3%. The cross-section uncertainty for  $tZq$  production is found to be +5.3/-1.6% as reported in Ref. [203], combining in quadrature the effects of scale variations and PDF uncertainties. A cross-section uncertainty of 5.3% is therefore applied to processes with a single top quark.
- Cross-section uncertainties of 12% and 10%, respectively, are applied to the  $t\bar{t}Z$  and  $t\bar{t}H$  processes, based on calculations reported in Ref. [169]. The cross-sections for these processes are consistent with more recent calculations documented in Ref. [204] for which the theoretical uncertainties are seen to be reduced.
- A larger uncertainty of 30% is applied to diboson processes for which discrepancies

between data and SHERPA 2.2.2 MC samples have been observed in jet multiplicity distributions [205].

- A 50% cross-section uncertainty is applied to the  $t\bar{t}W$  process to account for the significant difference observed between the theoretical prediction of the cross-section<sup>5</sup> for this process and the latest measured value [194, 206, 207].
- A 50% normalisation uncertainty is applied to backgrounds in the “Other SM” category, for which the largest contributions are  $t\bar{t}WW$ ,  $t\bar{t}t\bar{t}$ ,  $ll\nu\nu jj$  and  $t\bar{t}t$ .
- A 50% normalisation uncertainty is also applied to the small contribution from processes which enter the event selection by the presence of an electron from a photon conversion or non-prompt electrons from heavy flavour decays. This includes  $t\bar{t}\gamma$ ,  $Z\gamma$ , as well as  $t\bar{t}$  or  $Z$ +jets events with a non-prompt electron.

#### 6.7.4 Fake estimation uncertainties

**Non-prompt muon estimation:** estimation of this background is performed simultaneously with the profile likelihood fit. Therefore all of the above sources of uncertainty are accounted for in the same manner as the prompt backgrounds.

**Fake  $\tau_{\text{had-vis}}$  estimation:** each of the instrumental and modelling systematics described above is propagated through the scale factor method. Systematic variations for each source are applied to MC samples in all analysis regions and the derivation and application of SFs is repeated.

As discussed in Section 6.4.6 the quark-gluon composition of fake  $\tau_{\text{had-vis}}$  is seen to be

---

<sup>5</sup>The cross-section used to normalise the  $t\bar{t}W$  process follows the current LHC Top working group recommendation of 722.4 fb based on Ref. [206].

consistent between  $CR_\tau$  and the SR; no additional uncertainties are included to cover any differences in fake composition. This is true also for the non-prompt muon estimation. The fake  $\tau_{\text{had-vis}}$  SFs should be binned in all kinematic variables to which they are sensitive. Due to the limited statistics of the SR, it is not feasible to bin the SFs in additional variables beyond jet width and track multiplicity. However, binning in additional variables was tested, as discussed in Section 6.5; no significant kinematic dependencies were seen with alternative parametrisations so no additional uncertainty on the choice of parametrisation of the SFs is included.

# Chapter 7

## CLFV search results

### 7.1 Statistical analysis framework

The signal strength of a possible CLFV  $t\mu\tau u_k$  interaction is extracted by a binned profile likelihood fit. The observed data are compared to a model of the expected signal and SM background and the most likely value of the signal strength is estimated using a maximum likelihood approach.

A likelihood function is constructed which is related to the probability for observing a particular data distribution as a function of a set of parameters. By maximising the likelihood function the maximum-likelihood estimates of the parameter space are found. In a simple experiment counting the number of signal events,  $n_S$ , over a precisely known number of background events,  $n_B$ , in which the number of observed events is  $n_{obs}$ , the likelihood function is given by the Poisson distribution with mean  $n_S + n_B$ . In this case the only free parameter is  $n_S$ . Uncertainties on the measurement are incorporated by introducing additional nuisance parameters (NPs),  $\theta$ , into the likelihood which can affect the values of  $n_S$  and  $n_B$ . Under the

assumption that each parameter  $\theta$  is Gaussian-distributed, an associated “constraint” term is included which reduces the likelihood for values which deviate from the pre-fit value,  $\theta_0$ . As the fitted NP values,  $\hat{\theta}$ , are not of interest to the measurement, these are “profiled” by finding the most likely values of each for a given value of the parameter of interest (POI),  $\hat{\theta}$ , to produce a profile likelihood

$$\mathcal{L}(\mathbf{x}; \mu_{\text{CLFV}}) = \mathcal{L}(\mathbf{x}; \mu_{\text{CLFV}}, \hat{\theta}), \quad (7.1)$$

where  $\mathbf{x}$  is the number of events observed in each bin of the fitted distribution and  $\mu_{\text{CLFV}}$  is a multiplicative factor which controls the signal normalisation relative to a chosen reference normalisation.

The statistical analysis is performed using a profile likelihood fit framework, known as *TRExFitter*, developed by members of the ATLAS collaboration [208]. *TRExFitter* uses the *HistFactory* format to build statistical models in *RooFit* and employs *RooStats* to perform statistical tests on the resulting model [209, 210]. NPs are included to capture the effects of each of the systematic uncertainties discussed in Section 6.7.

### 7.1.1 Parameter estimation

SR and  $\text{CR}t\bar{t}\mu$  are the analysis regions entering the fit.  $\text{VR}\mu$  is also included in the fit setup but serves only as a spectator region to validate the non-prompt muon background estimation. The POI is the signal strength modifier,  $\mu_{\text{CLFV}}$ , which is a normalisation factor applied to the signal sample. For the nominal fit it is assumed that all of the SMEFT operators capable of introducing a CLFV  $t\mu\tau u_k$  interaction, as shown in Table 6.1, contribute. The pre-fit signal normalisation corresponds to a Wilson coefficient value of  $|c| = 0.3$  for all EFT operators for  $\Lambda = 1$  TeV.

As discussed in Section 6.4.5, the normalisation of the non-prompt muon background

is corrected in the fit by floating an unconstrained normalisation factor,  $k(\text{NP}\mu)$ , which forms an additional NP. MC events with fake  $\tau_{\text{had-vis}}$  are corrected by the scale factors discussed in Section 6.5 before being included in the fit setup; this applies to events with a fake  $\tau_{\text{had-vis}}$  and two prompt muons as well as those with a fake  $\tau_{\text{had-vis}}$ , one non-prompt muon and one prompt muon. The best-fit signal strength is extracted by a signal-plus-background fit to the SR and  $\text{CR}t\bar{t}\mu$ .

To evaluate the performance of the fit and calculate expected exclusion limits on the signal process, two fits have been run in which the data in the SR are not used. In these fits, “blinding” is applied to any bin in the fit setup with a signal-to-background ratio of greater than 5% but this is only seen in the SR. In place of real ATLAS data, an “Asimov” dataset is used. An Asimov dataset is constructed as the exact sum of all backgrounds in each bin according to simulation, using the expected values for all NPs; this construction assumes that the observed data match the background model exactly.

- A full Asimov fit uses an Asimov dataset in all regions to check the expected sensitivity of the fit and to ensure that there are no spurious NP constraints.
- A mixed data and Asimov setup is used to understand the effect of including data in  $\text{CR}t\bar{t}\mu$  while the SR remains blinded. This fit is also used to obtain a preliminary estimation of the non-prompt muon background. In this case the fit is handled in two stages. First a background-only fit is performed to data in  $\text{CR}t\bar{t}\mu$  which finds best-fit values for  $k(\text{NP}\mu)$  and each of the other NPs. An Asimov dataset is then constructed for the SR using the values of the NPs found in the first step. A second fit is then performed using this modified Asimov dataset in the SR and data in  $\text{CR}t\bar{t}\mu$ .

No signal is included in the construction of the Asimov datasets, hence the best-fit value of  $\mu_{\text{CLFV}}$  should be found to be zero in both cases.

### 7.1.2 Nuisance parameter treatment

For each NP in the fit, shape and normalisation terms are included in the likelihood. However, some of these systematic uncertainties correspond to very small differences in the fitted distributions. A pruning procedure is applied to remove NPs with a very small impact on the yield or shape of a process from the fit. This is done to simplify the fit model, to reduce the computational time to run the fit and ensure its stability. Pruning is applied per sample and per region and is applied separately to the shape and normalisation of each NP with the pruning threshold set to 0.2%. The normalisation component of a NP for a given sample which results in a change of more than 0.2% in the expected yield of the sample will be retained. The shape component of a NP is considered if the yield in at least one bin differs from the nominal bin yield by more than 0.2% (when the overall normalisation of the systematic variation is equal to that of the nominal sample).

The default *TRExFitter* algorithm [208] is also applied to the systematic variation templates associated with each NP to reduce the effect of fluctuations resulting from limited MC statistics. Bins in the systematic variation histogram are grouped together until the relative MC statistical uncertainty of the group is below a predefined threshold. The TH1::Smooth function is then used, which employs the ‘353QH twice’ algorithm [211]. To further reduce the impact of fluctuations due to limited MC statistics, a symmetrisation procedure is applied to all instrumental systematic uncertainties. This calculates half the difference in the up and down systematic variations for each bin and applies this value as symmetric up and down variations. Modelling uncertainties are, in general, not symmetrised except in the case where both systematic variations are seen to move in the same direction; in such cases the larger of the two variations is mirrored around the nominal value for each bin. This is done to avoid artificially under-constraining NPs. Additionally, some modelling uncertainties have “one-sided” variations, where samples from two different generators are

compared. For these, the one-sided variation is symmetrised to generate up and down variations, taking the full difference between the two cases as the uncertainty. This procedure may be considered “conservative” but is the standard ATLAS procedure for constructing uncertainties from a comparison of two samples.

### 7.1.3 Extracting limits on the CLFV process

In the absence of a significant observed excess of data over the expected background distribution, limits are set on the maximum presence of signal allowed by the statistical model at a given confidence level (CL). To distinguish between the hypothesis of only background being present and the hypothesis of signal being present alongside the background, a test statistic is constructed. The test statistic is a single number depending on the observed data and is distributed differently under these hypotheses. The profile log likelihood ratio,  $\Lambda(\mu)$ , is frequently used to construct a test statistic in searches for new physics at the LHC [212]:

$$\Lambda(\mu) = -2 \ln \frac{\mathcal{L}(\mu, \hat{\theta})}{\mathcal{L}(\hat{\mu}, \hat{\theta})}. \quad (7.2)$$

In the case of a small signal, it is possible that the test statistic is distributed similarly under both hypotheses which can result in the exclusion of values of  $\mu$  to which there is very little experimental sensitivity. To avoid this situation the “ $CL_s$ ” procedure [213] is employed, in which the signal-plus-background and background-only hypotheses are tested simultaneously. The exclusion limit on the signal process is constructed using a modified  $p$ -value,  $CL_s$ , with the signal-plus-background hypothesis for a given value of  $\mu$  excluded with a confidence level (CL)  $1-\alpha$  if  $CL_s < \alpha$ . For search analyses such as this it is standard to reject hypotheses which are excluded at the 95% CL ( $\alpha = 0.05$ ). By scanning over values of  $\mu$ , the hypothesis test can be inverted and used to find a confidence interval in  $\mu$  which is bounded by the value for which  $CL_s = \alpha$ .

In general the distribution of the test statistic is not known and must be found by sampling many “toy” Monte Carlo (MC) datasets. Since this toy MC approach is computationally expensive, an alternative is to extract the exclusion limits relying on Wilks’ theorem [214]. For a single parameter-of-interest, this states that the test statistic is distributed as a chi-squared distribution with one degree of freedom under the hypothesis of  $\mu = \mu_0$  if  $\mu_0$  is the true value of the  $\mu$ . Wilks’ theorem is valid in the asymptotic limit, where the number of expected events in each bin tends to the infinite. For this analysis, exclusion limits are extracted at 95% confidence level using the  $CL_s$  method under the asymptotic approximation using the profile log likelihood ratio as the test statistic. The validity of using this approximation has been validated by building the distribution of the test statistic using toy datasets. The expected limits extracted using the two approaches were seen to be consistent to within 5%. More details can be found in Appendix D.1.

Using the EFT framework, exclusion limits on the cross-section of the CLFV process, given by  $\mu_{\text{CLFV}}$ , can be translated into constraints on SMEFT Wilson coefficients and on the branching ratio of the decay  $t \rightarrow \mu\tau u_k$ . Eq. (6.3) shows the dependence of the cross-section of the CLFV  $t\bar{t}$  decay process on the Wilson coefficient values for each of the operators in Table 6.1. The cross-section of the  $gu_k \rightarrow t\mu\tau$  process also scales with the square of the Wilson coefficient values for a fixed scale of new physics,  $\Lambda$ . The total cross-section is given by:

$$\sigma_{\text{CLFV}} = \left( \sigma(qg \rightarrow t\mu\tau) + \sigma(pp \rightarrow t(\rightarrow \mu\tau q)\bar{t}) \right) \propto |c|^2. \quad (7.3)$$

An exclusion limit on the modulus squared of the Wilson coefficient,  $|c^{95\%CL}|^2$ , is found using the exclusion limit on the cross-section,  $\sigma^{95\%CL}$ , and the cross-section for a Wilson coefficient value of unity,  $\sigma^{|c|=1.0}$  as

$$\left| c^{95\%CL} \right|^2 = \frac{\sigma^{95\%CL}}{\sigma^{|c|=1.0}}. \quad (7.4)$$

The limit on the modulus of the Wilson coefficient is then obtained trivially as the square

root of this. From the limit on the Wilson coefficient it is straightforward to derive a limit on the branching ratio of the  $t \rightarrow \mu\tau u_k$  decay using Eq. (6.3).

#### 7.1.4 Expected results: full Asimov fit

In this setup the Asimov dataset perfectly matches the background model in all fitted regions. This is used as an initial validation of the fit performance while the mixed data and Asimov fit provides a more useful indication of the expected sensitivity of the analysis.

Pre- and post-fit plots of the two analysis regions included in the fit are shown in Fig. 7.1. It can be seen that, before fitting, the SR is overwhelmed by signal events, arising primarily from the production channel process. Following the fit,  $\mu_{\text{CLFV}}$  is consistent with zero and the background breakdown of these regions can be seen more clearly. Fitted values of the signal strength,  $\mu_{\text{CLFV}}$ , and  $k(\text{NP}\mu)$  can be seen in Fig. 7.2.  $k(\text{NP}\mu)$  is found to be unity since the background model already agrees perfectly with the Asimov data and no scaling is required. The expected limit on the cross-section for the CLFV processes at 95% CL is found to be:

$$\sigma_{\text{CLFV}} < 4.2 \text{ fb} \quad (95\% \text{ CL}).$$

If the pre- and post-fit values of a NP differ it is said to be “pulled”. Since there is already perfect agreement between the background model and the Asimov dataset, no NP pulls are observed for the fit to an Asimov dataset in all regions. In some cases the post-fit NP uncertainty differs from the assigned pre-fit uncertainty and the NP is said to be constrained. Small constraints are seen for the NPs corresponding to  $t\bar{t}$  NLO matching, FSR and the choice of the  $h_{\text{damp}}$  parameter. Constraints on NPs imply that the fit is able to reduce the size of the corresponding uncertainties based on information extracted from the regions provided. This constraining power is likely to be a result of the small correlations

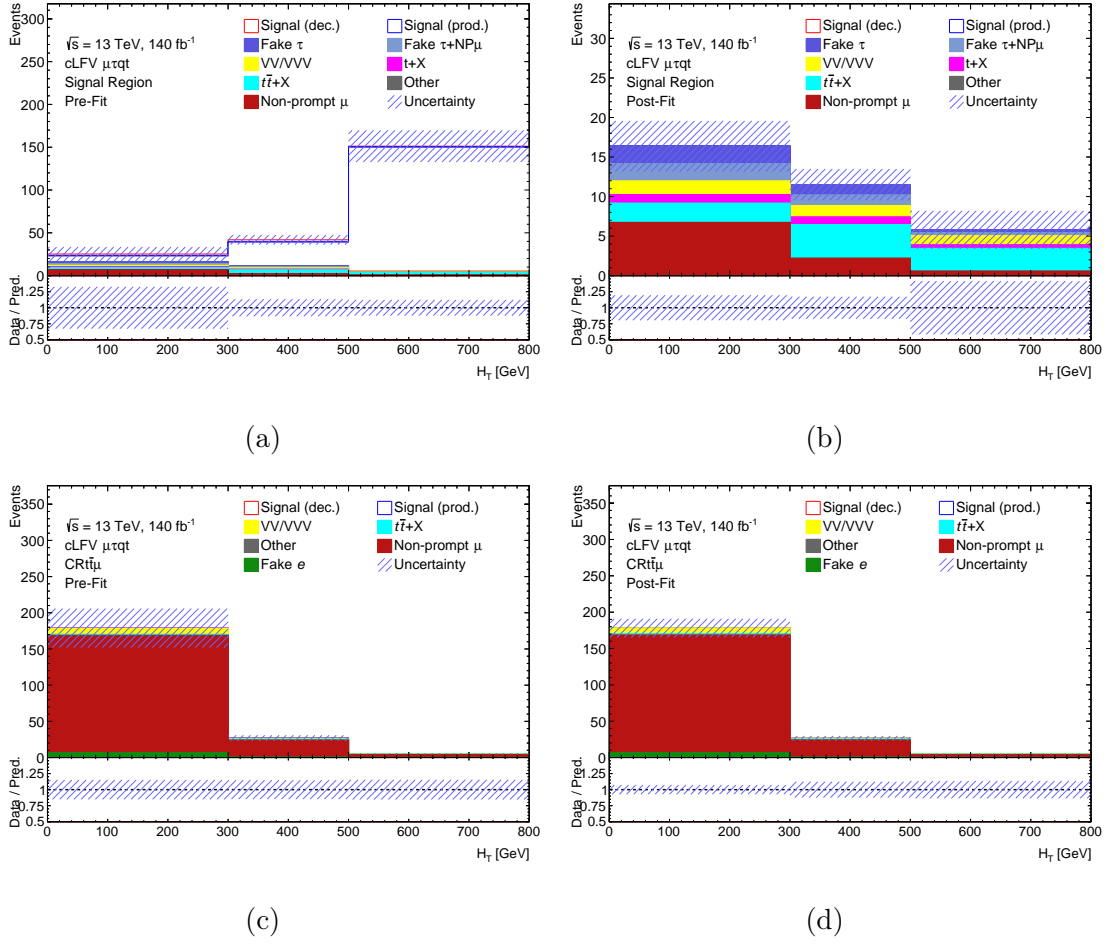


Figure 7.1: Pre-fit (a,c) and post-fit (b,d) plots of the SR and  $CRt\bar{t}\mu$  for signal-plus-background fit to an Asimov dataset in the SR and  $CRt\bar{t}\mu$ . The final bin does not have an upper bound. The uncertainty band includes both the statistical and systematic uncertainties.

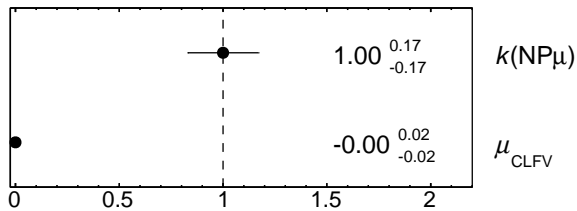


Figure 7.2: Normalisation factors computed in the signal-plus-background fit to an Asimov dataset in the SR and  $CRt\bar{t}\mu$ .

seen between these NPs, shown by the correlation matrix in Fig. 7.3.

Correlations between NPs and the parameter-of-interest,  $\mu_{\text{CLFV}}$ , are determined automatically during the minimisation of the negative log likelihood function. Correlations between significant NPs and  $\mu_{\text{CLFV}}$  are expected as these indicate that varying these parameters has a large impact on the expected signal strength. Large correlations are also seen between  $t\bar{t}$  modelling systematics with large normalisation uncertainties and  $k(\text{NP}\mu)$ , since each of these affect the normalisation of the  $t\bar{t}$  background.  $k(\text{NP}\mu)$  and  $\mu_{\text{CLFV}}$  are expected to be anti-correlated; an increase in  $k(\text{NP}\mu)$  increases the yield of non-prompt muons in the SR. Increasing the expected background yield relative to the (Asimov) data will necessarily reduce the signal strength.

The NLO matching uncertainty is evaluated by comparing  $t\bar{t}$  samples using different matching schemes; the shape and normalisation of the distribution for intermediate values of the NP are unknown and it is therefore undesirable for it to be pulled or constrained. To prevent the reduction in uncertainty arising from the constraint in  $\text{CR}t\bar{t}\mu$  being propagated to the SR, this NP has been decorrelated between analysis regions.

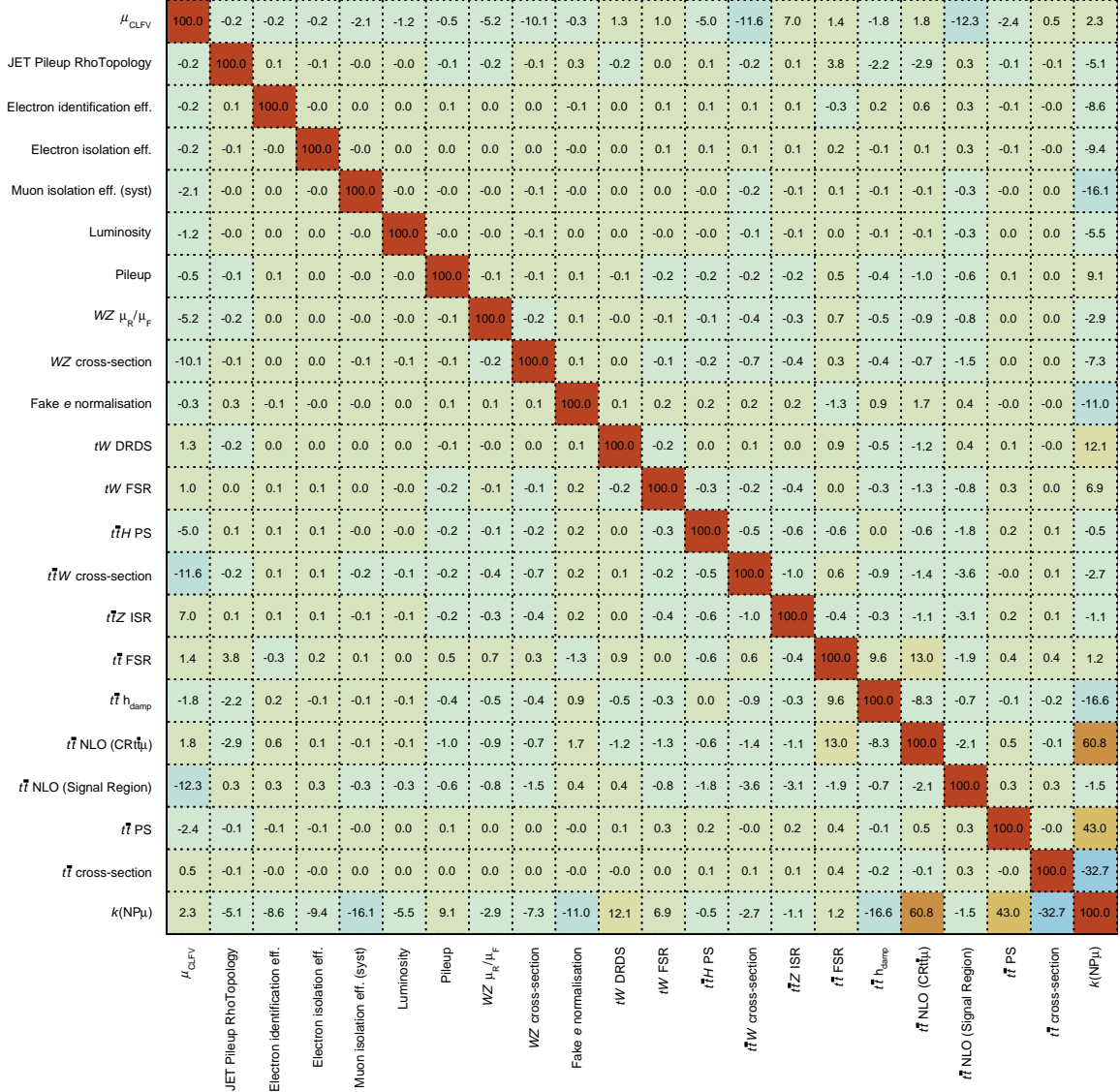


Figure 7.3: Correlation matrix for the signal-plus-background fit to an Asimov dataset. Correlations between NPs and the parameter-of-interest,  $\mu_{\text{CLFV}}$ , are determined automatically during the minimisation of the negative log likelihood function. To improve readability, NPs which are not correlated with any other parameter at the level of 5% are dropped.

### 7.1.5 Expected results: Mixed data and Asimov fit

The mixed data and Asimov fit is used to evaluate the expected sensitivity of the analysis. For this fit, any bin in any region with at least 5% signal contribution remains blinded and the SR is blinded entirely. This setup also provides expected results of the non-prompt muon background estimation. While the value of  $k(\text{NP}\mu)$ , which controls the rate of the non-prompt muon background, may differ slightly when fitted to data in the SR, the sensitivity to this parameter is dominated by  $\text{CR}t\bar{t}\mu$ .

Pre- and post-fit plots of the two analysis regions included in the fit are shown in Fig. 7.4. The best-fit values of  $\mu_{\text{CLFV}}$  and  $k(\text{NP}\mu)$  can be seen in Fig. 7.5; the value of  $k(\text{NP}\mu)$  is found to be consistent with unity. The best-fit value of  $\mu_{\text{CLFV}}$  is compatible with zero and the expected limit on the cross-section for the CLFV processes at 95% CL is found to be:

$$\sigma_{\text{CLFV}} < 4.2 \text{ fb} \quad (95\% \text{ CL}),$$

as for the full Asimov dataset. The limits on  $\mathcal{B}(t \rightarrow \mu\tau q)$  obtained using a full Asimov dataset are compared to the limits using the mixed data and Asimov dataset in Table 7.1.

Table 7.1: Expected upper exclusion limits on the CLFV decay  $\mathcal{B}(t \rightarrow \mu\tau q)$  at 95% CL from fits to an Asimov dataset and to a mixed data and Asimov dataset. In the “stat. only” case no NPs are included in the fit and only the statistical uncertainty is considered; it can be seen that the fit is statistically dominated.

	Upper limits on $\mathcal{B}(t \rightarrow \mu\tau q)$ at 95% CL	
	Stat. only	All systematics
Asimov	$4.6 \times 10^{-7}$	$4.9 \times 10^{-7}$
Mixed data and Asimov	$4.6 \times 10^{-7}$	$4.9 \times 10^{-7}$

The difference between pre- and post-fit values and uncertainties for all NPs are shown in Fig. 7.6. As with the full Asimov fit, the NPs corresponding to  $t\bar{t}$  modelling uncertainties

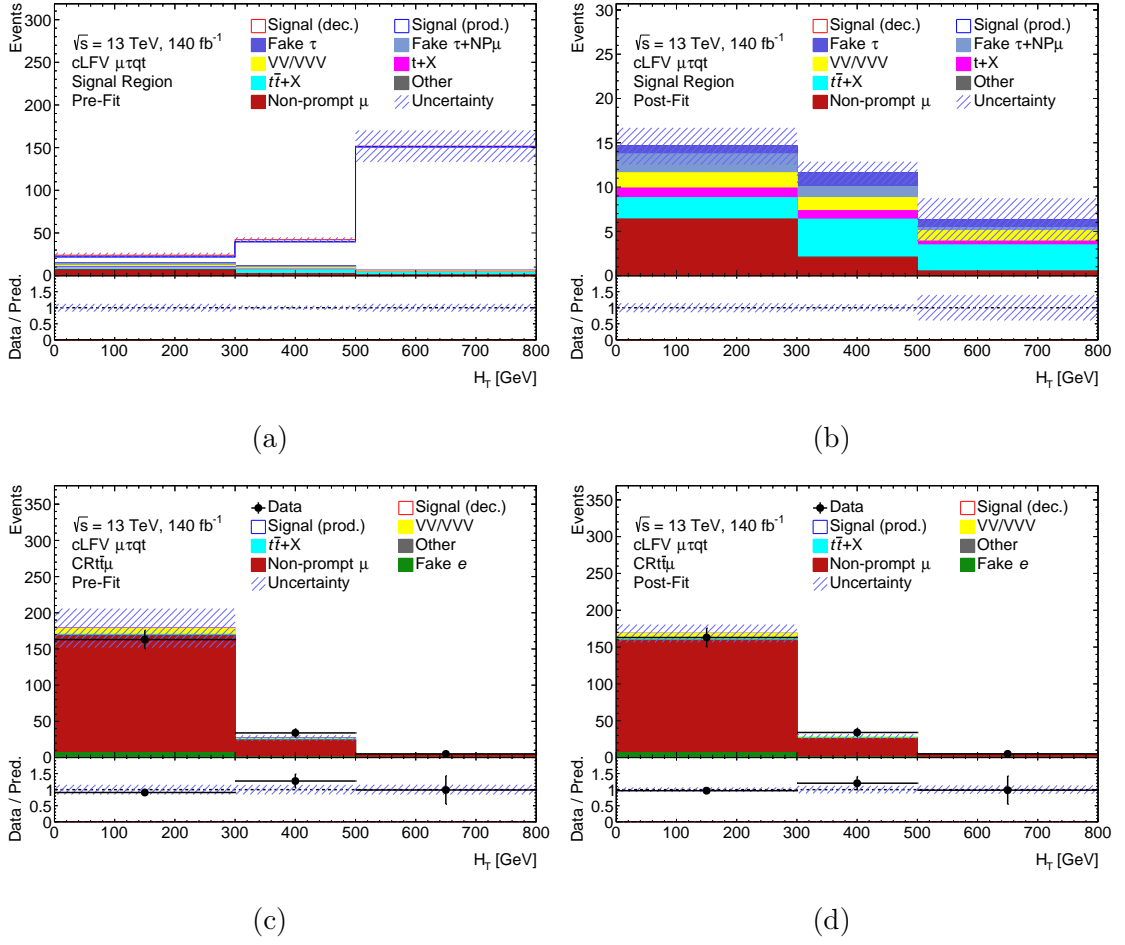


Figure 7.4: Pre-fit (a,c) and post-fit (b,d) plots of the SR and CR $t\bar{t}\mu$  for signal-plus-background fit to a mixed data and Asimov dataset. The final bin does not have an upper bound. The uncertainty band includes both the statistical and systematic uncertainties.

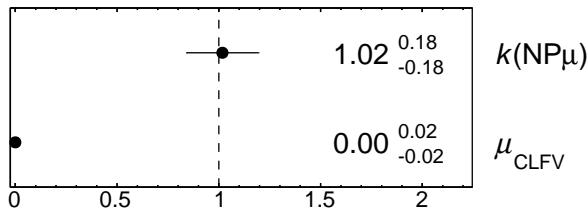


Figure 7.5: Normalisation factors computed in the signal-plus-background fit to a mixed data and Asimov dataset in the SR and CR $t\bar{t}\mu$ .

from NLO matching, FSR, and variation of the  $h_{\text{damp}}$  parameter are slightly constrained by the fit. The majority of the NPs maintain their pre-fit values or show small deviations while pulls are seen for NPs related to  $t\bar{t}$  NLO matching, FSR and  $h_{\text{damp}}$ ; these are the NPs which are seen to be slightly constrained. A pull implies that the initial value of the parameter, sometimes taken from an auxiliary measurement, was incorrect. However, it could be that the fit is pulling this NP to correct for a different effect, such as the mismodelling of a background process. Smaller pulls at the level of 10% are also seen on NPs corresponding to the modelling of jets.

Pulls originate from the background-only fit performed to data in  $CRt\bar{t}\mu$ . Figs. 7.4c and 7.4d shows that the background model slightly overestimates (underestimates) the data in the first (second) bin in the  $H_T$  distribution of  $CRt\bar{t}\mu$ . The differences between data and MC are not significant, slightly exceeding  $1\sigma$ . The  $\pm 1\sigma$  systematic variations of each of the pulled NPs are shown in Fig. 7.7. It can be seen that the upward pull on the  $t\bar{t}$  NLO matching NP has the effect of reducing the MC yield in the first bin of the distribution. The other pulled NPs have little effect on the first bin but contribute to increasing the MC yield in the second (and third) bin to close the difference between data and the background model.

Different binning choices for  $CRt\bar{t}\mu$  were investigated and were seen to change the pulls on these NPs or remove them completely; none of these choices led to a difference in the expected limit on  $\mu_{\text{CLFV}}$  of greater than 1%. The effect of not applying the smoothing algorithm to these NPs was also tested; this changed the direction of the pull on the  $t\bar{t}$  FSR NP but was seen to have a negligible effect on the sensitivity. It was concluded that the observed pulls are likely to be a result of these NPs being used by the fit to correct for slight data/MC differences, rather than encoding real physics effects. The small differences seen are likely to result from a statistical fluctuation or from the non-prompt muon modelling which  $CRt\bar{t}\mu$  exists to correct. All of the alternative binning schemes tested and their associated pulls are seen to have a negligible effect on the expected limits obtained on the signal process.

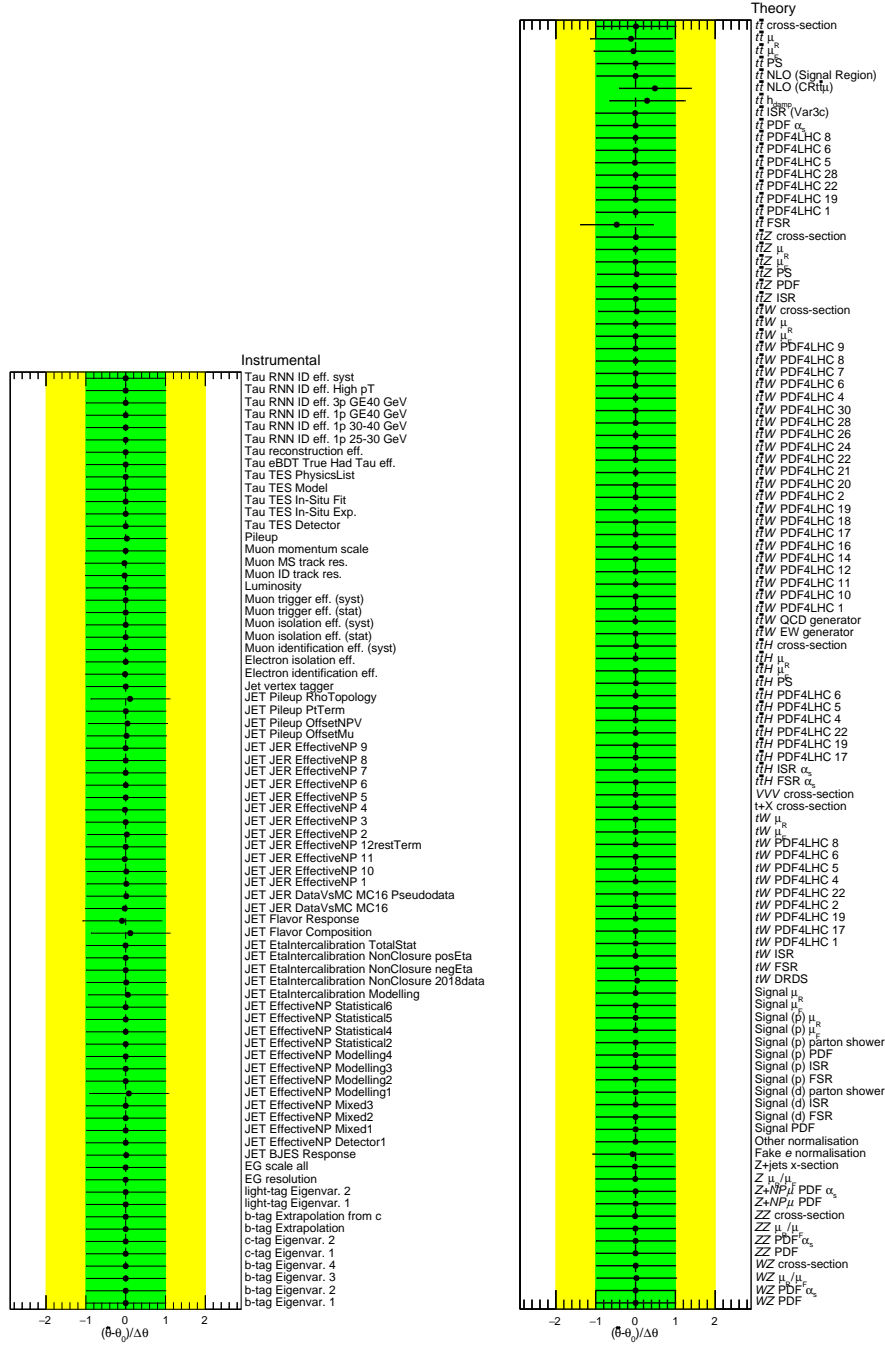


Figure 7.6: Post-fit nuisance parameter values,  $\hat{\theta}$ , and their uncertainties relative to pre-fit values,  $\theta_0$ , for the signal-plus-background fit to a mixed data and Asimov dataset. Points represent the change in NP value (“pull”) relative to the pre-fit uncertainty,  $\Delta\theta$ , while the green (yellow) band covers the range of post-fit parameter values within one (two) sigma, respectively, of  $\theta_0$ . The error bar on each point represents the post-fit uncertainty,  $\Delta\hat{\theta}$ , relative to  $\Delta\theta$ .

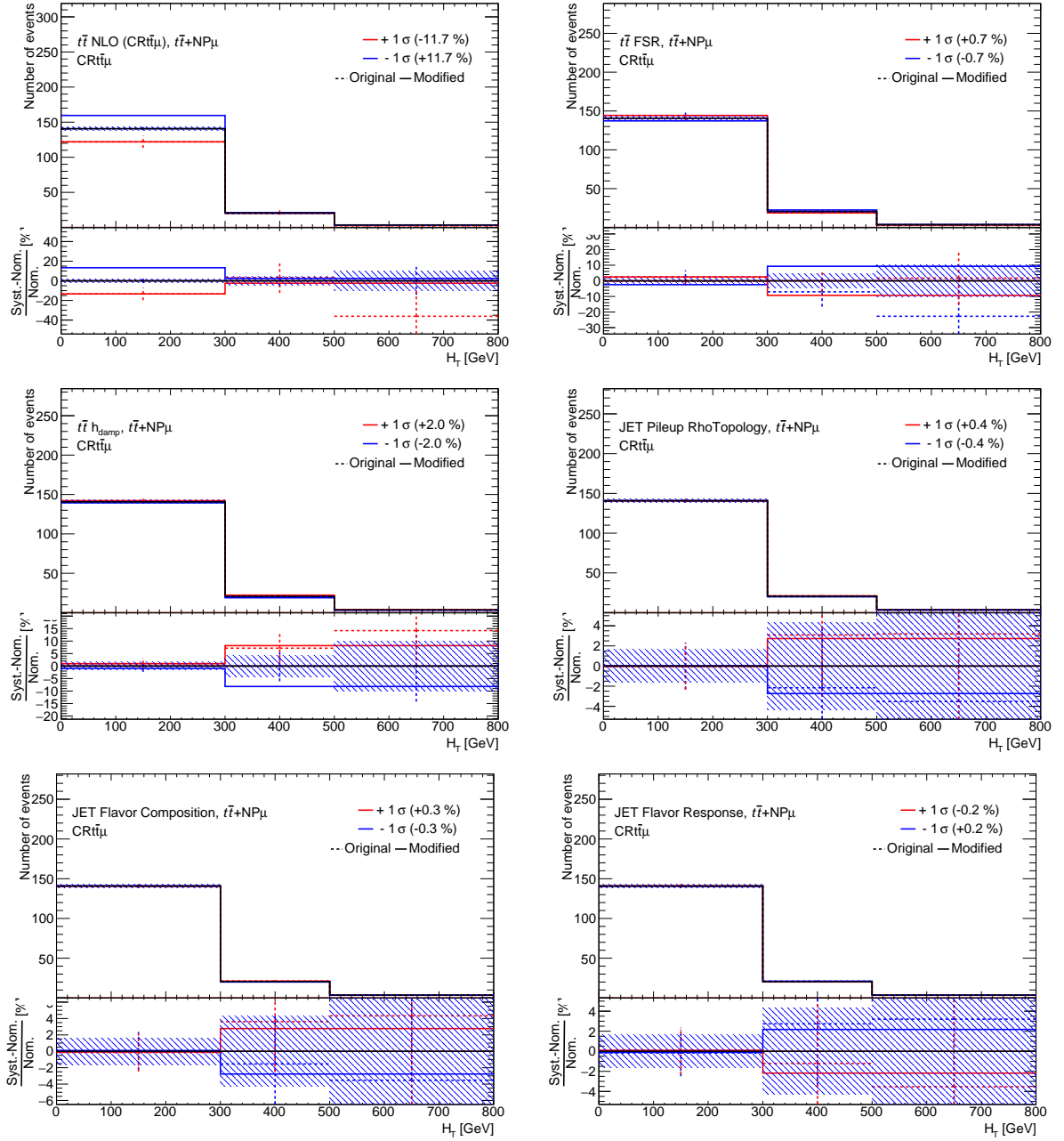


Figure 7.7: Plots showing the effect of  $\pm 1\sigma$  variations in  $CRt\bar{t}\mu$  of NPs showing the largest pulls in the signal-plus-background fit to a mixed data and Asimov dataset. The final bin does not have an upper bound. “Original” (“modified”) shows the systematic variations before (after) the application of smoothing and symmetrisation algorithms. The hatched band represents the MC statistical uncertainty.

At high  $H_T$ , where the analysis is most sensitive to signal, the agreement between data and the background model is good. As discussed in Section 7.1.4, the NP corresponding to the  $t\bar{t}$  NLO matching uncertainty has been decorrelated between  $CRt\bar{t}\mu$  and the SR. The pull arising from  $CRt\bar{t}\mu$  therefore does not affect the  $t\bar{t}$  background in the SR.

A very small pull is also seen on the fake electron normalisation NP, corresponding to the 50% uncertainty; this is applied to events from  $t\bar{t}\gamma$  and  $Z\gamma$  in which a photon is misidentified as an electron, and to  $t\bar{t}$  and  $Z$ +jets events with a non-prompt electron. These processes represent less than 4% of the events in  $CRt\bar{t}\mu$  according to simulation and are not present in the SR. It can be seen from Fig. 7.4 that this contribution (dark green) falls mostly in the first bin of the  $H_T$  distribution in  $CRt\bar{t}\mu$  so can also be used by the fit to correct the small data/MC difference in this bin. The pull corresponds to a negligible change in the combined yield of these processes, from  $7.5\pm 3.8$  to  $7.2\pm 3.7$ .

Pre- and post-fit plots of  $VR\mu$ , used to validate the modelling of the non-prompt muon background, are shown in Fig. 7.8. Data-MC agreement is good for the  $p_T$  distribution of the third muon, which tends to be the non-prompt muon, but there is some mismodelling in the  $H_T$  distribution. The source of the disagreement originates in the jet multiplicity and jet  $p_T$  modelling and appears to be introduced by the cut to remove signal contamination. Without this cut the  $H_T$  data-MC distribution in  $VR\mu$  is seen to be much better, as will be discussed further in Section 7.2. The same cut is applied to  $CRt\bar{t}\mu$  but is not seen to introduce the same mismodelling. As for  $CRt\bar{t}\mu$ , at high  $H_T$ , where the analysis is most sensitive to signal, the agreement between data and the background model is good. This will be discussed further in the context of the unblinded results in Section 7.2.2.

The correlation matrix for the mixed data and Asimov fit is shown in Fig. 7.9. The matrix is very similar to that seen for the full Asimov fit in Fig. 7.3 with some small changes of a few percentage points.

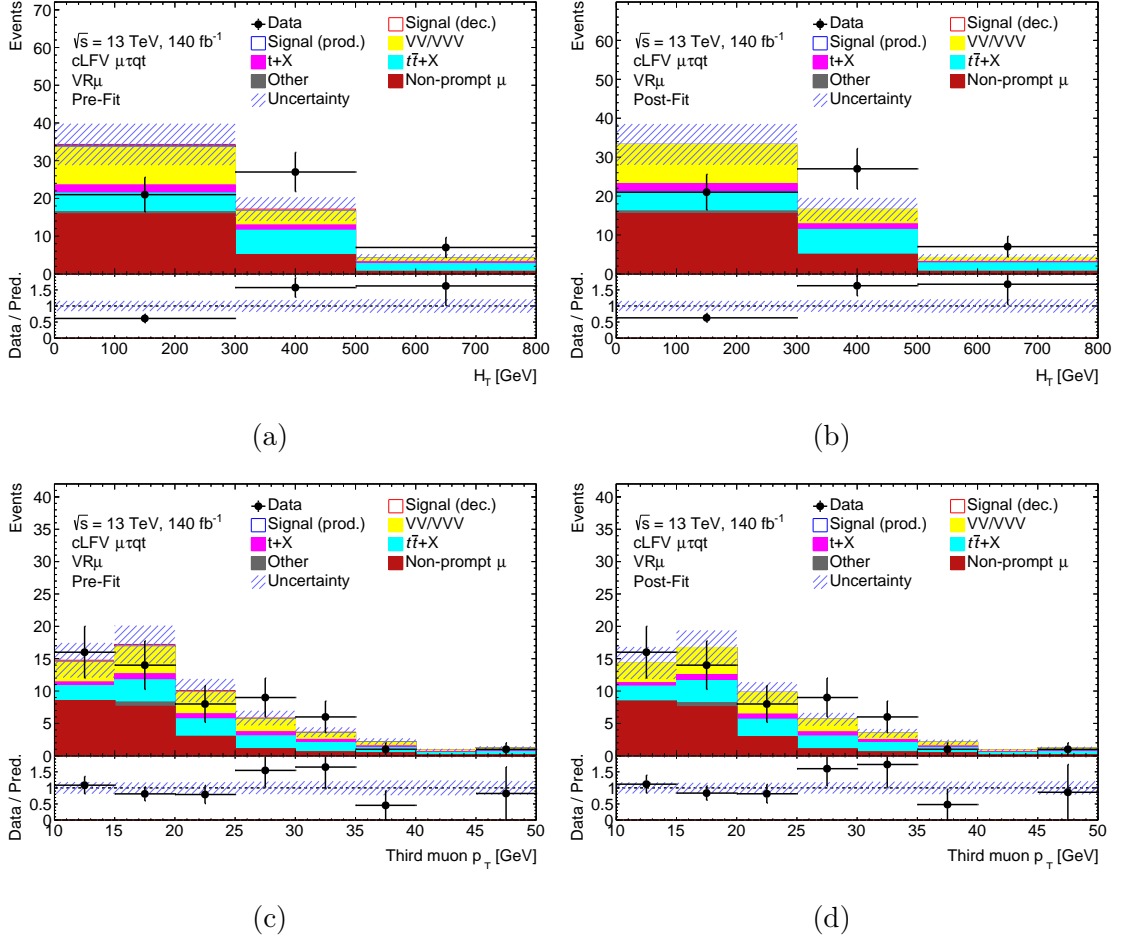


Figure 7.8: Pre-fit (a,c) and post-fit (b,d) plots of  $VR\mu$  for signal-plus-background fit to a mixed data and Asimov dataset, showing the  $p_T$  of the third muon and  $H_T$ . The final bin does not have an upper bound.  $VR\mu$  is a spectator region in the fit and does not feature in the likelihood function. The uncertainty band includes both the statistical and systematic uncertainties.

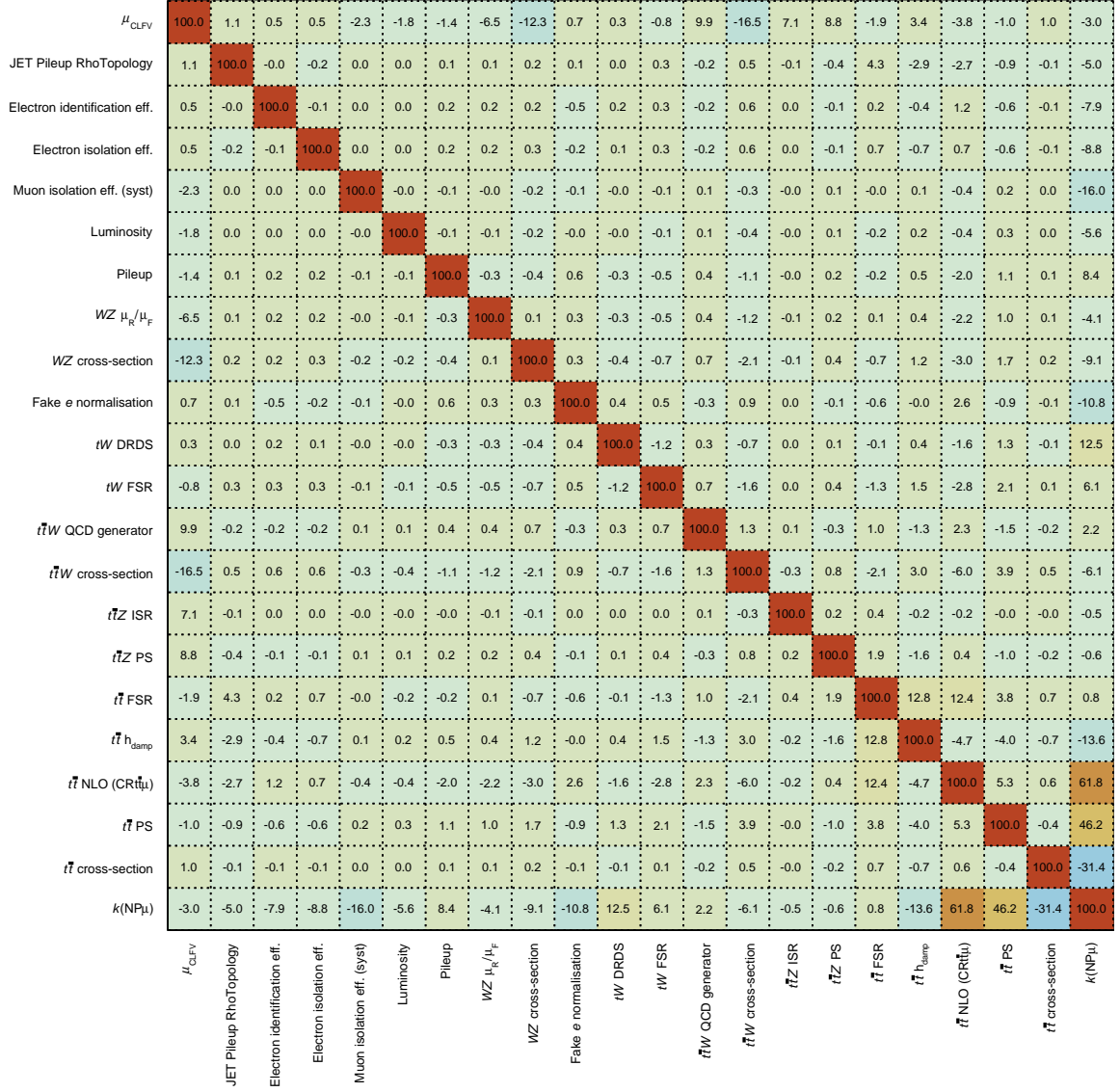


Figure 7.9: Correlation matrix for the signal-plus-background fit to a mixed data and Asimov dataset. Correlations between NPs and the parameter-of-interest,  $\mu_{\text{CLFV}}$ , are determined automatically during the minimisation of the negative log likelihood function. To improve readability, NPs which are not correlated with any other parameter at the level of 5% are dropped.

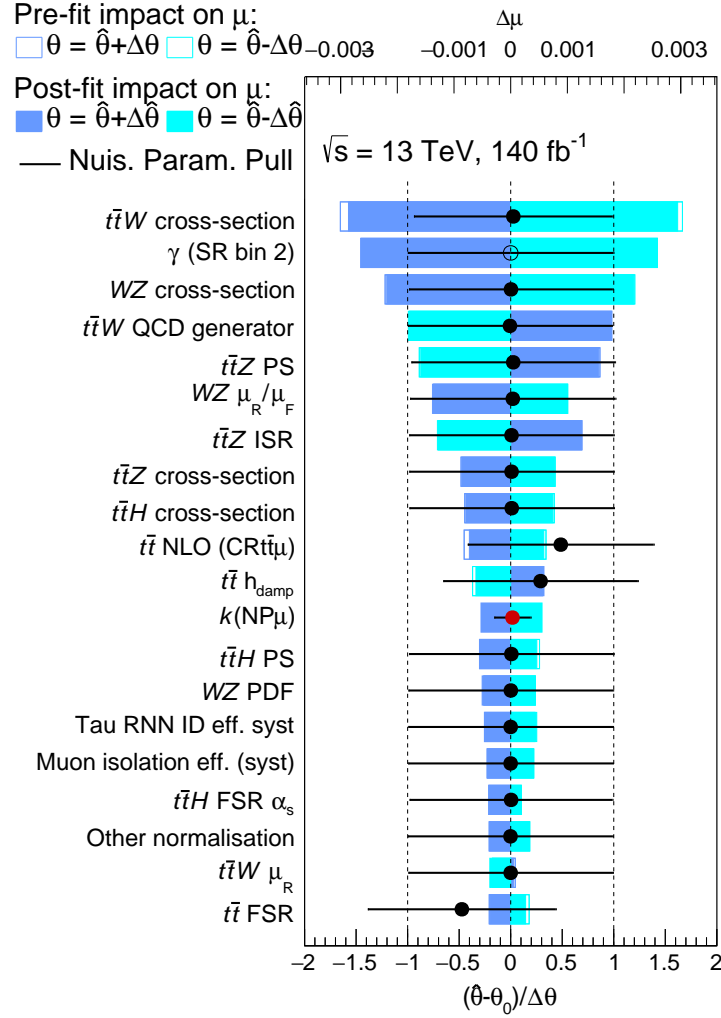


Figure 7.10: Ranking of NPs according to their impact on the signal strength parameter,  $\mu$  ( $= \mu_{\text{CLFV}}$ ), for the signal-plus-background fit to a mixed data and Asimov dataset. Each NP is varied around its post-fit value,  $\hat{\theta}$ , by its pre-fit (post-fit) uncertainties,  $\Delta\theta$  ( $\Delta\hat{\theta}$ ), and the profile likelihood fit is repeated with this NP fixed; the resulting shift,  $\Delta\mu$ , in the best-fit value of  $\mu$  is defined as the impact. Pre-fit (post-fit) impacts are indicated by unfilled (filled) blue boxes. Points represent the change in NP value (“pull”) relative to the pre-fit uncertainty,  $\Delta\theta$ , while the error bar represents the post-fit uncertainty,  $\Delta\hat{\theta}$ , relative to  $\Delta\theta$ . Filled (unfilled) black points denote NP for which a Gaussian (Poisson) constraint term is included in the likelihood. Filled red points represent unconstrained normalisation factors.

Fig. 7.10 shows the most significant systematic uncertainties contributing to the analysis ranked by their impact. The pre-fit (post-fit) impact of a given NP,  $\theta$ , is defined as the shift in  $\mu_{\text{CLFV}}$  observed when the fit is repeated with  $\theta$  fixed to  $\hat{\theta} \pm \Delta\theta$  ( $\hat{\theta} \pm \Delta\hat{\theta}$ ), where  $\Delta\theta$  ( $\Delta\hat{\theta}$ ) is the pre-fit (post-fit) uncertainty. It therefore shows the dominant systematics affecting the analysis. However, Table 7.1 shows that the sensitivity of the analysis is heavily limited by statistics: the limit only changes by 7% when all systematic uncertainties are included. It has been seen that even a factor five reduction in the leading systematic uncertainty has a percent-level effect on the sensitivity of the analysis. Nevertheless, the dominant systematic uncertainties are discussed below.

The dominant systematics are seen to arise from theoretical uncertainties and the modelling of  $t\bar{t} + X$  and diboson processes. These processes are expected to populate the final bin of the SR, from which most of the sensitivity to the signal process derives (see Fig. 7.4b). The ranking of NPs is consistent with the size of the correlations of each NP with  $\mu_{\text{CLFV}}$ . The leading systematic contribution comes from the large 50% cross-section uncertainty assigned to the  $t\bar{t}W$  process. The cross-section of this process is measured to be higher than that predicted by the latest theoretical calculations with no firm understanding of the source of the difference [194, 206, 207]. The effect of reducing the uncertainty on the  $t\bar{t}W$  cross-section and of injecting a  $t\bar{t}W$  excess into an Asimov dataset have both been checked and are seen to be small. The combined generator uncertainty on  $t\bar{t}W$  also has a large impact on  $\mu_{\text{CLFV}}$ , with a significant normalisation component in the SR.

The limited MC statistics of the SR, represented by the “ $\gamma$ ” factors seen in Fig. 7.10, also have a significant impact. The leading contributions to these  $\gamma$  factors originate from the  $t\bar{t}$  samples. The 30% theoretical uncertainty on the cross-section of the  $WZ$  process is another leading systematic contribution, as are other large cross-section uncertainties, shown in Section 6.7.2. Sensitivity is also seen to  $t\bar{t}$  and  $t\bar{t}Z$  modelling, with the NPs corresponding to  $t\bar{t}$  FSR and NLO matching uncertainties and  $t\bar{t}Z$  parton shower/hadronisation and ISR

uncertainties appearing in the highest ranked parameters. The  $t\bar{t}Z$  contribution is expected to be a dominant component of the final SR bin, while the high purity of  $t\bar{t}$  in  $CRt\bar{t}\mu$  is understood to make the analysis sensitive to  $t\bar{t}$  modelling.

### Sensitivity to signal systematic uncertainties

Since the best-fit value of  $\mu_{\text{CLFV}}$  is found to be zero in the above fits, systematic uncertainties on the signal processes do not appear in Fig. 7.10. To determine the sensitivity of the result to any excess in data observed above the background model after unblinding, a fit has been run with signal injected at the expected limit obtained above. The ranking of NPs for this fit is shown in Figure 7.11. It can be seen that theoretical uncertainties and the modelling of  $t\bar{t}+X$  backgrounds remain significant NPs; however, the signal parton shower uncertainty for the  $gu_k \rightarrow t\mu\tau$  process is now the highest ranked NP. As discussed in Appendix B, this uncertainty is deliberately large to cover any uncertainty resulting from the reweighting process applied to the alternative HERWIG signal samples.

Additionally it can be seen that uncertainties associated to the identification and electron-rejection SFs for  $\tau_{\text{had-vis}}$  and identification and isolation SFs for muons are more significant in this case. This is understood to be a consequence of signal events having higher  $p_{\text{T}}$  final state objects than the background and these uncertainties being larger at higher  $p_{\text{T}}$ .

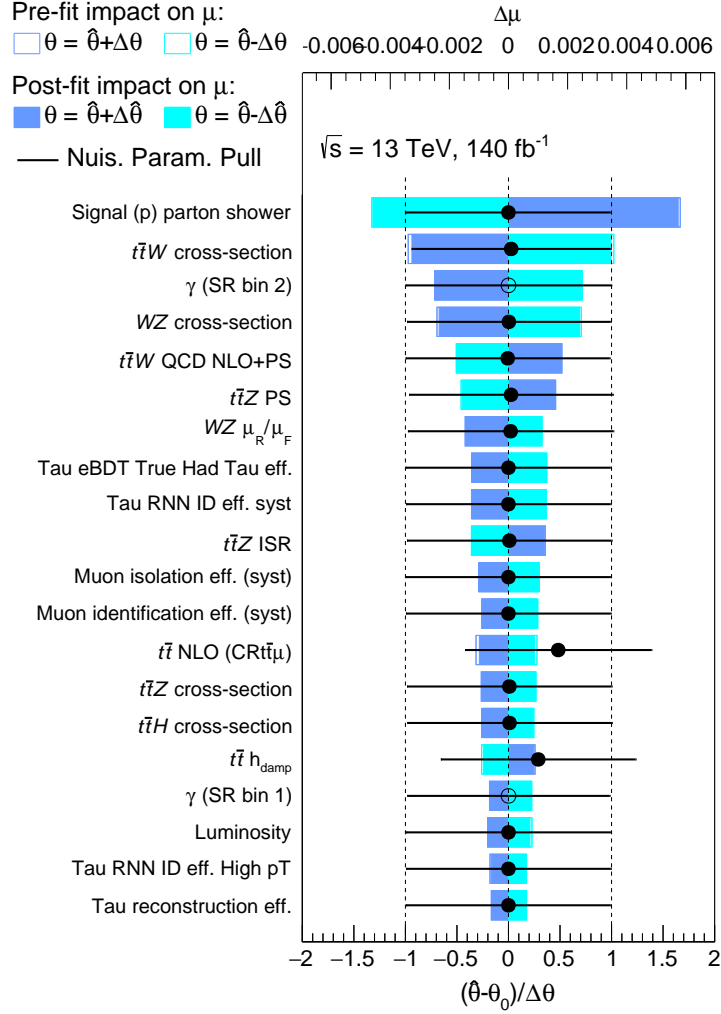


Figure 7.11: Ranking of NPs according to their impact on the signal strength parameter,  $\mu$  ( $= \mu_{\text{CLFV}}$ ), for the signal-plus-background fit to a mixed data and Asimov dataset with signal injection. Each NP is varied around its post-fit value,  $\hat{\theta}$ , by its pre-fit (post-fit) uncertainties,  $\Delta\theta$  ( $\Delta\hat{\theta}$ ), and the profile likelihood fit is repeated with this NP fixed; the resulting shift,  $\Delta\mu$ , in the best-fit value of  $\mu$  is defined as the impact. Pre-fit (post-fit) impacts are indicated by unfilled (filled) blue boxes. Points represent the change in NP value (“pull”) relative to the pre-fit uncertainty,  $\Delta\theta$ , while the error bar represents the post-fit uncertainty,  $\Delta\hat{\theta}$ , relative to  $\Delta\theta$ . Filled (unfilled) black points denote NP for which a Gaussian (Poisson) constraint term is included in the likelihood.

## 7.2 Results

This section documents the findings of the analysis. A preliminary set of results, released as an ATLAS Conference Note [2], is discussed in Section 7.2.1 before the full results are presented in Sections 7.2.2, 7.3 and 7.4.

The preliminary results were also derived using the profile likelihood setup described in Section 7.1 but used two unbinned SRs which are subsets of the binned SR described in Section 6.4.3. These SRs differed in their jet multiplicity requirement, but otherwise are defined according to the SR definition in Table 6.8. SR1 required events to have at least two jets, while SR2 required events to have exactly one jet. This division was intended to distinguish between the CLFV  $t\bar{t}$  decay and  $gu_k \rightarrow t\mu\tau$  signals. Due to the low statistics of the two regions, these were not parametrised in any kinematic variable and were unbinned. Other small differences between the preliminary analysis and the full analysis are described in Appendix A.1 but were not seen to significantly affect the analysis sensitivity.

### 7.2.1 Preliminary results

The observed event yields in  $CRt\bar{t}\mu$  and the two SRs used in the preliminary result compared to pre-fit and post-fit expectations from simulation are shown in Fig. 7.12. The SM background prediction is in good agreement with the data and no significant signal contribution is allowed by the fit. Fig. 7.13 shows the fitted signal strength in fits with statistical uncertainty only and with all systematic uncertainties included; in both cases  $\mu_{\text{CLFV}}$  is consistent with zero, as expected in the SM. The fitted values of  $\mu_{\text{CLFV}}$  differ slightly due to the inclusion of NPs but the values are consistent within the uncertainties. The normalisation factor applied to the non-prompt muon background was estimated to be  $1.02 \pm 0.18$ , determined by the profile-likelihood fit.

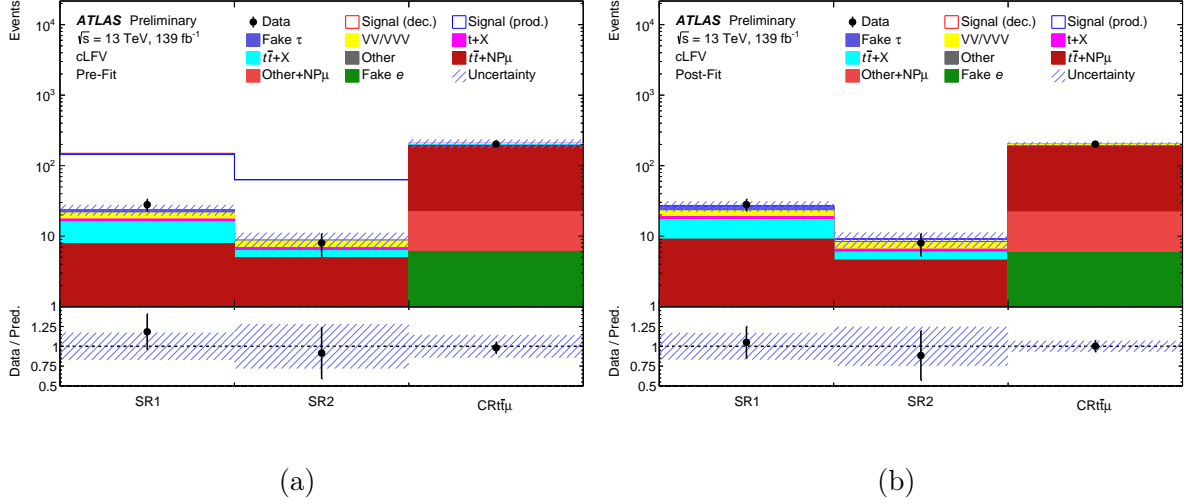


Figure 7.12: Pre-fit (a) and post-fit (b) plots of  $CRt\bar{t}\mu$  and the two SRs used in a preliminary result [2] following a signal-plus-background fit to the unblinded dataset. The uncertainty band includes both the statistical and systematic uncertainties.

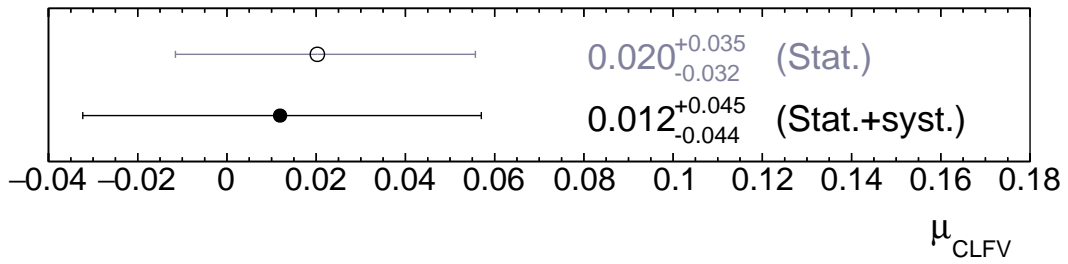


Figure 7.13: Fitted value of the signal strength modifier  $\mu_{\text{CLFV}}$ , defined relative to the “inclusive” EFT sample with Wilson coefficients set to 0.3 for  $\Lambda = 1$  TeV, as found in the preliminary analysis for fits with and without systematic uncertainties [2].

Table 7.2: Expected and observed upper exclusion limits on the CLFV decay of a top quark,  $\mathcal{B}(t \rightarrow \mu\tau q)$ , at 95% CL, considering the case in which all EFT operators contribute with the same effective coupling strength [2].

	Upper limits on $\mathcal{B}(t \rightarrow \mu\tau q)$ at 95% CL	
	Stat. only	All systematics
<b>Expected</b>	$8 \times 10^{-7}$	$10 \times 10^{-7}$
<b>Observed</b>	$9 \times 10^{-7}$	$11 \times 10^{-7}$

In the absence of an observed CLFV signal, exclusion limits are set on the signal process. The observed exclusion limit on the cross-section for the CLFV processes at 95% CL is found to be:

$$\sigma_{\text{CLFV}} < 8.1 \text{ fb} \quad (95\% \text{ CL}).$$

Observed and expected limits on the CLFV top quark decay  $\mathcal{B}(t \rightarrow \mu\tau q)$  at 95% CL are shown in Table 7.2, considering the case in which all EFT operators contribute with the same effective coupling strength. It can be seen that the sensitivity of the analysis is limited by statistics; the inclusion of systematic uncertainties reduces the sensitivity by just 15%. Table 7.3 shows the observed and expected exclusion limits on SMEFT Wilson coefficients, along with the existing limits on these coefficients from Ref. [143]. From Table 6.4 it can be seen that the  $gu \rightarrow t\mu\tau$  process has a significantly larger cross-section than  $gc \rightarrow t\mu\tau$ , due to the presence of valence up quarks in the proton PDF. For this reason the exclusion limits on Wilson coefficients corresponding to  $t\mu\tau u$  interactions are more stringent than those corresponding to  $t\mu\tau c$  interactions by a factor of three.

The systematic uncertainties with the largest impact on  $\mu_{\text{CLFV}}$  are due to the modelling of the  $t\bar{t}$  and  $t\bar{t}W$  processes. Signal modelling uncertainties are not found to have a large impact due to the absence of a significant post-fit signal contribution.

Table 7.3: Preliminary expected and observed upper exclusion limits at 95% CL on Wilson coefficients corresponding to four-fermion EFT operators which could introduce CLFV  $t\mu\tau u_k$  interactions [2], along with existing (“previous”) limits from Ref. [143], assuming a scale of new physics  $\Lambda = 1$  TeV. Results are shown separately for  $t\mu\tau u$  and  $t\mu\tau c$  interactions. The limit on a given Wilson coefficient assumes contributions from other operators are set to zero. Limits on  $c_{lequ}^{1(ijk3)}$  and  $c_{lequ}^{3(ijk3)}$  from Ref. [143] have been scaled down by a factor of  $\sqrt{2}$  to account for the inclusion of the Hermitian conjugate of the corresponding operator ( $c_{lequ}^{1(ij3k)}$  and  $c_{lequ}^{3(ij3k)}$ , respectively).

	Exclusion limits on SMEFT					
	Wilson coefficients at 95% CL					
	$c_{lq}^{-(ijk3)}$	$c_{eq}^{(ijk3)}$	$c_{lu}^{(ijk3)}$	$c_{eu}^{(ijk3)}$	$c_{lequ}^{1(ijk3)}$	$c_{lequ}^{3(ijk3)}$
<b>Previous (u) [143]</b>	12.0	12.0	12.0	12.0	18.4	2.4
<b>Expected (u) [2]</b>	0.47	0.44	0.43	0.46	0.49	0.11
<b>Observed (u) [2]</b>	0.49	0.47	0.46	0.48	0.51	0.11
<b>Previous (c) [143]</b>	14.0	14.0	14.0	14.0	20.5	2.6
<b>Expected (c) [2]</b>	1.6	1.6	1.5	1.6	1.8	0.35
<b>Observed (c) [2]</b>	1.7	1.6	1.6	1.6	1.9	0.37

The sensitivity of the analysis to the inclusive CLFV process is seen to be dominated by the CLFV single top production process, with the CLFV  $t\bar{t}$  decay process improving the limits by just 2.7% relative to considering only the single top signal. The choice to have two SRs was made in order to distinguish between the CLFV  $t\bar{t}$  decay and single top production signals. However, a combined fit to SR1 and SR2 was not seen to give a more stringent expected exclusion limit on the CLFV process than a fit to the two regions merged into one. This was the motivation for re-optimising the analysis and using the parametrisation presented in Section 6.4.3, which was seen to improve the expected sensitivity to the CLFV signal by almost a factor of two.

## 7.2.2 Full results

Observed event yields in  $CRt\bar{t}\mu$  and the SR compared to pre-fit and post-fit expectations from simulation for the refined analysis are shown in Fig. 7.14. The data is seen to be consistent with the background-only hypothesis in the first two bins of the SR but a slight excess of data events is observed in the highest  $H_T$  bin, with a significance of  $1.6\sigma$ . The post-fit yields of each process are listed in Table 7.4 and a breakdown of the bin-by-bin yields of data events compared to the total post-fit prediction is shown in Table 7.5. The normalisation factor applied to the non-prompt muon background was estimated to be  $1.01 \pm 0.18$ , determined by the profile-likelihood fit. Fig. 7.15 shows the fitted signal strength when considering only the statistical uncertainty and considering also systematic uncertainties; in both cases  $\mu_{\text{CLFV}}$  is consistent with zero within two sigma.

The observed event yields for  $VR\mu$  can be seen in Fig. 7.16. Figs. 7.16a and 7.16b show the  $H_T$  distribution of  $VR\mu$  as defined in Table 6.8 which includes the cut to remove signal contamination, while Figs. 7.16c and 7.16d show  $VR\mu$  with this cut removed. When the cut is removed the agreement between the data and prediction is seen to improve significantly.

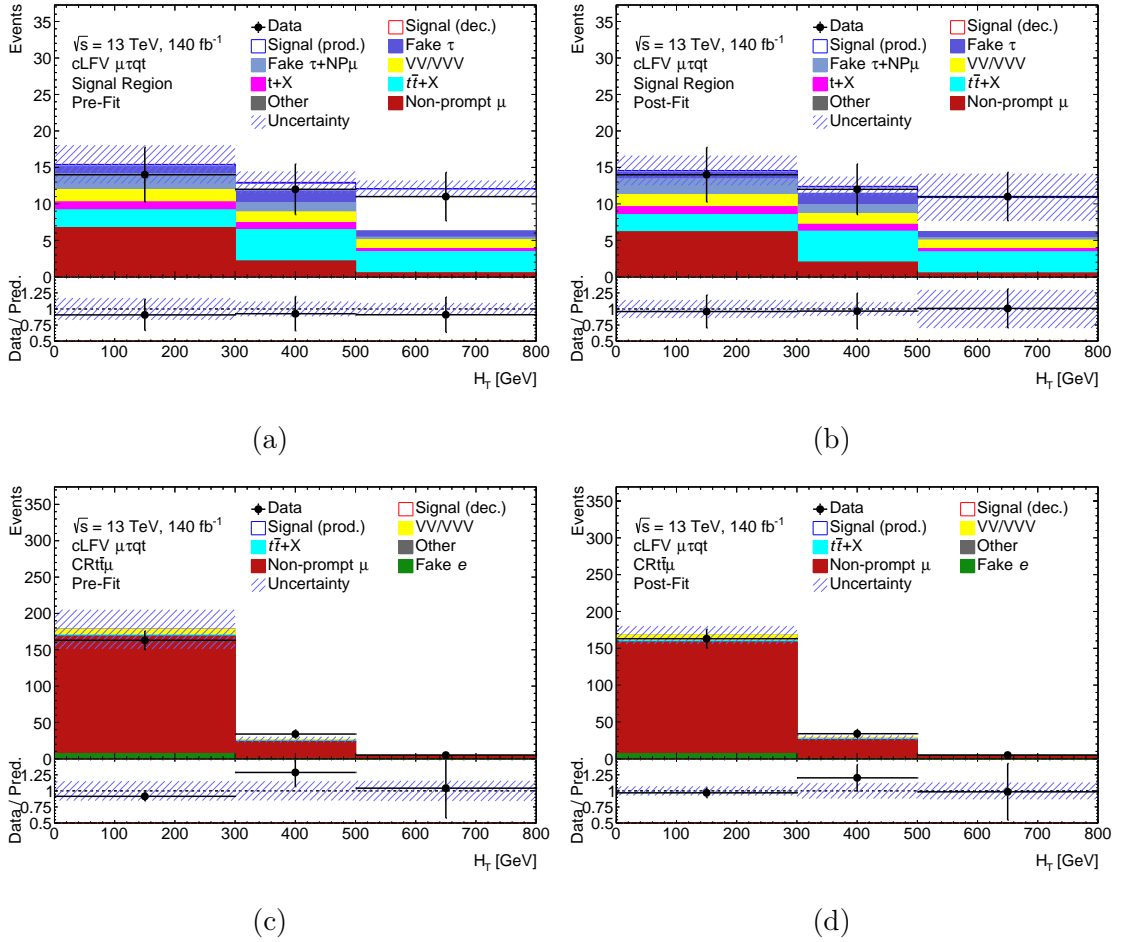


Figure 7.14: Pre-fit (a,c) and post-fit (b,d) plots of the SR and CR $t\bar{t}\mu$  for signal-plus-background fit to the unblinded dataset. The final bin does not have an upper bound. The uncertainty band includes both the statistical and systematic uncertainties. Note for the ratio in the lower panel the prediction (‘Pred’) includes the allowed signal contribution.

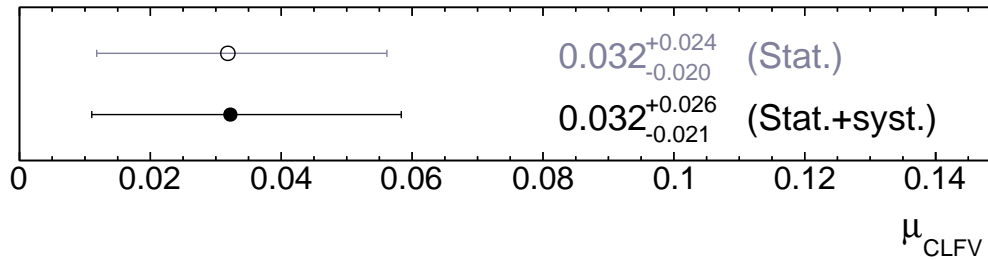


Figure 7.15: Fitted value of the signal strength modifier  $\mu_{\text{CLFV}}$ , defined relative to the “inclusive” EFT sample with Wilson coefficients set to 0.3 for  $\Lambda = 1$  TeV, for fits with and without systematic uncertainties.

No signal events are present in this region post-fit and the agreement between the data and the background model in the middle and high  $H_T$  bins is good.

The behaviour of the nuisance parameters is seen to be very similar to that seen in the mixed data and Asimov fit described in Section 7.1.5. No additional NP pulls originate from the unblinding of the SR since the deviation between data and the prediction is absorbed by  $\mu_{\text{CLFV}}$ . The NP pulls can be seen in Fig. 7.17. A background-only fit has also been run to the unblinded data to check the behaviour in the fit when  $\mu_{\text{CLFV}}$  is not included; this does not result in any significant new pulls.

The systematic ranking of NPs, shown in Fig. 7.18, is very similar to that shown in Fig. 7.10. However, the presence of a small post-fit signal contribution results in signal modelling uncertainties having a significant impact, as was found for the signal injection tests in Section 7.1.5. In particular, the NP associated to the signal parton shower and hadronisation uncertainty is now the most important NP. This is to be expected as this uncertainty is deliberately conservative to cover the effects of both the choice of parton shower and hadronisation mode as well as any uncertainty in the reweighting of the HERWIG signal samples. It carries significant shape and normalisation components, as can be seen from Fig. B.2, which shows the effect of  $\pm 1\sigma$  variations of this uncertainty. Nevertheless, as

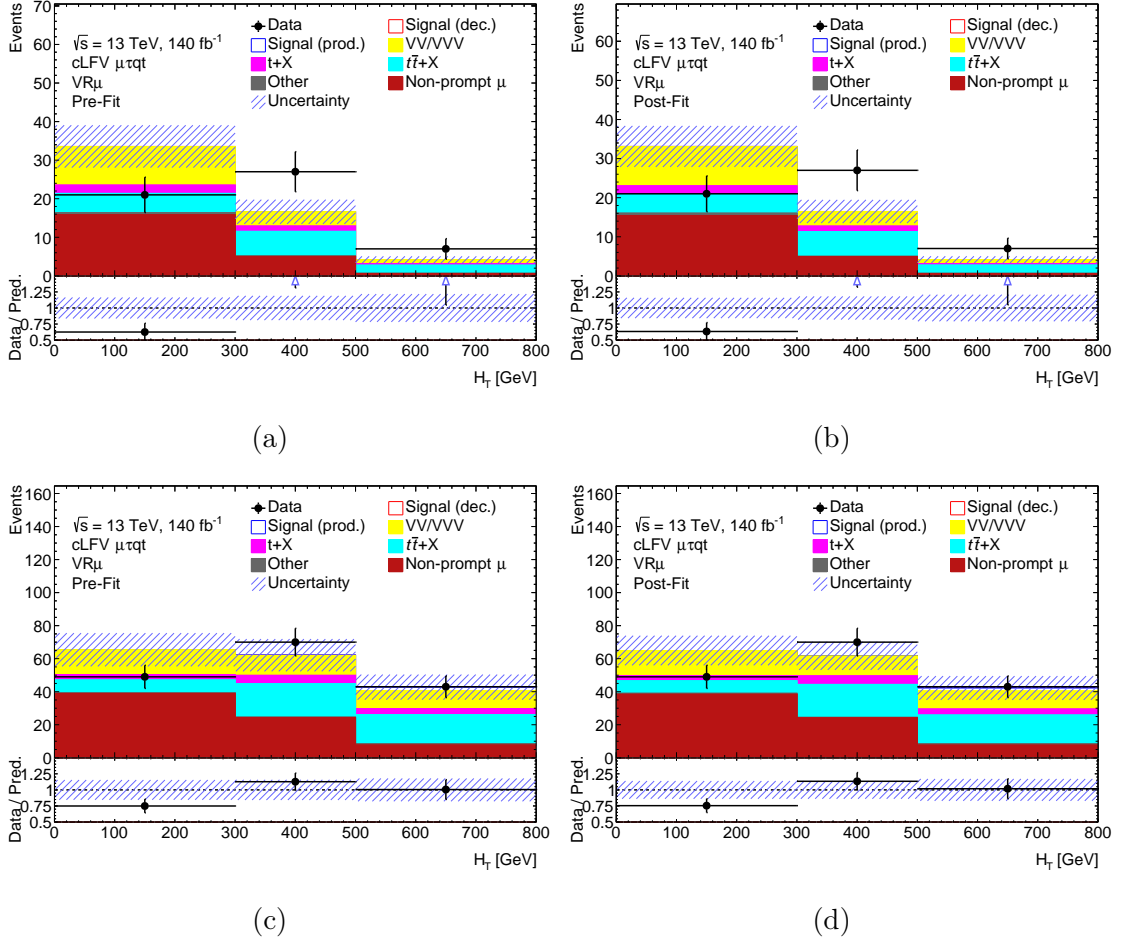


Figure 7.16: Pre-fit (a,c) and post-fit (b,d) plots of the  $VR\mu$ , with (top) and without (bottom) the cut to remove signal contamination, for signal-plus-background fit to the unblinded dataset. The final bin does not have an upper bound. The uncertainty band includes both the statistical and systematic uncertainties. Note for the ratio in the lower panel the prediction (‘Pred’) includes the allowed signal contribution.

Table 7.4: Post-fit event yields for the SR and  $CRt\bar{t}\mu$ . ‘Total’ refers to the sum of the signal and background yields, with the systematic uncertainty taking into account correlations as determined by the fit.

Process	SR	$CRt\bar{t}\mu$
$t\bar{t} + NP\mu$	$7.9 \pm 3.4$	$164 \pm 14$
$t\bar{t}W$	$3.5 \pm 1.8$	$1.17 \pm 0.60$
$t\bar{t}H$	$3.07 \pm 0.36$	$1.26 \pm 0.14$
$t\bar{t}Z$	$2.85 \pm 0.52$	$0.88 \pm 0.33$
$t+X$	$2.48 \pm 0.18$	-
$WZ$	$3.6 \pm 1.3$	$7.3 \pm 2.4$
$ZZ$	$0.59 \pm 0.22$	$1.78 \pm 0.58$
$VVV$	$0.010 \pm 0.050$	$0.47 \pm 0.24$
Other	$0.23 \pm 0.11$	$1.12 \pm 0.57$
Fake electron	-	$7.2 \pm 3.7$
Fake $\tau_{\text{had-vis}}$	$3.26 \pm 0.43$	-
Fake $\tau_{\text{had-vis}} + NP\mu$	$3.7 \pm 2.7$	-
$t+X + NP\mu$	$0.29 \pm 0.31$	$14.7 \pm 5.1$
$Z + NP\mu$	$0.192 \pm 0.010$	$1.84 \pm 0.99$
Other $NP\mu$	$0.0506 \pm 0.0095$	-
Signal (decay)	$0.19 \pm 0.14$	$0.025 \pm 0.019$
Signal (production)	$5.8 \pm 4.1$	$0.022 \pm 0.023$
Total	$37.9 \pm 4.8$	$201 \pm 14$
Data	37	202

Table 7.5: Post-fit signal-plus-background yields compared to observed data events in each bin of the SR.

	SR yield			Total
	Bin 1	Bin 2	Bin 3	
<b>Post-fit S+B</b>	$14.6 \pm 2.0$	$12.4 \pm 1.3$	$10.9 \pm 3.2$	$37.9 \pm 4.8$
<b>Data</b>	14	12	11	37

will be discussed below, the analysis is heavily statistically limited and the addition of this uncertainty compared to a fit considering only statistical uncertainty is seen to have a small effect.

Since no statistically significant excess over the expected background is observed, exclusion limits are placed on the cross-section of the signal process at 95% CL. The observed exclusion limit on the cross-section for the CLFV processes at 95% CL is found to be:

$$\sigma_{\text{CLFV}} < 7.5 \text{ fb} \quad (95\% \text{ CL}).$$

The observed and expected limits on the CLFV top quark decay  $\mathcal{B}(t \rightarrow \mu\tau q)$  are presented in Table 7.6. The small excess of data above the background-only prediction means the limits are weakened by approximately 75% with respect to the expected results. The inclusion of systematic uncertainties only weakens the observed limits by 6.3% relative to the case in which only statistical uncertainty is considered. Even more so than for the preliminary results, the sensitivity to the inclusive CLFV process is dominated by the CLFV single top production process, with inclusion of the  $t\bar{t}$  decay process improving the observed limits by just 1%. Interpretations are also performed in the EFT framework and in the context of a scalar LQ model, as discussed in Sections 7.3 and 7.4.

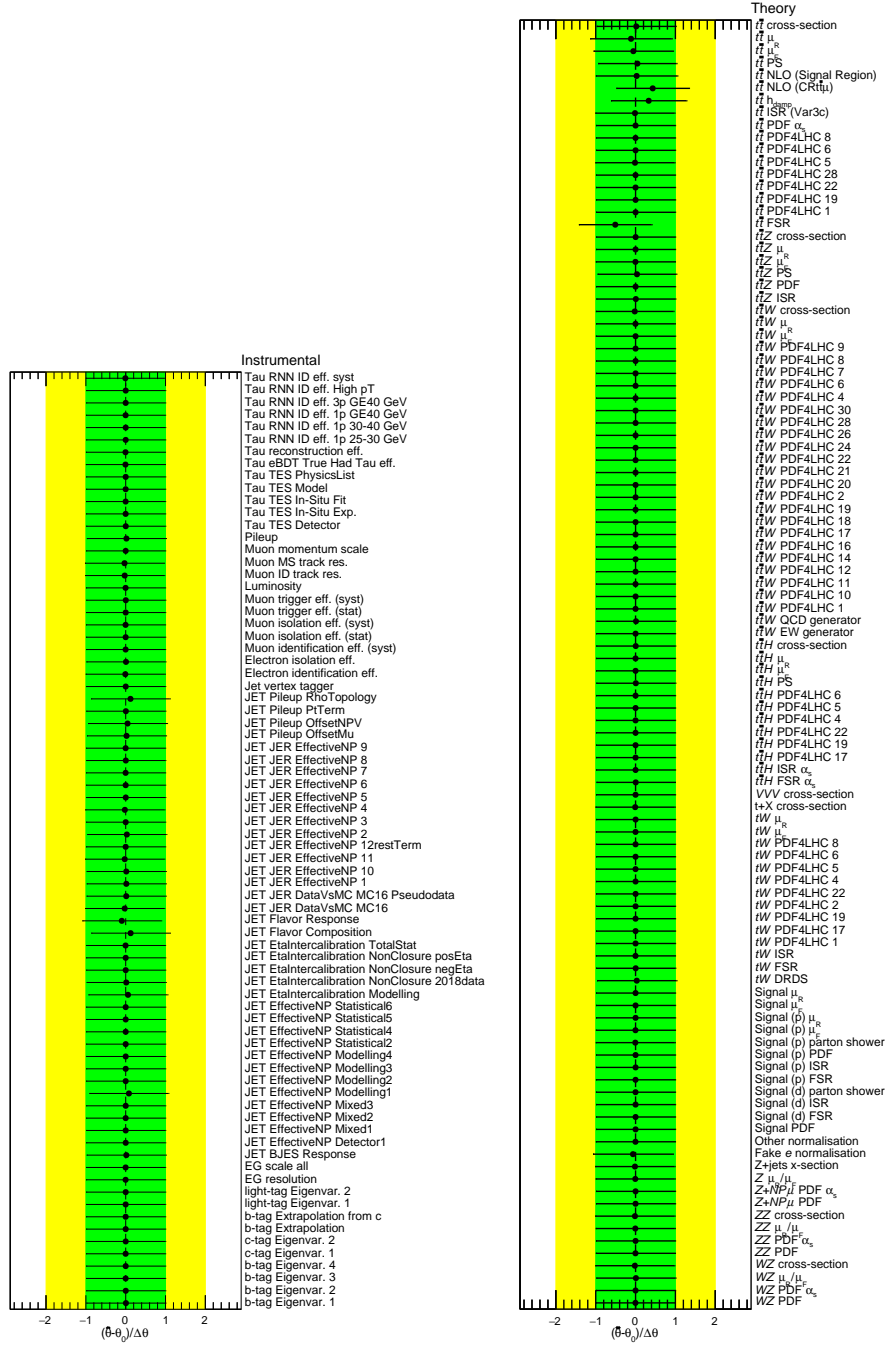


Figure 7.17: Post-fit nuisance parameter values,  $\hat{\theta}$ , and their uncertainties relative to pre-fit values,  $\theta_0$ , for the signal-plus-background fit using data across all analysis regions. Points represent the change in NP value (“pull”) relative to the pre-fit uncertainty,  $\Delta\theta$ , while the green (yellow) band covers the range of post-fit parameter values within one (two) sigma, respectively, of  $\theta_0$ . The error bar on each point represents the post-fit uncertainty,  $\Delta\hat{\theta}$ , relative to  $\Delta\theta$ .

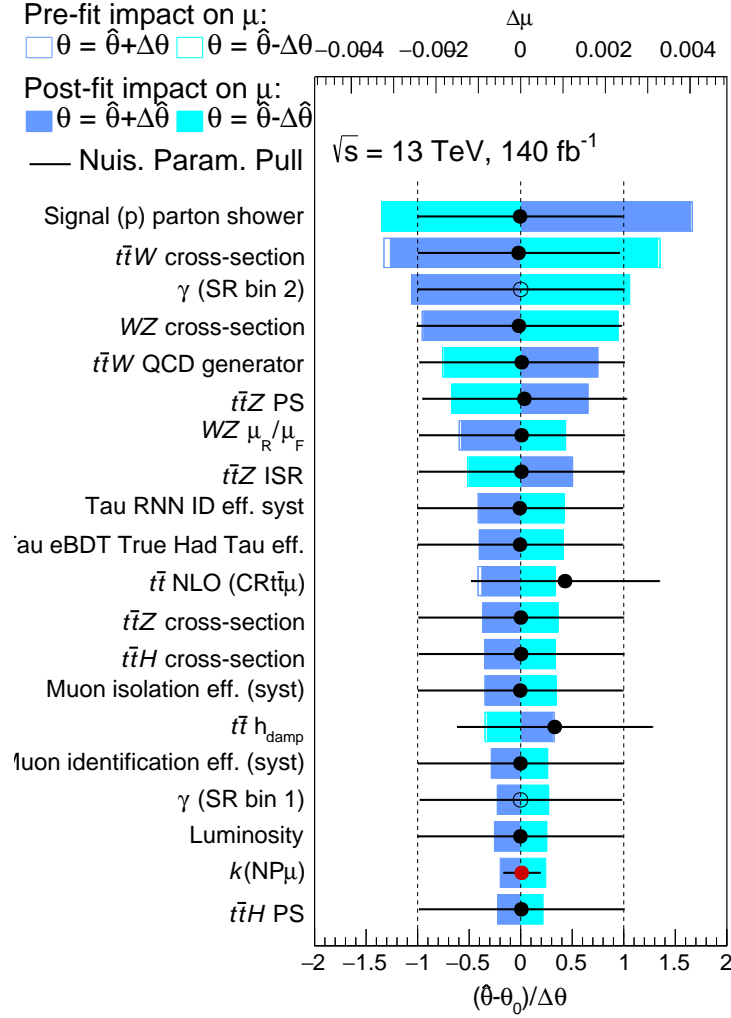


Figure 7.18: Ranking of NPs according to their impact on the signal strength parameter,  $\mu$  ( $= \mu_{\text{CLFV}}$ ), for the signal-plus-background fit using data across all analysis regions. Each NP is varied around its post-fit value,  $\hat{\theta}$ , by its pre-fit (post-fit) uncertainties,  $\Delta\theta$  ( $\Delta\hat{\theta}$ ), and the profile likelihood fit is repeated with this NP fixed; the resulting shift,  $\Delta\mu$ , in the best-fit value of  $\mu$  is defined as the impact. Pre-fit (post-fit) impacts are indicated by unfilled (filled) blue boxes. Points represent the change in NP value (“pull”) relative to the pre-fit uncertainty,  $\Delta\theta$ , while the error bar represents the post-fit uncertainty,  $\Delta\hat{\theta}$ , relative to  $\Delta\theta$ . Filled (unfilled) black points denote NP for which a Gaussian (Poisson) constraint term is included in the likelihood. Filled red points represent unconstrained normalisation factors.

Table 7.6: Expected and observed upper exclusion limits on the CLFV decay  $\mathcal{B}(t \rightarrow \mu\tau q)$  at 95% CL from the signal-plus-background fit to the unblinded dataset.

	Upper limits on $\mathcal{B}(t \rightarrow \mu\tau q)$ at 95% CL	
	Stat. only	All systematics
Expected	$4.6 \times 10^{-7}$	$5.0 \times 10^{-7}$
Observed	$8.2 \times 10^{-7}$	$8.7 \times 10^{-7}$

## 7.3 EFT interpretation

The exclusion limit on the cross-section of the  $t\mu\tau u_k$  CLFV process can be interpreted in the SMEFT framework. As discussed in Section 6.2, the  $H_T$  distribution used in the profile likelihood fit is not capable of separating the different EFT operator contributions; instead each operator is considered independently. Additionally, while there is expected to be a difference in the kinematics of CLFV  $gu_k \rightarrow t\mu\tau$  signal due to the different PDFs of  $u$  and  $c$  quarks, these contributions are not resolved and are considered independently.

### 7.3.1 EFT interpretation procedure

The EFT interpretation is performed using the profile likelihood fit discussed in Section 7.1. By replacing the “inclusive” sample made up of contributions from all of the SMEFT operators in Table 6.1 with the contributions from individual operators, the sensitivity to different structures of new physics is probed. As with the fit to the “inclusive” sample the initial value of the Wilson coefficient is taken to be 0.3 for  $\Lambda = 1$  TeV. This amounts to twelve fits, corresponding to the six EFT operators in Table 6.1 split by up-type quark flavour. In addition it is interesting to consider the case in which all of the vector operators contribute equally, by setting these Wilson couplings equal, corresponding to the assumption that the new physics interaction couples equally to left- and right-handed fermion fields.

For the CLFV signal in  $t\bar{t}$  decay there are six MC samples, as described in Section 6.3.2, which are inclusive of quark flavour. The decays  $t \rightarrow \mu\tau u$  and  $t \rightarrow \mu\tau c$  are expected to proceed in equal proportions in the MC, with small differences possible due to the different  $u$  and  $c$  quark masses. This has been checked using the flavour of the quark in the MC truth record. Table 7.7 shows the split of signal events with  $u$  and  $c$  quarks in the CLFV vertex in the “inclusive” decay sample for events entering any of the analysis regions. For

Table 7.7: Quark flavour in the CLFV vertex for  $t\bar{t}$  decay signal events in an operator-inclusive sample. The fractions are used to split each decay MC sample into separate  $u$  and  $c$  quark contributions.

	Yield	Fraction of matched
No match	$0.44 \pm 0.01$	-
$u$ quark	$6.35 \pm 0.04$	0.493
$c$ quark	$6.54 \pm 0.04$	0.507

a small fraction of events the truth matching procedure failed so these events are labelled as “no match”. The yield of each EFT decay MC sample is scaled using the fraction in the final column of the table, to split the quark flavour-inclusive samples into separate  $u$  and  $c$  quark contributions. Since the sensitivity to the CLFV signal is dominated by the  $gu_k \rightarrow t\mu\tau$  process, small variations of this fraction are expected to have negligible impact on the exclusion limits.

### 7.3.2 EFT results

The NP behaviour for each of the individual fits is seen to be consistent with the fit described in Section 7.2.2, with pulls on NPs seen to be in very close agreement. This is to be expected since the data and background models are identical. Some differences are seen in the relative importance of different signal modelling systematics between the EFT fits. For  $t\mu\tau c$  samples the PDF uncertainty on the  $gu_k \rightarrow t\mu\tau$  signal process has a larger impact than the parton shower and hadronisation uncertainty. For charm quark-initiated processes the PDF uncertainties are much larger than for up quark-initiated processes, as can be seen from the inclusive cross-sections for these processes in Table 6.4. Since the sensitivity of the fit is limited predominantly by the size of the dataset, the ranking of systematic NPs is not

discussed further.

Table 7.8: Observed and expected exclusion limits at 95% CL on each of the Wilson coefficients probed by the analysis, corresponding to the SMEFT operators shown in Table 6.1, along with existing (“previous”) limits from Ref. [143]. The limit on a given Wilson coefficient assumes contributions from other operators are set to zero. Limits on  $c_{lequ}^{1(ijk3)}$  and  $c_{lequ}^{3(ijk3)}$  from Ref. [143] have been scaled down by a factor of  $\sqrt{2}$  to account for the inclusion of the Hermitian conjugate of the corresponding operator ( $c_{lequ}^{1(ij3k)}$  and  $c_{lequ}^{3(ij3k)}$ , respectively).

$i, j = \mu, \tau$	Exclusion limits on SMEFT					
	Wilson coefficients at 95% CL					
	$c_{lq}^{-(ijk3)}$	$c_{eq}^{(ijk3)}$	$c_{lu}^{(ijk3)}$	$c_{eu}^{(ijk3)}$	$c_{lequ}^{1(ijk3)}$	$c_{lequ}^{3(ijk3)}$
<b>Previous (u) [143]</b>	12.0	12.0	12.0	12.0	18.4	2.4
<b>Expected (u)</b>	0.33	0.31	0.3	0.32	0.33	0.08
<b>Observed (u)</b>	0.43	0.41	0.4	0.42	0.44	0.10
<b>Previous (c) [143]</b>	14.0	14.0	14.0	14.0	20.5	2.6
<b>Expected (c)</b>	1.25	1.23	1.22	1.24	1.36	0.28
<b>Observed (c)</b>	1.62	1.59	1.58	1.60	1.78	0.36

Table 7.8 shows the existing limits on the relevant Wilson coefficients from Ref. [143] along with the expected and observed limits from this analysis. The observed limits are weaker compared to the expected limits by approximately 30% due to the slight excess observed in the data. The same expected and observed limits are shown graphically in Fig. 7.19. The exclusion limits on Wilson coefficients for each of the scalar and vector operators were similar since these processes have comparable cross-sections (see Table 6.4) and kinematic differences are small. The exclusion limits on the Wilson coefficients of the tensor operators are around three times stronger due to the larger cross-section of this process. The case in which each of the vector operators contributes equally has also been considered, assuming equal couplings of the hypothetical new physics to left- and right-handed fermions, as is the case in QED

and QCD. In this scenario the upper exclusion limit at 95% on the Wilson coefficients of vector operators is  $|c| < 0.21$  ( $|c| < 0.80$ ) for the  $t\mu\tau u$  ( $t\mu\tau c$ ) coupling. The exclusion limits on the branching ratio of the  $t \rightarrow \mu\tau u_k$  decay and on the Wilson coefficient values for the combined vector case are shown in Fig. 7.20, along with the scalar and tensor contributions.

The decay process has a more significant impact when considering the charm quark EFT operators, for which it contributes up to 11% of the sensitivity. The limits obtained on the Wilson coefficients significantly improve upon the previous results from Ref. [143]. The improvements range from a factor 7 for  $c_{lq}^{3(2323)}$  to 41 for  $c_{lequ}^{1(2313)}$ , where the upper indices 2323 (2313) represent a  $t\mu\tau c$  ( $t\mu\tau u$ ) vertex.

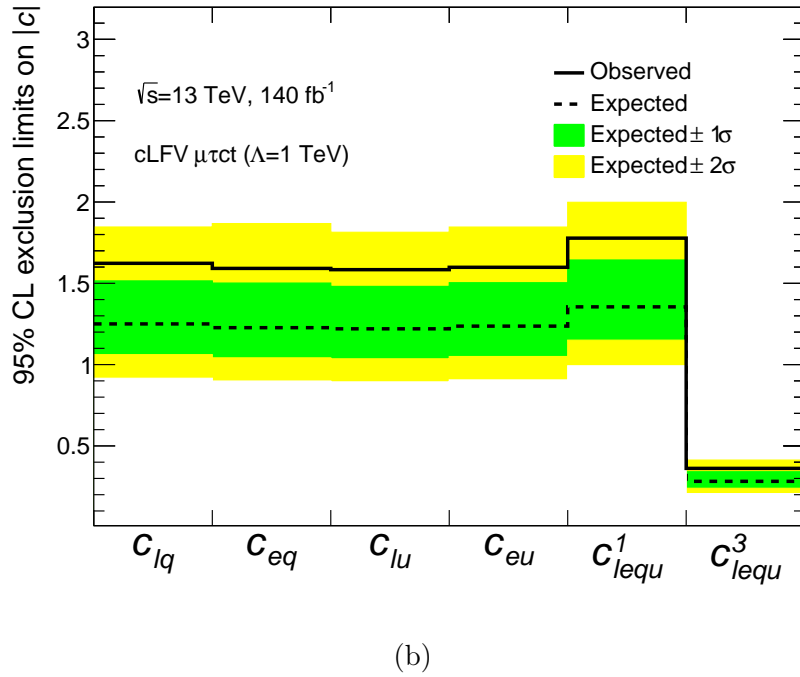
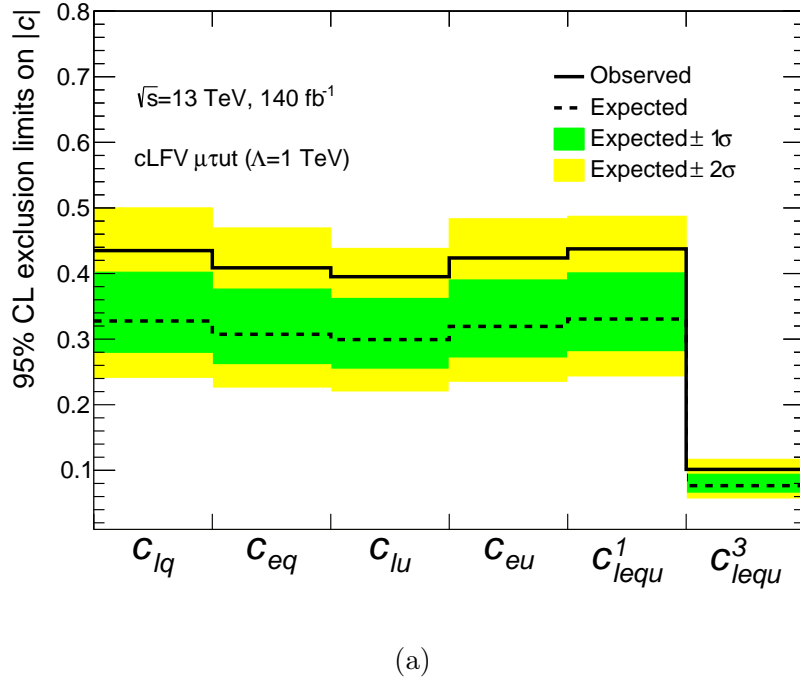
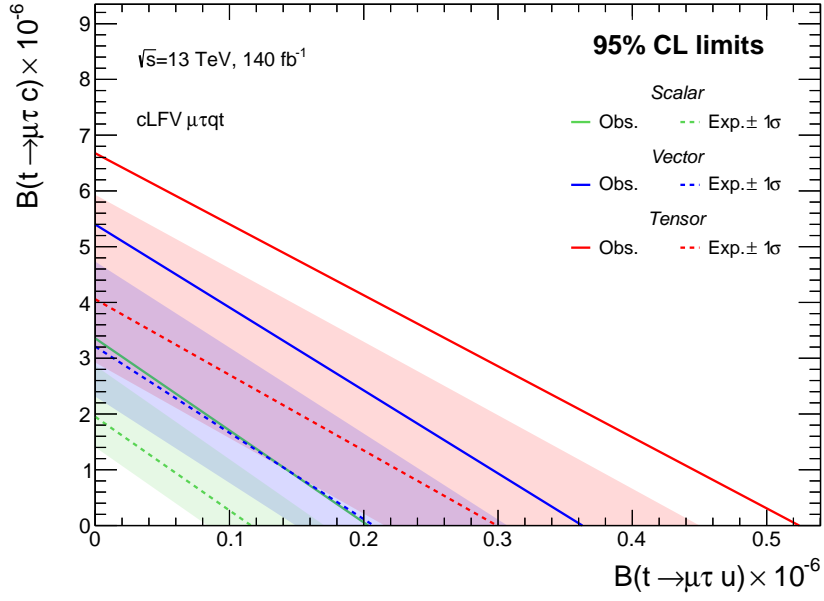
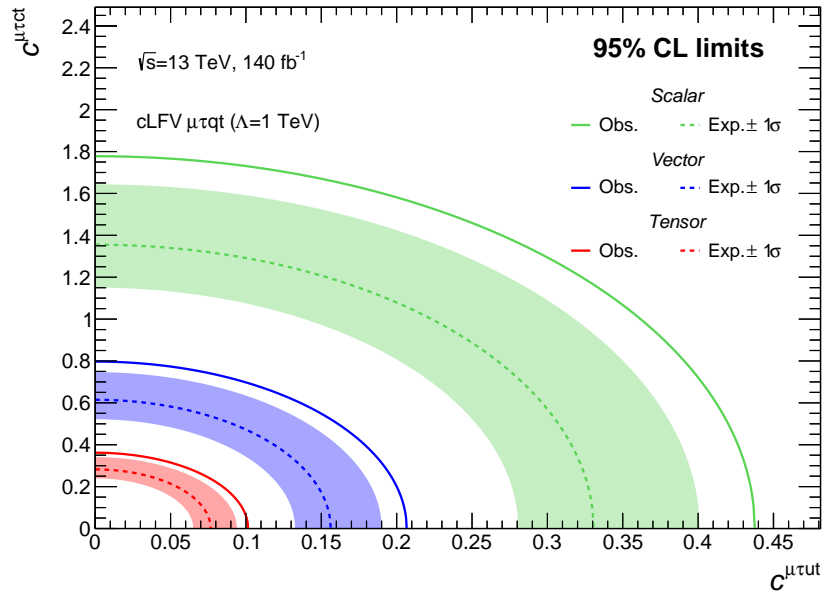


Figure 7.19: Observed and expected exclusion limits at 95% CL on each of the Wilson coefficients probed by the analysis, corresponding to the SMEFT operators shown in Table 6.1.  $\Lambda = 1$  TeV is the assumed scale of new physics. The limit on a given Wilson coefficient assumes contributions from other operators are set to zero.



(a)



(b)

Figure 7.20: Observed and expected exclusion limits at 95% CL on the branching ratio of the  $t \rightarrow \mu\tau u_k$  decay (a) and on the relevant Wilson coefficients (b) for scalar, vector and tensor couplings. Vector coupling here means all of the vector EFT operators contribute with equal values of their Wilson coefficients.  $\Lambda = 1$  TeV is the assumed scale of new physics.

## 7.4 Leptoquark interpretation

Leptoquarks would provide a clear source of tree-level CLFV processes. The model-independent CLFV search can therefore be reinterpreted in the context of an  $S_1$  scalar LQ capable of mediating the  $gu_k \rightarrow t\mu\tau$  process. The LQ interpretation is performed using the profile likelihood fit discussed in Section 7.1, replacing the “inclusive” EFT signal sample with the dedicated LQ samples introduced in Section 6.3.3. The analysis has not been re-optimised to search for a LQ signal so the event selections and fitted variables remain the same.

### 7.4.1 LQ interpretation procedure

Since a number of Yukawa couplings to lepton-quark pairs are probed simultaneously in the  $gu_k \rightarrow t\mu\tau$  process, a flavour hierarchy is assumed, as discussed in Section 6.2.2. Under this assumption the LQ model is fully described by a single coupling parameter  $\lambda$ , defined in Eq. (6.2), and the mass of the new scalar,  $m_{S_1}$ .

Simulated samples of LQ events have been produced for the process  $gc \rightarrow S_1\ell \rightarrow t\ell\ell'$  where  $\ell\ell' = \mu\tau$  and reweighted to account for the expected contribution of  $gu \rightarrow S_1\ell \rightarrow t\ell\ell'$  diagrams, which are suppressed by the flavour hierarchy. Generator-level samples have been produced for both processes for each mass and coupling point in Table 6.5 and used to derive a number of reweighting factors. Independent reweighting factors are derived for each mass and coupling point and for each bin of the  $H_T$  distribution in the SR. These correct for three effects:

- The increase in the total cross-section as a result of the  $gu \rightarrow S_1\ell \rightarrow t\ell\ell'$  contributions;
- Kinematic differences between the two processes; the main expected difference here is due to the effect of the PDFs which should lead to harder  $H_T$  distributions in

up-initiated processes;

- Differences in acceptance between the two processes for a given  $H_T$  bin when applying SR selection cuts at truth level.

The inclusion of up-initiated diagrams contributes an additional 10-15% to the cross-sections of the process. The values of the reweighting factors can be seen in Table F.1.

The cross-section of the  $gu_k \rightarrow S_1 \ell \rightarrow t\ell\ell'$  process is expected to scale with  $\lambda^4$ . This dependence originates from the dominance of off-shell LQ production for the model parameters probed by the analysis. From Ref. [147] the width of a scalar LQ only coupling to a single lepton-quark pair  $ij$  in the absence of fermion masses<sup>1</sup> is

$$\Gamma_{S_1} = \frac{|\lambda_{ij}|^2}{16\pi} m_{S_1}. \quad (7.5)$$

In the case that multiple lepton-quark decay channels are possible the width is found by summing over the possible fermion flavours  $i, j$ :

$$\Gamma_{S_1} = \frac{\sum_{i,j} |\lambda_{ij}|^2}{16\pi} m_{S_1}. \quad (7.6)$$

The width of the LQ model in this analysis is therefore driven by the  $t\tau$  coupling. The large width leads to an effective four-fermion interaction in which powers of  $\lambda^2$  from both LQ production and decay vertices contribute to the cross-section.

Fig. 7.21 shows the pre-fit signal-plus-background distribution in the SR according to simulation for  $m_{S_1} = 1$  TeV and coupling strengths of  $\lambda = 1.0$  and  $\lambda = 2.0$ . The signal yield is seen to increase significantly with coupling as a result of the  $\sigma \propto \lambda^4$  dependence.

---

<sup>1</sup>The top quark mass is clearly not negligible compared to a 500 GeV LQ; an expression for the width including fermion masses can be found in Ref. [52].

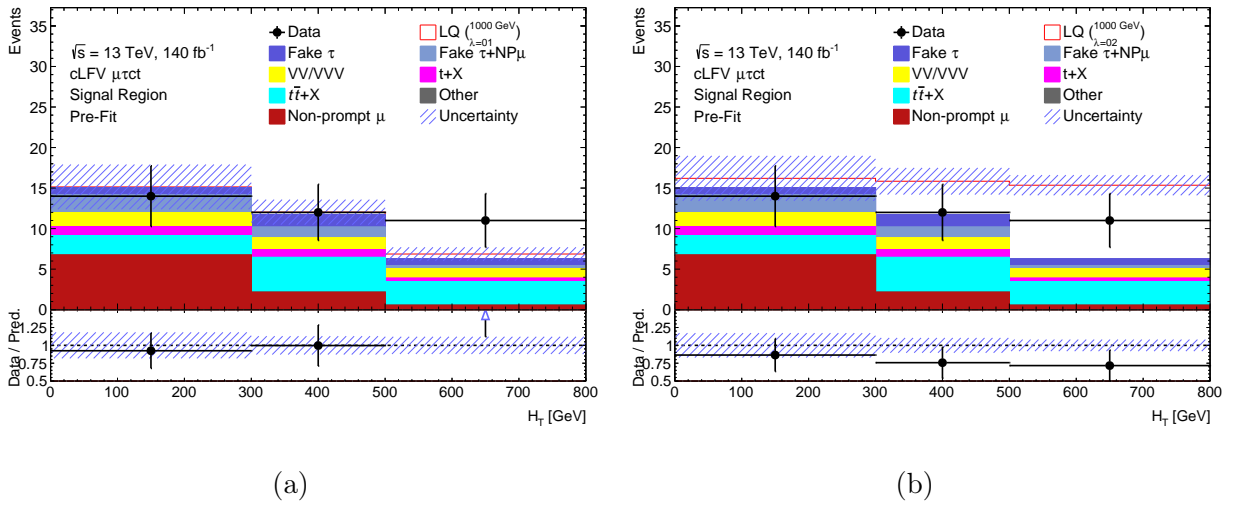


Figure 7.21: Expected pre-fit event yields in the SR according to simulation including signal contributions from an  $S_1$  leptoquark with  $m_{S_1} = 1 \text{ TeV}$  for coupling strengths of  $\lambda = 1.0$  (a) and  $\lambda = 2.0$  (b). The final bin does not have an upper bound. The uncertainty band includes both the statistical and systematic uncertainties. Note for the ratio in the lower panel the prediction (‘Pred’) includes the allowed signal contribution.

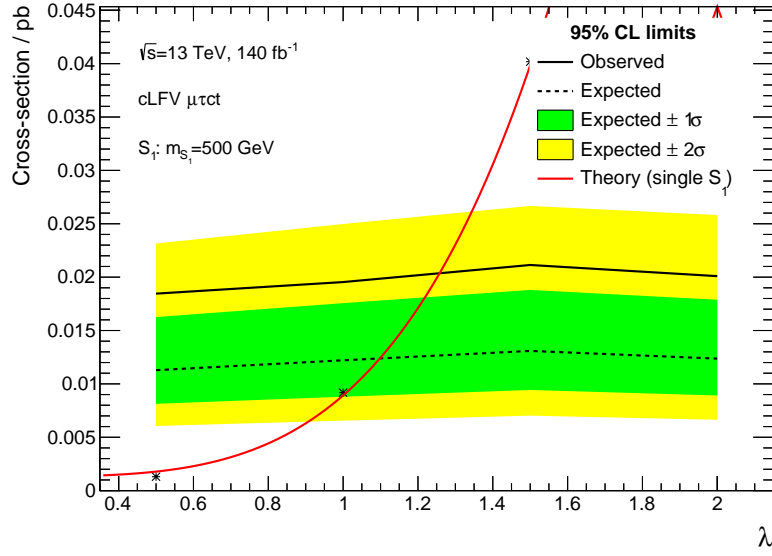
### 7.4.2 Exclusion limits on the LQ model

In the absence of an observed excess above the background model, exclusion limits are placed on the cross-section of each LQ sample. For a given value of  $\lambda$  and  $m_{S_1}$  the cross-section is predicted by the theory, in practice calculated at LO using the MG\_AMC@NLO generator. For a given  $m_{S_1}$  the exclusion limits on the cross-section for particular values of  $\lambda$  can be compared to the theoretical cross-section to extract an exclusion limit on  $\lambda$ . The resulting exclusion limits on  $\lambda$  as a function of  $m_{S_1}$  are used to construct an exclusion contour in  $\lambda$ - $m_{S_1}$  parameter space at 95% CL for the  $S_1$  model under the assumed flavour hierarchy.

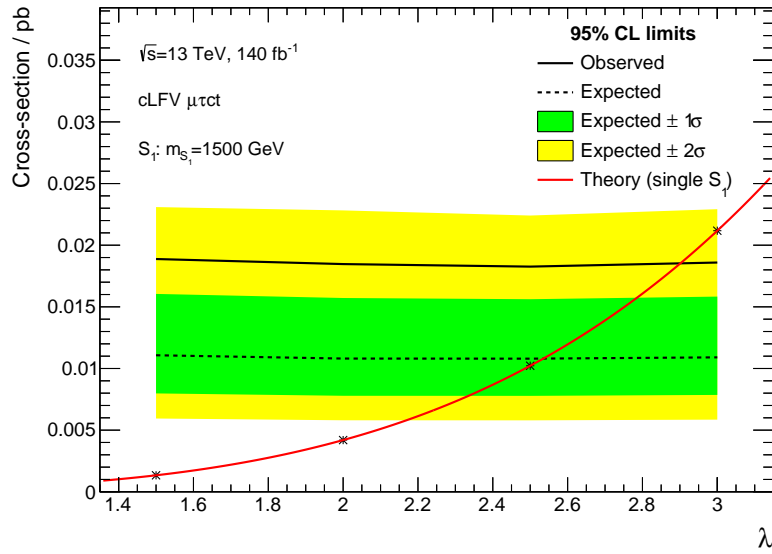
Exclusion limits on the cross-section of the  $gu_k \rightarrow S_1 \ell \rightarrow t\ell\ell'$  process as a function of  $\lambda$  for LQ masses of 0.5 and 1.5 TeV can be seen in Fig. 7.22. Similar plots for the other LQ mass points can be seen in Appendix F. The upper exclusion limit on  $\lambda$  corresponds to the value which would produce a cross-section equal to that which has been excluded by the fit. The excluded cross-section is stable as a function of  $\lambda$  and  $m_{S_1}$ , suggesting the kinematics of the process are similar across this range of mass and coupling values. Simple linear interpolation is therefore performed between excluded cross-section values. Interpolation between the generated theoretical cross-sections uses a quartic function since the cross-section is expected to scale with  $\lambda^4$ . The observed (expected) limits are found by extracting the value of  $\lambda$  for which the solid (dashed) black line intersects with the fit to the theoretical cross-section values, shown by the solid red line.

### 7.4.3 LQ results

As with the fits performed in the EFT interpretation, the NP behaviour is seen to be consistent with that of the fit described in Section 7.2.2. The NP ranking is also very similar to that described for the inclusive EFT fit with the dominant systematics originating from the



(a)



(b)

Figure 7.22: Exclusion limits at 95% CL on the cross-section of the  $gu_k \rightarrow S_1 \ell \rightarrow t\ell\ell'$  process as a function of the coupling  $\lambda$  for LQ masses of 0.5 (a) and 1.5 TeV (b). Expected limits are shown by the dashed black line with the  $\pm 1\sigma$  ( $\pm 2\sigma$ ) uncertainty bands shown in green (yellow); observed limits are shown by the solid black line. Black cross markers show theoretical predictions of the cross-section for particular values of  $\lambda$  and the solid red line show the quartic fit to these.

cross-section uncertainties on the  $t\bar{t}W$  and  $WZ$  processes and the limited MC statistics in the final bin of the SR. In some cases the signal FSR NP is also highly ranked. Nevertheless, the sensitivity to the signal process remains limited by the size of the dataset.

The exclusion limit on the cross-section of the  $gu_k \rightarrow S_1\ell \rightarrow t\ell\ell'$  process is observed to be approximately 18-20 fb across the range of mass and coupling values studied, as can be seen in Fig. 7.22. This is a weaker constraint than is obtained on the EFT signal due to the softer  $H_T$  distribution of the LQ signal which results in poorer signal-background separation. The observed and expected exclusion limits on  $\lambda$  as a function of  $m_{S_1}$  are shown in Table 7.9. The observed limits are weaker compared to the expected limits by approximately 15% due to the slight excess observed in the data. The same limits are also presented in Fig. 7.23 across the probed  $\lambda$ - $m_{S_1}$  parameter space. Observed (expected) upper exclusion limits on the coupling strength  $\lambda$  of an  $S_1$  LQ range from 1.26 (1.10) for a mass of 0.50 TeV to 3.68 (3.22) for a mass of 2.00 TeV. MC samples have also been generated for masses of 2.25 and 2.50 TeV; however, the cross-sections of these samples are lower than the excluded cross-section in all cases so none of the simulated coupling values are excluded at 95% CL.

As discussed in Section 6.2.2, interpreting the search for a hypothetical  $t\mu\tau u_k$  coupling in a LQ model requires the consideration of multi-generational LQ couplings. Other existing collider searches, a summary of which is given in Ref. [147], usually consider couplings to a single generation. More recently, searches considering couplings to different lepton and quark generations have been performed [215, 216], but still allowing only a single  $q - \ell$  coupling. To the best of the author's knowledge, this interpretation represents the first direct search for multi-generational LQ couplings.

Other collider searches are often based on searches for LQ pair production which provides the best sensitivity for low coupling strength; for higher coupling strengths, which are currently not excluded for third generation couplings, single LQ production is expected

Table 7.9: Upper exclusion limits at 95% CL on the  $S_1$  leptoquark coupling strength  $\lambda$  as a function of LQ mass.

$m_{S_1} / \text{GeV}$	Limit on $\lambda$ (95% CL)	
	Obs.	(Exp.)
500.0	1.26	(1.10)
750.0	1.66	(1.46)
1000.0	2.08	(1.82)
1250.0	2.48	(2.18)
1500.0	2.90	(2.54)
1750.0	3.31	(2.92)
2000.0	3.68	(3.22)

to be dominant [147]. The results in Table 7.9 and Fig. 7.23 depend on the assumed coupling hierarchy but demonstrate the power of considering single LQ production in extending exclusion sensitivity to higher masses than in the pair production searches.

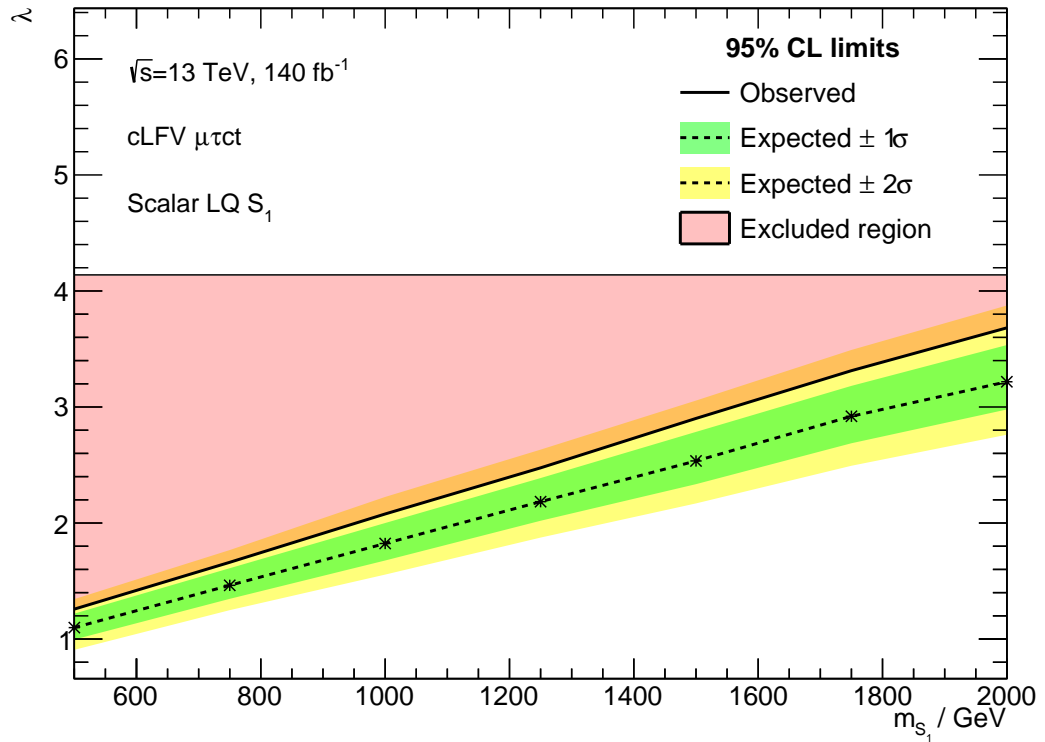


Figure 7.23: Exclusion limits at 95% CL on the  $S_1$  leptoquark model as a function of both coupling strength  $\lambda$  and LQ mass  $m_{S_1}$ . Expected limits are shown by the dashed black line with the  $\pm 1\sigma$  ( $\pm 2\sigma$ ) uncertainty bands shown in green (yellow); observed limits are shown by the solid black line. The region above the solid black line, shaded in red, is excluded and also extends upwards beyond  $\lambda = 4$ .

# Chapter 8

## Conclusions

Despite successfully explaining the behaviour of all known particles through the strong and unified electroweak interactions, the SM does not provide a complete description of the universe. Its failure to provide a candidate for dark matter or an origin for the large number of free parameters upon which it is built, among other issues, illustrate the need for further understanding. Precision measurements of SM predictions, which may yet show discrepancies from the theory, and direct searches for new physics processes will both be necessary to solve these outstanding problems. The ATLAS detector, along with the other LHC experiments, will continue to play an important role in such studies. The search analysis described in this thesis demonstrates the power of the existing ATLAS dataset to probe the effective coupling strengths of BSM operators in the EFT framework. The significantly larger datasets expected in coming years will allow SM parameters to be measured more precisely and smaller values of effective coupling strengths to be probed.

The planned upgrades to the LHC experiments are vital to allow these detectors to continue to record high quality data. The HL-LHC era in particular will provide new challenges to the detector in the form of increased pileup and higher radiation fields. Studies

presented in this thesis highlight the role of quality assurance procedures in providing confidence that new technologies developed for the ATLAS Inner Tracker (ITk) strip sensors will meet their performance requirements. Test devices have demonstrated good agreement with QA specifications; the few areas of disagreement are understood and are not expected to degrade the performance of the sensors. Strip sensor QA forms just a small part of the ongoing ITk project which will ensure that the upgraded ATLAS detector maintains its vertexing and tracking capabilities to allow precise object reconstruction for physics analyses throughout the HL-LHC era.

The search for charged lepton flavour violation (CLFV) in  $t\mu\tau u_k$  interactions presented in this thesis makes use of the full ATLAS Run 2 dataset and considers the processes  $t \rightarrow \mu\tau u_k$  in  $t\bar{t}$  decay and  $gu_k \rightarrow t\mu\tau$ . It is performed in a model-independent EFT framework to provide sensitivity to a range of new physics models which could induce such processes. The fitted observables are seen to be consistent with the SM hypothesis with no evidence for a CLFV signal observed. Exclusion limits are placed on the Wilson coefficients of SMEFT operators capable of inducing CLFV  $t\mu\tau u_k$  interactions, considering only dimension-6 operators which are expected to provide the leading contribution to such processes. The resulting limits significantly improve upon previous exclusion limits from Ref. [143], from a factor 8 for  $c_{lq}^{-(2323)}$  to a factor 59 for  $c_{lequ}^{1(2313)}$ , where the upper indices 2323 (2313) represent a  $t\mu\tau c$  ( $t\mu\tau u$ ) vertex. The sensitivity of the search is seen to be dominated by the  $gu_k \rightarrow t\mu\tau$  production process with the CLFV  $t\bar{t}$  decay processes improving the sensitivity by between 1-11% depending on the EFT operators considered.

The CLFV search is also interpreted in the context of a scalar  $S_1$  leptoquark model coupling to all flavours of up-type quarks and charged leptons, in which the couplings to each generation obey a fixed hierarchy. In this scenario, exclusion limits are placed at 95% CL on LQ coupling strengths in the range  $\lambda = 1.26$  to  $\lambda = 3.68$  for LQ masses of 500 to 2000 GeV.

The CLFV analysis is seen to be heavily statistically-limited. Even without any reduction of systematic uncertainties, significant improvements in sensitivity can be expected from extending the analysis to include data from Run 3 of the LHC and, further in the future, the HL-LHC datasets. A simple projection of the expected limits of the CLFV  $t\mu\tau u_k$  search to larger datasets recorded in future runs of the LHC is shown in Table 8.1. This projection was performed by using an Asimov dataset in all fitted regions, as was done in Section 7.1.4, thereby assuming the data matches the background expectation perfectly. The Asimov dataset is then scaled to the expected integrated luminosities of the future datasets and used to compute exclusion limits on the inclusive EFT signal process using the method described in Section 7.1.3. A total integrated luminosity of  $300 \text{ fb}^{-1}$  is expected to have been recorded by the ATLAS detector by the end of Run 3, including the Run 2 data. By the end of the HL-LHC era a total integrated luminosity of  $3000 \text{ fb}^{-1}$  is anticipated.

The baseline scenario assumes the relative sizes of all systematic uncertainties remain unchanged while the amount of data available increases. Scenarios in which the systematic uncertainties are reduced by 25% and 50% relative to their current size are also considered. Dominant systematic uncertainties contributing to the analysis include cross-section and modelling uncertainties applied to  $t\bar{t} + X$  and diboson processes. Some of these uncertainties are deliberately large, such as the 50% uncertainty applied to the  $t\bar{t}W$  process to cover differences between the observed and predicted cross-section [194, 206, 207], or the 30% uncertainty on the  $WZ$  process to account for poor modelling in jet multiplicity distributions [205]. Improvements in the MC modelling of these processes, along with updated theoretical calculations of their inclusive and differential cross-sections will allow such uncertainties to be reduced. Modelling uncertainties aside, reductions in the statistical uncertainties associated with efficiency scale factors applied to MC simulations, along with improvements in their measurement techniques, are expected to reduce a large number of instrumental sources of uncertainty.

Table 8.1: Expected exclusion limits on the branching ratio of the CLFV  $t \rightarrow \mu\tau u_k$  decay and on the relevant Wilson coefficients at 95% CL in the absence of evidence for signal with the inclusion of Run 3 and HL-LHC datasets.

ATLAS dataset	Systematic treatment	Expected limits (95% CL)	
		$\mathcal{B}(t \rightarrow \mu\tau q)$	$ c $
Run 2 (140 fb <sup>-1</sup> )	Run 2	$4.89 \times 10^{-7}$	0.064
Run 3 (300 fb <sup>-1</sup> )	Run 2	$3.25 \times 10^{-7}$	0.052
HL-LHC (3000 fb <sup>-1</sup> )	Run 2	$1.37 \times 10^{-7}$	0.034
HL-LHC (3000 fb <sup>-1</sup> )	Improved by 25%	$1.29 \times 10^{-7}$	0.033
HL-LHC (3000 fb <sup>-1</sup> )	Improved by 50%	$1.23 \times 10^{-7}$	0.032

The baseline scenario is already seen to give a large increase in sensitivity due to the statistically-limited nature of the analysis; inclusion of the Run 3 data with no improvements to the analysis sees a 35% improvement in sensitivity to  $\mathcal{B}(t \rightarrow \mu\tau q)$  and 20% improvement in sensitivity to SMEFT operators. In the best-case scenario, using the full HL-LHC dataset with systematic uncertainties reduced by 50%, a four-fold improvement is expected in sensitivity to  $\mathcal{B}(t \rightarrow \mu\tau q)$  and a factor of two improvement is expected in sensitivity to SMEFT operators.

It is worth noting that this projection assumes a centre-of-mass energy of 13.0 TeV is used in Run 3 and beyond which is not the case. The increase in the centre-of-mass energy from 13.0 to 13.6 TeV will alter the cross-sections of signal and background processes, changing their relative contributions to the SR. The cross-section of the  $gu_k \rightarrow t\mu\tau$  process, considering all SMEFT operators and including both  $u$ -initiated and  $c$ -initiated diagrams, increases by 14% from  $2.9_{-15\%}^{+19\%} \pm 0.9\%$  pb to  $3.3_{-15\%}^{+19\%} \pm 0.9\%$  fb<sup>1</sup>. The cross-sections of  $t\bar{t}$  and  $tW$  production increase by 11% from 13.0 to 13.6 TeV (see Table 8.2) so further sensitivity improvements may result from lower background yields relative to the signal size.

<sup>1</sup>These values are computed at LO with MG\_AMC@NLO 2.9.5 using the same setup as in Section 6.3.2.

Table 8.2: Theoretical cross-sections for  $gu_k \rightarrow t\mu\tau$  EFT signal and selected background processes in  $pp$  collisions at centre-of-mass energies of 13.0 and 13.6 TeV. The scale variation and PDF uncertainties are given.

Process	Cross-section as a function of $\sqrt{s}$ / pb		
	13.0 TeV	13.6 TeV	Change
$gu_k \rightarrow t\mu\tau$	$2.90^{+19\%}_{-15\%} \pm 0.9\%$	$3.31^{+19\%}_{-15\%} \pm 0.9\%$	+14%
$t\bar{t}$ [217]	$832^{+2.4\%}_{-3.5\%} \pm 4.2\%$	$924^{+2.4\%}_{-3.2\%} \pm 2.5\%$	+11%
$tW$ [218]	$79.3^{+2.4\%}_{-2.3\%} \pm 2.8\%$	$87.9^{+2.3\%}_{-2.2\%} \pm 2.7\%$	+11%

The results of the CLFV search complement searches for four-fermion  $te\mu u_k$  interactions by ATLAS [140] and CMS [141, 142], with the latter setting the most stringent limits to-date on SMEFT operators capable of inducing CLFV  $te\mu u_k$  interactions. Combination of the exclusion limits on  $te\mu u_k$  and  $t\mu\tau u_k$  operators is not of interest in the context of the SMEFT framework, but may become relevant in the context of specific models which predict relationships between their effective coupling strengths. The LQ model discussed in Section 6.2.2 is one such example. Due to the statistically-limited nature of the search discussed in this thesis, a combination with any future CMS  $t\mu\tau u_k$  search could prove fruitful. Such combinations are complicated by the unknown correlations between the systematic uncertainties considered by the two collaborations. However, the effect of assumptions about such correlations is of sub-leading importance for statistically-limited searches.

Another future avenue of interest would be a search for a  $te\tau u_k$  interaction, which has not yet been explored directly, though indirect constraints can be found in Ref. [143]. Some sensitivity to this coupling exists in the ATLAS and CMS  $te\mu u_k$  searches [140–142] due to the possibility for leptonic  $\tau$ -lepton decays. The ATLAS analysis constrained the branching ratio  $\mathcal{B}(t \rightarrow \ell^\pm \ell'^\mp q) < 1.86 \times 10^{-5}$  at 95% CL, where  $q = \{u, c\}$  and  $\ell, \ell' = \{e, \mu, \tau\}$  [140], but this has not been interpreted in the context of  $te\tau u_k$  SMEFT operators.

# References

- [1] ATLAS Collaboration, *The ATLAS Experiment at the CERN Large Hadron Collider*, [JINST](#) **3** (2008) S08003.
- [2] ATLAS Collaboration, *Search for charged-lepton-flavour violating  $\mu\tau q t$  interactions in top-quark production and decay with the ATLAS detector at the LHC*, ATLAS-CONF-2023-001, 2023, URL: <https://cds.cern.ch/record/2845451>.
- [3] ATLAS Collaboration, *Observation of a new particle in the search for the Standard Model Higgs boson with the ATLAS detector at the LHC*, [Physics Letters B](#) **716** (2012) 1.
- [4] CMS Collaboration, *Observation of a new boson at a mass of 125 GeV with the CMS experiment at the LHC*, [Physics Letters B](#) **716** (2012) 30.
- [5] ATLAS Collaboration, *Luminosity determination in pp collisions at  $\sqrt{s} = 13$  TeV using the ATLAS detector at the LHC*, (2022), arXiv: [2212.09379](https://arxiv.org/abs/2212.09379) [[hep-ex](#)].
- [6] E. Fermi, *Sulla quantizzazione del gas perfetto monoatomico (On the Quantization of the Monoatomic Ideal Gas)*, [Rendiconti Lincei](#) **3** (1926) 145.
- [7] P. A. M. Dirac, *On the theory of quantum mechanics*, [Proceedings of the Royal Society A](#) **112** (762 1926) 661–677.
- [8] S. N. Bose, *Plancks Gesetz und Lichtquantenhypothese (Planck’s law and hypothesis of light quanta)*, [Zeitschrift für Physik](#) **26** (1924) 178.
- [9] A. Einstein, *Quantentheorie des einatomigen idealen Gases (Quantum theory of the monatomic ideal gas.)*, [Sitzungsberichte der Preussischen Akademie der Wissenschaften, Physikalisch-mathematische Klasse](#) (1924) 261.
- [10] A. Einstein, *Quantentheorie des einatomigen idealen Gases. Zweite Abhandlung. (Quantum theory of the monatomic ideal gas. Second Treatise)*, [Sitzungsberichte der Preussischen Akademie der Wissenschaften, Physikalisch-mathematische Klasse](#) (1925) 3.
- [11] W. Pauli, *Über den Zusammenhang des Abschlusses der Elektronengruppen im Atom mit der Komplexstruktur der Spektren (On the Connection between the Completion of Electron Groups in an Atom with the Complex Structure of Spectra)*, [Zeitschrift für Physik](#) **31** (1925) 765.

- 
- [12] N. Bohr, *I. On the constitution of atoms and molecules*, *The London, Edinburgh, and Dublin Philosophical Magazine and Journal of Science* **26** (1913) 1.
- [13] J. J. Thomson, *XL. Cathode Rays*, *The London, Edinburgh, and Dublin Philosophical Magazine and Journal of Science* **44** (1897) 293.
- [14] S. H. Neddermeyer et al., *Note on the Nature of Cosmic-Ray Particles*, *Phys. Rev.* **51** (10 1937) 884.
- [15] H. Yukawa, *On the Interaction of Elementary Particles. I*, *Progress of Theoretical Physics Supplement* **1** (1955) 1.
- [16] C. Lattes et al., *Processes involving charged mesons*, *Nature* **159** (1947).
- [17] G. D. Rochester et al., *Evidence for the Existence of New Unstable Elementary Particles*, *Nature* **160** (1947).
- [18] M. Gell-Mann, *The Eightfold Way: A Theory of Strong Interaction Symmetry*, (1961).
- [19] G. Zweig, *An  $SU_3$  model for strong interaction symmetry and its breaking; Version 1*, (1964), An updated version of the paper is available as CERN-TH-412, Feb. 1964., URL: <http://cds.cern.ch/record/352337>.
- [20] E. M. Riordan, *The Discovery of quarks*, *Science* **256** (1992) 1287.
- [21] E. Rutherford, *LXXIX. The scattering of  $\alpha$  and  $\beta$  particles by matter and the structure of the atom*, *The London, Edinburgh, and Dublin Philosophical Magazine and Journal of Science* **21** (1911) 669.
- [22] O. W. Greenberg, *Spin and Unitary-Spin Independence in a Paraquark Model of Baryons and Mesons*, *Phys. Rev. Lett.* **13** (20 1964) 598.
- [23] M. Y. Han et al., *Three-Triplet Model with Double  $SU(3)$  Symmetry*, *Phys. Rev.* **139** (4B 1965) B1006.
- [24] M. L. Perl et al., *Evidence for Anomalous Lepton Production in  $e^+ - e^-$  Annihilation*, *Phys. Rev. Lett.* **35** (22 1975) 1489.
- [25] F. Abe et al., *Observation of Top Quark Production in  $\bar{p}p$  Collisions with the Collider Detector at Fermilab*, *Phys. Rev. Lett.* **74** (14 1995) 2626.
- [26] S. Abachi et al., *Observation of the Top Quark*, *Phys. Rev. Lett.* **74** (14 1995) 2632.
- [27] K. Kodama et al., *Observation of tau neutrino interactions*, *Physics Letters B* **504** (2001) 218.
- [28] A. Einstein, *Generation and conversion of light with regard to a heuristic point of view*, *Annalen der Physik* **17** (1905) 132.
- [29] *The Nobel Prize in Physics 1965*, NobelPrize.org. Nobel Prize Outreach AB 2023. [Online; accessed 12 June 2023]., 1965, URL: <https://www.nobelprize.org/prizes/physics/1965/summary/>.
- [30] A. Salam et al., *Electromagnetic and weak interactions*, *Physics Letters* **13** (1964) 168.
- [31] S. Weinberg, *A Model of Leptons*, *Phys. Rev. Lett.* **19** (21 1967) 1264.

- 
- [32] G. Arnison et al., *Experimental observation of isolated large transverse energy electrons with associated missing energy at  $\sqrt{s}=540$  GeV*, *Physics Letters B* **122** (1983) 103.
- [33] M. Banner et al., *Observation of single isolated electrons of high transverse momentum in events with missing transverse energy at the CERN pp collider*, *Physics Letters B* **122** (1983) 476.
- [34] G. Arnison et al., *Experimental observation of lepton pairs of invariant mass around  $95$  GeV/ $c^2$  at the CERN SPS collider*, *Physics Letters B* **126** (1983) 398.
- [35] P. Bagnaia et al., *Evidence for  $Z^0 \rightarrow e^+e^-$  at the CERN pp collider*, *Physics Letters B* **129** (1983) 130.
- [36] H. Fritzsch et al., *Advantages of the color octet gluon picture*, *Physics Letters B* **47** (1973) 365.
- [37] D. P. Barber et al., *Discovery of Three-Jet Events and a Test of Quantum Chromodynamics at PETRA*, *Phys. Rev. Lett.* **43** (12 1979) 830.
- [38] M. W. Guidry, *Gauge field theories: an introduction with applications*, Wiley, 1999, ISBN: 978-0-471-63117-5.
- [39] M. Thomson, *Modern particle physics*, Cambridge University Press, 2013, ISBN: 978-1-107-03426-6.
- [40] P. W. Higgs, *Broken Symmetries and the Masses of Gauge Bosons*, *Phys. Rev. Lett.* **13** (16 1964) 508.
- [41] F. Englert et al., *Broken Symmetry and the Mass of Gauge Vector Mesons*, *Phys. Rev. Lett.* **13** (9 1964) 321.
- [42] G. S. Guralnik et al., *Global Conservation Laws and Massless Particles*, *Phys. Rev. Lett.* **13** (20 1964) 585.
- [43] P. Langacker, *Grand unified theories and proton decay*, *Physics Reports* **72** (1981) 185.
- [44] L. Calibbi et al., *Charged Lepton Flavour Violation: An Experimental and Theoretical Introduction*, *La Rivista del Nuovo Cimento* **41** (2018) 71–174.
- [45] Y. Fukuda et al., *Evidence for Oscillation of Atmospheric Neutrinos*, *Phys. Rev. Lett.* **81** (8 1998) 1562.
- [46] Q. R. Ahmad et al., *Measurement of the Rate of  $\nu_e + d \rightarrow p + p + e^-$  Interactions Produced by  $^8\text{B}$  Solar Neutrinos at the Sudbury Neutrino Observatory*, *Phys. Rev. Lett.* **87** (7 2001) 071301.
- [47] Q. R. Ahmad et al., *Direct Evidence for Neutrino Flavor Transformation from Neutral-Current Interactions in the Sudbury Neutrino Observatory*, *Phys. Rev. Lett.* **89** (1 2002) 011301.
- [48] T. J. Kim et al., *Correlation between  $R_{D^{(*)}}$  and top quark FCNC decays in leptoquark models*, *JHEP* **2019** (2019).
- [49] G. Branco et al., *Theory and phenomenology of two-Higgs-doublet models*, *Physics Reports* **516** (2012).

- 
- [50] R. Primulando et al., *Collider constraints on lepton flavor violation in the 2HDM*, *Phys. Rev. D* **101** (2020).
- [51] H. Georgi et al., *Unity of All Elementary-Particle Forces*, *Phys. Rev. Lett.* **32** (8 1974) 438.
- [52] I. Doršner and S. Fajfer and A. Greljo and J.F. Kamenik and N. Košnik, *Physics of leptoquarks in precision experiments and at particle colliders*, *Physics Reports* **641** (2016) 1.
- [53] Particle Data Group et al., *Review of Particle Physics*, *PTEP* **2022** (2022) 083C01.
- [54] E. Fermi, *An attempt of a theory of beta radiation. 1.*, *Z. Phys.* **88** (1934) 161.
- [55] B. Grzadkowski et al., *Dimension-six terms in the Standard Model Lagrangian*, *JHEP* **2010** (2010).
- [56] L. Evans et al., *LHC Machine*, *JINST* **3** (2008) S08001.
- [57] *LHC / HL-LHC Plan updated in February 2022*, [Online; accessed 18 September 2023], URL: <https://hilumilhc.web.cern.ch/article/ls3-schedule-change>.
- [58] CMS Collaboration, *The CMS experiment at the CERN LHC. The Compact Muon Solenoid experiment*, *JINST* **3** (2008) S08004.
- [59] LHCb Collaboration, *The LHCb Detector at the LHC*, *JINST* **3** (2008) S08005.
- [60] ALICE Collaboration, *The ALICE experiment at the CERN LHC*, *JINST* **3** (2008) S08002.
- [61] E. Lopienska, *The CERN accelerator complex, layout in 2022.*, (2022), General Photo, URL: <https://cds.cern.ch/record/2800984>.
- [62] B Salvachua, *Overview of Proton-Proton Physics during Run 2*, (2019) 7, URL: <https://cds.cern.ch/record/2750272>.
- [63] R. Reed, *The Upgrade of the ATLAS Tile Calorimeter Readout Electronics for Phase II*, *Journal of Physics Conference Series* 1742-6588 **623** (2014).
- [64] ATLAS Collaboration, *Experiment Briefing: Keeping the ATLAS Inner Detector in perfect alignment*, General Photo, 2020, URL: <https://cds.cern.ch/record/2723878>.
- [65] ATLAS Collaboration, *ATLAS Insertable B-Layer: Technical Design Report*, ATLAS-TDR-19; CERN-LHCC-2010-013, 2010, URL: <https://cds.cern.ch/record/1291633>.
- [66] J. Pequeno, *Computer Generated image of the ATLAS calorimeter*, 2008, URL: <https://cds.cern.ch/record/1095927>.
- [67] Particle Data Group et al., *Review of Particle Physics*, *PTEP* **2020** (2020) 083C01.
- [68] P. Camarri et al., *RPCs for the ATLAS Level-1 muon trigger: test beam results*, tech. rep., CERN, 1998, URL: <http://cds.cern.ch/record/683756>.
- [69] ATLAS Collaboration, *Operation of the ATLAS trigger system in Run 2*, *JINST* **15** (2020) P10004, arXiv: 2007.12539 [hep-ex].

- 
- [70] O. Aberle et al., *High-Luminosity Large Hadron Collider (HL-LHC): Technical design report*, CERN Yellow Reports: Monographs, Geneva: CERN, 2020, URL: <https://cds.cern.ch/record/2749422>.
- [71] ATLAS Collaboration, *Technical Design Report for the ATLAS Inner Tracker Strip Detector*, tech. rep., CERN, 2017, URL: <https://cds.cern.ch/record/2257755>.
- [72] G. Lutz, *Semiconductor radiation detectors: device physics*, Berlin: Springer, 1999 43, URL: <https://cds.cern.ch/record/411172>.
- [73] *Pn-junction-equilibrium-graphs.png*, on Wikimedia Commons under the [CC-BY-SA-3.0](https://creativecommons.org/licenses/by-sa/3.0/) Unported license; [Online; accessed 10 March 2021], URL: <https://commons.wikimedia.org/wiki/File:Pn-junction-equilibrium-graphs.png>.
- [74] A. Chilingarov, *Temperature dependence of the current generated in Si bulk*, *JINST* **8** (2013) 10003.
- [75] M. Moll, *Displacement Damage in Silicon Detectors for High Energy Physics*, *IEEE Transactions on Nuclear Science* **65** (2018) 1561.
- [76] ATLAS Collaboration, *The ATLAS Experiment at the CERN Large Hadron Collider*, *JINST* **3** (2008) S08003.
- [77] ATLAS Collaboration, *ITk Pixel Layout Updates*, <https://atlas.web.cern.ch/Atlas/GROUPS/PHY/2020-002>, 2020.
- [78] M. Ullán et al., *Quality Assurance methodology for the ATLAS Inner Tracker strip sensor production*, *Nucl. Instrum. Meth. A* **981** (2020) 164521.
- [79] P. Allport et al., *Pre-production results from ATLAS ITk Strip Sensors Quality Assurance Testchip*, *JINST* **17** (2022) C11002.
- [80] G. Lindstrom, *Radiation damage in silicon detectors*, *Nucl. Instrum. Meth. A* **512** (2003) 30, ed. by P. Holl et al.
- [81] V. Latoňová et al., *Characterization of the polysilicon resistor in silicon strip sensors for ATLAS inner tracker as a function of temperature, pre- and post-irradiation*, *Nucl. Instrum. Meth. A* **1050** (2023) 168119.
- [82] S. Hirose et al., *ATLAS ITk strip sensor quality assurance tests and results of ATLAS18 pre-production sensors*, tech. rep., CERN, 2023, URL: <https://cds.cern.ch/record/2846069>.
- [83] A. Buckley et al., *LHAPDF6: parton density access in the LHC precision era*, *Eur. Phys. J. C* **75** (2015).
- [84] HERA Study Group, *HERA - A Proposal for a Large Electron Proton Colliding Beam Facility at DESY*, DESY-HERA-81-10, 1981, URL: <https://bib-pubdb1.desy.de/record/318643>.
- [85] R. R. Wilson, *Tevatron*, *Phys. Today* **30** (1977) 23.
- [86] J. Butterworth et al., *PDF4LHC recommendations for LHC Run II*, *J. Phys. G* **43** (2016) 023001, arXiv: 1510.03865 [[hep-ph](https://arxiv.org/abs/1510.03865)].

- 
- [87] E. Bothmann et al., *Event generation with Sherpa 2.2*, *SciPost Phys.* **7** (2019) 034, arXiv: [1905.09127 \[hep-ph\]](#).
- [88] J. Alwall et al., *The automated computation of tree-level and next-to-leading order differential cross sections, and their matching to parton shower simulations*, *JHEP* **07** (2014) 079, arXiv: [1405.0301 \[hep-ph\]](#).
- [89] S. Frixione et al., *A positive-weight next-to-leading-order Monte Carlo for heavy flavour hadroproduction*, *JHEP* **09** (2007) 126, arXiv: [0707.3088 \[hep-ph\]](#).
- [90] P. Nason, *A new method for combining NLO QCD with shower Monte Carlo algorithms*, *JHEP* **11** (2004) 040, arXiv: [hep-ph/0409146](#).
- [91] S. Frixione et al., *Matching NLO QCD computations with parton shower simulations: the POWHEG method*, *JHEP* **11** (2007) 070, arXiv: [0709.2092 \[hep-ph\]](#).
- [92] S. Alioli et al., *A general framework for implementing NLO calculations in shower Monte Carlo programs: the POWHEG BOX*, *JHEP* **06** (2010) 043, arXiv: [1002.2581 \[hep-ph\]](#).
- [93] T. Sjöstrand et al., *An introduction to PYTHIA 8.2*, *Comput. Phys. Commun.* **191** (2015) 159, arXiv: [1410.3012 \[hep-ph\]](#).
- [94] J. Bellm et al., *Herwig 7.0/Herwig++ 3.0 release note*, *Eur. Phys. J. C* **76** (2016) 196, arXiv: [1512.01178 \[hep-ph\]](#).
- [95] J. Bellm et al., *Herwig 7.1 Release Note*, (2017), arXiv: [1705.06919 \[hep-ph\]](#).
- [96] ATLAS Collaboration, *ATLAS Run 1 Pythia8 tunes*, tech. rep. ATL-PHYS-PUB-2014-021, CERN, 2014, URL: <https://cds.cern.ch/record/1966419>.
- [97] R. D. Ball et al., *Parton distributions with LHC data*, *Nucl. Phys. B* **867** (2013) 244, arXiv: [1207.1303 \[hep-ph\]](#).
- [98] S. Schumann et al., *A parton shower algorithm based on Catani–Seymour dipole factorisation*, *JHEP* **03** (2008) 038, arXiv: [0709.1027 \[hep-ph\]](#).
- [99] D. J. Lange, *The EvtGen particle decay simulation package*, *Nucl. Instrum. Meth. A* **462** (2001) 152.
- [100] T. Sjöstrand et al., *A brief introduction to PYTHIA 8.1*, *Comput. Phys. Commun.* **178** (2008) 852, arXiv: [0710.3820 \[hep-ph\]](#).
- [101] ATLAS Collaboration, *The Pythia 8 A3 tune description of ATLAS minimum bias and inelastic measurements incorporating the Donnachie–Landshoff diffractive model*, ATL-PHYS-PUB-2016-017, 2016, URL: <https://cds.cern.ch/record/2206965>.
- [102] ATLAS Collaboration, *Public ATLAS Luminosity Results for Run-2 of the LHC*, 2019, URL: <https://twiki.cern.ch/twiki/bin/view/AtlasPublic/LuminosityPublicResultsRun2>.
- [103] ATLAS Collaboration, *ATLAS data quality operations and performance for 2015–2018 data-taking*, *JINST* **15** (2020) P04003, arXiv: [1911.04632 \[physics.ins-det\]](#).
- [104] GEANT4 Collaboration et al., *GEANT4 – a simulation toolkit*, *Nucl. Instrum. Meth. A* **506** (2003) 250.

- 
- [105] ATLAS Collaboration, *The simulation principle and performance of the ATLAS fast calorimeter simulation FastCaloSim*, ATL-PHYS-PUB-2010-013, 2010, URL: <https://cds.cern.ch/record/1300517>.
- [106] ATLAS Collaboration, *Electron and photon performance measurements with the ATLAS detector using the 2015–2017 LHC proton–proton collision data*, *JINST* **14** (2019) P12006, arXiv: 1908.00005 [hep-ex].
- [107] G. Aad et al., *Electron and photon energy calibration with the ATLAS detector using LHC Run 2 data*, (2023), arXiv: 2309.05471, URL: <https://cds.cern.ch/record/2870086>.
- [108] ATLAS Collaboration, *Electron reconstruction and identification in the ATLAS experiment using the 2015 and 2016 LHC proton–proton collision data at  $\sqrt{s} = 13$  TeV*, *Eur. Phys. J. C* **79** (2019) 639, arXiv: 1902.04655 [hep-ex].
- [109] ATLAS Collaboration, *Muon reconstruction and identification efficiency in ATLAS using the full Run 2 pp collision data set at  $\sqrt{s} = 13$  TeV*, *Eur. Phys. J. C* **81** (2021) 578, arXiv: 2012.00578 [hep-ex].
- [110] ATLAS Collaboration, *Studies of the muon momentum calibration and performance of the ATLAS detector with pp collisions at  $\sqrt{s} = 13$  TeV.*, *Eur. Phys. J. C* **83** (2023) 686, arXiv: 2212.07338 [hep-ex].
- [111] ATLAS Collaboration, *Muon reconstruction performance of the ATLAS detector in proton–proton collision data at  $\sqrt{s} = 13$  TeV*, *Eur. Phys. J. C* **76** (2016) 292, arXiv: 1603.05598 [hep-ex].
- [112] M. Cacciari et al., *The anti- $k_t$  jet clustering algorithm*, *JHEP* **04** (2008) 063, arXiv: 0802.1189 [hep-ph].
- [113] ATLAS Collaboration, *Topological cell clustering in the ATLAS calorimeters and its performance in LHC Run 1*, *Eur. Phys. J. C* **77** (2017) 490, arXiv: 1603.02934 [hep-ex].
- [114] ATLAS Collaboration, *Properties of jets and inputs to jet reconstruction and calibration with the ATLAS detector using proton–proton collisions at  $\sqrt{s} = 13$  TeV*, ATL-PHYS-PUB-2015-036, 2015, URL: <https://cds.cern.ch/record/2044564>.
- [115] ATLAS Collaboration, *Jet reconstruction and performance using particle flow with the ATLAS Detector*, *Eur. Phys. J. C* **77** (2017) 466, arXiv: 1703.10485 [hep-ex].
- [116] ATLAS Collaboration, *Jet energy scale and resolution measured in proton–proton collisions at  $\sqrt{s} = 13$  TeV with the ATLAS detector*, *Eur. Phys. J. C* **81** (2020) 689, arXiv: 2007.02645 [hep-ex].
- [117] ATLAS Collaboration, *Performance of pile-up mitigation techniques for jets in pp collisions at  $\sqrt{s} = 8$  TeV using the ATLAS detector*, *Eur. Phys. J. C* **76** (2016) 581, arXiv: 1510.03823 [hep-ex].
- [118] ATLAS Collaboration, *ATLAS flavour-tagging algorithms for the LHC Run 2 pp collision dataset*, (2022), arXiv: 2211.16345 [physics.data-an].

- 
- [119] ATLAS Collaboration, *ATLAS  $b$ -jet identification performance and efficiency measurement with  $t\bar{t}$  events in  $pp$  collisions at  $\sqrt{s} = 13$  TeV*, *Eur. Phys. J. C* **79** (2019) 970, arXiv: 1907.05120 [hep-ex].
- [120] ATLAS Collaboration, *Measurement of the  $c$ -jet mistagging efficiency in  $t\bar{t}$  events using  $pp$  collision data at  $\sqrt{s} = 13$  TeV collected with the ATLAS detector*, *Eur. Phys. J. C* **82** (2021) 95, arXiv: 2109.10627 [hep-ex].
- [121] ATLAS Collaboration, *Calibration of the light-flavour jet mistagging efficiency of the  $b$ -tagging algorithms with  $Z$ +jets events using  $139\text{ fb}^{-1}$  of ATLAS proton–proton collision data at  $\sqrt{s} = 13$  TeV*, *Eur. Phys. J. C* **83** (2023) 728, arXiv: 2301.06319 [hep-ex].
- [122] ATLAS Collaboration,  *$E_T^{\text{miss}}$  performance in the ATLAS detector using 2015–2016 LHC  $pp$  collisions*, ATLAS-CONF-2018-023, 2018, URL: <https://cds.cern.ch/record/2625233>.
- [123] ATLAS Collaboration, *Identification and energy calibration of hadronically decaying tau leptons with the ATLAS experiment in  $pp$  collisions at  $\sqrt{s} = 8$  TeV*, *Eur. Phys. J. C* **75** (2015) 303, arXiv: 1412.7086 [hep-ex].
- [124] ATLAS Collaboration, *Reconstruction, Energy Calibration, and Identification of Hadronically Decaying Tau Leptons in the ATLAS Experiment for Run-2 of the LHC*, ATL-PHYS-PUB-2015-045, 2015, URL: <https://cds.cern.ch/record/2064383>.
- [125] ATLAS Collaboration, *Measurement of the tau lepton reconstruction and identification performance in the ATLAS experiment using  $pp$  collisions at  $\sqrt{s} = 13$  TeV*, ATLAS-CONF-2017-029, 2017, URL: <https://cds.cern.ch/record/2261772>.
- [126] T Barillari et al., *Local Hadronic Calibration*, tech. rep., CERN, 2008, URL: <https://cds.cern.ch/record/1112035>.
- [127] ATLAS Collaboration, *Reconstruction of hadronic decay products of tau leptons with the ATLAS experiment*, *Eur. Phys. J. C* **76** (2016) 295, arXiv: 1512.05955 [hep-ex].
- [128] ATLAS Collaboration, *Identification of hadronic tau lepton decays using neural networks in the ATLAS experiment*, ATL-PHYS-PUB-2019-033, 2019, URL: <https://cds.cern.ch/record/2688062>.
- [129] ATLAS Collaboration, *PromptLeptonTaggerIFF*, (ATLAS internal document) [Online; accessed 30 August 2023], URL: <https://twiki.cern.ch/twiki/bin/view/AtlasProtected/PromptLeptonTaggerIFF>.
- [130] ATLAS Collaboration, *Evidence for the associated production of the Higgs boson and a top quark pair with the ATLAS detector*, *Phys. Rev. D* **97** (2018) 072003, arXiv: 1712.08891 [hep-ex].
- [131] D Adams et al., *Recommendations of the Physics Objects and Analysis Harmonisation Study Groups 2014*, (ATLAS internal document), Geneva, 2014, URL: <https://cds.cern.ch/record/1700874>.
- [132] ATLAS Collaboration, *ATLAS Software Documentation: Introduction to Overlap Removal*, [Online; accessed 26 August 2023], URL: [https://atlassoftwaredocs.web.cern.ch/AnalysisSWTutorial/obj\\_olr\\_intro](https://atlassoftwaredocs.web.cern.ch/AnalysisSWTutorial/obj_olr_intro).

- 
- [133] MEG Collaboration, *Search for the lepton flavour violating decay  $\mu^+ \rightarrow e^+ \gamma$  with the full dataset of the MEG experiment*, *Eur. Phys. J. C* **76** (2016).
- [134] SINDRUM Collaboration, *Search for the decay  $\mu^+ \rightarrow e^+ e^+ e^-$* , *Nuclear Phys. B* **299** (1988) 1.
- [135] ATLAS Collaboration, *Searches for lepton-flavour-violating decays of the Higgs boson in  $\sqrt{s} = 13$  TeV pp collisions with the ATLAS detector*, *Phys. Lett. B* **800** (2020) 135069, arXiv: 1907.06131 [hep-ex].
- [136] ATLAS Collaboration, *Search for charged-lepton-flavour violation in Z-boson decays with the ATLAS detector*, *Nature Phys.* **17** (2021) 819, arXiv: 2010.02566 [hep-ex].
- [137] CMS Collaboration, *Search for lepton flavour violating decays of the Higgs boson to  $\mu\tau$  and  $e\tau$  in proton–proton collisions at  $\sqrt{s} = 13$  TeV*, *JHEP* **06** (2018) 001, arXiv: 1712.07173 [hep-ex].
- [138] Belle Collaboration, *Search for lepton-flavor-violating  $\tau$  decays into three leptons with 719 million produced  $\tau^+ \tau^-$  pairs*, *Physics Letters B* **687** (2010) 139, arXiv: 1001.3221 [hep-ex].
- [139] LHCb Collaboration, *Search for the lepton flavour violating decay  $\tau^- \rightarrow \mu^- \mu^+ \mu^-$* , *JHEP* **02** (2015) 121, arXiv: 1409.8548 [hep-ex].
- [140] ATLAS Collaboration, *Search for charged lepton-flavour violation in top-quark decays at the LHC with the ATLAS detector*, ATLAS-CONF-2018-044, 2018, URL: <https://cds.cern.ch/record/2638305>.
- [141] CMS Collaboration, *Search for charged-lepton flavor violation in top quark production and decay in pp collisions at  $\sqrt{s} = 13$  TeV*, *JHEP* **06** (2022) 082, arXiv: 2201.07859 [hep-ex].
- [142] CMS Collaboration, *Search for charged lepton flavor violation in the top quark sector in trilepton final states with the CMS detector at  $\sqrt{s} = 13$  TeV*, CMS-PAS-TOP-22-005, 2023, URL: <https://cds.cern.ch/record/2851002>.
- [143] M. Chala et al., *Constraining four-fermion operators using rare top decays*, *JHEP* **2019** (2019), arXiv: 1809.09624 [hep-ph].
- [144] ATLAS Collaboration, *Search for flavour-changing neutral current top-quark decays  $t \rightarrow qZ$  in proton–proton collisions at  $\sqrt{s} = 13$  TeV with the ATLAS detector*, *JHEP* **07** (2018) 176, arXiv: 1803.09923 [hep-ex].
- [145] D. Bečirević et al., *Scalar leptoquarks from GUT to accommodate the B-physics anomalies*, *Phys. Rev. D* **98** (2018), arXiv: 1806.05689 [hep-ph].
- [146] B. Diaz et al., *The leptoquark Hunter’s guide: Pair production*, *JHEP* **10** (2017) 097, arXiv: 1706.05033 [hep-ph].
- [147] M. Schmaltz et al., *The leptoquark Hunter’s guide: large coupling*, *JHEP* **01** (2019) 132, arXiv: 1810.10017 [hep-ph].
- [148] E. Alvarez et al., *Nonresonant leptoquark with multigeneration couplings for  $\mu\mu jj$  and  $\mu\nu jj$  at the LHC*, *Phys. Rev. D* **99** (2019) 095004, arXiv: 1811.05944 [hep-ph].

- 
- [149] I. de Medeiros Varzielas et al., *Simplified Models of Flavourful Leptoquarks*, *Eur. Phys. J. C* **79** (2019) 536, arXiv: 1901.10484 [hep-ph].
- [150] W.-F. Chang et al., *Charged Lepton Flavor Violating Processes and Scalar Leptoquark Decay Branching Ratios in the Colored Zee-Babu Model*, *JHEP* **10** (2016) 106, arXiv: 1608.05511 [hep-ph].
- [151] S. Höche et al., *QCD matrix elements + parton showers. The NLO case*, *JHEP* **04** (2013) 027, arXiv: 1207.5030 [hep-ph].
- [152] E. Re, *Single-top  $Wt$ -channel production matched with parton showers using the POWHEG method*, *Eur. Phys. J. C* **71** (2011) 1547, arXiv: 1009.2450 [hep-ph].
- [153] S. Alioli et al., *NLO single-top production matched with shower in POWHEG:  $s$ - and  $t$ -channel contributions*, *JHEP* **09** (2009) 111, arXiv: 0907.4076 [hep-ph].
- [154] R. Frederix et al., *Single-top  $t$ -channel hadroproduction in the four-flavour scheme with POWHEG and aMC@NLO*, *JHEP* **09** (2012) 130, arXiv: 1207.5391 [hep-ph].
- [155] C. Degrande et al., *UFO - The Universal FeynRules Output*, *Comput. Phys. Commun.* **183** (2012) 1201, arXiv: 1108.2040 [hep-ph].
- [156] A. Alloul et al., *FeynRules 2.0 - A complete toolbox for tree-level phenomenology*, *Comput. Phys. Commun.* **185** (2014) 2250, arXiv: 1310.1921 [hep-ph].
- [157] J. A. A. Saavedra et al., *Interpreting top-quark LHC measurements in the standard-model effective field theory*, (2018), arXiv: 1802.07237 [hep-ph], URL: <http://cds.cern.ch/record/2305783>.
- [158] Particle Data Group et al., *Review of Particle Physics*, *PTEP* **2020** (2020) 083C01.
- [159] ATLAS Collaboration, *Studies on top-quark Monte Carlo modelling for Top2016*, ATL-PHYS-PUB-2016-020, 2016, URL: <https://cds.cern.ch/record/2216168>.
- [160] ATLAS Collaboration, *Measurement of the charge asymmetry in top-quark pair production in association with a photon with the ATLAS experiment*, *Physics Letters B* **843** (2022) 137848, arXiv: 2212.10552 [hep-ex].
- [161] M. Beneke et al., *Hadronic top-quark pair production with NNLL threshold resummation*, *Nucl. Phys. B* **855** (2012) 695, arXiv: 1109.1536 [hep-ph].
- [162] M. Cacciari et al., *Top-pair production at hadron colliders with next-to-next-to-leading logarithmic soft-gluon resummation*, *Phys. Lett. B* **710** (2012) 612, arXiv: 1111.5869 [hep-ph].
- [163] P. Bärnreuther et al., *Percent-Level-Precision Physics at the Tevatron: Next-to-Next-to-Leading Order QCD Corrections to  $q\bar{q} \rightarrow t\bar{t} + X$* , *Phys. Rev. Lett.* **109** (2012) 132001, arXiv: 1204.5201 [hep-ph].
- [164] M. Czakon et al., *NNLO corrections to top-pair production at hadron colliders: the all-fermionic scattering channels*, *JHEP* **12** (2012) 054, arXiv: 1207.0236 [hep-ph].
- [165] M. Czakon et al., *NNLO corrections to top pair production at hadron colliders: the quark-gluon reaction*, *JHEP* **01** (2013) 080, arXiv: 1210.6832 [hep-ph].

- [166] M. Czakon et al., *Total Top-Quark Pair-Production Cross Section at Hadron Colliders Through  $O(\alpha_S^4)$* , *Phys. Rev. Lett.* **110** (2013) 252004, arXiv: 1303.6254 [hep-ph].
- [167] M. Czakon et al., *Top++: A program for the calculation of the top-pair cross-section at hadron colliders*, *Comput. Phys. Commun.* **185** (2014) 2930, arXiv: 1112.5675 [hep-ph].
- [168] S. Frixione et al., *Single-top hadroproduction in association with a W boson*, *JHEP* **07** (2008) 029, arXiv: 0805.3067 [hep-ph].
- [169] D. de Florian et al., *Handbook of LHC Higgs Cross Sections: 4. Deciphering the Nature of the Higgs Sector*, (2016), arXiv: 1610.07922 [hep-ph].
- [170] T. Gleisberg et al., *Comix, a new matrix element generator*, *JHEP* **12** (2008) 039, arXiv: 0808.3674 [hep-ph].
- [171] F. Buccioni et al., *OpenLoops 2*, *Eur. Phys. J. C* **79** (2019) 866, arXiv: 1907.13071 [hep-ph].
- [172] F. Cascioli et al., *Scattering Amplitudes with Open Loops*, *Phys. Rev. Lett.* **108** (2012) 111601, arXiv: 1111.5206 [hep-ph].
- [173] A. Denner et al., *COLLIER: A fortran-based complex one-loop library in extended regularizations*, *Comput. Phys. Commun.* **212** (2017) 220, arXiv: 1604.06792 [hep-ph].
- [174] S. Höche et al., *A critical appraisal of NLO+PS matching methods*, *JHEP* **09** (2012) 049, arXiv: 1111.1220 [hep-ph].
- [175] S. Catani et al., *QCD Matrix Elements + Parton Showers*, *JHEP* **11** (2001) 063, arXiv: hep-ph/0109231.
- [176] S. Höche et al., *QCD matrix elements and truncated showers*, *JHEP* **05** (2009) 053, arXiv: 0903.1219 [hep-ph].
- [177] ATLAS Collaboration, *Performance of the ATLAS trigger system in 2015*, *Eur. Phys. J. C* **77** (2017) 317, arXiv: 1611.09661 [hep-ex].
- [178] ATLAS Collaboration, *Performance of electron and photon triggers in ATLAS during LHC Run 2*, *Eur. Phys. J. C* **80** (2020) 47, arXiv: 1909.00761 [hep-ex].
- [179] ATLAS Collaboration, *Performance of the ATLAS muon triggers in Run 2*, *JINST* **15** (2020) P09015, arXiv: 2004.13447 [hep-ex].
- [180] ATLAS Collaboration,  *$E/\gamma$  trigger recommendations for Run 2 data*, URL: <https://twiki.cern.ch/twiki/bin/view/Atlas/TrigEgammaRecommendations2015>.
- [181] ATLAS Collaboration, *Muon Trigger Physics Recommendations Rel. 21 2017*, URL: <https://twiki.cern.ch/twiki/bin/view/Atlas/MuonTriggerPhysicsRecommendationsRel212017>.
- [182] ATLAS Collaboration, *Vertex Reconstruction Performance of the ATLAS Detector at  $\sqrt{s} = 13$  TeV*, ATL-PHYS-PUB-2015-026, 2015, URL: <https://cds.cern.ch/record/2037717>.
- [183] ATLAS Collaboration, *Comparison of vertex reconstruction quantities in ATLAS software releases 21 and 20.7 for 2016 proton-proton data*, URL: <https://atlas.web.cern.ch/Atlas/GROUPS/PHYSICS/PLOTS/IDTR-2017-006>.

- 
- [184] ATLAS Collaboration, *Selection of jets produced in 13 TeV proton–proton collisions with the ATLAS detector*, ATLAS-CONF-2015-029, 2015, URL: <https://cds.cern.ch/record/2037702>.
- [185] ATLAS Collaboration, *Quark versus Gluon Jet Tagging Using Charged-Particle Constituent Multiplicity with the ATLAS Detector*, ATL-PHYS-PUB-2017-009, 2017, URL: <https://cds.cern.ch/record/2263679>.
- [186] ATLAS Collaboration, *Measurements of b-jet tagging efficiency with the ATLAS detector using  $t\bar{t}$  events at  $\sqrt{s} = 13$  TeV*, *JHEP* **08** (2018) 089, arXiv: 1805.01845 [hep-ex].
- [187] ATLAS Collaboration, *Measurement of the  $t\bar{t}$  production cross-section in the lepton+jets channel at  $\sqrt{s} = 13$  TeV with the ATLAS experiment*, *Phys. Lett. B* **810** (2020) 135797, arXiv: 2006.13076 [hep-ex].
- [188] S. Frixione et al., *Matching NLO QCD computations and parton shower simulations*, *JHEP* **06** (2002) 029, arXiv: hep-ph/0204244.
- [189] S. Frixione et al., *Matching NLO QCD and parton showers in heavy flavour production*, *JHEP* **08** (2003) 007, arXiv: hep-ph/0305252.
- [190] ATLAS Collaboration, *ATLAS Pythia 8 tunes to 7 TeV data*, ATL-PHYS-PUB-2014-021, 2014, URL: <https://cds.cern.ch/record/1966419>.
- [191] L. A. Harland-Lang et al., *Parton distributions in the LHC era: MMHT 2014 PDFs*, *Eur. Phys. J. C* **75** (2015) 204, arXiv: 1412.3989 [hep-ph].
- [192] G. Bevilacqua et al., *Modeling uncertainties of  $t\bar{t}W^\pm$  multilepton signatures*, *Phys. Rev. D* **105** (2022).
- [193] L. Ferencz et al., *Study of  $t\bar{t}b\bar{b}$  and  $t\bar{t}W$  background modelling for  $t\bar{t}H$  analyses*, tech. rep., CERN, 2022, URL: <https://cds.cern.ch/record/2812088>.
- [194] ATLAS Collaboration, *Measurement of the total and differential cross-sections of  $t\bar{t}W$  production in pp collisions at 13 TeV with the ATLAS detector*, ATLAS-CONF-2023-019, 2023, URL: <https://cds.cern.ch/record/2855337>.
- [195] A. D. Martin et al., *Parton distributions for the LHC*, *Eur. Phys. J. C* **63** (2009) 189, arXiv: 0901.0002 [hep-ph].
- [196] A. D. Martin et al., *Uncertainties on  $\alpha_S$  in global PDF analyses and implications for predicted hadronic cross sections*, *Eur. Phys. J. C* **64** (2009) 653, arXiv: 0905.3531 [hep-ph].
- [197] H.-L. Lai et al., *New parton distributions for collider physics*, *Phys. Rev. D* **82** (2010) 074024, arXiv: 1007.2241 [hep-ph].
- [198] J. Gao et al., *CT10 next-to-next-to-leading order global analysis of QCD*, *Phys. Rev. D* **89** (2014) 033009, arXiv: 1302.6246 [hep-ph].
- [199] ATLAS and CMS Collaborations, *Combination of ATLAS and CMS results on the mass of the top-quark using up to  $4.9\text{ fb}^{-1}$  of  $\sqrt{s} = 7$  TeV LHC data*, ATLAS-CONF-2013-102, 2013, URL: <https://cds.cern.ch/record/1601811>.

- 
- [200] LHCTopWG, *NLO single-top channel cross sections*, 2015, URL: <https://twiki.cern.ch/twiki/bin/view/LHCPhysics/SingleTopRefXsec>.
- [201] N. Kidonakis, *Two-loop soft anomalous dimensions for single top quark associated production with a  $W^-$  or  $H^-$* , *Phys. Rev. D* **82** (2010) 054018, arXiv: 1005.4451 [hep-ph].
- [202] N. Kidonakis, “Top Quark Production”, *Proceedings, Helmholtz International Summer School on Physics of Heavy Quarks and Hadrons (HQ 2013)* (JINR, Dubna, Russia, July 15–28, 2013) 139, arXiv: 1311.0283 [hep-ph].
- [203] ATLAS Collaboration, *Observation of the associated production of a top quark and a  $Z$  boson in  $pp$  collisions at  $\sqrt{s} = 13$  TeV with the ATLAS detector*, *JHEP* **07** (2020) 124, arXiv: 2002.07546 [hep-ex].
- [204] A. Kulesza et al., *Associated top quark pair production with a heavy boson: differential cross sections at NLO + NNLL accuracy*, *Eur. Phys. J. C* **80** (2020) 428.
- [205] ATLAS Collaboration, *Measurement of  $W^\pm Z$  production cross sections and gauge boson polarisation in  $pp$  collisions at  $\sqrt{s} = 13$  TeV with the ATLAS detector*, *Eur. Phys. J. C* **79** (2019) 535, arXiv: 1902.05759 [hep-ex].
- [206] R. Frederix et al., *On improving NLO merging for  $ttW$  production*, *JHEP* **2021** (2021).
- [207] L. Buonocore et al., *Associated production of a  $W$  boson with a top-antitop quark pair: next-to-next-to-leading order QCD predictions for the LHC*, 2023, arXiv: 2306.16311 [hep-ph].
- [208] M. Pinamonti et al., *Documentation for TRExFitter*, [Online; accessed 4 September 2023], URL: <https://trexfitter-docs.web.cern.ch/trexfitter-docs/>.
- [209] W. Verkerke et al., *The RooFit toolkit for data modeling*, 2003, arXiv: physics/0306116 [physics.data-an].
- [210] K. Cranmer et al., *HistFactory: A tool for creating statistical models for use with RooFit and RooStats*, tech. rep., New York U., 2012, URL: <https://cds.cern.ch/record/1456844>.
- [211] *Friedman in Proc. of the 1974 CERN School of Computing*, Norway, 1974, URL: <https://cds.cern.ch/record/186223>.
- [212] G. Cowan et al., *Asymptotic formulae for likelihood-based tests of new physics*, *Eur. Phys. J. C* **71** (2011).
- [213] A. L. Read, *Modified frequentist analysis of search results (the  $CL_s$  method)*, (2000), URL: <https://cds.cern.ch/record/451614>.
- [214] S. S. Wilks, *The Large-Sample Distribution of the Likelihood Ratio for Testing Composite Hypotheses*, *The Annals of Mathematical Statistics* **9** (1938) 60 .
- [215] ATLAS Collaboration, *Search for pair-produced scalar and vector leptoquarks decaying into third-generation quarks and first- or second-generation leptons in  $pp$  collisions with the ATLAS detector*, *JHEP* **2023** (2023).

- 
- [216] ATLAS Collaboration, *Search for leptoquark pair production decaying into  $te^{-}\bar{t}e^{+}$  or  $t\mu^{-}\bar{t}\mu^{+}$  in multi-lepton final states in  $pp$  collisions at 13 TeV with the ATLAS detector*, 2023, arXiv: [2306.17642](https://arxiv.org/abs/2306.17642) [[hep-ex](#)].
- [217] LHCTopWG, *NNLO+NNLL top-quark-pair cross sections*, 2015, URL: <https://twiki.cern.ch/twiki/bin/view/LHCPhysics/TtbarNNLO>.
- [218] LHCTopWG, *Predictions at NNLO of single top-quark production cross-sections*, 2023, URL: <https://twiki.cern.ch/twiki/bin/view/LHCPhysics/SingleTopNNLORef>.
- [219] A. Buckley et al., *Rivet user manual*, *Comput. Phys. Commun.* **184** (2013) 2803.
- [220] P. Richardson, *Rivet analyses reference: MC\_TAU\_Decay - Analysis of Kinematic distributions for  $\tau$  lepton decays*, URL: [https://rivet.hepforge.org/analyses/MC\\_TAU\\_Decay.html](https://rivet.hepforge.org/analyses/MC_TAU_Decay.html).

# Appendices

# Appendix A

## Event selection

### A.1 Analysis framework for preliminary results

A preliminary set of results for the CLFV analysis were released in [2], as discussed in Section 7.2.1. In addition to the SR definition discussed there, other small differences between the preliminary analysis and the full analysis are as follows:

- The luminosity and its uncertainty have been updated to reflect the final ATLAS Run 2 measurement, presented in [5].
- The overlap removal procedure described in Section 5.3.8 previously included muons with no isolation requirements applied.
- The treatment of the uncertainties on the fake  $\tau_{\text{had-vis}}$  background were updated to propagate the individual sources of uncertainty discussed in Section 6.7. Previously an envelope around these was taken for real and fake  $\tau_{\text{had-vis}}$  candidates in  $\text{CR}\tau$ .
- The cross-section for the  $t\bar{t}W$  process was updated to reflect the latest LHC Top working group recommendation of 722.4 fb based on [206].

The analysis is heavily statistically-limited so changes to the systematic model are seen to have a very small effect on the sensitivity.

## A.2 Signal contamination removal

Section 6.4.2 introduces a simultaneous cut on the leading muon  $p_T$  and the invariant masses of oppositely-charged muon pairs. This cut was derived using a region with the same selection as  $VR_\mu$  except that it requires exactly one jet instead of two or more jets. This region,  $CR_\mu$ , was originally used as a non-prompt muon CR but was replaced with  $CRt\bar{t}\mu$  which was seen to provide a larger event sample and to be better enriched in events with non-prompt muons. Having identified suitable pair of variables, scans were performed over linear combinations of these variables to identify the combination which minimised the signal-over-background ratio while maintaining a sufficient background yield. The effect of this cut on simulation and data in  $VR_\mu$  is shown in Fig. A.2.

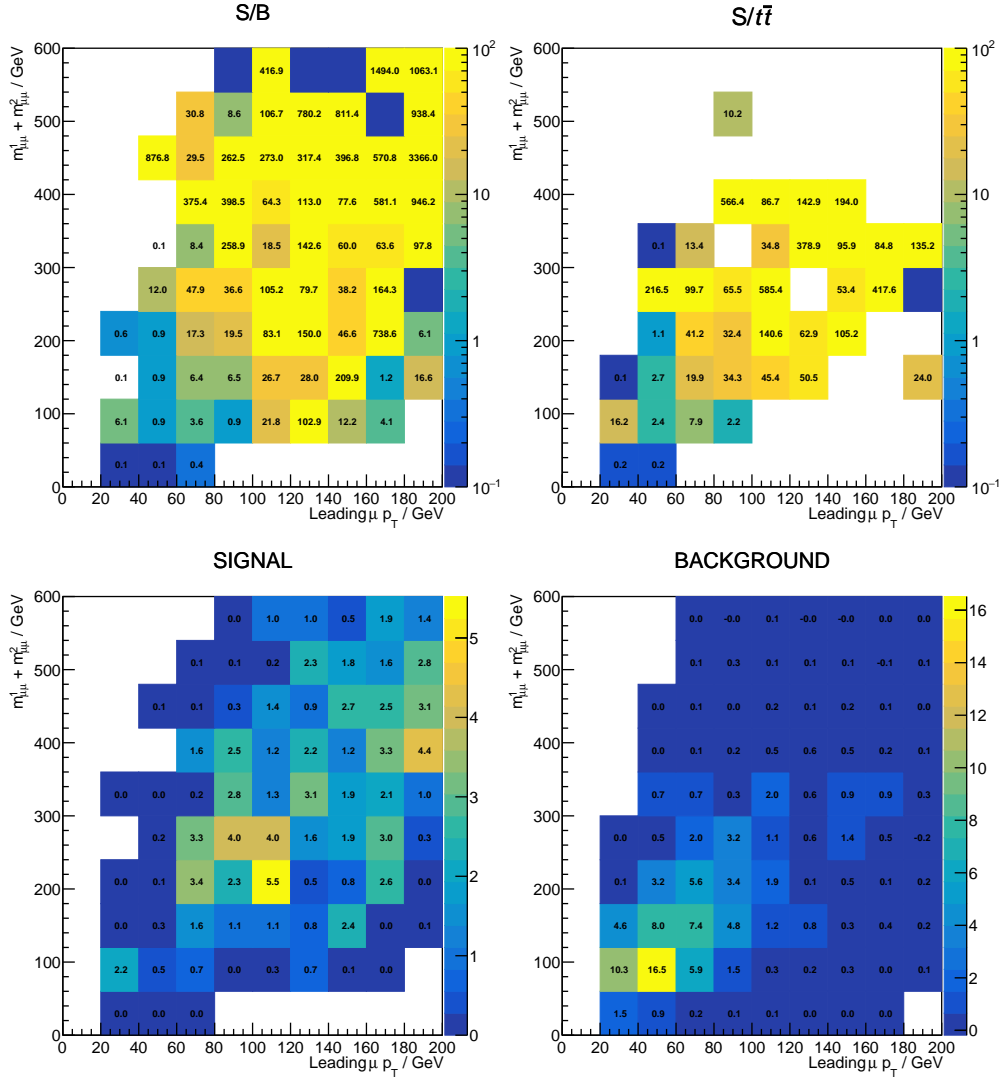


Figure A.1: Distributions of signal and background yields in a previous analysis region,  $CR\mu$ , motivating the use of a simultaneous cut on leading muon  $p_T$  and dimuon invariant mass to remove signal contamination from  $VR\mu$  and  $CRTt\bar{t}\mu$ . The bottom left (right) panel shows the percentage of the inclusive EFT signal (total background) entering each bin; the top left (right) panel shows the ratio of the signal distribution to the total background ( $t\bar{t}$  background).

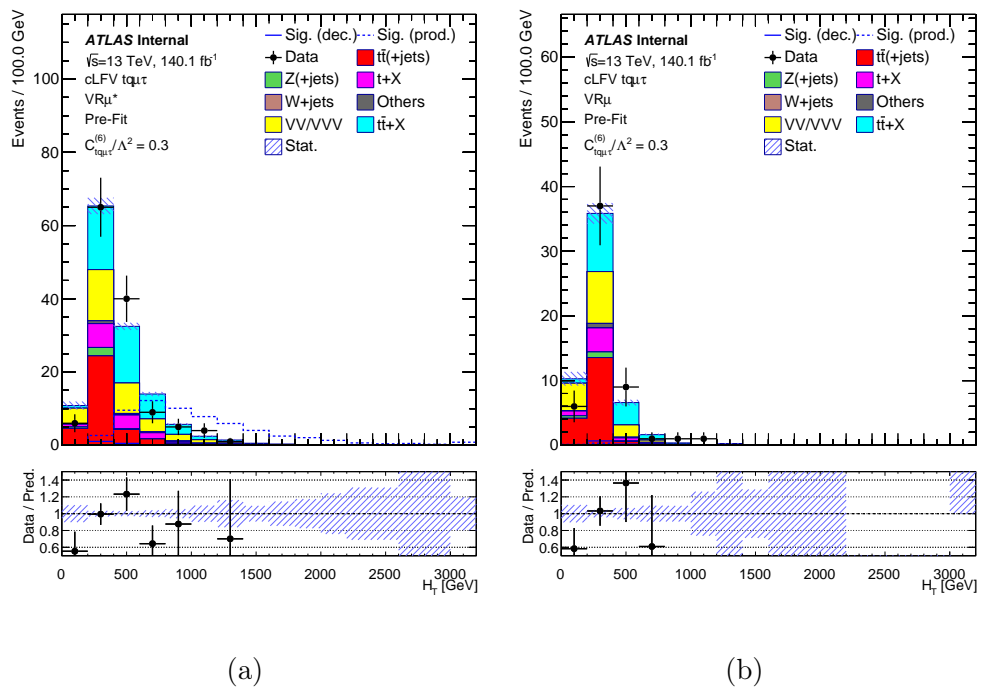


Figure A.2: Distribution of the  $H_T$  variable, corresponding to the scalar sum of lepton and jet  $p_T$ , in VR $\mu$  according to MC simulation before (a) and after (b) the application of the cut to remove signal contamination. The final bin does not have an upper bound.

# Appendix B

## Herwig alternative signal sample reweighting

The branching fractions (BFs) for tau lepton decays are seen to be mismodelled in the alternative signal samples showered with HERWIG 7.1.6 which are used to evaluate the signal parton shower and hadronisation uncertainty. The alternative signal samples have been showered with HERWIG 7.1.6 but the problem has also been seen in HERWIG 7.2 and the origin of this problem is not well understood. The problem affects both leptonic and hadronic tau decays. The mismodelling is seen only to affect the BFs, while the kinematics of the decays do not appear to be mismodelled. Therefore the samples have been reweighted to correct the tau decay BFs.

Table B.1 shows the BFs of different tau decays for the inclusive signal samples showered with PYTHIA 8 and HERWIG 7.1, compared to world-average measurements from [53]. The relative MC statistical uncertainties on the BFs shown range from approximately 0.6% to 3.0% and are larger for the smaller BFs. Samples showered with PYTHIA 8 have BFs which are generally consistent with the values in [53]. The CLFV  $gu_k \rightarrow t\mu\tau$  production

Table B.1: Tau lepton BF's for inclusive EFT signal samples showered with PYTHIA 8 and HERWIG 7.1, compared to world-average measurements from [53]. The derived reweighting factors,  $f_{RW}$ , are also shown. Production refers to the CLFV  $gu_k \rightarrow t\mu\tau$  process while decay refers to the CLFV  $t\bar{t}$  decay process.

Decay mode	Production			Decay			PDG [53]
	Pythia	Herwig	$f_{RW}$	Pythia	Herwig	$f_{RW}$	
$\tau^\pm \rightarrow \nu_\tau \pi^\pm \pi^0$	25.6%	10.9%	2.35	25.6%	23.8%	1.08	25.5%
$\tau^\pm \rightarrow \nu_\tau e^\pm \nu_e$	17.4%	10.0%	1.74	17.4%	17.3%	1.01	17.8%
$\tau^\pm \rightarrow \nu_\tau \mu^\pm \nu_\mu$	17.4%	10.1%	1.71	17.4%	17.2%	1.01	17.4%
$\tau^\pm \rightarrow \nu_\tau \pi^\pm$	10.8%	9.8%	1.11	10.8%	11.5%	0.94	10.8%
$\tau^\pm \rightarrow \nu_\tau \pi^\pm 2\pi^0$	9.2%	13.1%	0.70	9.3%	9.8%	0.94	9.3%
$\tau^\pm \rightarrow \nu_\tau 3\pi^\pm$	9.3%	12.5%	0.74	9.2%	9.6%	0.96	9.0%
$\tau^\pm \rightarrow \nu_\tau 3\pi^\pm \pi^0$	4.6%	12.9%	0.36	4.6%	4.9%	0.95	2.7%
$\tau^\pm \rightarrow \nu_\tau \pi^\pm 3\pi^0$	1.0%	4.3%	0.24	1.0%	1.1%	0.91	1.0%
$\tau^\pm \rightarrow \text{Other}$	4.6%	16.3%	0.28	4.6%	4.8%	0.97	6.5%

sample showered with HERWIG 7.1 shows clear deviations from both the PYTHIA 8 sample and the PDG values, while the CLFV  $t\bar{t}$  decay sample showered with HERWIG 7.1 shows smaller deviations.

Plots showing the invariant mass distributions of the decay products in dominant tau decay modes can be seen in Fig. B.1 for the inclusive EFT CLFV  $t\bar{t}$  decay sample and the  $\mathcal{O}_{lequ}^{1(2313)} gu_k \rightarrow t\mu\tau$  production sample. The  $\mathcal{O}_{lequ}^{1(2313)}$  production sample shows particularly poor modelling of the tau BF's while the inclusive decay sample shows much better agreement with PYTHIA 8. Kinematic differences between the PYTHIA 8 and HERWIG 7.1 samples are seen for some of the hadronic tau decay modes while the leptonic tau decay modes are seen to be very similar, as would be expected when using different parton shower and hadronisation

models. Additionally, those differences seen between PYTHIA 8 and HERWIG 7.1 samples are present in both the  $\mathcal{O}_{lequ}^{1(2313)}$  production and inclusive decay samples. It is concluded therefore that the mismodelling in the HERWIG 7.1 samples affects predominantly affects the BF's and not the kinematics of individual decays.

## B.1 Reweighting procedure

Reweighting factors,  $f_{RW}$ , are used to correct the BF's of each tau decay in the HERWIG 7.1 samples to match those seen in the equivalent PYTHIA 8 signal samples. These have been derived using MC truth information with a modified version of the MC TAU Decay Rivet routine [219, 220] for the nine decay modes shown in Table B.1. Events falling into the ' $\tau^\pm \rightarrow$  other' category are not further subdivided as reweighting factors for these have been seen to be consistent with MC statistical uncertainties and these events represent only a small fraction of tau decay modes. The propagated MC statistical uncertainty on the reweighting factors ranges from 1.0% to 5.2%. The procedure results in nine reweighting factors for each HERWIG 7.1 sample where each reweighting factor is defined as the ratio of the BF of the corresponding decay in the PYTHIA 8 sample to that in the HERWIG 7.1 sample. Reweighting factors are defined such that the total sum of weights for the sample remains the same.

To apply the correct reweighting factors to the events at the reconstruction-level, reconstructed  $\tau_{\text{had-vis}}$  candidates are truth-matched. If the candidate is matched to a true  $\tau_{\text{had-vis}}$  then it is classified according to the decay products of the truth tau. Reconstructed  $\tau_{\text{had-vis}}$  which are not truth-matched to a tau lepton have no reweighting applied since these are likely to be fake  $\tau_{\text{had-vis}}$  candidates. Events with light leptons originating from leptonic tau decays are also reweighted. For events with more than one  $\tau_{\text{had-vis}}/\tau_{\text{lep}}$ , the product of reweighting factors is used to provide the overall reweighting factor for the event.

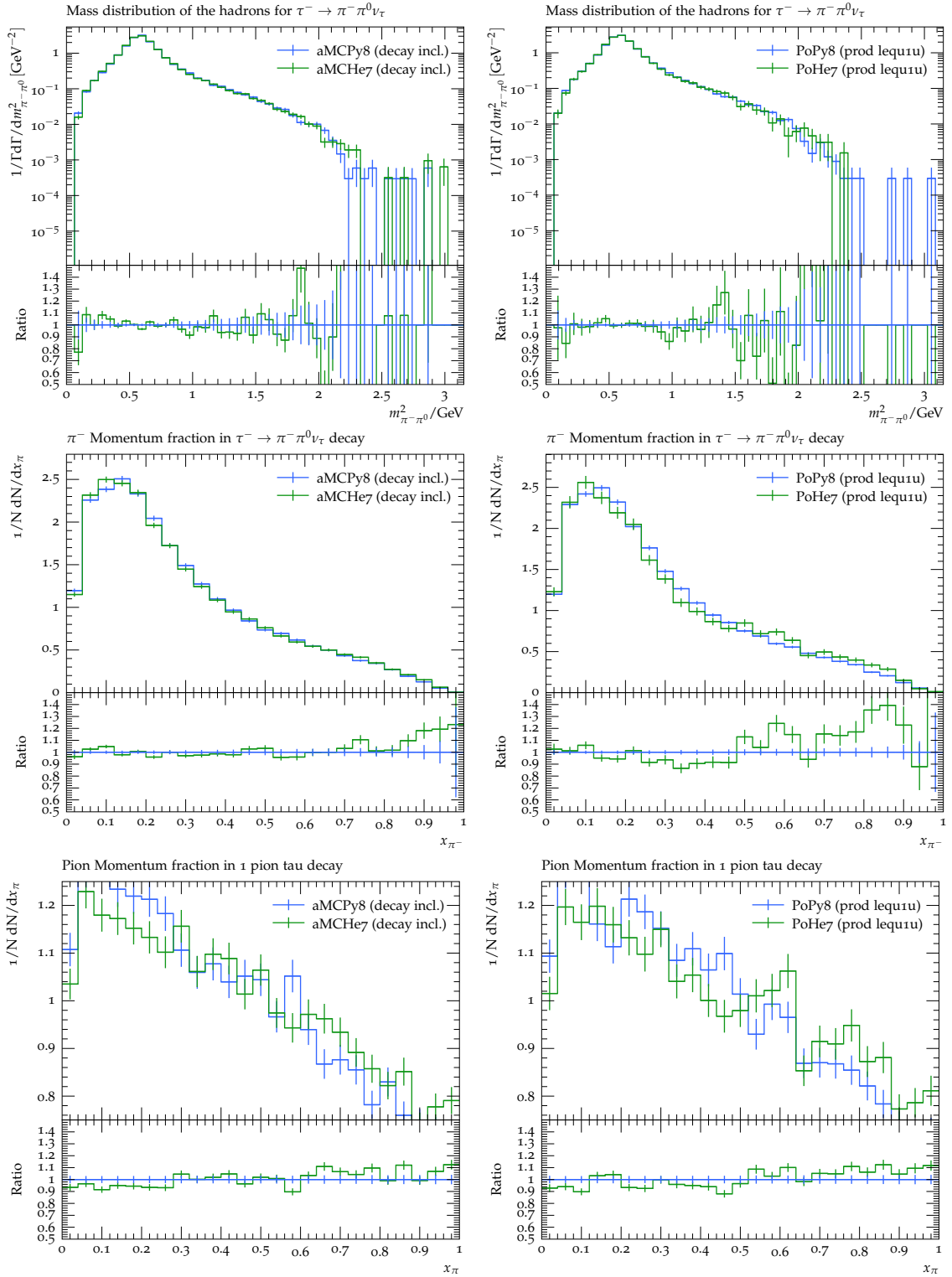


Figure B.1: Invariant mass plots for hadronic taus decays  $\tau^\pm \rightarrow \nu_\tau \pi^\pm \pi^0$  (25.5% BF [53]) &  $\tau^\pm \rightarrow \nu_\tau \pi^\pm$  (10.8% BF) for inclusive decay (left) and  $\mathcal{O}_{lequ}^{1(2313)}$  production (right) samples.

## B.2 Signal parton shower uncertainty

The reweighted HERWIG 7.1 sample is used to evaluate the EFT signal parton shower and hadronisation modelling uncertainty. Any uncertainty on the reweighting procedure is taken into account by ensuring the resulting systematic shift covers this uncertainty. The MC statistical uncertainty,  $\delta f_{RW}$ , on each of the reweighting factors is found and events are reweighted using up and down variations given by a conservative band of  $f_{RW} \pm 3\delta f_{RW}$ , as well as with the nominal values of  $f_{RW}$ . The largest overall deviation between the reweighted HERWIG 7.1 samples (either  $f_{RW}$  or  $f_{RW} \pm 3\delta f_{RW}$ ) and the equivalent nominal PYTHIA 8 signal sample, is taken as the conservative parton shower variation. The resulting systematic shifts for the inclusive EFT samples in the SR can be seen in Fig. B.2, before and after reweighting. The effect of reweighting is small for the CLFV decay sample but has a larger effect for the production sample, where more significant mismodelling of the BFs is observed. In both cases reweighting increases the size of the parton shower and hadronisation uncertainty.

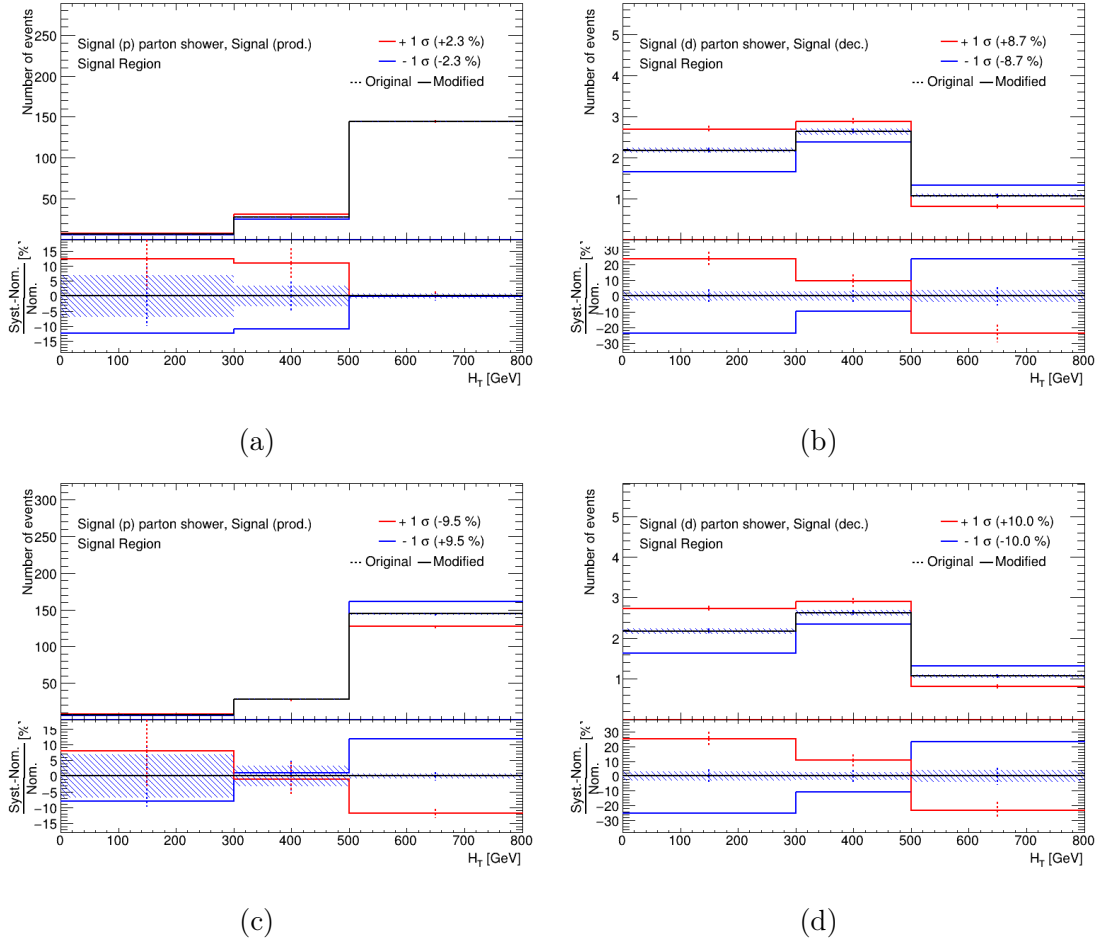


Figure B.2: Effect of  $\pm 1\sigma$  variations of the signal parton shower nuisance parameters for inclusive decay and production signal samples in the SR before (a-b) and after reweighting (c-d).

# Appendix C

## Fake $\tau_{\text{had-vis}}$ background estimation

This appendix documents studies made during the development of the fake  $\tau_{\text{had-vis}}$  background estimation and provides cross-checks of the default technique used in the analysis.

### C.1 Fake $\tau_{\text{had-vis}}$ SF parametrisation

The SFs used to correct the shape and normalisation of the fake  $\tau_{\text{had-vis}}$  background, described in Section 6.5, are binned in the jet width and track multiplicity of the  $\tau_{\text{had-vis}}$  candidate. A number of different variables have also been checked to ensure all significant kinematic dependence is captured by the SFs. Fig. C.1 shows these SFs binned in different kinematic variables.

For each plot, the binned SFs in red are compared to an inclusive (unbinned) SF indicated by the dashed black line. Smaller deviations from the inclusive SF are seen in  $H_T$ ,  $E_T^{\text{miss}}$  and  $p_T$  of the  $\tau_{\text{had-vis}}$  candidate. Deviations from the inclusive SF are seen for binned SFs at low  $H_T$  and high  $E_T^{\text{miss}}$ , both of which are sparsely populated regions of phase space

in  $CR\tau$ . For SFs binned in  $\tau_{\text{had-vis}}$   $p_T$ , deviations from the inclusive SF are seen at low  $p_T$  which where most  $\tau_{\text{had-vis}}$  feature in  $CR\tau$ . A slight asymmetry is observed in the SFs binned in  $\tau_{\text{had-vis}}$   $\eta$ , however, it is expected that the rate of production of fake  $\tau_{\text{had-vis}}$  should be  $\eta$ -symmetric since the production of additional jets in  $Z$  boson production should not depend on the sign of  $\eta$ . This is therefore not taken into account in the parametrisation of the SF method.

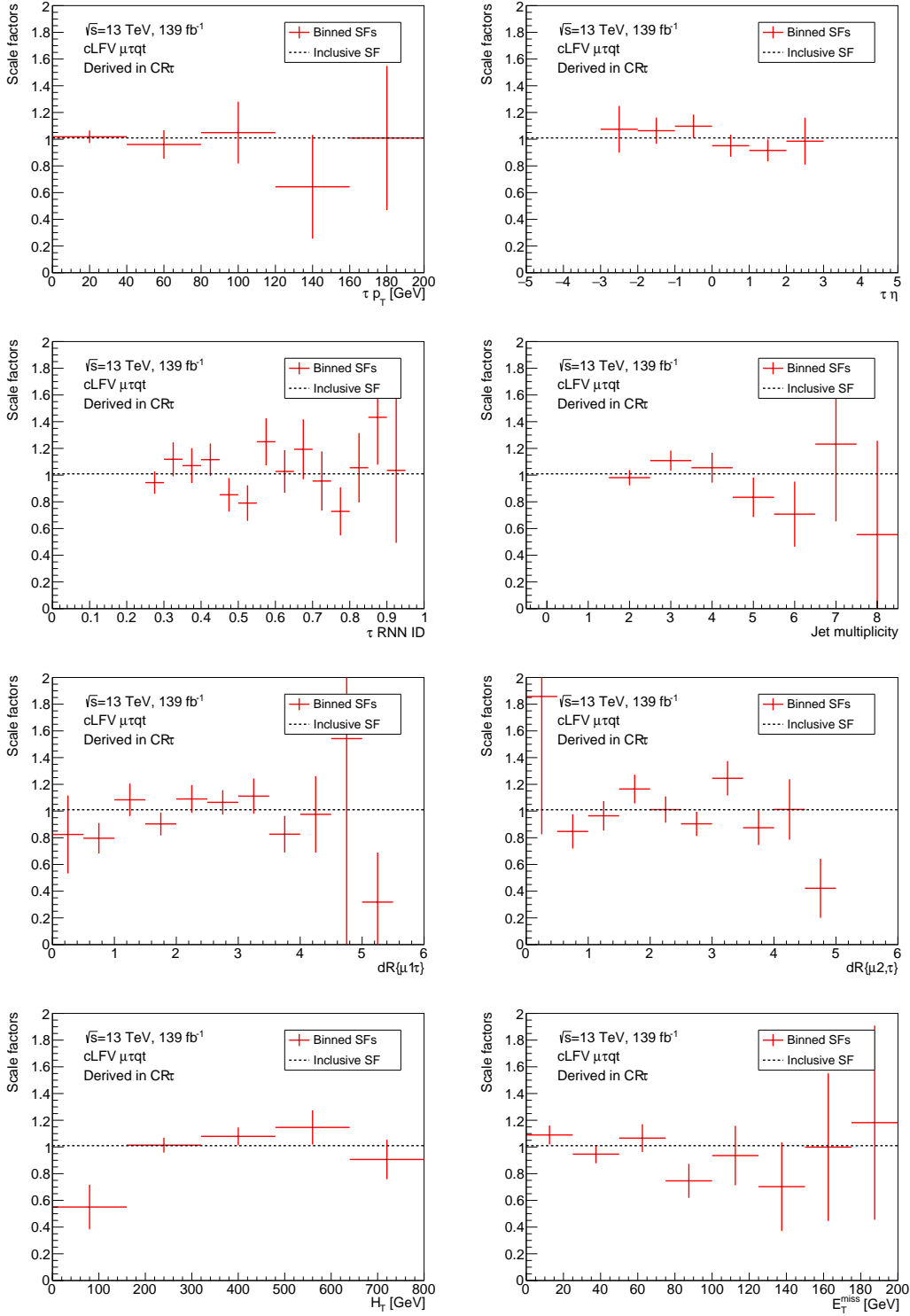


Figure C.1: Alternative parametrisation of fake  $\tau_{\text{had-vis}}$  scale factors derived in  $CR\tau$ . For each plot, the binned SFs in red are compared to an inclusive SF shown by the dashed black line.

# Appendix D

## Statistical analysis

### D.1 Validity of asymptotic approximation in limit-setting

The method used to extract exclusion limits, discussed in Section 7.1.3, relies on Wilks' theorem [214] to assume the distribution of the test statistic. The final bin of the SR  $H_T$  distribution contains few events under the background-only hypothesis. Since the production signal distribution peaks at high  $H_T$ , the signal sensitivity derives predominantly from this final bin so it is necessary to check that the asymptotic approximation is still valid. The generation of toy datasets has been used to evaluate the distribution of the test statistic under different hypotheses and validate the use of the asymptotic approximation for this fit setup.

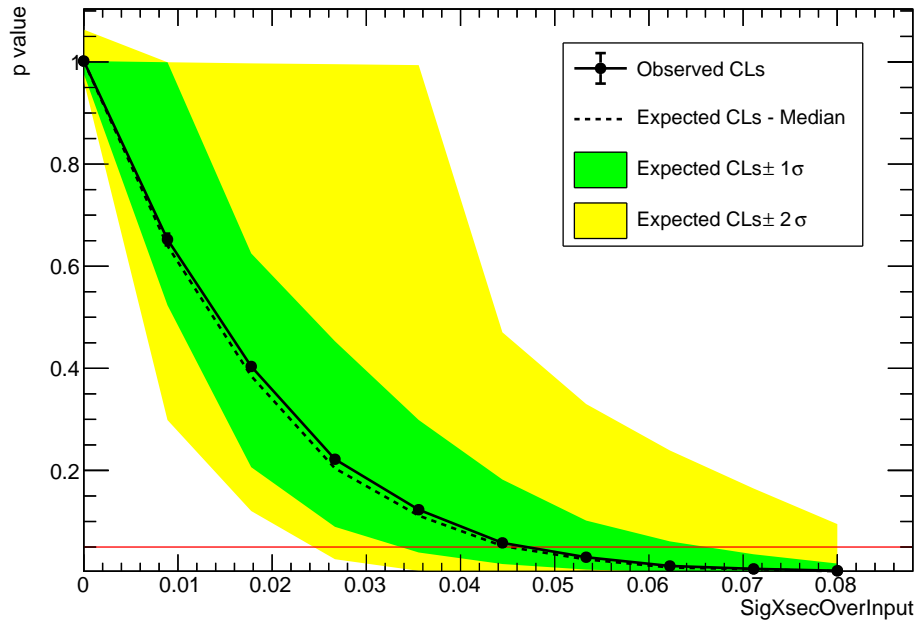
A total of 13000 signal-plus-background and 5000 background-only toy distributions have been generated for ten evenly-spaced points in the range  $0.0 \leq \mu_{\text{CLFV}} \leq 0.08$ . The resulting  $p$ -values under the signal-plus-background hypothesis are shown as a function of  $\mu_{\text{CLFV}}$  in Fig. D.1a. The exclusion limit at 95% CL corresponds to the point where the  $p$ -value reaches 0.05 on the y-axis. Fig. D.1b compares the expected limit on the signal process using

the two methods to extract the limits. These limits are also shown in Table D.1, from which it can be seen that the limit extracted using the asymptotic approximation is consistent with that using toys within 5%.

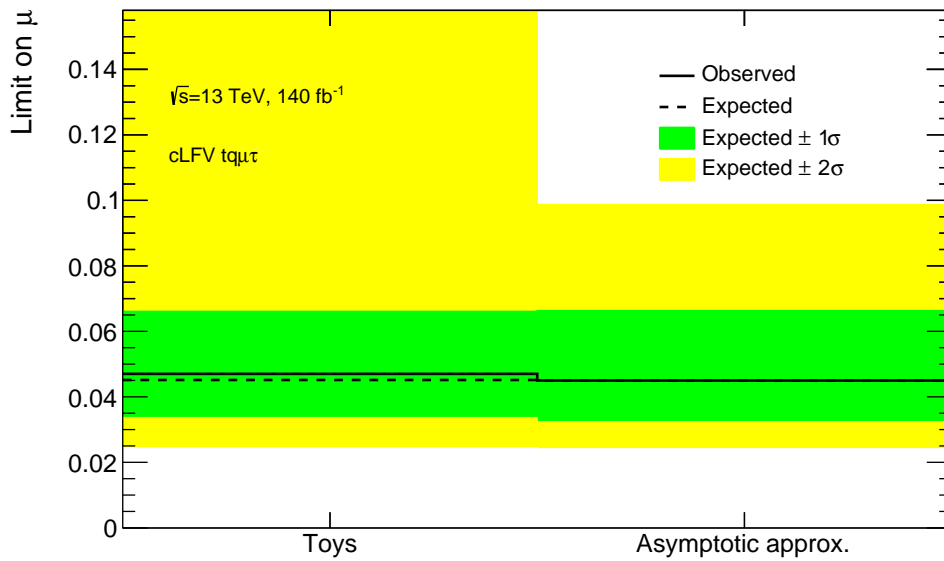
As can be seen from Fig. D.1a the maximum scan value of  $\mu_{\text{CLFV}}$  was not large enough to extract the  $+2\sigma$  exclusion edge but all other limits and bands can be seen to be compatible in Fig. D.1b.

Table D.1: Expected exclusion limits on  $\mu_{\text{CLFV}}$  extracted from the mixed data and Asimov fit using both MC toys and the asymptotic approximation. “Observed” reflects the fact that data from  $\text{CR}t\bar{t}\mu$  has been used in the limit-setting while the SR remains blinded, hence the observed and median expected values are almost identical.

	<b>Exclusion limit (95% CL)</b>	
	<b>MC toys</b>	<b>Asymptotic approx.</b>
Observed	0.0470	0.0451
Expected	0.0452	0.0451
Expected $\pm 1\sigma$	0.066/0.034	0.067/0.032
Expected $\pm 2\sigma$	-/0.024	0.099/0.024



(a)



(b)

Figure D.1: Plots of p-values for signal-plus-background and background-only hypotheses using toy datasets (a) and comparison of limits obtained using toys to limits using the asymptotic approximation (b). “Observed” reflects the fact that data from  $CRt\bar{t}\mu$  has been used in the limit-setting while the SR remains blinded, hence the observed and median expected values are almost identical.

# Appendix E

## EFT interpretation

### E.1 Additional information on EFT samples

Fig. E.1 shows the  $H_T$  distributions for different SMEFT operator contributions to the CLFV  $t\mu\tau u_k$  process. It can be seen that there are not significant shape difference between the operators in this distribution, which is why no attempt is made to resolve these different contributions in a single fit. The  $H_T$  parametrisation is chosen as it provides very good signal-background discrimination.

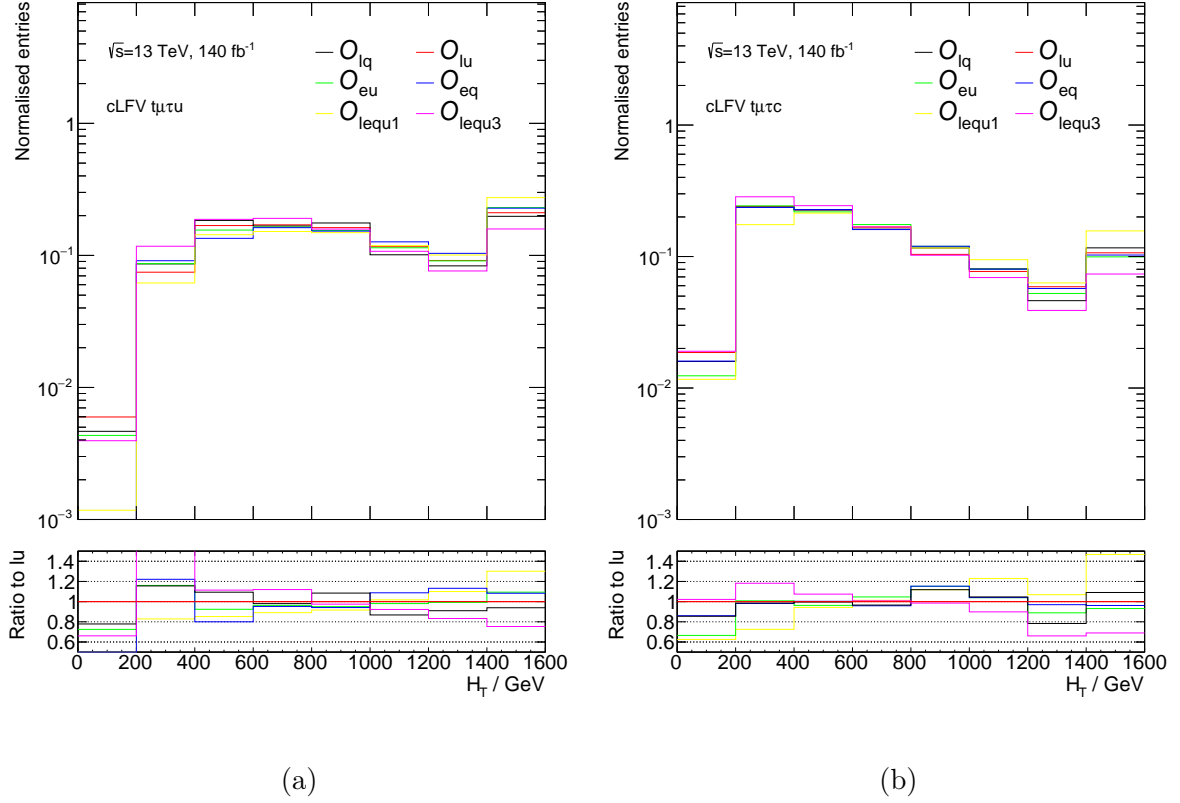


Figure E.1:  $H_T$  distributions for each of the EFT contributions in  $t\mu\tau\nu$  (a) and  $t\mu\tau c$  (b) interactions. The final bin does not have an upper bound. Contributions from the CLFV production and decay process are summed together before the whole distribution is normalised to unity to show any differences in shape.

# Appendix F

## Leptoquark interpretation

Table F.1 shows the cross-sections for the  $gc \rightarrow S_1 \ell \rightarrow t \ell \ell'$  LQ samples for all masses and coupling strengths studied. The cross-sections are computed with the MG\_AMC@NLO 2.9.5 generator at LO using the UFO model described in [146, 147]. Table F.1 also shows the scale factors used to reweight the  $gc \rightarrow S_1 \ell \rightarrow t \ell \ell'$  samples to include the expected effect of  $gu \rightarrow S_1 \ell \rightarrow t \ell \ell'$  contributions.

Fig. F.1 shows the observed and expected exclusion limits at 95% CL on the cross-section of the  $gu_k \rightarrow S_1 \ell \rightarrow t \ell \ell'$  process, where  $u_k = \{u, c\}$ , as a function of  $\lambda$  for different LQ masses. In general, the observed and expected upper exclusion limits set on the cross-section of the LQ process do not vary significantly as a function of LQ mass or coupling. Fig. F.2d shows the exclusion limits for  $m_{S_1} = 2250$  GeV, where it can be seen that the theoretical cross-section (in red) does not intersect the expected or observed cross-section limits and hence no limit is derived. The same is true for  $m_{S_1} = 2500$  GeV, for which the plot of exclusion limits is not shown. Due to the slight excess observed in the data, in some cases the observed exclusion limit on the cross-section exceeds that of the range of coupling values generated, as can be seen for example in Fig. F.1c. In this case extrapolation has been

performed using a linear fit to the observed exclusion limits as a function of  $\lambda$  since these are observed to be roughly constant across the range of mass and coupling values studied. Extrapolation by fitting a zeroth order polynomial to the observed exclusion limits has also been tested but a linear fit was seen to give slightly more conservative limits.

Table F.1: Theoretical cross-sections for single leptoquark production by the process  $gc \rightarrow S_1 \ell \rightarrow t \ell \ell'$  and scale factors used to reweight each sample to include the expected contribution of  $gu \rightarrow S_1 \ell \rightarrow t \ell \ell'$  diagrams. Cross-section and scale factor values are shown as a function of LQ mass,  $m_{S_1}$ , and coupling strength,  $\lambda$ . The uncertainties on the cross-sections from scale variations are in the range 13-20% while PDFs uncertainties are approximately 1% for  $gu \rightarrow S_1 \ell \rightarrow t \ell \ell'$  and 4% for  $gc \rightarrow S_1 \ell \rightarrow t \ell \ell'$ ; cross-section values have been rounded to three significant figures to reflect this. Values in this table have been derived by Dr Jacob Kempster.

$m_{S_1} / \text{GeV}$	$\lambda$	Cross-section / fb ( $gc \rightarrow S_1 \ell \rightarrow t \ell \ell'$ )	Reweighting			
			SF bin 1	SF bin 2	SF bin 3	Cross-section ratio
500	0.5	1.21	1.04	1.05	1.09	1.08
500	1.0	8.49	1.04	1.05	1.11	1.08
500	1.5	37.2	1.04	1.05	1.11	1.08
500	2.0	114	1.04	1.05	1.10	1.08
750	0.5	0.257	1.04	1.06	1.11	1.10
750	1.0	2.47	1.04	1.05	1.11	1.09
750	1.5	11.5	1.03	1.05	1.12	1.09
750	2.0	35.8	1.04	1.05	1.11	1.09
1000	0.5	0.087	1.04	1.05	1.13	1.11
1000	1.0	0.979	1.04	1.06	1.12	1.10
1000	1.5	4.69	1.04	1.06	1.12	1.10
1000	2.0	14.6	1.03	1.05	1.12	1.10
1250	1.0	0.464	1.05	1.05	1.13	1.11
1250	1.5	2.25	1.03	1.06	1.12	1.11
1250	2.0	7.04	1.03	1.05	1.12	1.11
1250	2.5	17.1	1.04	1.05	1.13	1.11
1500	1.5	1.20	1.04	1.05	1.14	1.11
1500	2.0	3.77	1.04	1.05	1.14	1.11
1500	2.5	9.20	1.04	1.05	1.13	1.11
1500	3.0	19.0	1.05	1.05	1.13	1.11
1750	1.5	0.699	1.06	1.05	1.14	1.12
1750	2.0	2.20	1.04	1.05	1.14	1.12
1750	2.5	5.35	1.04	1.06	1.14	1.12
1750	3.0	11.1	1.06	1.05	1.14	1.12

Table F.2: Theoretical cross-sections for single leptoquark production by the process  $gc \rightarrow S_1\ell \rightarrow t\ell\ell'$  and scale factors used to reweight each sample to include the expected contribution of  $gu \rightarrow S_1\ell \rightarrow t\ell\ell'$  diagrams. Cross-section and scale factor values are shown as a function of LQ mass,  $m_{S_1}$ , and coupling strength,  $\lambda$ . The uncertainties on the cross-sections from scale variations are in the range 13-20% while PDFs uncertainties are approximately 1% for  $gu \rightarrow S_1\ell \rightarrow t\ell\ell'$  and 4% for  $gc \rightarrow S_1\ell \rightarrow t\ell\ell'$ ; cross-section values have been rounded to three significant figures to reflect this. Values in this table have been derived by Dr Jacob Kempster.

$m_{S_1} / \text{GeV}$	$\lambda$	Cross-section / fb ( $gc \rightarrow S_1\ell \rightarrow t\ell\ell'$ )	Reweighting			
			SF bin 1	SF bin 2	SF bin 3	Cross-section ratio
2000	2.0	1.36	1.06	1.06	1.15	1.12
2000	2.5	3.32	1.09	1.06	1.13	1.12
2000	3.0	6.88	1.04	1.06	1.15	1.12
2000	3.5	12.7	1.04	1.06	1.14	1.12
2250	2.0	0.886	1.04	1.05	1.14	1.12
2250	2.5	2.16	1.02	1.06	1.15	1.12
2250	3.0	4.47	1.06	1.05	1.15	1.12
2250	3.5	8.28	1.07	1.06	1.15	1.12
2500	2.5	1.46	1.04	1.06	1.15	1.13
2500	3.0	3.03	1.04	1.05	1.15	1.13
2500	3.5	5.60	1.02	1.05	1.15	1.13

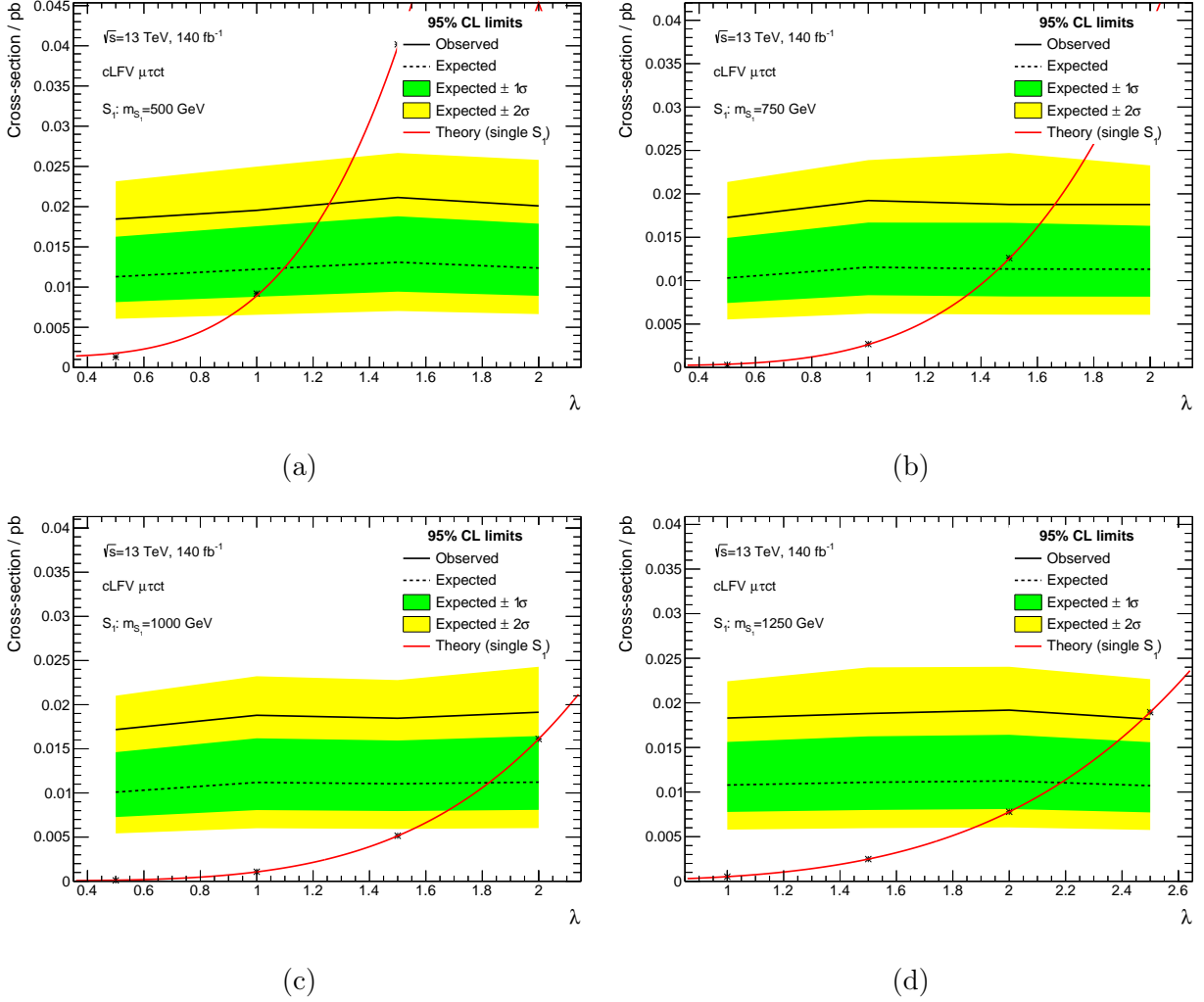


Figure F.1: Exclusion limits at 95% CL on the cross-section of the  $gu_k \rightarrow S_1 \ell \rightarrow t \ell \ell'$  process as a function of the coupling  $\lambda$  for LQ masses of 500 GeV (a), 750 GeV (b), 1000 GeV (c), and 1250 GeV (d). Expected limits are shown by the dashed black line with the  $\pm 1\sigma$  ( $\pm 2\sigma$ ) uncertainty bands shown in green (yellow); observed limits are shown by the solid black line. Black cross markers show theoretical predictions of the cross-section for particular values of  $\lambda$  and the solid red line shows the quartic fit to these.

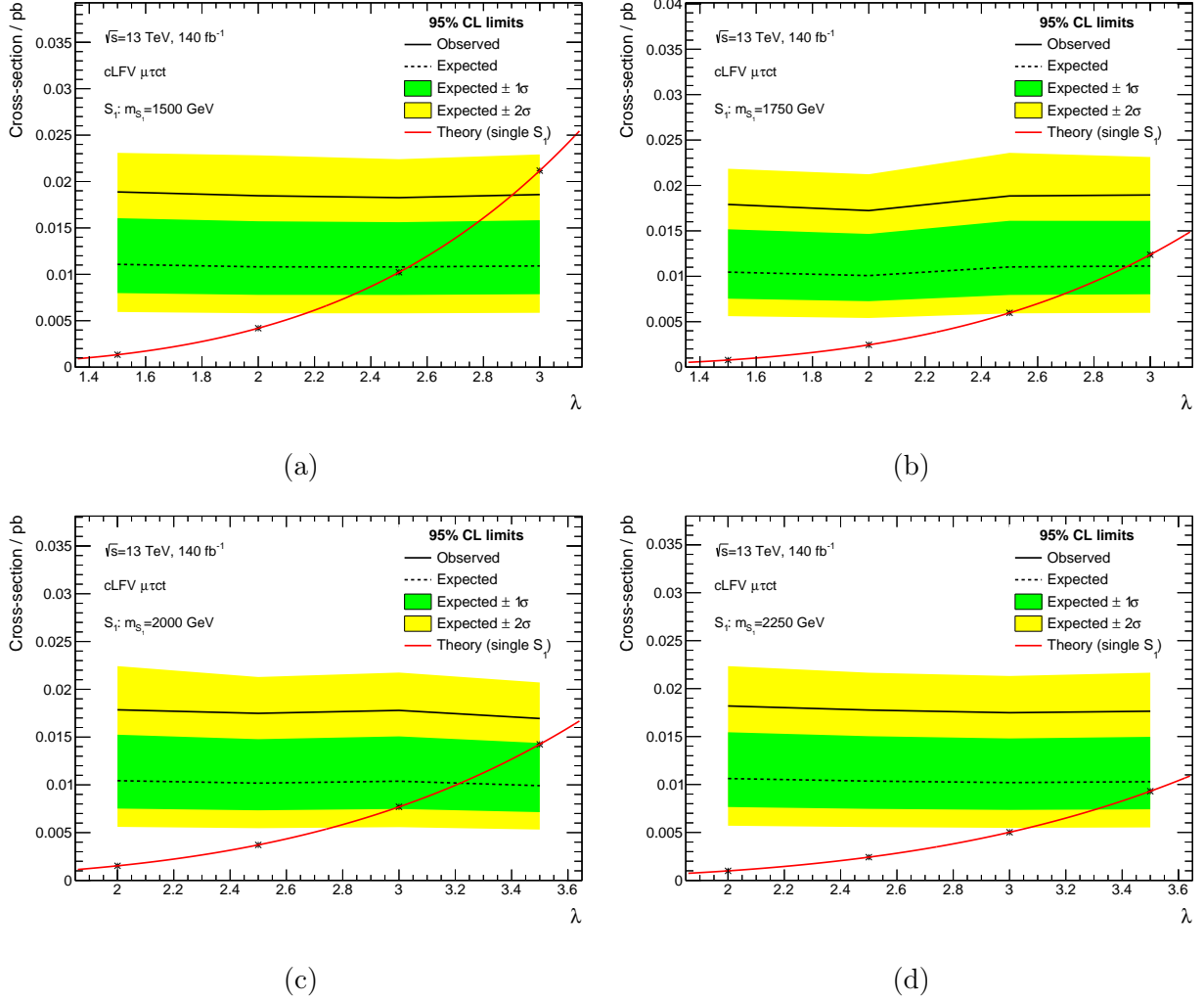


Figure F.2: Exclusion limits at 95% CL on the cross-section of the  $gu_k \rightarrow S_1 \ell \rightarrow t \ell \ell'$  process as a function of the coupling  $\lambda$  for for LQ masses of 1500 GeV (a), 1750 GeV (b), 2000 GeV (c), and 2250 TeV (d). Expected limits are shown by the dashed black line with the  $\pm 1\sigma$  ( $\pm 2\sigma$ ) uncertainty bands shown in green (yellow); observed limits are shown by the solid black line. Black cross markers show theoretical predictions of the cross-section for particular values of  $\lambda$  and the solid red line show the the quartic fit to these.